國立成功大學

地球科學研究所

博士論文

有孔蟲殼體微量元素比與穩定同位素組成：南海之校正與古海洋應用

Trace Element Ratios and Stable Isotopic Compositions of Planktonic Foraminiferal Shell collected from the South China Sea: *Geochemical Calibration and Paleoceanographic Implication*

研　究　生：黃國芳

指導教授：游鎮烽

中華民國九十六年七月

國立成功大學

博士論文

有孔蟲殼體微量元素比與穩定同位素組成：
南海之校正與古海洋應用
Trace Element Ratios and Stable Isotopic Compositions of Planktonic Foraminifera Shell Collected from the South China Sea: Geochemical Calibration and Paleoceanographic Implication

研究生：黃國芳

本論文業經審查及口試合格特此證明

論文考試委員：何恭算
謝英宗
楊懷仁
何東垣

指導教授：游鎮烽

系(所)主管：

中 華 民 國 96 年 7 月 12 日

ABSTRACT OF THE DISSERTATION

Long-term climatic and environmental reconstruction from marine sediments relies heavily on the reliable geochemical proxies from foraminiferal shells. Therefore, the aim of this dissertation is to improve our understanding and confidence in planktonic foraminiferal proxies as indicators of seawater physical (e.g., sea surface temperature, SST) and chemical (e.g., composition and pH value) properties. Toward this goal, natural laboratory calibration works of foraminiferal shell chemistry have been carried out by using specimens collected from sediment traps and core-top sediments in the South China Sea (SCS).

First of all, high-precision and high-accurate measurements on trace element ratios, boron and strontium isotopic compositions in planktonic foraminifera were investigated, and have been successfully developed for carbonate samples (CHAPTER 2). This technique would allow us to obtain more reliable trace elements and isotopic compositions in foraminiferal shell calcites, and provides a powerful tool to study the paleoceanographic reconstructions in the SCS. Applying this analytical technique, in situ Mg/Ca-SST calibration equation for the three abundant planktonic species in the SCS can be described as $Mg/Ca = 0.32 \exp(0.090*T)$ using time-series sediment trap, and intense dissolution artifact has also been taken into account for obtaining more accurate SST records (CHAPTER 3). In addition, a dissolution-corrected equation was developed using trap data from different depths. These temperature equations are $Mg/Ca = (0.38-0.02* \text{water depth (km)}) \exp(0.090*T)$ and $Mg/Ca = 0.30 \exp(0.090*T)$ for fall-winter and spring-summer season, respectively. These equations can be applied for accurate reconstruction of mixed layer and thermocline temperatures in sediment cores.

Changes in the local SST and freshwater budget over the last 22 kyrs have been reconstructed from the tropical SCS (CHAPTER 4). Through the comparison of the east-west (zonal) SST gradient between western and eastern Pacific, a persistent ENSO-like pattern can

be seen during the Last Glacial Maximum (LGM). This is contrasted with mid-Holocene cooling suggest a La Niña-like pattern with enhanced SST gradients and strengthened trade winds. Low salinity in the northern SCS during the LGM probably reflects an increase in freshwater inputs from several emerged rivers across the Sunda Shelf during glacial shelf exposure. Alternatively, an influence by the closure of the southern straits would cut off the inflow of high saline waters from the Indo-Pacific into the SCS cannot be excluded. For the thermal structure of the upper water column, Mg/Ca-based temperature variability reconstructed by three different planktonic species shows a strong mixing during the LGM, and becomes more stratified during the Holocene. Combining with shell chemistry, the covariation of Mg/Ca and Ba/Ca over the last 220 kyrs indicates a variation in the continental input associated with the glacial-interglacial changes.

Results from core-top sediments in the SCS demonstrate that B/Ca ratios in the three planktonic foraminiferal species are strongly affected by seawater temperature and pH (CHAPTER 5). Species-specific foraminiferal B/Ca ratios from core-top sediments are in equilibrium with ambient seawater $[B(OH)_4^-/HCO_3^-]$ in response to their habitat depths in the modern water column, indicating shell B/Ca can be used as a reliable paleo-pH proxy by applying the dissolution-corrected Mg/Ca-derived SST and K_D of B/Ca. The pH and pCO_2 reconstructions at Site 1145 indicate that the variability of surface-ocean pCO_2 shows a more variability than atmospheric CO_2 records, and the ocean-atmosphere CO_2 flux has substantially changed with time in the SCS. The pCO_2 (or pH) in glacial surface waters was approximately 150 ppmv lower (or 0.3 pH units higher) than the Holocene. This amplitude in surface-water pCO_2 is significantly larger than changes in atmospheric pCO_2 recorded in the ice cores (~ 90 ppmv). This observation indicates that this area was a strong CO_2 sink to the atmosphere at the LGM, and presumably reflects a significant increase in regional primary productivity in the north SCS during the LGM.

The B isotopic analyses presented here have been successfully developed, and extend its potential applications for various natural samples, including seawaters, pore waters and biogenic carbonates (CHAPTER 6). For the natural seawaters, $\delta^{11}B$ shows a rather homogeneous distribution in the open ocean ($\delta^{11}B$= 39.6±0.2‰), but slightly negative $\delta^{11}B$ value can be determined in the coastal ocean ($\delta^{11}B$= 38.6±0.3‰). This can be attributed to the influence of riverine inputs (averaged $\delta^{11}B$= +10‰, [*Lemarchand et al.*, 2000]) with substantially lighter $\delta^{11}B$ relative to seawater. B and $\delta^{11}B$ in pore fluids collected from the southern Okinawa Trough and South China Sea show a complicated distribution pattern with depths, indicating distinct geochemical processes or admixtures of fluids with various source end-members of B were involved in different geological settings. Because of the large variability of B (200-2000 μM) and $\delta^{11}B$ (+32-+51‰) in pore fluids, the approach using foraminiferal $\delta^{11}B$ to estimate pH into long-term and short-term timescale needs to be interpreted cautiously due to potential influences of diagenetic processes that reacted with the surrounding sediment pore waters.

The result also indicates that the recovery yields of B extraction by microsublimation is close to 100%, and shows that a precise determination of B isotopic ratios is possible for coral skeletons and foraminiferal shells. This advance would offer an opportunity to evaluate the empirical calibration of $\delta^{11}B$/pH, and further refine the relationship between surface water pCO_2 and atmospheric CO_2 level in short- and long-term timescales.

The first detailed observations of Sr isotopic compositions (Sr ICs) in surface and vertical seawater profiles in the SCS and around Taiwan were investigated through the high-precision Sr isotopic measurement (CHAPTER 7). Combining results of Sr ICs, T, S and $\delta^{18}O$, we have found that Sr ICs are distributed rather complicated and in-homogeneously both in vertical ($\Delta^{87}Sr$ variation >40 ppm) and surface (>50 ppm) distributions after a heavy flood event. In the Kao-ping river-sea system, the surface Sr ICs were affected by mixing of three end-members water masses: two episodic continental runoffs with radiogenic Sr ICs and a modified SCSSW. The two radiogenic sources were most likely resulted from: (1) unusual inputs of radiogenic Sr due to typhoon disturbance in the upper stream (i.e., top soils or ambient rocks), (2) intense water/sediment interaction in seawater column in response to heavy rainfalls, or (3) normal river discharge plume into the coastal zone. Vertical Δ^{87}Sr profiles along the Kao-ping canyon show large isotopic variations in the upper most 200 m, possibly were affected by continental runoffs (e.g., Kao-ping River: Δ^{87}Sr~ 5500 ppm) and local seawater masses. Below 200 m, Sr ICs gradually become radiogenic while decreasing distance toward river mouth and reflect relatively high contribution of terrestrial inputs.

Sr isotopic composition in planktonic foraminifera shows a species dependency, but is independent of pre-cleaning method, and is in equilibrium with ambient seawater Sr isotopes. The results presented here strongly suggest that the use of foraminiferal Sr isotopes for reconstructing seawater ^{87}Sr/^{86}Sr ratios with time. A small, but significant variation of about 40 ppm in the seawater ^{87}Sr/^{86}Sr can be found in the SCS, and seems to follow a cycle to the previously reported 100-kyr cycle. This periodicity can be linked to one of the prominent cycles in the Earth's orbital parameters, which are known to modulate the patterns of solar insolation and climate. On this short timescale these changes are most likely be controlled by variations in the riverine Sr input.

ACKNOWLEDGEMENT

There have been countless people who have ever helped make this thesis possible. Foremost, I would like to thank my thesis advisor Dr. Chen-Feng You. Under his introduction and guidance I was able to work on an exciting and fruitful project. Furthermore, his always supported me on many geochemical topics which I was interested, and let me try many different studies and helped me to think about sciences in different ways. Also, his constant enthusiasm and scientific expertise made a tremendous impact on me. I also think Dr. Ying-Tzung Shieh for introducing me to the field of Paleoceanography, and Dr. Hui-Ling Lin for her continuous support of the studying materials from sediment traps, core-tops, and sediment cores. Dr. Yair Rosenthal was also thanked for taking care of my life in the US and providing scientific suggestions in Chemical Oceanography and Paleoceanography.

I thank my many colleagues for helping in the lab and fields. I was very fortunate to work in a very supportive community. Drs. Shangde Luo, Kung-Suan Ho, Huei-Jen Yang, and Tung-Yuan Ho were appreciated for their contribution and very useful comments on my thesis work. Dr. Hong-Chuan Li was enormously helpful in the Quaternary Climatology. Dr. Wen-Chien Chou was especially thanked for selflessly providing me many data regarding carbonate parameters. Bear and Bo were tremendously helpful with the analytical work necessary to complete the methodology in my thesis. I also thank Miss Hsuen-Tzu Chen for taking care of the administrative details of graduate school, and many funny things from Ming-Lin, Mr. Bean (Tuan-Fu), Miao-Ching, Ruo-Mei, Nai-Jung, Hsin-Pei, and other lab members during these years. My dear classmates, Jun-Jung, Mei-I, Yi-Tzu, Su-Ying, and dear friends, Rob, Paul, Sindia, Marina, Eleni, Michelle, Emily and Kate, from IMCS were also thanked for their helps both on life and researches.

Finally, I would like to thank my dad, my mom, my young brother and Yung-Hsin for their outstanding source of inspiration and support on these years.

TABLE OF CONTENTS

CHAPTER 1. Introduction

CHAPTER 2. Methods

2.1 High Resolution ICP-MS (HR-ICP-MS)

2.2 Thermal Ionization Mass Spectrometry (TIMS)

2.3 Foraminiferal Methods

2.4 Seawater and Pore waters Methods

References

CHAPTER 3. In situ Calibration of Mg/Ca Ratio in Planktonic Foraminiferal Shell using Time-series Sediment Trap: A case study of intense dissolution artifact in the South China Sea

3.4 Materials and Methods

3.5 Sediment Trap Results

3.6 Discussion

3.7. Comparison of Existing Calibrations

References

CHAPTER 4. Reconstructions of Paleo-SSTs and Paleo-climatic changes in the South China Sea

4.3 Results and Discussion

References

CHAPTER 5. Reconstruction of changes in surface water pCO_2 in tropical South China Sea using foraminiferal multi-proxy approach

5.2 Materials and Methods

5.3 Results

5.4 Discussion

5.5 Paleoceanographic Implication

References

CHAPTER 6. Boron Isotopic Compositions in Seawater and Planktonic Foraminifera: Calibration and Paleo-application

6.3 Column Chemistry

6.4 Results and Discussion

References

CHAPTER 7. Strontium Isotopic Composition in Seawater and Planktonic Foraminifera: Calibration and Paleo-application

7.3 Column Chemistry

7.4 Results and Discussion

References

APPENDIX 1. Supplementary Data

APPENDIX 2. Curriculum Vitae

LIST OF TABLES

CHAPTER 1

CHAPTER 2

CHAPTER 3

CHAPTER 5

CHAPTER 6

CHAPTER 7

LIST OF FIGURES

CHAPTER 1

CHAPTER 2

CHAPETR 3

CHAPTER 4

CHAPTER 5

CHAPTER 6

CHAPTER 7

CHAPTER 1.

Introduction

1.1. General Background and motivation

Knowledge of the driving force and amplitude of natural fluctuation in past climate systems can be used to understand the stability and linkage of the terrestrial, marine and atmosphere subsystems and their potential variations in the future. Changes in orbital forcing, solar radiation as well as cycling of inorganic and organic carbon in the ocean [*Falkowski et al.*, 2000; *Raven and Falkowski*, 1999; *Sigma and Boyle*, 2000] have been proposed as major mechanisms leading to the glacial-interglacial cycles in atmospheric carbon dioxide and temperature variability in high-latitude ice cores [*Petit et al.*, 1999]. In spite of such an important role in controlling Earth's climate on glacial-interglacial timescales, the relevant information regarding how the ocean regulate and response to abrupt climatic event are still poorly constrained and needed to be further refine in order to better constrain the real controlling factors and driving forces on climate change.

Determining the SST evolution and the variation of the marine carbonate system in the ocean are the most fundamental and important elements for addressing past climatic issues and problems. Furthermore, both of the two parameters have been known to significantly influence the long- and short-term global climate change through the transports of heat and moisture from tropical oceans to high latitude regions, as well as the biogeochemical cycle of carbon (Figure 1.1). An understanding of the dynamics of the global carbon cycle and of changes in CO_2 between atmosphere and oceans, as well as sea surface temperature in the past and future therefore demands a comprehension of the role of the ocean in the thermal structure of water column and the carbon cycle. Although a growing body of paleo-proxy approaches in foraminiferal calcite for reconstructing these two parameters have been well established over the past several decades, the more information we get, the more questions being raising because of the complicated mechanisms in the nature system. Therefore, this work was mainly focused on investigating the complexity of these two fundamental factors through the *in situ* sediment-trap and core-top calibrations, and then applied the empirical calibrations to down-core sediments to extract more accurate climatic and environmental information in the past ocean.

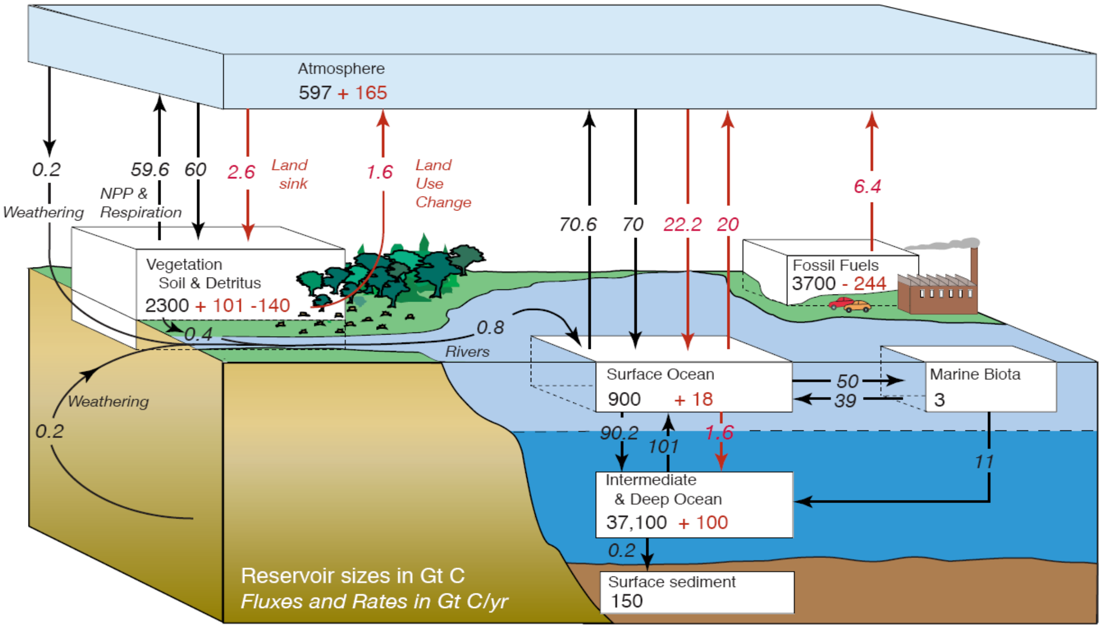

Figure 1.1 Global carbon budget and fluxes in the Earth's reservoirs (adapted from IPCC, 2006). Numbers in black show the amount of storage of carbon in each reservoir, and numbers in red indicate the rate in each reservoir. Numbers on the arrows are the net flux between the reservoirs.

1.1.2. Ocean Temperature

Understanding the temperature evolution of the ocean is a fundamental problem in the Paleoceanography studies. Temperature is the most primary representation of the state of the climate system and oceanic temperature is critical because the ocean is the most important component of the Earth's climate system. In the modern ocean, temperature is a conservative variable that is highly correlated with other oceanographic parameters. For instance, it correlates positively with salinity and seawater [CO_3^{2-}] in the open ocean, which would cause an apparent difficulty in separation of these hydrological parameters in the natural system. Thus, in this study, a continuous time-series monitor and in situ measurement of regional hydrological data in the South China Sea (SCS) were used to solve this difficulty.

More recently, studies of El Niño-Southern Oscillation (ENSO) and La Niña dynamics and impacts demonstrate that the tropical Pacific ocean-temperature system influence global climate on interannual to decadal time scales [*Trenberth et al.*, 1998]. Therefore, sea surface temperature also provides some important information regarding the intensity or the occurrence of the ENSO or La Niña events (Figure 1.2). Because of the locality and climatic characteristics, the studying area in the present study, South China Sea, can provide the valauable information regarding the SST records in the western Pacific region, and thus can be attempted to understand the mechanisms for controlling the short-term and long-term El Niño and La Niña behaviors [*Koutavas et al.*, 2002].

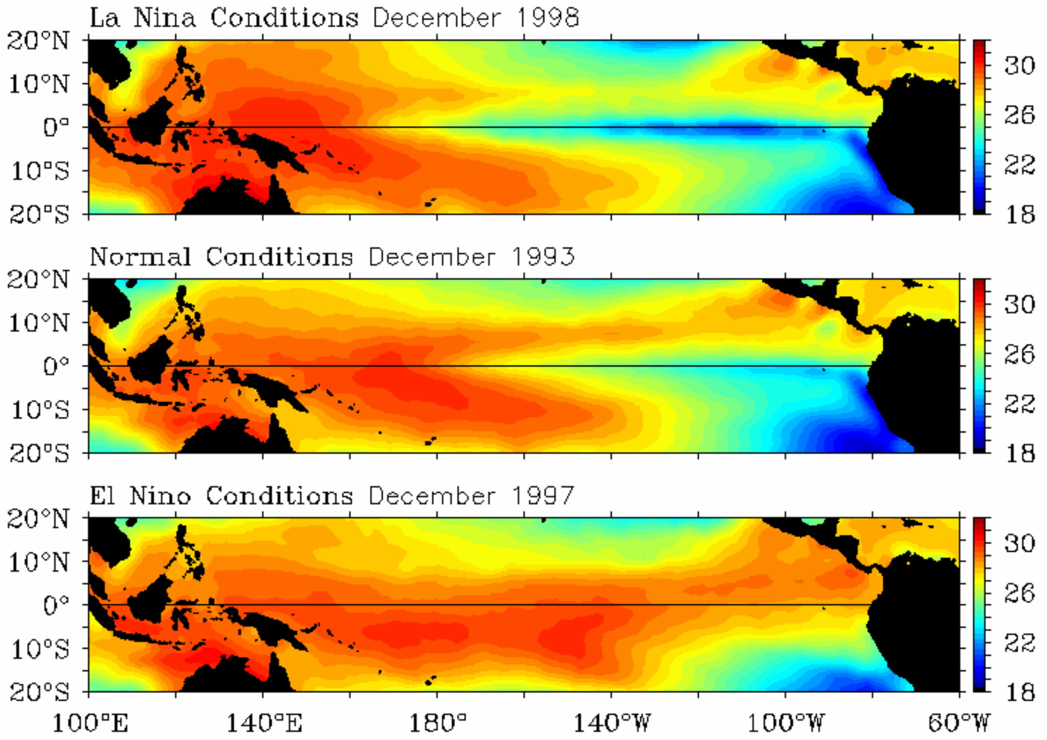

Figure 1.2 Sea surface temperature of the east-west Equotrial Pacific during La Niña, normal and El Niño conditions (adapted from NOAA).

1.1.3. Marine carbonate system

Carbon dioxide is the most important greenhouse gas after water vapor in the atmosphere of the Earth, and more than 98% of the carbon of the atmosphere-ocean system is stored in the oceans as dissolved inorganic carbon (Figure 1.3). In the ocean, carbon dioxide exists in several different inorganic species: true carbonic acid (H_2CO_3, much smaller than that of $CO_{2(aq)}$), free carbon dioxide ($CO_{2(aq)}$), bicarbonate (HCO_3^-) and carbonate ion (CO_3^{2-}), and their relative abundances in seawater are as a function of oceanic pH value (see Figure 1.4).

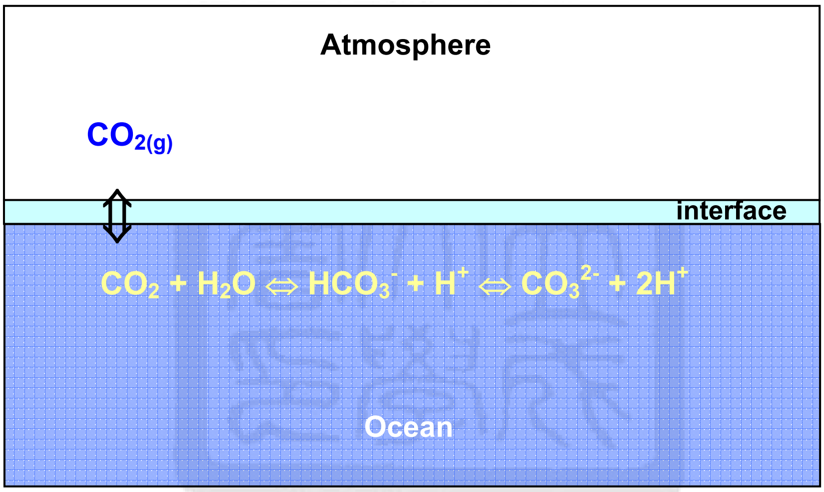

Figure 1.3 Schematic illustration of the carbonate system in the ocean.

The sum of the two electrically neutral species, H_2CO_3 and $CO_{2(aq)}$, which is chemically not separable and is usually denoted by CO_2 or $H_2CO_3^*$ (i.e., $[CO_2]=[CO_{2(aq)}]+[H_2CO_3]$). In thermodynamic equilibrium with gaseous $CO_{2(g)}$ and following Henry's law, gaseous CO_2 dissolves into surface seawater directly proportional to the atmospheric partial pressure of CO_2 (pCO_2):

$$CO_{2(g)} \xleftrightarrow{Ko} CO_2, \quad [CO_2]= K_0(T, S) * pCO_2 \tag{1}$$

where K_0 is the solubility coefficient of CO_2 in seawater, and is mainly as a function of temperature (T) at a given salinity (S). The carbonate species of dissolved CO_2 are related by the following equilibrium:

$$CO_{2(aq)} + H_2O \Leftrightarrow H_2CO_3 \Leftrightarrow HCO_3^- + H^+ \Leftrightarrow CO_3^{2-} + 2H^+ \quad (2)$$

CO_2 is therefore not only dissolved physically but also dissociates to ionic species which do not contribute to the aquatic partial pressure of CO_2. This is the reason why significantly more CO_2 dissolves in seawater than any other abundant gas such as N_2 and O_2. Using CO_2 instead of carbonic acid and aqueous carbon dioxide, the equilibrium can be simplified as:

$$CO_2 + H_2O \xleftrightarrow{K_1} HCO_3^- + H^+ \xleftrightarrow{K_2} CO_3^{2-} + 2H^+ \quad (3)$$

where K_1 and K_2 are stoichiometric equilibrium constants, often referred to as the first and second dissociation constants of carbonic acid, respectively. For the description of the carbonate system in seawater, *K1* and *K2* are used which are related to ion concentrations and depend on temperature, pressure (P) and salinity:

$$K_1(T,\ S,\ P) = \frac{[H^+][HCO_3^-]}{[CO_2]} \quad (4)$$

$$K_2\ (T,\ S,\ P) = \frac{[H^+][CO_3^{2-}]}{[HCO_3^-]} \quad (5)$$

In colder, deeper, and less salinity waters, $[CO_3^{2-}]$ will decrease and $[CO_2]_{(aq)}$ increase because of decreases in T and S, together with increasing P would cause a shift of the relative ion concentration to the left-hand side of the equation (2).

The sum of the dissolved inorganic carbon species can be denoted by DIC (or $\sum CO_2$, TCO_2, and C_T are used) and defined as follows:

$$DIC \equiv \sum CO_2 = [CO_2] + [HCO_3^-] + [CO_3^{2-}] \quad (6)$$

Another essential quantify for describing the carbonate system is the alkalinity, which is related to the electrical charge balance in seawater. DIC keeps track of the total carbon (i.e., the mass balance for total inorganic carbon) and the alkalinity keeps track of the charges (i.e., the charge balance). The carbonate alkalinity, CA, is defined as:

$$\mathrm{CA} = [\mathrm{HCO_3^-}] + 2\,[\mathrm{CO_3^{2-}}] \tag{7}$$

Note that the CA is part of the total alkalinity (TA), which is regarded in terms of buffer capacity (i.e., the ability to neutralize strong acids) and includes boron compounds and other minor constituents:

$$\mathrm{TA} = [\mathrm{HCO_3^-}] + 2\,[\mathrm{CO_3^{2-}}] + [\mathrm{B(OH)_4^-}] + [\mathrm{OH^-}] - [\mathrm{H^+}] \pm \text{minor constituents} \tag{8}$$

Equation 4 and 5, together with the mass balance for DIC (equation 6) and the charge balance (equation 7), comprise four equations and six variables ($[CO_2]$, $[HCO_3^-]$, $[CO_3^{2-}]$, $[H^+]$, DIC, and CA). Given any two variables, the system is determined and all the other parameters can be calculated. Theoretically, this could be achieved by measuring any two of the six parameters, however, only $[CO_2]$, $[H^+]$, DIC and TA can be measured directly (see *DOE*, 1994 for details).

As an example, consider the case in which DIC and $[H^+]$ have been determined by directly measurement. The contents of CO_2, HCO_3^-, CO_3^{2-} and CA can be expressed as functions of DIC and $[H^+]$:

$$[\mathrm{CO_2}] = \frac{DIC}{\left(1+\dfrac{K_1}{[H^+]}+\dfrac{K_1K_2}{[H^+]^2}\right)} \tag{9}$$

$$[\mathrm{HCO_3^-}] = \frac{DIC}{(1+\dfrac{[H^+]}{K_1}+\dfrac{K_2}{[H^+]})} \tag{10}$$

$$[\mathrm{CO_3^{2-}}] = \frac{DIC}{(1+\dfrac{[H^+]}{K_2}+\dfrac{[H^+]^2}{K_1K_2})} \tag{11}$$

Assume that a surface seawater in equilibrium with today's atmosphere at pCO2 = 365 μatm has a pH of 8.1 and DIC= 2.1 mmol kg^{-1} at a salinity of 35 and a temperature of 25°C. Using the constants summarized in DOE (1994), the percentage of the solved species is [CO_2] : [HCO_3^-] : [CO_3^{2-}] ≅ 0.5% : 86.5% : 13%. Therefore bicarbonate is the dominant species at typical seawater condition (Figure 1.4).

This was a very brief summary of the marine carbonate system. A detailed description can be found in *Zeebe and Wolf-Gladrow* [2001].

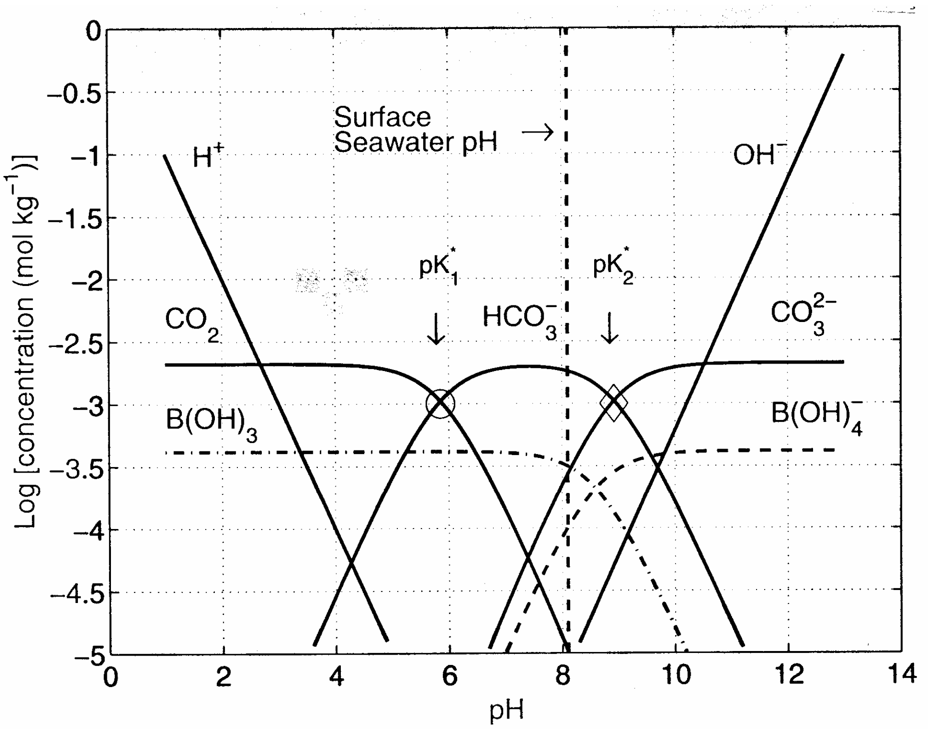

Figure 1.4 Carbonate system: Bjerrum plot; DIC= 2.1 mmol kg^{-1}, S= 35, T_c= 25°C. The circle and diamond indicate pK_1*= 5.86 and pK_2*= 8.92 of carbonic acid. The values of pK_B* and pK_W* used here are 8.60 and 13.22, respectively [*DOE*, 1994] (adapted from *Zeebe and Wolf-Gladrow*, 2001).

1.1.4. Carbonate chemistry in the biological activity

There are four dominant processes involved in neutralizing the excess atmospheric CO_2 in the ocean, including: 1) gas exchange at the air-sea interface and reaction with the carbonate ion to form bicarbonate; 2) net primary productivity; 3) formation and dissolution of $CaCO_3$; 4) ocean circulation. Most of these processes are biologically mediated and important in surface tropical regions where the exchange with atmosphere is more direct.

Marine photosynthesis and oxidation of organic matter are closely linked to calcification and dissolution to control the oceanic pH, and to a larger extent, the atmospheric CO_2 levels. The reactions are given as follows:

$$Ca^{2+} + 2HCO_3^- \underset{\text{Dissolution}}{\overset{\text{Calcification}}{\Leftrightarrow}} CaCO_3 + H_2O + CO_2 \underset{\text{Respiration}}{\overset{\text{Photosynthesis}}{\Leftrightarrow}} CH_2O + O_2 \tag{12}$$

There is a clear spatial decoupling between the forward reactions, which are limited to the upper ocean (mainly take place in the euphotic/photic zone), and the backward reactions, which occur primarily on the seafloor. In detail, two biological carbon pumps can be distinguished, the organic carbon and the inorganic calcium carbonate pumps. These two pumps have opposite influences on the CO_2 partitioning between ocean and atmosphere. While photosynthetically active organisms uptake CO_2 for biomass production, the secretion of calcitic and aragonitic skeletons by foraminifera, corals, pteropods and coccolithophores primarily increase surface water CO_2. Respiration in the deep ocean inverts reaction and releases CO_2 which leads to lower the pH in the deep ocean in addition to the effects of higher pressure and lower temperature, to the dissolution of $CaCO_3$.

1.1.5. Glacial-interglacial changes in oceanic temperature and atmospheric CO_2

Previous observation from high-resolution ice-core records have shown that the cyclic changes in air temperature and atmospheric CO_2 levels occurred over the last 400,000 years [*Petit et al.*, 1999] (see Figure 1.5). The significant covariation of the past glacial-interglacial cycles between air temperature and atmospheric CO_2 suggests that

CO_2 may be an important driving force for Earth's climate [*Cuffey and Vimeux*, 2001]. However, *Fischer et al*. [1999] observed that the pCO_2 change lags the warming of the last three deglaciations by 600±400 years, arguing for an important feedback mechanism than a real climate forcing function of CO_2 concentration. Therefore, even many approached have been made to determine the main processes that control the state of the glacial ocean (e.g., [*Boyle*, 1988; *Broecker et al*., 1997]), contradictions between theories and observations could not be excluded and interactions between atmospheric CO_2 and oceanic carbon remain elusive. In the study area, South China Sea, a much strong glacial-interglacial variation can be observed due to its climate-sensitivie locality and the intense influences of East Asian Monsoon system. Hence, a better understanding of the linkage between the atmosphere and the ocean can be obtained based on the study of oceanic pH and pCO_2 in the South China Sea.

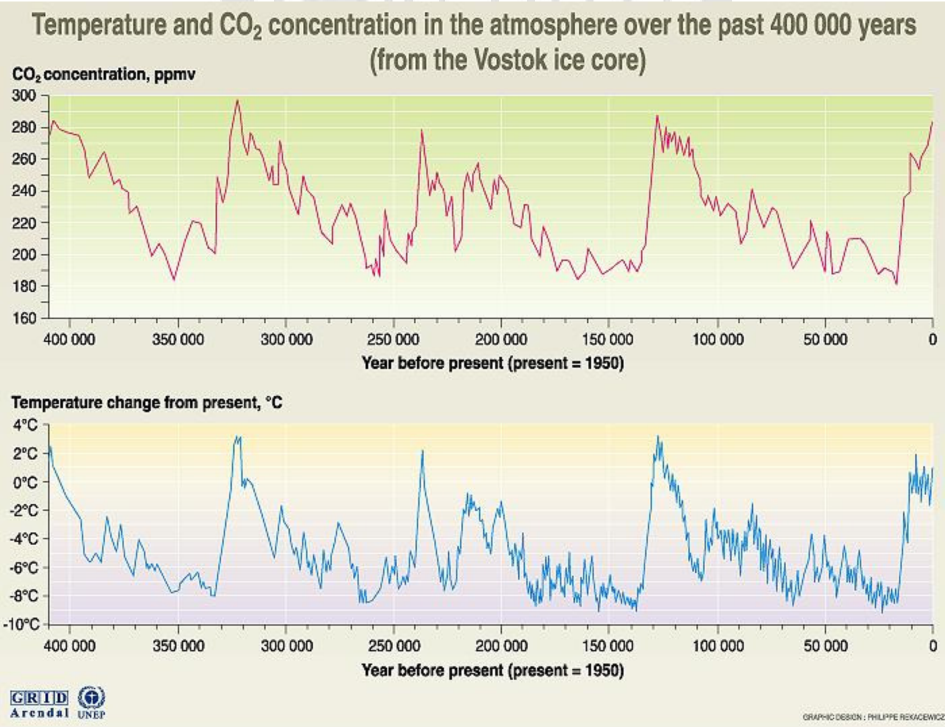

Source: J.R. Petit, J. Jouzel, et al. Climate and atmospheric history of the past 420 000 years from the Vostok ice core in Antarctica, Nature 399 (3JUne), pp 429-436, 1999.

Figure 1.5 Glacial-interglacial variations of atmospheric CO_2 and temperature records over the last 400,000 years from the Vostok ice core. (adapted from *IPCC*, 2000)

1.2 Biomineralization in Foraminifera

Foraminifera are unicellular calcifying ameba, taxonomically part of the Protista, and are strictly marine organisms [*Erez*, 2003, and references therein]. Over 40,000 species have been identified in the fossil record, while roughly 4,000 species are extant. The process of biomineralization is a major modifier of the paleoceanographic proxies stored in their shells, but it may mask the real signals recorded in foraminiferal shells. More detail and reliable information will be extracted from shell chemistry if their biomineralization process is well understood. Furthermore, foraminifera can be cultured in the laboratory and provide a very informative experimental preparation to study the biomineralization at the cellular level. These organisms are particularly suitable for light and confocal microscopy. Therefore, the biomineralization of foraminifera can be well established and provide many valuable information regarding how they calcify their shell and what kinds of role biological activity may play [*Bentov and Erez*, 2005; 2006].

1.2.1. Test structure, Function and Chamber Formation

Detailed investigations on foraminiferal morphology, micro-texture, and chemical composition have been made since late 1970s [*Hedley and Adams*, 1978]. Four groups of foraminifera can be divided with regard to their shell: the first two groups are with organic tests and with tests composed of particles collected by the organism and incorporated into the test. The latter may have organic matter or $CaCO_3$ as their calcifying agent and hence may be considered as performing biomineralization. In contrast, the other two types are known as imperforate or porcelaneous (mainly Milliolids) and the perforate or calcitic radial. The perforate foraminifera are the ones that dominant today's oceans, and imperforate are more primitive and evolved before the calcitic radial perforate ones, probably in the Paleozoic.

There is a major difference in the calcification mechanisms of the perforate and imperforate (porcelaneous) foraminifera. The porcelaneous species precipitate their needle-shaped calcite crystals (high-Mg calcite) within intracellular vacuoles [*Hemleben et al.*, 1986]. The crystals are then deposited at the sites of chamber formation without any preferred orientation, within the organic matrix, which forms the shape of their chamber. Most of the porcelaneous foraminifera are not perforated as opposed to the calcitic radial ones. Since their shell is rather permeable to gases and solutions, the microelectrode technique can be used to deduce the compositional gradients [*Kohler-Rink and Kuhl*, 2000; 2001]. Another approach is that radioactive exchanges of ^{14}C and ^{45}Ca are high in the porcelaneous species compared to the perforate ones [*Kuile and Erez*, 1987].

The tests of perforate foraminifera can be one or few chambers, or complex with many chambers arranged in various three-dimensional configurations. The most common feature is spherical coiling with planispiral or low trochospiral tests. Their shells are usually made of low Mg calcite (some may approach 6-7 mol % Mg), and their crystals are oriented in a structure known as calcitic radial. This group is also perforated with numerous micro-pores (ranged from few microns up to 10 μm in diameter) that are found on the surface area of the shells, and sealed by an organic pore plug that prevents the intra-shell cytoplasm from flowing out of the shell [*Hemleben*, 1989]. As in all foraminifera, the flow of cytoplasm is mainly via the aperture or apertures through which pseudopods can propagate to perform the life function of these organisms including feeding, excretion, and chamber formation.

Another major feature found in the perforate calcitic-radial foraminifera is their “lamination”, which is obtained when these organisms cover their pre-formed shell (Primary calcite) with a new layer of calcite that the organism builds a new chamber

(Secondary calcite). The bulk of the $CaCO_3$ test is composed of this secondary lamination, and the pores and spines (when present) are not covered by the secondary lamination. Toward the end of their life cycle many planktonic species deposit several different type of $CaCO_3$ either in the form of thick crust or gametogenic calcite (or GAM calcite). This $CaCO_3$ often shows different chemical and possibly isotopic compositions [*Bé*, 1980; 1982; *Bé et al.*, 1977]. This can be in part interpreted by deposition in deeper water where water chemistry and physical properties are different from those where their skeleton was deposited, and in part because the mechanism of calcification may be different.

Not much is known regarding the organic matrices and their roles in the calcification process in foraminifera. The abundance of acidic amino acids and the present of glycosaminoglycans have been documented in tests and organic lining of various foraminifera [*Weiner and Erez*, 1984; *Langer*, 1992]. Obviously an organic matrix is involved in determining the shape of the newly formed chambers and may also function as a nucleating and as an inhibiting agent of mineralization.

On the basis of the light microscopy, SEM and TEM observations, chamber formation could be further understood (*Bé*, 1982; *Spero*, 1988; *Hemleben et al.*, 1989]. In perforate foraminifera the first step is delineation of a space that partially isolates the organism from their environment. This is done with the aid of the ectoplasmic pseudopods. The next step is the formation of the organic template in the shape of newly formed chamber (represents a small fraction of $CaCO_3$ deposited during the growth). This is made by the formation of a cytoplasmic bulge that serves as a mold for the organic matrix, and also provides a template for nucleation. The third step is the precipitation of $CaCO_3$ on both sides of a thin organic layer (termed the Primary Organic Membrane or Sheet, POM or POS). During the entire process there is an intensive involvement of the granoreticulate pseudopodia, with strong cytoplasmic and vacuole streaming [*Erez*, 2003].

1.3 Trace Elements in Foraminiferal Calcite

Environmental variables such as temperature, salinity and seawater pH cannot be directly measured for the past. Therefore, the trace element composition in foraminiferal shell has become an important mean by which paleoceanographers produce data about the past oceanic condition in the Earth's climate system if the partition coefficients can be constrained. Trace elements are incorporated directly into calcite shell from ambient seawater [*Lea*, 1999; *Erez*, 2003]. For this reason, shell chemistry reflects both seawater composition and the physical and biological condition occur during the formation.

Abundances of trace elements (TE) in foraminiferal shells (Figure 1.6, [*Lea*, 1999]) are commonly presented in molar ratios (i.e., mol element per mol Ca), so that they can directly compare with elemental ratios in seawater. So far, at least fifteen trace elements have been investigated. Four elements, Mg, Na, Sr and F, are presented at abundances of greater than 10^{-3} mol/mol Ca, and often termed "minor elements". For five of the trace elements, such as B, Li, Mn, Zn and Ba, their abundances range from 10^{-3} to 10^{-6} mol/mol Ca, and the remaining six trace elements, Fe Cu, Nd, Cd, V, and U are presented at abundances between 10^{-6} to 10^{-9} mol/mol Ca. The metals Mg, Sr, Mn, Zn, Ba, Fe, Nd and Cd are known to form solid solutions isomorphous with either calcite or aragonite (see Table 1.1) [*Speer*, 1983], so that these metals are most likely to be directly linked with their chemical behaviors in shells with respect to thermodynamic control. This study mainly focuses on Mg, Sr, B, and U in the planktonic foraminifera, and further understands the controlling factors on their distributions in foraminiferal shells. Detailed discussion will be given in Chapters 3, 4 and 5.

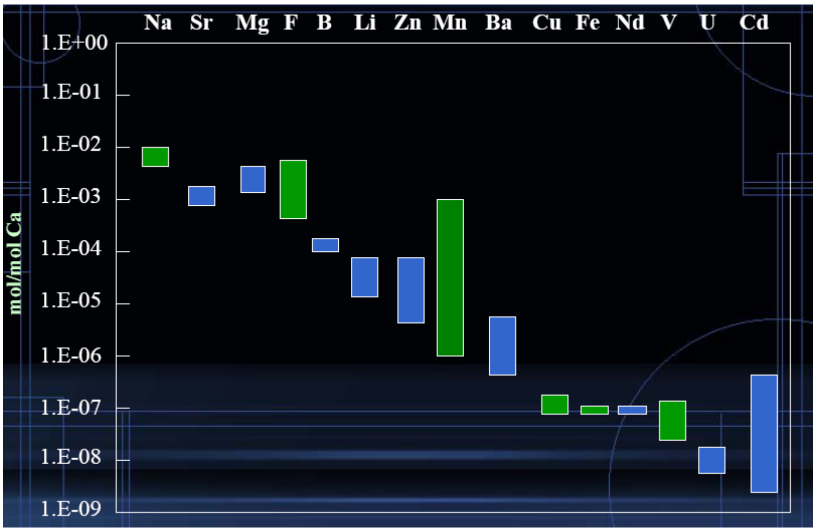

Figure 1.6 Trace element abundances in foraminifer shells im moles of element per mol Ca. The ranges of trace element ratios are shown in Table 1.1.

The ideal situation is that the trace elements are homogeneously incorporated into shell calcite and followed by strict thermodynamic laws. This pure thermodynamic control is the most important concept to interpret the trace element compositions in shell calcite. The relationship between shell chemistry and seawater is best express by an empirical partition coefficient, K_D, which is defined as follow:

$$K_D = \frac{[TE/Ca]_{foram}}{[TE/Ca]_{seawater}}$$

where the bracketed concentrations indicate the actual concentration ratios of trace element (TE) to Ca in calcite and seawater [*Morse and Bender*, 1990; *Mucci and Morse*, 1990]. Trace element abundances in foraminiferal calcite and relevant information are also shown in Table 1.1. However, it is important to realize that the K_D is not only controlled by thermodynamic property, but also related to other physical (i.g., kinetic effect) and biological (i.e., vital effect) controls.

Table 1.1 Trace element abundances in foraminiferal calcite and coralline aragonite. Ionic radii are from *Shannon* [1976]. Partition coefficients are calculated from references (adapted from Bo-Sen Wang)

Element	Valence	Radius (Å)	$[X/Ca]_{foram}$	$[X/Ca]_{coral}$	$[X/Ca]_{seawater}$	$D_{p(coral)}$	$D_{p(foram)}$	References
Li	1	0.92	$1.20\text{-}1.60\times10^{-5}$	6.16×10^{-6}	2.37×10^{-3}	0.0026	0.0054~0.0068*	14
Mg	2	0.89	$1\text{-}5\times10^{-3}$	4.40×10^{-3}	5.15×10^{0}	0.01	0.002~0.01**	9, 10
Ca	2	1.12	1	1	1	–	–	
Sr	2	1.26	1.14×10^{-3}	9.18×10^{-3}	8.59×10^{-3}	1.07	0.133	11
Ba	2	1.42	1.47×10^{-6}	5.27×10^{-6}	4.52×10^{-6}	1.16	0.30	3, 14
Cd	2	1.10	0.12×10^{-6}	3.69×10^{-9}	4.36×10^{-9}	0.85	27.5	1, 2
Pb	2	1.29	–	3.00×10^{-8}	1.24×10^{-8}	2.41	–	6
Zn	2	0.90	8.0×10^{-6}	7.80×10^{-9}	5.83×10^{-9}	1.34	1372	5, 7
Mn	2	0.96	5.7×10^{-6}	2.40×10^{-8}	2.23×10^{-7}	0.11	25.6	4, 5
S	2	1.84 (VI)	$0.2\text{-}1.9\times10^{-3}$		2.81×10^{0}		0.000071-0.00068	
B	3	0.27 (VI)	6.0×10^{-5}	5.28×10^{-4}	4.3×10^{-2}	0.0122	0.0014	15, 16
La	3	1.16		1.76×10^{-9}	1.59×10^{-9}	1.11		12, 13
Ce	3	1.14		3.39×10^{-9}	1.54×10^{-9}	2.21		12, 13
Nd	3	1.11	2.0×10^{-6}	2.48×10^{-9}	1.60×10^{-9}	1.55	1250	12, 13, 18
Sm	3	1.08		7.64×10^{-10}	3.58×10^{-10}	2.14		12, 13
Eu	3	1.00		1.39×10^{-10}	9.43×10^{-11}	1.47		12, 13
Gd	3	1.05		1.04×10^{-9}	5.24×10^{-10}	1.98		12, 13
Dy	3	1.03		9.40×10^{-10}	6.17×10^{-10}	1.52		12, 13
Er	3	1.00		7.84×10^{-10}	4.82×10^{-10}	1.62		12, 13
Yb	3	0.99		6.90×10^{-10}	4.17×10^{-10}	1.66		12, 13
Lu	3	0.98		1.01×10^{-10}	5.72×10^{-11}	1.76		12, 13
V	4	0.72		1.01×10^{-7}	3.79×10^{-6}	0.03		7, 8
U	6	0.86	8.0×10^{-9}	1.15×10^{-6}	1.32×10^{-6}	0.87	0.0061	17

References for foram, coral, and seawater elemental ratios:

1. Shen et al. (1987) EPSL 82, 289-304.
2. Boyle and Huested (1983) Trace Metals in Seawater, 379-395.
3. Lea et al. (1989) Nature 338, 751-753.
4. Shen et al. (1991) Coral Reef 10, 91-100.
5. Bruland and Franks (1983), 395-414.
6. Shen and Boyle (1987) Nature 328, 794-796.
7. Shen (1986) P.h.D. thesis
8. Huizenga and Kester (1982) EOS
9. Mitsuguchi et al. (1996) Science 274, 961-963.
10. Broecker and Peng (1982) Tracers in the Sea.
11. de Villiers et al. (1994) GCA 58, 197-208.
12. Sholkovitz and Shen (1995) GCA 59, 2749-2756.
13. Sholkovitz and Schneider (1991) GCA 55, 2737-2743.
14. Hall (2002) P.h.D. thesis
15. Fallon et al. (2003) Coral Reef 22, 389-404.
16. Wara et al. (2003) Paleoceanography 18, 4, doi:10.1029/2002PA000797
17. Russell et al. (2004) GCA 68, 4347-4361.
18. Vance et al. (2004) Paleoceanography 19, doi:10.1029/2003PA000957.

The effective ionic radii (octahedral coordination) for all ions are taken from Shannon (1976)
* Planktonic (low)~ benthic forams (high)
** depend on species

1.4 Isotopic Composition in Foraminiferal Calcite

Analyses of stable isotopes, especially oxygen and carbon, from foraminiferal shells have played a pivotal role in paleoceanography since the pioneering study of *Emiliani* [1995], who interpreted the isotopic composition from deep-sea cores as a temperature proxy. *Shackleton and Opdyke* [1973] demonstrated that the δ^{18}O signal predominantly reflects fluctuations in global ice volume, and temperature plays a second role. Besides, they also correlated the oxygen isotopic stratigraphy with magnetic stratigraphy, and recognized 22 isotopic stages. Since then, oxygen isotopic composition has become not only a global correlation tool, but also an established dating tool. Turning attention to down-core δ^{13}C in benthic foraminifera, *Shackleton* [1977] showed the potential use in studying water mass movement and paleoproductivity, and further purposed a connection between changes in the terrestrial biosphere induced by global climate variations with carbonate dissolution cycles and the flux of dissolved CO_2 in the oceans.

Although these two stable isotope systems have been widely used and become the most essential information for paleoceanographic studies since 1970's, several processes cause deviations from the originally isotopic signals, both in planktonic and benthic foraminifers. For the oxygen isotopes, equilibrium fractionations between water and the shell carbonates are the most important assumption to make foraminiferal δ^{18}O to be "isotopic paleothermometers" [*Urey*, 1947; *Epstein et al.*, 1953; *O' Neil et al.*, 1969; *Shackleton*, 1974], however, Ontogenic effect [*Spero and Lea*, 1996], Symbiont photosynthesis [*Spero and Lea*, 1993], respiration [*Grossman*, 1987], formation of gametogenic calcite [*Spero and Lea*, 1993; *Rosenthal et al.*, 2000], and carbonate ion effect [*Spero et al.*, 1997; *Bemis et al.*, 1998] would significantly deviate the δ^{18}O from equilibrium δ^{18}O in foraminiferal calcite [*Rohling and Cooke*, 1999]. Therefore, specific influence for each process should be considered very carefully and further quantified in order to obtain more reliable climate change in the past.

Carbon isotopes in seawater are rather complicated than seawater oxygen isotopes, which is mainly due to extensive influences of biological activity (photosynthesis, respiration, export productivity, and regional surface-deep $\delta^{13}C$ gradients, [*Broecker and Peng*, 1982; *Boyle and Keigwin*, 1982; *Ortiz et al.*, 1996] or the organic carbon cycle between terrestrial and marine carbon cycles, other than interaction with $\delta^{13}C$ of atmospheric CO_2. Furthermore, several processes could also cause the disequilibrium between carbonate and dissolved inorganic carbon, such as utilization of metabolic CO2 during shell formation [*Ortiz et al.*, 1996], photosynthetic activity of symbionts [*Spero and Lea*, 1993], changes in growth rate [*Spero and Parker*, 1985], and variations in carbonate ion concentration [*Spero et al.*, 1997].

For the isotopic composition, the principal aim of this study was to develop instrumental and chemical techniques applicable to the study of boron and strontium isotopes in natural samples (e.g., seawater and planktonic foraminifera) using high precision Thermal Ionization Mass Spectrometry (TIMS), and further evaluate the potentials for paleoceanographic reconstructions using isotopic compositions in planktonic foraminifers. Detailed discussions were given in Chapters 6 and 7.

References

Bé, A. W. H., 1980. Gametogenic calcification in a spinoso planktonic foraminifer *Globigerinoides sacculifer* (Brady). Mar. Micropaleont. 5, 283-310.

Bé, A. W. H., 1982. Biology of planktonic foraminifera. In: Foraminifera: Notes for a short course. Studies in Geology Vol. 6. Broadhead TW (ed) Univ. Tenn. Knoxville 51-92.

Bé, A. W. H., Hemleben, C., Anderson, O. R., Spindler, M., Hacunda, J., Tunitivate-Choy, S., 1977. Laboratory and field observation of living planktonic foraminifera. Micropaleont. 23, 155-179.

Bemis, B. E., Spero, H. J., Bijma, J., Lea D. W., 1998. Reevaluation of the oxygen isotopic composition of planktonic foraminifer: Experimental results and revised paleotemperature equations. Paleoceanography 13, 150-160.

Bentov, S., Erez, J., 2005. Novel observations on biomineralization processes in foraminifera and implications for Mg/Ca ratio in the shells. Geology 33, 841-844.

Bentov, S., Erez, J., 2006. Impact of biomineralization processes on the Mg content of foraminiferal shells: A biological perspective. Geochem. Geophys. Geosys. 7, doi:10.1029/2005GC001015.

Boyle, E. A., Keigwin, L. D., 1982. Deep circulation of the North Atlantic over the last 200,000 years: Geochemical evidence. Science 218, 784-787.

Boyle, E. A., 1988. The role of vertical chemical fractionation in controlling late Quaternary atmospheric carbon dioxide. J. Geophys. Res. 15701-15714.

Broecker, W. S., Peng T.-H. , 1982. Tracers in the Sea, Eldigio Press, New York.

Broecker, W. S., 1997. Thermohaline circulation, the Achilles heel of our climate system: Will man-made CO2 upset the current balance? Science 278, 1582-1588.

Cuffey, K. M., Vimeux, F., 2001. Covariation of carbon dioxide and temperature from Vostok ice core after deuterium-excess correction. Nature 412, 523-527.

DOE., 1994. Handbook of methods for the analysis of the various parameters of the carbon dioxide system in seawater. Version 2. Dickson, A. G., and Goyet, C., editors. ORNL/CDIAC-74.

Emiliani, C., 1955. Pleistocene temperatures. J. Geol. 63, 538-578.

Epstein, S., Buchsbaum, R., Lowenstam, H. A., Urey, H. C., 1953. Revised carbonate-water temperature scale. Bull. Geol. Soc. Am. 64, 1315-1326.

Erez, J., 2003. The source of ions for biomineralization in foraminifera and their implications for paleoceanographic proxies. Reviews in mineralogy and Geochemistry 54, Biomineralization, 115-149.

Falkowski, P. G. et al., 2000. The global carbon cycle: A test of our knowledge of earth as a system. Science 290, 291-296.

Fischer, H., Wahlen, M., Smith, J., Mastroianni, D, Deck, B., 1999. Ice core records of atmospheric CO2 around the last three glacial terminations. Science 283, 1712-1714.

Grossman, E. L., 1987. Stable isotopes in modern benthic foraminifera: A study of vital effect. J. Foramin. Res. 17, 48-61.

Hedley, R. H., Adam, C. G., 1978. Foraminifera. Vol. 3. Academic Press, London.

Hemleben, C., Spindler, M., Anderson, O. R., 1989. Modern Olanktonic Foraminifera.

Spring-Verlag, New York.

Kohler-Rink, S., Kuhl, M., 2000. Microsensor studies of photosynthesis and respiration in large symbiotic foraminifera. The physico-chemical microenvironment of Marginopora vertebralis, Amphistegina lobifera and Amphisorus hemprichii. Mar. Biol.137, 473-486.

Kohler-Rink, S., Kuhl, M., 2001. Microsensor studies of photosynthesis and respiration in large symbiont bearing foraminifera, Amphistegina lobifera and Amphisorus hemprichii. Ophelia 55, 111-122.

Kuile, B., Erez, J., 1987. Uptake of inorganic carbon and internal carbon cycling in symbiont-bearing benthic foraminifera. Mar. Biol. 94, 499-510.

Langer, M. R., 1992. Biosynthesis of glycosaminoglycans in foraminifera: a review. Mar. Micropaleont. 19, 245-255.

Lea, D. W., 1999. Trace elements in foraminiferal calcite. Modern Foraminifera, 259-277.

Morse, J. W., Bender, M. L., 1990. Partition coefficients in calicite: Examination of factors influencing the validity of experimental results and their application to natural systems. Chem. Geol. 82, 265-277.

Mucci, A., Morse, J. W., 1990. Chemistry of low-temperature abiotic calcites: experimental studies on coprecipitation, stability and fractionation. Aquatic Sci. 2, 217-254.

O’Neil, J. R., R. N. Clayton, and T. K. Mayeda, Oxygen isotope fractionation in divalent metal carbonates, *The Journal of Chemical Physics*, *51*, 5547-5558, 1969.

Ortiz, J. D., Mix, A. C., Rugh, W., 1996. Deep-dwelling planktonic foraminifera of the northeastern Pacific Ocean reveal environmenta; control of oxygen and carbon isotopic disequilibria. Geochim. Cosmochim. Acta 60, 4509-4523.

Petit, J. R. et al., 1999. Climatic and atmospheric history of the past 420,000 years from the Vostok ice core, Antarctica. Nature 399, 429-436.

Raven, J. A., Falkowski, P. G., 1999. Oceanic sinks for atmospheric CO_2. Plant. Cell and Environment 22, 741-755.

Rohling, E., Cooke, S., 1999. Stable oxygen and carbon isotopes in foraminiferal carbonate shells. Modern Foraminifera, 239-258.

Rosenthal, Y., Lohmann, G. P., Lohmann, K. C., Sherrell, R. M., 2000. Incorporation and preservation of Mg in *Globigerinoides sacculifer*: Implication for reconstructing the temperature and $^{18}O/^{16}O$ of seawater. Paleoceanography 15, 135-145.

Sigman, D. M., Boyle, E. A., 2000. Glacial/interglacial variations in atmospheric carbon dioxide. Nature 407, 859-869.

Shackleton, N. J., 1974. Attainment of isotopic equilibrium between ocean water and the benthic foraminiferal genus Uvigerina: Isotopic changes in the ocean during the last glacial, Cent. Natl. Rech. Sci. Colloq. Int. *219*, 203-209.

Shackleton, N. J., Opdyke, N. D., 1973. Oxygen isotope and paleomagnetic stratigraphy of equatorial Pacific core V28-238: oxygen isotope temperatures and ice volumes on a 105 and 106 years scale. Quarter. Res. 3, 39-55.

Shackleton, N. J., 1977. ^{13}C in Uvigerina: tropical rainforest history and the equatorial Pacific carbonate dissolution cycles, in Fate of Fossil Fuel CO_2 in the oceans, Plenum, New York, 401-427.

Shannon, 1976. Revised effective ionic radii. Acta crystallog. A32, 751-767.

Speer, J. A., 1983. Crystal chemistry and phase relations of orthorhombic carbonates, in carbonates: Mineralogy and Chemistry, (ed R. J. Reeder), Mineralogical society of America, Washington, D. C., 145-190.

Spero, H. J., Parker, S. L., 1985. Photosynthesis in the symbiotic planktonic foraminifer Orbulina universa and its potential contribution to oceanic primary productivity. J. Foram. Res. 15, 273-281.

Spero, H. J., 1988. Ultrastructural examination of chamber morphogenesis and biomineralization in the planktonic foraminifera Orbulina universa. Mar. Biol. 99, 9-20.

Spero, H. J., Lea, D. W., 1993. Intraspecific stable isotope variability in the planktonic foraminifera Globigerinoides sacculifer: results from laboratory experiments. Mar. Micropaleont. 22, 221-234.

Spero, H. J., Lea, D. W., 1996. Experimental determination of stable isotope variability in Globigerina bulloides: implications for paleoceanographic reconstructions. Mar. Micropaleont. 28, 231-246.

Spero, H. J. et al., 1997. Effect of seawater carbonate concentration on foraminiferal carbon and oxygen isotopes. Nature 390, 497-500.

Trenberth, K. E. et al., 1998. J. Geophys. Res. 103, 14291.

Urey, H. C., 1947. The thermodynamic properties of isotopic substances. J. Chem. Soc. 562-581.

Weiner, S., Erez, J., 1984. Organic matrix of the shell of the foraminifer. Heterostegina depressa. J. Foramin. Res. 14, 206-212.

Zeebe, R. E., Wolf-Gladrow, D. A., 2001. CO2 in seawater: Equilibrium, kinetics, isotopes.

Elsevier Oceanography Series 65. Elsevier. p. 346.

CHAPTER 2.

Methodology

2.1 High Resolution ICP-MS (HR-ICP-MS)

2.1.1 Instrumentation

Trace elements ratios in planktonic foraminifera were measured using Thermo-Fisher Scientific instruments HR-ICP-MS, Element 2 (at NCKU) and Element XR (at Rutger University). Both instruments are double-focusing magnetic sector (equipped with Electrical Sector Field Analyzer, ESA) mass spectrometry with variable ion optics and a single ion detector with three (analog, counting and both modes, dynamic range: 10^9) and four (analog, counting, Faraday and triple modes, dynamic range: 10^{12}) detection modes for Element 2 and Element-XR, respectively (see Figures 2.1 and 2.2). Samples were introduced through a stable sample introduction spray dual chamber (Elemental Scientific, Inc.) or PFA spray chamber (Elemental Scientific, Inc.) coupled with PFA MicroFlow nebulizer (50-100 µL/min, Elemental Scientific, Inc.) in order to obtain stable signals. All the instrumental setting and detailed methodology for trace element ratios are shown in Tables 2.1, 2.2 and 2.3. Measurements of trace element ratios on the home-made and international trace element standards (CBN-1) (SGS, provided by Dr. Yair Rosenthal, Rutgers University) over a period of about one year are presented (followed by the method of *Rosenthal et al*. [1999], see Figure 2.6 and Table 2.5), and will be further described in the following section of this chapter.

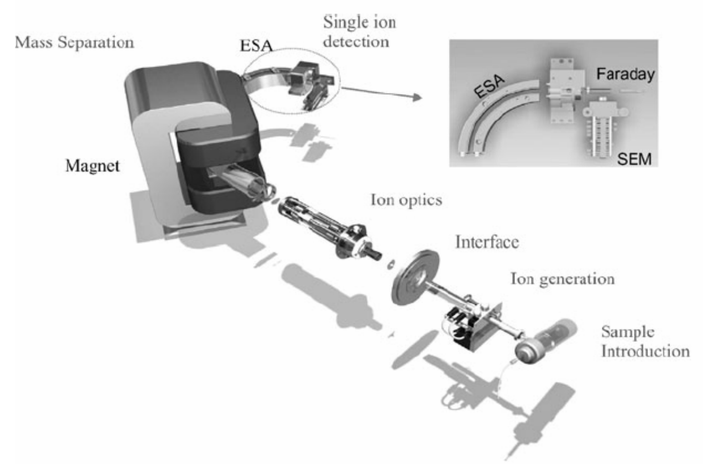

Figure 2.1 Double-focusing sector field ICP-MS (Element XR, Thermo-Fisher Scientific).

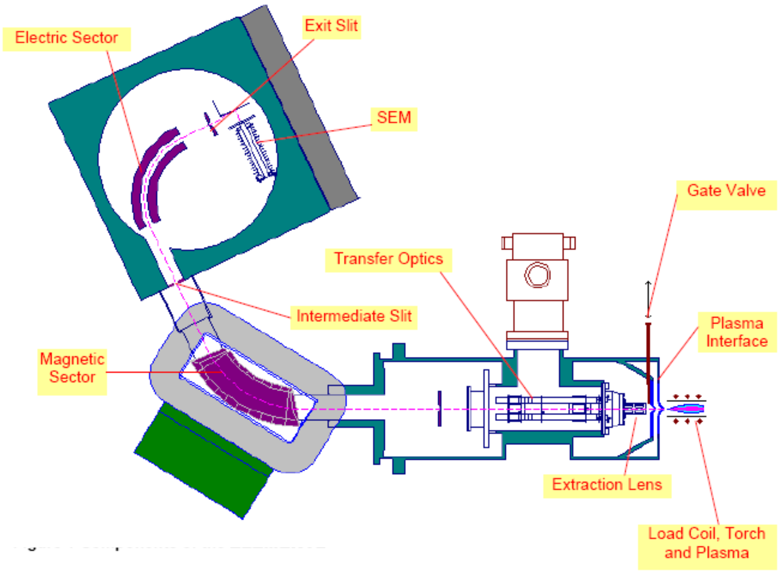

Figure 2.2 Schematic diagram of HR-ICP-MS, Element 2 (Thermo-Fisher Scientific).

2.1.2 Spectral interference

There are three common types of spectral overlaps in ICP-MS (Table 2.4, *Thomas*, 2002): (1) Polyatomic or molecular spectral interference, which can be produced by the combination of two or more atomic ions due to introductions of gases (Ar, N_2 and O_2, for example, $^{40}Ar^{16}O^+$ on ^{56}Fe) and major components in the solvent and samples (e.g., in a hydrochloric acid medium, $^{40}Ar^{35}Cl$ interferes with the only isotope of As at mass 75); (2) Oxides, Hydroxides, hydrides, and doubly charged species, which can be formed by elements in the sample combining with ^{1}H, ^{16}O or $^{16}O^{1}H$, and typically take place in the cooler zone of the plasma right before the interface system. For example, $^{138}Ba^{1}H$ on ^{139}La, $^{48}Ti^{16}O$ on ^{64}Zn and $^{88}Sr^{++}$ on ^{44}Ca; (3) Isobaric overlaps, which are

Table 2.1 Instrumental parameters of HR-ICP-MS (Element 2 and XR)

RF power	1250-1350 W
Cool gas flow	18 L/min
Auxiliary gas flow	0.8 L/min
Sample gas flow	0.950-1.120 L/min
Extraction voltage	-2000 V

mainly due to different isotopes of other elements in the sample. For instance, ^{144}Sm and ^{87}Rb would influence the signals of ^{144}Nd and ^{87}Sr.

Table 2.2 Acquisition Methods

acquisition mode	E-scan
resolution m/Δm	300 and 4000
mass window (%)	10
samples per peak	100
acquisition points	10
analysis time (min)	2.5
uptake time (s)	30
sample vol (μL)	250

Table 2.3 Multiratio Method (run/passes 3 × 60 for LR and 3 × 5 for MR)

Resolution	Isotope	Detection mode	Settling time (s)	Sample Time (s)
Low Resolution (LR)	Li-7	counting	0.300	0.005
	B-11	counting	0.015	0.005
	Na-23	analog	0.030	0.001
	Mg-24	analog	0.001	0.001
	Mg-25	analog	0.001	0.001
	Al-27	counting	0.001	0.001
	Ca-43	analog	0.031	0.001
	Ca-46	counting	0.002	0.001
	Sr-87++	counting	0.001	0.001
	Ti-47	counting	0.001	0.001
	Ca-48	analog	0.001	0.001
	Mn-55	analog	0.001	0.001
	Zn-66	counting	0.025	0.001
	Sr-88	analog	0.019	0.001
	Cd-111	counting	0.001	0.005
	Ba-138	counting	0.034	0.001
	U-238	counting	0.050	0.005
Median Resolution (MR)	S-32	counting	0.300	0.010
	Ca-43	analog	0.041	0.005
	Ca-46	counting	0.041	0.005
	Fe-56	counting	0.040	0.005

HR-ICP-MS (Element 2 and XR, Thermo-Fisher Scientific) provides not only a unique opportunity to resolve isobaric overlaps, but also a very fast scan speed of magnetic (m/z=7 to 238 to 7, less than 150 ms) and electric field (1 ms/jump, and independent of mass range). Thus an almost simultaneous, high-precision and high-accuracy determination can be achieved through the recent advance in these instruments. In this HR-ICP-MS, three mass resolutions (300, 4000, and 10000, defined as m/Δm in 10% valley, equivalent to 5% height) can be selected to the measurement of any trace element. The main designs for this purpose are to adjust relative widths of two slits, entrance slit and exit slit, located at before and after magnetic field (see schematic Figure 2.3). For instance, applying the median-resolution (m/Δm= 4,000) mode, $^{40}Ar^{16}O^+$ on $^{56}Fe^+$ and $^{16}O^{16}O^+$ on $^{32}S^+$ can be completely separated without any desolvation system (e.g., Aridus, Cetac Technologies). However, the intensity is lower than that of low-resolution mode by a factor of ~20 for much smaller width of exit slit.

Table 2.4 Some common spectral interferences seen in ICP-MS

m/z	Analyte/Isotope	Matrix/Solvent	Interference	Resolution
Polyatomic/oxide/hydride species				
31	^{31}P	H_2O	$^{15}N^{16}O$	1460
34	^{34}S	H_2O	$^{16}O^{18}O$	1300
39	^{39}K	H_2O	$^{38}Ar^{1}H$	5570
56	^{56}Fe	H_2O	$^{40}Ar^{16}O$	2504
51	^{51}V	HCl	$^{35}Cl^{16}O$	2572
75	^{75}As	HCl	$^{40}Ar^{35}Cl$	7725
44	^{44}Ca	HNO_3	$^{14}N^{14}N^{16}O$	970
55	^{55}Mn	HNO_3	$^{40}Ar^{15}N$	2300
64	^{64}Zn	H_2SO_4	$^{32}S^{16}O^{16}O$	1950
24	^{24}Mg	Organics	$^{12}C^{12}C$	1600
52	^{52}Cr	Organics	$^{40}Ar^{12}C$	2370
doubly charged species				
44	^{44}Ca		$^{88}Sr^{2+}$	
69	^{69}Ga		$^{138}Ba^{2+}$	
Isobaric interference				
40	^{40}Ca		^{40}Ar	199,800
144	^{144}Nd		^{144}Sm	

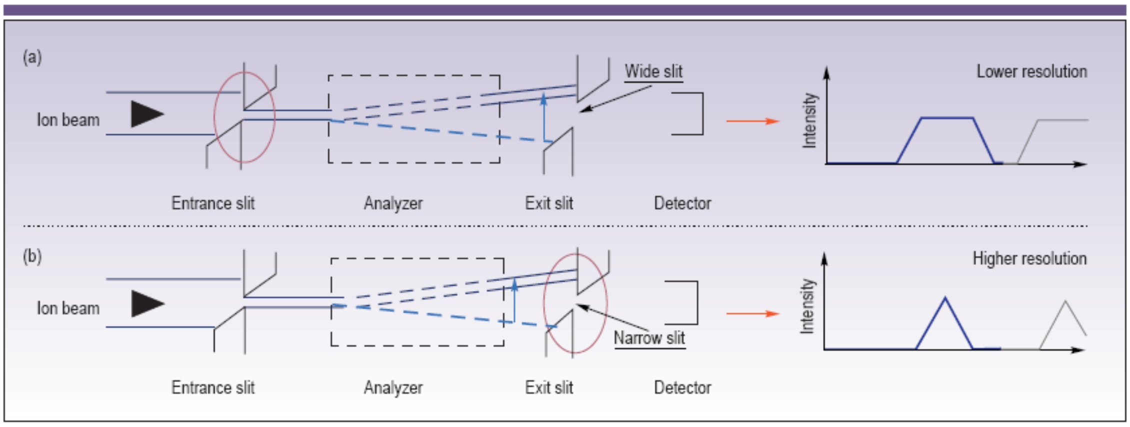

Figure 2.3 Schematic diagram for controlling the mass resolution in HR-ICP-MS (Thomas, 2001). The entrance slit widths are the same in (a) and (b).

Because the abundances of the interestedtrace elements in foraminiferal calcites varies by several orders of magnitudes, all these trace elements (less than ppm level), together with Ca (~40 wt% of the calcite) were determined by using the same detection mode to avoid any intensity bias on ion detection system even the Analog-Counting (A/C) converting factor had been calibrated before analyses. For example, ^{25}Mg and ^{43}Ca (or ^{46}Ca) were selected to precisely determine the Mg/Ca ratios in foraminiferal calcite. Besides, ^{24}Mg and ^{46}Ca were also detected simultaneously to evaluate if any appearance of spectral interference would influence the isotopic ratios (e.g., ^{25}Mg/^{24}Mg= 0.1266, and ^{46}Ca/^{43}Ca= 0.0296, see Figure 2.4). Furthermore, ^{24}Mg and ^{43}Ca were also monitored by median-resolution (m/Δm= 4000) to check the potential influence from doubly-charged ^{48}Ca and ^{86}Sr. Based on two-years duration of the runs, all of the trace elements were not significantly affected by any spectral interference even samples with high Ca contents, indicating the contributions of all spectral interferences to trace elements are always less than 0.1%.

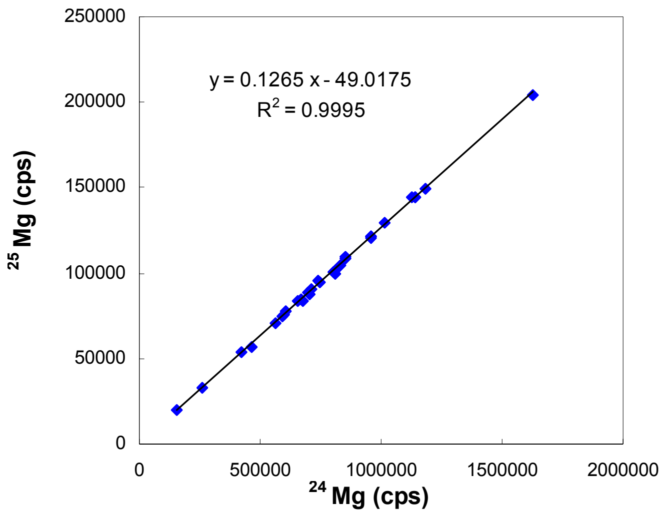

Figure 2.4 Raw data of ^{24}Mg versus ^{25}Mg in the samples, the slope of the two Mg isotope shows the similar ratio for their natural abundances (^{25}Mg/^{24}Mg=0.1266).

2.1.3 Matrix-induced mass discrimination

Many early researchers reported that the intensity of signals in ICP-MS decreased with increasing concentrations of the major elements in the analyzed sample, and the magnitude of signal suppression in ICP-MS increased with decreasing atomic mass of the ions [*Olivares and Houk*, 1986; *Rosenthal et al.*, 1999]. More recently it has been suggested that the main cause of the intensity suppression results from the poor transmission of ions through the ion optics due to matrix-induced space charge effects [*Tanner et al.*, 1994]. This effect would cause the defocusing of the ion beam, which leads to poor sensitivity and detection limits., especially for trace levels of low mass elements in the present of large concentrations of high-mass matrix elements [*Thomas*, 2002].

In this study, because of the high calcium contents in all of the samples, matrix effects on instrumental mass bias were examined by analyzing six serial solutions with various calcium contents (1.5-8.0 mM Ca, corresponding to 60-320 ppm Ca) during the sample measurements. The results show a negligible effect of calcium concentration on

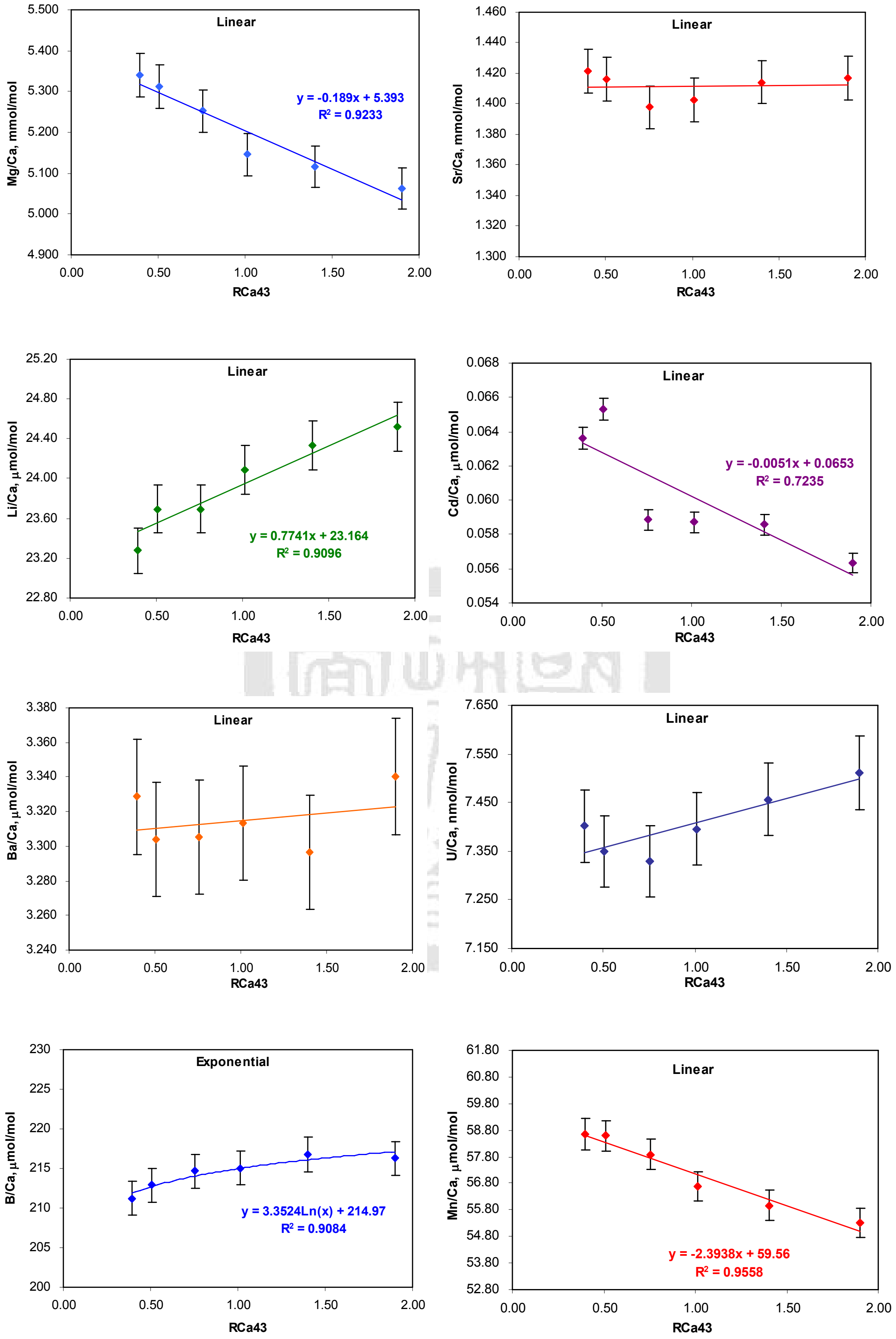

Figure 2.5 Variations of trace element/calcium ratios as a function of the matrix calcium concentration at different runs over a one-year period. RCa43 were calculated by the ratios of ^{43}Ca intensity between SGS and samples. Each point was an average value from at least 20 duplicates, and the error bar for each elemental ratio was presented the long-term variation at 2σ standard deviation. All the regression modes (linear and exponential) were selected based on the better R^2.

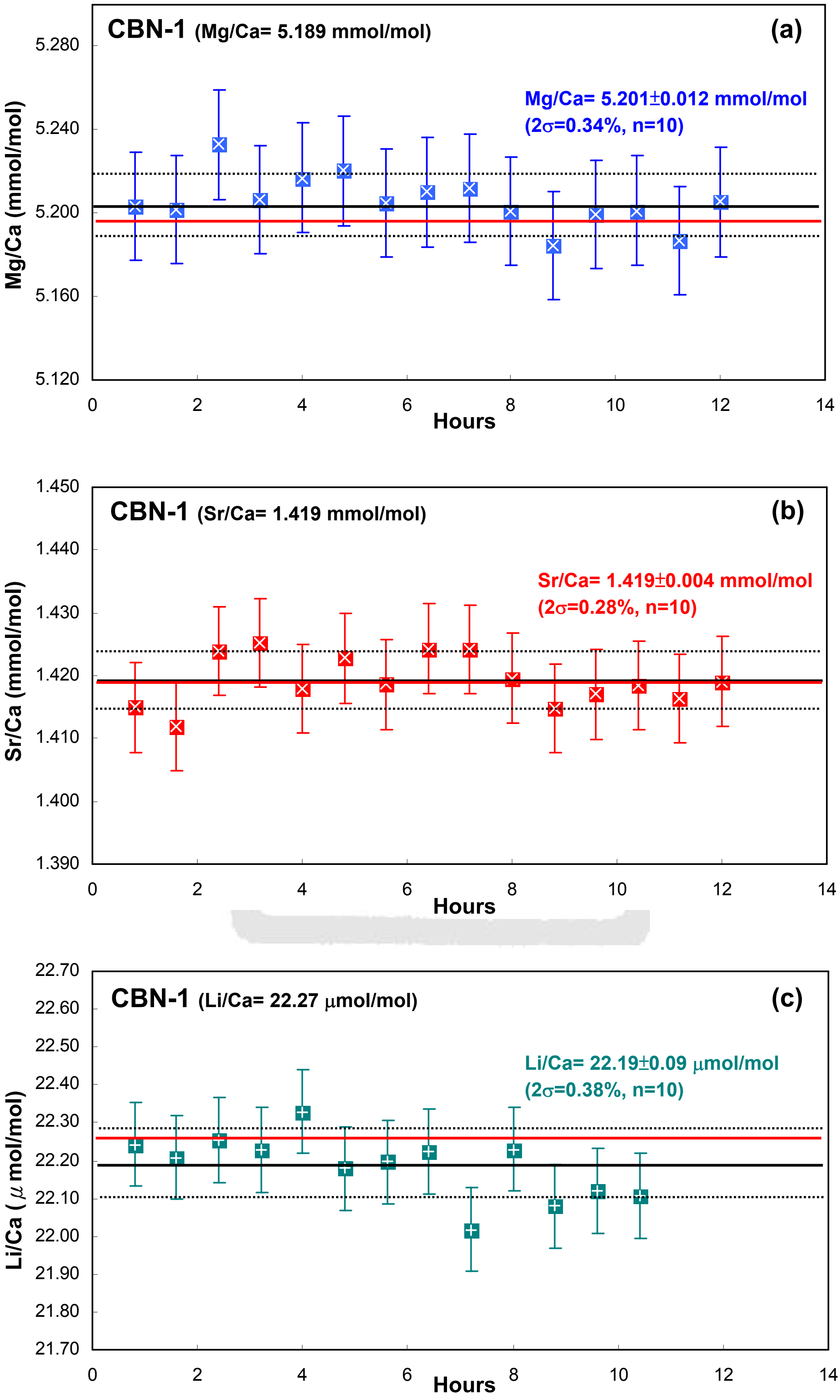

Figure 2.6 Analytical reproducibility for multiratio analysis examined on a solution with a chemical composition typical of planktonic foraminifera. The analytical precision was calculated from results of 12-hr runs over a one-year period. (a) Mg/Ca, (b) Sr/Ca and (c) Li/Ca ratio. Black and red solid lines represented an average value of measurements and the true value, respectively. Black dashed line represent 2 s.d. external precision. All errors on the trace element ratios are reported 2 s.d. external precision based on six duplicated data. .

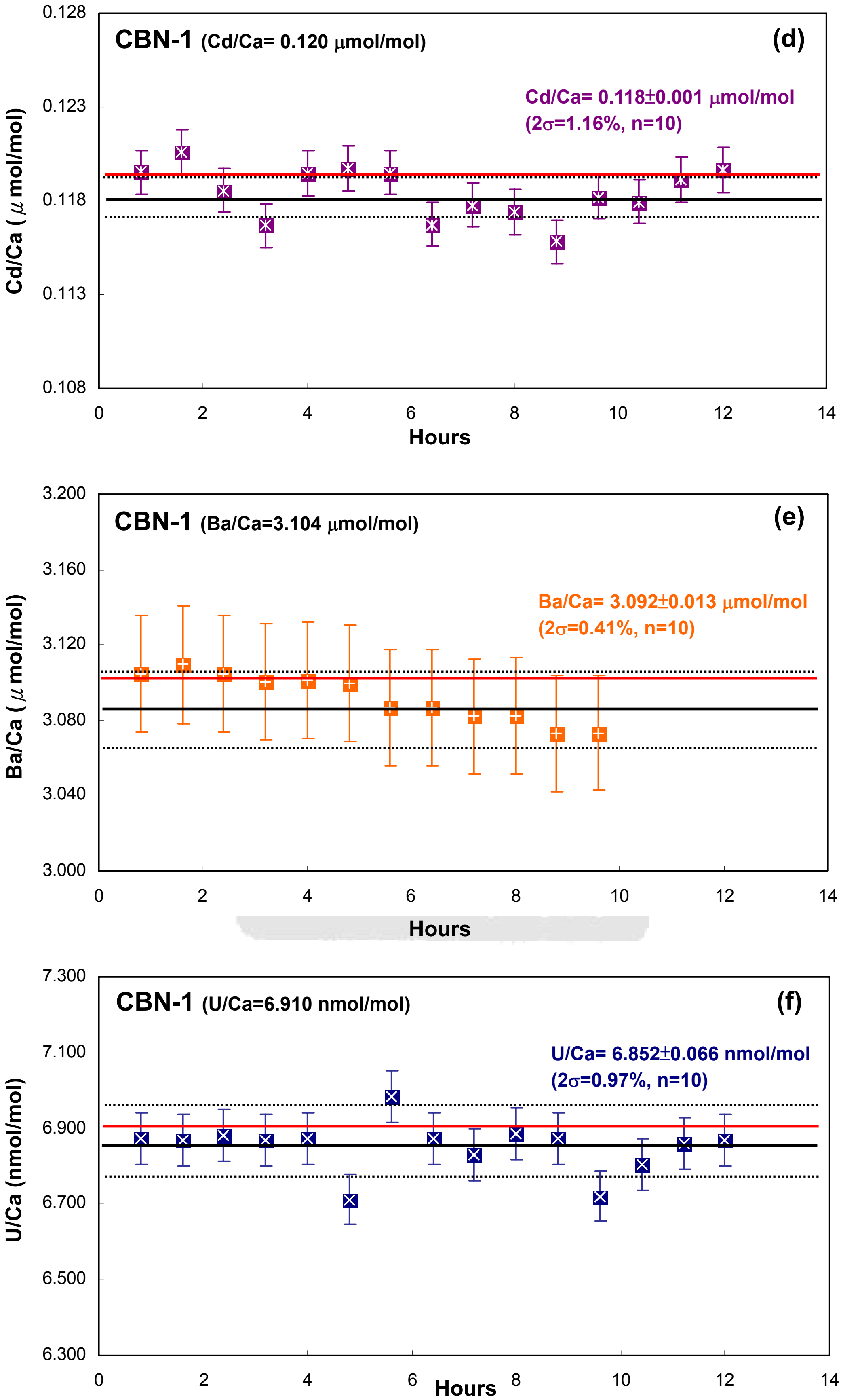

Figure 2.6 (Continued) Analytical reproducibility for multiratio analysis examined on a solution with a chemical composition typical of planktonic foraminifera. The analytical precision was calculated from results of 12-hr runs over a one-year period. (d) Cd/Ca, (e) Ba/Ca and (f) U/Ca ratio. Black and red solid lines represented an average value of measurements and the true value, respectively. Black dashed line represent 2 s.d. external precision. All errors on the trace element ratios are reported 2 s.d. external precision based on six duplicated data. .

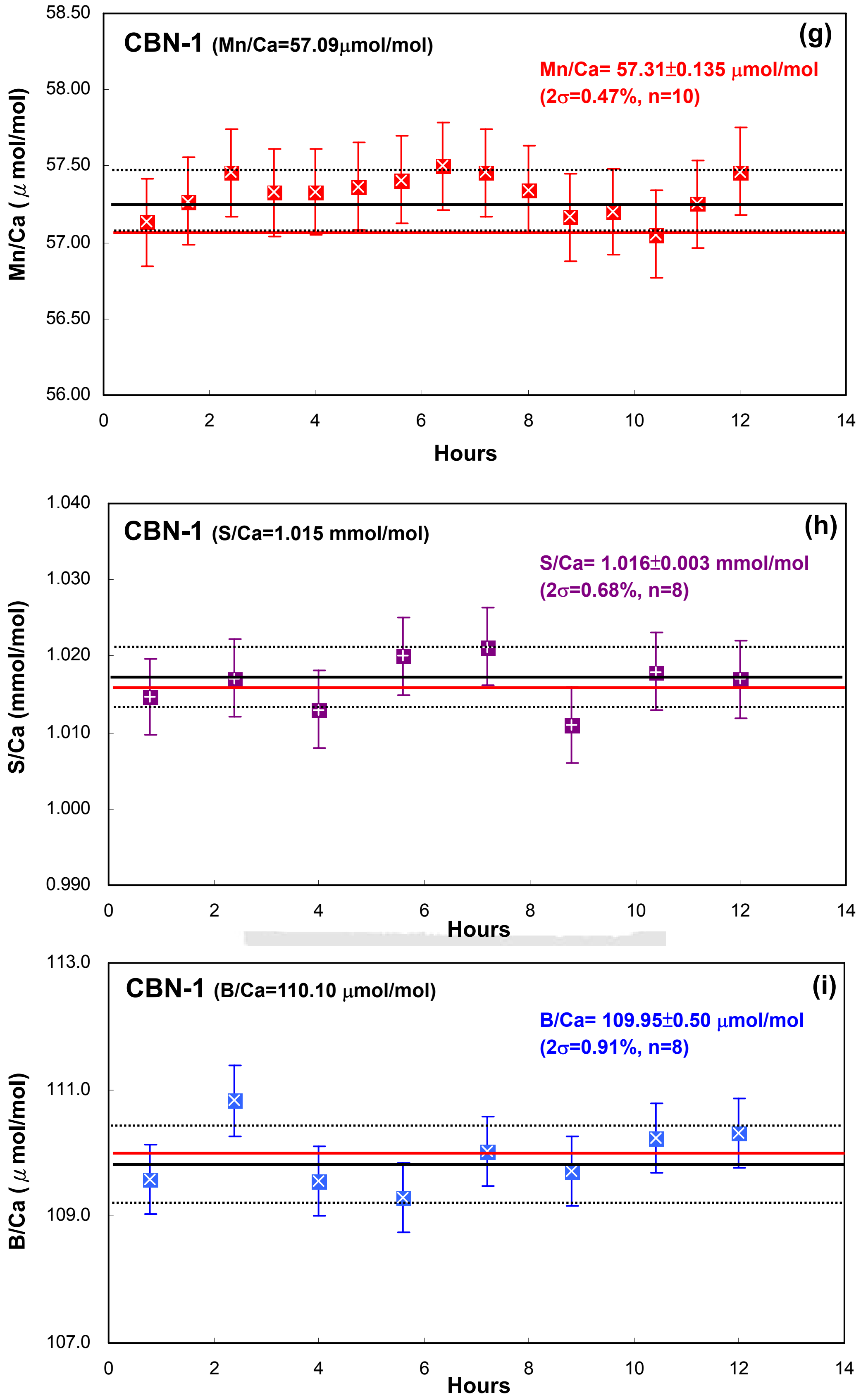

Figure 2.6 (Continued) Analytical reproducibility for multiratio analysis examined on a solution with a chemical composition typical of planktonic foraminifera. The analytical precision was calculated from results of 12-hr runs over a one-year period. (g) Mn/Ca, (h) S/Ca and (i) B/Ca ratio. Black and red solid lines represented an average value of measurements and the true value, respectively. Black dashed line represent 2 s.d. external precision. All errors on the trace element ratios are reported 2 s.d. external precision based on six duplicated data. .

the signal intensity for Sr/Ca, Ba/Ca, U/Ca and S/Ca. For these ratios, changes in mass bias were within the analytical precision of the method at the 1σ level for daily and long-term precisions. Within the range of 1.5-8.0 mM Ca, Mg/Ca, Cd/Ca and Mn/Ca ratios showed significant inverse relationships to calcium concentration (Figure 2.5). For the others, elemental ratios displayed a linear or exponential (e.g., B/Ca) increase with elevated calcium concentration. Some of these matrix-induced mass bias differ significantly from previous studies reported by *Rosenthal et al.* [1999], but the good reproducibility for this study over a one-year period confirms that this artifact is fairly constant for each trace element ratio in the instrument, and can be used to correct for the matrix effect to obtain more accurate data.

2.1.4 Precision and Accuracy

The short-term precisions for multiratio analysis were examined by CBN-1of the 12-hours runs over the six-month period (at least 6 runs), and were of 0.34% for Mg/Ca, 0.28% for Sr/Ca, 0.38% for Li/Ca, 1.16% for Cd/Ca, 0.41% for Ba/Ca, 0.97% for U/Ca, 0.47% for Mn/Ca, 0.68% for S/Ca and 0.91% for B/Ca (see Figure 2.6). The long-term reproducibility observed in this study over one-year period are of 0.44% on Mg/Ca, 0.48% on Sr/Ca, 1.00% on Ba/Ca, 1.12% on Mn/Ca, 1.10% on B/Ca, 1.66% on S/Ca, 2.46% on Cd/Ca and 2.38% on U/Ca (2σ, n=10), respectively. A comparison of currently published methods is presented in Table 2.5, suggesting that a much better precision (short- and long-term) can be achieved in the determination of trace element ratios in biogenic carbonates, and therefore provide a powerful analytical tool for studying the relationship between shell chemistry and global climate change.

Table 2.5 The comparison of analytical precision and method for the trace element ratios.

Method	Precision (%, 2σ)										Reference
	Mg/Ca	Sr/Ca	Mn/Ca	B/Ca	S/Ca	Cd/Ca	Ba/Ca	U/Ca	Transition metals	REY	
ICP-OES		0.4									Schrag, 1999
	0.6	0.6									de Villiers et al., 2002
	1.8	1.2									Andreasen et al., 2006
ID-TIMS		0.05									Shen et al., 1996
										0.2 - 6	Sholkovitz and Shen, 1995
Q-ICP-MS		2	10			6.6	4.8				Lea and martin, 1996
									4 (Cu)		Inoue et al., 2004
	2.8	1.8	1.8	8.4		9.6			10.2 (Zn)		Yu et al., 2005
										< 12 (except La)	Akagi et al., 2004
Q-ICP-MS (cool plasma)	0.84	0.49									Shen et al., 2007
ID-Q-ICP-MS		0.5						1			le Cornec and Correge, 1997
	4	2									Lea et al., 1999
	1.34	0.58					4.12	2.46			Sun and Sun, 2002
SF-ICP-MS	0.9	0.9	1.6			3.4	1.4	2.8			Rosenthal et al., 1999
	1.4										Lea et al., 2003
	1.8	1.2									Andreasen et al., 2006
SF-ICP-MS	***0.44***	***0.48***	***1.12***	***1.10***	***1.66***	***2.46***	***1.00***	***2.38***			***This study***
ID-SF-ICP-MS						4.4					Matthews et al., 2006

2.2 Thermal Ionization Mass Spectrometry (TIMS)

2.2.1 Instrumentation

TIMS provides the most precise isotopic ratio measurements compared to that of the other instruments. This is because its stable ionization process through heating the homogeneous metal filaments (e.g., Re, Ta, and W), together with a series of high-efficiency Faraday cup and highly sensitive secondary electron multiplier (SEM). TRITON TI (Thermo-Fisher Scientific), housed at the Department of Earth Sciences, Natioanl Cheng Kung University, is equipped with six movable Faraday cups (10^{11} Ω resistors), and one fixed central cup, and one secondary electron multiplier (SEM). The energy filter function of Retarding Potential Quadraple (RPQ) technique was applied to reduce the abundance sensitivity to less than 2 ppm.

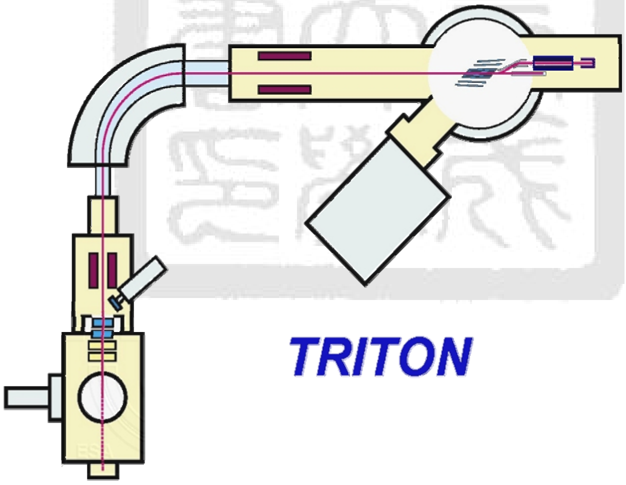

Figure 2.7 Schematic diagram of TRITON TI (Thermo-Fisher Scientific)

Because the natural abundances of measured isotopes for boron (^{11}B: 80.1% and ^{10}B: 19.9%) and strontium (^{86}Sr: 9.86%, ^{87}Sr: 7.00% and ^{88}Sr: 82.58%) are rather close, therefore, Faraday cups were the only detection system used for determining the isotopic ratios in this study. Thus, the yield calibration between Faraday cups and SEM can be ignored here. The gain calibrations of Faraday cup amplifiers were made daily via giving a constant ion beam with 30 V and the gain fluctuation is less than 3 ppm between days. The baseline of Faraday cup was measured for 180 seconds with defocusing the x-symmetry. The contributions of the error comes from baseline variability were always less than 0.2‰ for boron and strontium isotopic compositions.

2.2.2 Ionization process

In contrast to ICP-MS, the ionization technique of TIMS is via heating the filament to temperatures of about 1000°C to over 2000°C (for $Cs_2BO_2^+$ ions, less than 700°C) under a high vacuum (~2×10^{-7} mbar). The high temperatures are necessary to produce ions and neutrals through the evaporation and the ionization. There is a competition between the formation of positive ions and the evaporation of the neutral particles, so it is important for the TIMS to obtain the ratios of positive ions to neutrals as large as possible according to the equation:

$$n^+/n^0 = A \times \exp[(\phi\text{-}I)/kT]$$

where n^+/n^0 is the number ratio of positive ions to neutrals evaporated at temperature T (*K*). k is the Boltzmann constant and A is set to be 0.5. The above equation can be simply rewritten by:

$$n^+/n^0 = 0.5 \exp[11600(\phi\text{-}I)/T]$$

The expression (ϕ-I) is the difference between the work function (ϕ, see Table 3.2) of the metal filament and the ionization potential (I, see Table 3.1) of the element, and governs the ease with which positive ions can be formed from sample surface lying on the filament. For example, volatile elements with ionization potentials less than the metal filament work function (e.g., alkalis) produce ions at low evaporation temperature. In contrast, elements with higher ionization potentials (e.g., Th) have low ionization efficiency, and only can be improved by increasing the filament temperature. This would cause rapid exhaustion of the sample, and double- or triple-filament techniques need to be applied to reduce the temperature of the evaporation site [*Herbert and Johnstone*, 2003].

Another method to enhance the ionization efficiency is to add some appropriated activators (or "promoter"), which can change the work function of the metal filament. For example, Pb loaded with silica gel and H_3PO_4 onto a single Re filament can give a high-intensity and low-fractionation Pb^+ ion beam. However, these applications may contaminate the source of the facility.

Table 2.6 The first ionization potentials for some commonly examined elements.

Element	Ionization Potentials (eV)
Al	5.98
B	8.30
Ca	6.11
Ce	5.47
Cs	3.89
Cu	7.72
La	5.61
Li	5.39
Nd	5.49
Os	8.70
Pb	7.42
Rb	4.18
Sr	5.69
Th	6.95
U	6.08

Table 2.7 Values of the average work function and melting point for the commonly used metal filaments.

Element	Work Funciton (eV)	Melting Point (K)
Pt	6.2	2028
Re	4.8	3440
Ta	4.2	3120
W	4.5	3640

2.2.3 Isobaric interference

For the problems of isobaric overlaps on TIMS, unlike ICP-MS, most of the interferences can be eliminated by applying the purification step (e.g., column chemistry) for interested elements. Besides, this chemical procedure can also reduce the suppression of the ionization efficiency of the interested elements (e.g., the occurrence of Rb significantly suppresses the ionization of Sr). However, even involving the column chemistry for the specific element, significant amounts of organic compounds (mainly come from used ion exchange resins and chemical reagents) may be introduced and then bias the isotopic analysis. For instance, organic matter containing carbon, nitrogen, and oxygen can form CNO^- interference at mass 42, resulting in significant isobaric interferences on $^{10}B^{16}O_2^-$ (mass 42). Furthermore, boron is a highly volatile element and widely distributed in the surrounding environments, and its main source could come from glass containers, waters, regents, as well as filtered air [*Leeman et al.*, 1991; *Rosner et al.*, 2005].

To achieve the high-precision and high-accuracy isotopic analyses for boron and strontium, complete separation of Sr from Rb in the natural samples and reductions of organic compounds and the boron blank in the laboratory are the most essential and crucial challenges. Detailed descriptions regarding the column chemistry for B and Sr isotopes, as well as removals of organic matters will be given in Chapter 6 and 7.

2.2.4 Analysis protocols for the boron isotope

Boron (B) has two stable isotopes, ^{11}B (80.1%) and ^{10}B (19.9%), and B isotopes display large variations in natural system, ranging between -30‰ (magmatic rocks) to +40‰ (seawater) [*Spivack and Edmond*, 1987; *Palmer and Swihart*, 1996]. Due to such large isotopic fractionation in natural materials, analytical methods for the boron isotopic determination have been carried out since 1980's (reviewed by [*Palmer and Swihart*, 1996]). Four different approaches for the precise determination of B isotopes are used: [1] TIMS, either as positive ion-TIMS (P-TIMS) and negative ion-TIMS (N-TIMS), showing analytical precisions (2σ) of 0.2‰ [*Lemarchand et al*., 2002] and 0.3-1.0‰ [*Barth*, 1997], respectively; [2] HR-ICP-MS, the precision (2σ) is in the range of 2-4‰ [*Gäbler and Bahr*, 1999]; [3] Secondary Ion Mass Spectrometry (SIMS), the analytical precision (2σ) is within 2.5‰ [*Kasemann et al*., 2000]; [4] Multi-collector ICP-MS (MC-ICP-MS), the precision (2σ) is in the range of 0.3-0.4 ‰ [*Lemarchand et al*., 2003]. Because B isotopic variations in the natural foraminiferal calcite, seawaters, and pore waters are less than 10‰, both P-TIMS and N-TIMS were therefore developed in the present work. For the N-TIMS technique, it is characterized by high analytical sensitivity, and hence, is the preferred technique for isotopic analysis of natural waters which have low B concentration (< 1 μg/L)

Table 2.8 The operating parameters for BO_2^- N-TIMS and $Cs_2BO_2^+$ P-TIMS on TRITON TI.

BO_2^- N-TIMS		**$Cs_2BO_2^+$ P-TIMS**	
High Voltage (V)	9950	High Voltage (V)	9300
EVA current (mA)	1200-1350	EVA current (mA)	1100-1200
Pyrometer (°C)	950-1000	Pyrometer (°C)	<700
HV Source Press (mbar)	<2.0 × 10-7	HV Source Press (mbar)	<2.0 × 10-7
Ion Getter Press (mbar)	<5.0 × 10-9	Ion Getter Press (mbar)	<5.0 × 10-9
Lens Focus		**Lens Focus**	
Extraction Left (V)	8900-9000	Extraction Left (V)	7500-7700
Extraction Right (V)	8900-9000	Extraction Right (V)	7500-7700
Condenser (V)	7900-7980	Condenser (V)	7500-7600
X-symmetry (V)	50-70	X-symmetry (V)	50-70
Z-focus (V)	-5~-20	Z-focus (V)	0~-30
Data Acquisition		**Data Acquisition**	
Number of Block	10	Number of Block	10
Cycles/Block	10	Cycles/Block	10
Integration time (s)	4.194	Integration time (s)	4.194
Number of Integration	1	Number of Integration	1
Idle time (s)	3	Idle time (s)	3

For the BO_2^- N-TIMS technique, a mixture of 1 µL of the B solution containing 1-5 ng of B (NBS SRM 951, H_3BO_3, dissolved in B-free DIW) and B-free seawater (as an activator) was directly loaded onto pre-cleaned and outgassed (at 4 A for 2 h) single Re filaments, and heated nearly to dryness at 0.6 A. BO_2^- ions were then ionized at a current of ~1200 mA (850-870°C), and $^{10}B^{16}O_2^-$ (mass 42) and $^{11}B^{16}O_2^-$ (mass 43) were collected in Faraday L1 and Central cup C, respectively (see Figure 3.2). The operating parameters, the data acquisition and cup configuration are shown in Tables 3.3 and 3.4. When the signal intensity of $^{11}B^{16}O_2^-$ was larger than 0.01 V, lens focusing and ionic optics were made to obtain optimal signals. The current was then gradually increased at a constant heating rate of 10 mA/min until the intensity of mass 43 was ~1.6 V (~0.4 V for mass 42). Before data acquisition, peak centering and peak scanning were done to optimize the cup alignment and the peak shape, and CN^- (mass 26) was monitored in central cup using the SEM to make sure there is no CNO^- (mass 42) mass interference. Faraday cup baseline was also measured between each block.

Table 2.9 The cup configurations for BO_2^- N-TIMS and $Cs_2BO_2^+$ P-TIMS on TRITON TI.

	L2	L1	C/SEM	H1	H2	H3
BO_2^- N-TIMS	$^{42}BO_2^-$	$^{43}BO_2^-$	$^{44}BO_2^-$	$^{45}BO_2^-$	$^{46}BO_2^-$	$^{47}BO_2^-$
$Cs_2BO_2^+$ P-TIMS		$^{308}Cs_2BO_2^+$	$^{309}Cs_2BO_2^+$			

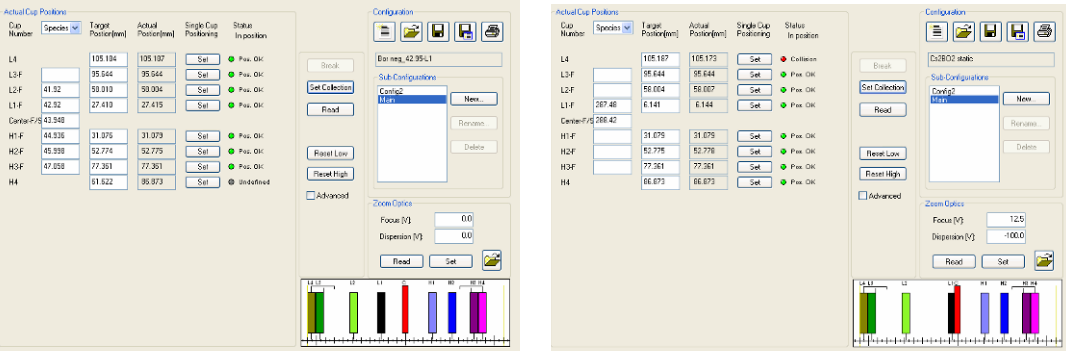

Cup Number	Species	Target Position[mm]	Actual Position[mm]	Single Cup Positioning	Status In position
L4		105.104	105.107	Set	Pos. OK
L3-F		95.644	95.644	Set	Pos. OK
L2-F	41.92	58.010	58.004	Set	Pos. OK
L1-F	42.92	27.410	27.415	Set	Pos. OK
Center-F/S	43.948				
H1-F	44.936	31.076	31.079	Set	Pos. OK
H2-F	45.998	52.774	52.775	Set	Pos. OK
H3-F	47.058	77.361	77.361	Set	Pos. OK
H4		61.622	86.873	Set	Undefined

Configuration: Bor neg_42.95-L1
Sub Configurations: Config2, Main
Focus [V]: 0.0
Dispersion [V]: 0.0

Cup Number	Species	Target Position[mm]	Actual Position[mm]	Single Cup Positioning	Status In position
L4		105.187	105.173	Set	Collision
L3-F		95.644	95.644	Set	Pos. OK
L2-F		58.004	58.007	Set	Pos. OK
L1-F	287.48	6.141	6.144	Set	Pos. OK
Center-F/S	288.42				
H1-F		31.079	31.079	Set	Pos. OK
H2-F		52.775	52.778	Set	Pos. OK
H3-F		77.361	77.361	Set	Pos. OK
H4		86.873	86.873	Set	Pos. OK

Configuration: Cs2BO2 static
Sub Configurations: Config2, Main
Focus [V]: 12.5
Dispersion [V]: -100.0

Figure 2.8 The schematic alignment of the collectors for N-TIMS and P-TIMS on B isotopes.

The boron isotopic compositions of the samples are reported as δ^{11}B values (‰) relative to a mean of ^{11}B/^{10}B ratio of the NIST SRM 951 standard, where

$$\delta^{11}B = \left[\frac{\left(\frac{^{11}B}{^{10}B} \right)_{sample}}{\left(\frac{^{11}B}{^{10}B} \right)_{SRM\,951}} - 1 \right] \times 10^3 \quad (‰)$$

The excellent analytical precision obtained on NIST SRM 951 boric acid standard (±0.51‰ (2σ) or 0.13‰ (2σ_m), corresponding to 2σ/n$^{0.5}$, where n=15 replicate analyses), and an average ^{11}B/^{10}B ratio of 4.0044 measured for the SRM 951 (see Figure 2.9). This mean value is well consistent with the published value (^{11}B/^{10}B: 3.982-4.012).

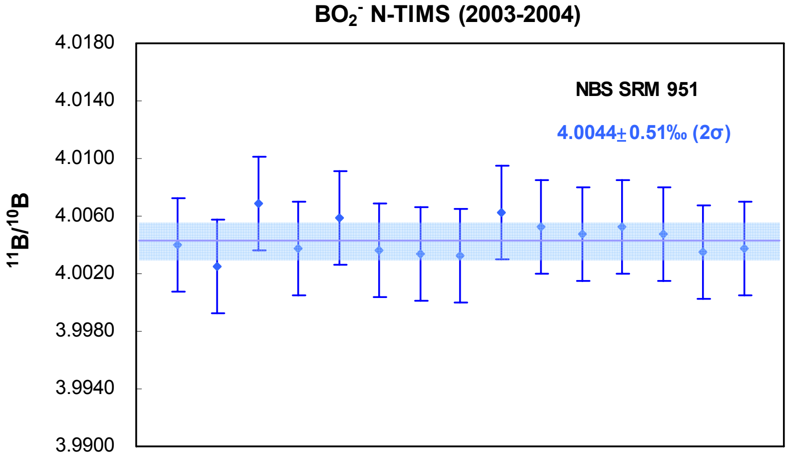

Figure 2.9 Replicate measurements of NIST SRM 951 by using BO_2^- N-TIMS technique over a period of 1 year. The mean values (solid blue line) and ±2σ (blue area) are also shown.

For the $Cs_2BO_2^+$ P-TIMS technique, a mixture of 1 μL of B-free CsOH (31 nmol), 1 μL of low-B d-mannitol solution (55 nmol), and 2 μL of 0.1N HCl containing 250-1,000 ng of B (NBS SRM 951) was prepared. The B/Cs and B/mannitol molar ratio are 3:4 and 1:2, respectively. Prior to loading B onto outgassed (at 4 A for 2 h) single Ta filaments, 1 μL of the graphite-ethanol slurry (as an activator) was used to coat the filament and heated nearly to dryness at 1 A. Special care is taken for not spreading graphite that cause significant in-run B isotopic fractionation and decrease the signal intensity. $Cs_2BO_2^+$ ions were then formed at a current of ~1050-1100 mA (<700°C), and $Cs_2{}^{10}BO_2^+$ (mass 308) and $Cs_2{}^{11}BO_2^+$ (mass 309) were collected in Faraday L1 and Central cup C, respectively (Figure 3.2). In order to measure the B isotopes simultaneously (so called "static mode"), a reduction of the accelerating voltage (or high voltage) (from 9950 to 9300 V) and the function of the Zoom Quad were used to further focus these two ion beams. This is because the closest cup distance between L1 and C still cannot collect the ion beams for mass 308 and 309 simultaneously. When the vacuum reached 5×10^{-9} mbar, the filament current was quickly raised to 0.3 A, followed by a gradual increase of 50 mA/min up to 1.1 A. At this moment, the Cs^+ signal could be used to focus the ion beam. The current was then gradually increased at a heating rate of 15 mA/min until a $Cs_2{}^{11}BO_2^+$ (m/z= 309) signal became detectable. At a signal intensity of ~400 mV for mass 309 (~100 mV for mass 308), the ion beams were then focused again by tuning lens focusing and ionic optics to gain optimal signals. Prior to acquiring data, peak centering and peak scanning were done to optimize the cup alignment and the peak shape. Note that the use of nitric acid has to be avoided due to potential isobaric interferences at mass 308 (Cs_2CNO^+). Faraday cup baseline was also measured between each block. The cup configuration and operating parameters are also shown in Table 3.3 and 3.4.

The isotopic ratios of 309/308 are measured by determining ion current intensities at mass 308 and 309. Measured values are routinely corrected for ^{17}O contribution (i.e., $Cs_2{}^{10}B^{16}O^{17}O^+$) at mass 309 by subtracting 0.00079 [*Spivack and Edmond*, 1986], and giving an oxygen corrected mean value of 4.051825 (0.2‰, 2σ, n=20) for NIST SRM 951 (Figure 3.4). The boron isotopic compositions are then normalize to that of SRM 951 to facilitate interlaboratory comparisons, and are expressed as $\delta^{11}B$ values (‰).

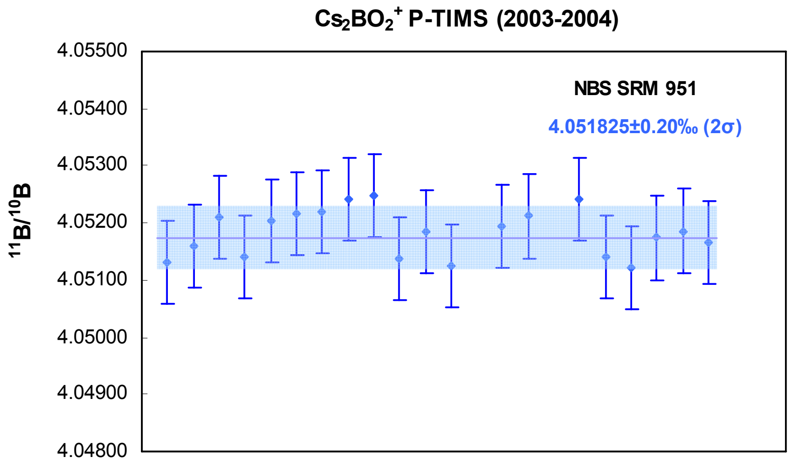

Figure 2.10 Replicate measurements of NIST SRM 951 by using P-TIMS technique over a period of 1 year. The mean values (solid blue line) and ±2σ (blue area) are also shown.

2.2.5 Analysis protocols for the strontium isotope

Strontium (Sr) has four isotopes, ^{84}Sr (0.56%), ^{86}Sr (9.86%), ^{87}Sr (7.00%) and ^{88}Sr (82.58%), and ^{87}Sr is the only Sr isotope that is affected by radioactive decay from ^{87}Rb ($T_{1/2}$= 4.88 × 10^{10} year, β^--decay). Sr isotopes in marine carbonates have been widely used in the geological and paleoceanographic studies (e.g., [*Burke et al.*, 1982]). These applications assume that strontium behaves conservatively in the ocean because of its much longer residence time (~2.5 Myr) relative to ocean mixing time [*Basu et al.*, 2001]. Homogeneous distributions of Sr isotopes are reported in the Hudson Bay, Pacific Ocean, Atlantic Ocean and Artic Ocean [*Capo and DePaolo*, 1992; *Winter et al.*, 1997]. Recent studies, however, have found considerable variations in regional Sr flux and Sr isotopic composition, especially in marginal seas [*Andersson et al.*, 1994; *Basu et al.*, 2001; *Huang and You*, 2007]. These new findings reflect recent advances in analytical precision over traditionally used techniques for the Sr isotope measurement, and also highlight the needs for understanding the Sr geochemical cycles in the coastal oceans.

For the Sr isotopic analysis, P-TIMS has been developed over the last few decades, and has been known as the most powerful and precise method for various fields of Earth Sciences. $^{87}Sr/^{86}Sr$ ratios were measured using the TRITON TI housed at NCKU and the double-filament technique (i.e., ionization side (ION): Re; evaporation side (EVA): Ta). Cup configuration, operating parameters and the data acquisition are shown in Table 2.10.

1 μL of the Sr solution containing 100-400 ng of Sr (NBS SRM 987, $SrCO_3$, dissolved in ultra-pure DIW) was directly loaded onto pre-cleaned and outgassed (at 4 A for 2 h) Ta filaments, and heated to dryness at 1.0 A. The ^{88}Sr beam was then ionized at an ION current of ~3400 mA (1450-1500°C) and an EVA current of ~300 mA. The ^{84}Sr, ^{85}Rb, ^{86}Sr, ^{87}Sr, and ^{88}Sr were collected in Faraday L2, L1, Central cup C, H1 and H2, respectively (see Figure 3.5). When the signal intensity of ^{88}Sr was larger than 0.01 V, lens focusing and ionic optics were made to obtain optimal signals. The current was then gradually increased at a constant heating rate of 50-100 mA/min until the intensity of ^{88}Sr was ~20 V. Prior to data acquisition, peak centering and peak scanning were done to optimize the cup alignment and the peak shape.

Table 2.10 The operating parameters, data acquisition and cup alignment for the Sr isotope.

Sr$^+$ P-TIMS	
High Voltage (V)	9950
EVA current (mA)	3500-3700
ION current (mA)	500-600
Pyrometer (°C)	1500-1550
HV Source Press (mbar)	<2.0 × 10-7
Ion Getter Press (mbar)	<5.0 × 10-9
Lens Focus	
Extraction Left (V)	8900-9000
Extraction Right (V)	8900-9000
Condenser (V)	7950-7990
X-symmetry (V)	50-70
Z-focus (V)	10~-10
Data Acquisition	
Number of Block	9
Cycles/Block	15
Integration time (s)	16.777
Number of Integration	1
Idle time (s)	1

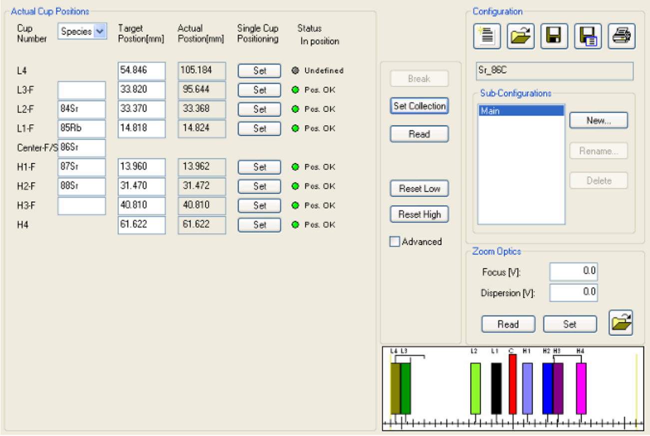

Actual Cup Positions

Cup Number	Species	Target Postion[mm]	Actual Postion[mm]	Single Cup Positioning	Status In position
L4		54.846	105.184	Set	● Undefined
L3-F		33.820	95.644	Set	● Pos. OK
L2-F	84Sr	33.370	33.368	Set	● Pos. OK
L1-F	85Rb	14.818	14.824	Set	● Pos. OK
Center-F/S	86Sr				
H1-F	87Sr	13.960	13.962	Set	● Pos. OK
H2-F	88Sr	31.470	31.472	Set	● Pos. OK
H3-F		40.810	40.810	Set	● Pos. OK
H4		61.622	61.622	Set	● Pos. OK

Configuration: Sr_86C

Sub-Configurations: Main

☐ Advanced

Zoom Optics

Focus [V]: 0.0

Dispersion [V]: 0.0

The $^{87}Sr/^{86}Sr$ ratios are measured by determining ion current intensities at mass 87 and 86. Measured values are routinely corrected for mass fractionation (assuming $^{86}Sr/^{88}Sr = 0.1194$) using an empirical linear combination of the power law fractionation. The effects of potential error associated with the mass fractionation correction can be minimized by running large Sr signals, which displays a narrow range of $^{86}Sr/^{88}Sr$ ratios (0.1205-0.1201) for samples. The Rb contribution was corrected by assuming the natural abundance of $^{87}Rb/^{85}Rb$ (=0.3858). An assessment of reproducibility is critical and was conducted by measuring NBS 987 standards. An average value was 0.710270±0.000003 (2σ, n=20), demonstrating a long-term reproducibility of ±4 ppm (2σ). Although the short-term reproducibility was even better, 4 ppm error has been used throughout this study.

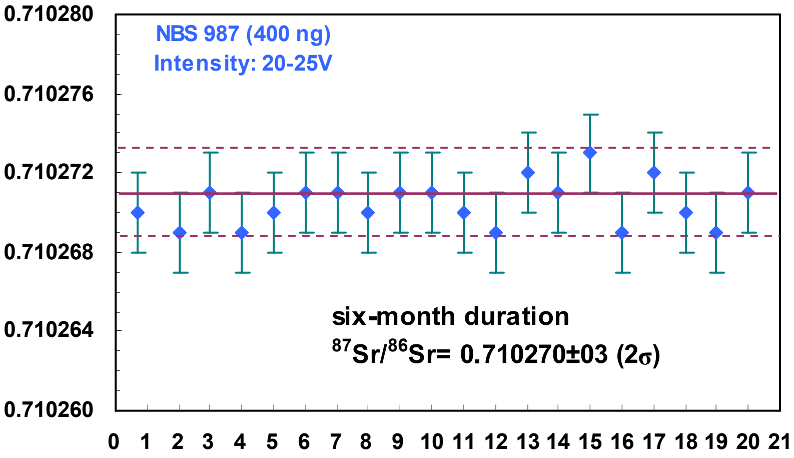

Figure 2.11 Replicate measurements of NIST SRM 987 by using P-TIMS technique over a period of 1 year. The mean values (solid purple line) and ±2σ (dashed purple lines) are also shown.

In summary, the analytical techniques using a new generation of TIMS TRITON TI were successfully developed to precisely determine the boron (±0.2‰ for P-TIMS and ±

0.5‰ for N-TIMS) and strontium isotope compositions (±4 ppm for P-TIMS with the double-filament technique) in the samples. This technique can, therefore, be applied to various materials, and further provides insights into the factors that influence or control the B and Sr isotopic signatures in the Earth's system derived by biological activity and the biogeochemical behavior.

2.3 Foraminiferal Methods

2.3.1 Sample selection

A series of sediment-trap (M1S, M2 and M3, Figure 3.6 and Table 3.6), core-top specimens (see Figure 3.7) and sediment core samples (SCS-15B, ODP Site 1144 and 1145, Figure 3.7 and Table 3.7) collected from SCS were used to measure trace element ratios, together with B and Sr isotopes in foraminiferal calcites for establishing the empirical calibrations and reconstructing past climate change in the SCS. Three dominant planktonic species (G*lobigerinoides ruber*, *Globigerinoides sacculifer* and *Neogloboquadrina dutertrei*) were selected in the studying site, and the size fraction of foraminifera ranged from 250 to 350 μm in order to minimize ontogenetic effects.

Table 2.11 Sediment trap deployments in the northern South China Sea that provided samples used in this study.

Trap ID	Latitude	Longitude	Water depth (m)	Trap depth (m)	sampling date	Season
M1s	21 30.86'N	119 27.87'E	2950	T2: 925 T3: 1925 T4: 2702	Dec/01, Jan/02 and Mar/02	Winter-Spring
M2	19 01.04'N	117 31.50'E	3740	T1: 240 T2: 1240 T3: 2240 T4: 3240	Oct/01 and Jan/01	Autumn-Winter
M3	20 30.27'N	118 14.05'E	2626	T1: 597 T2: 1126 T3: 1726 T4: 2326	May/02, July/02 and Aug/02	Spring-Summer

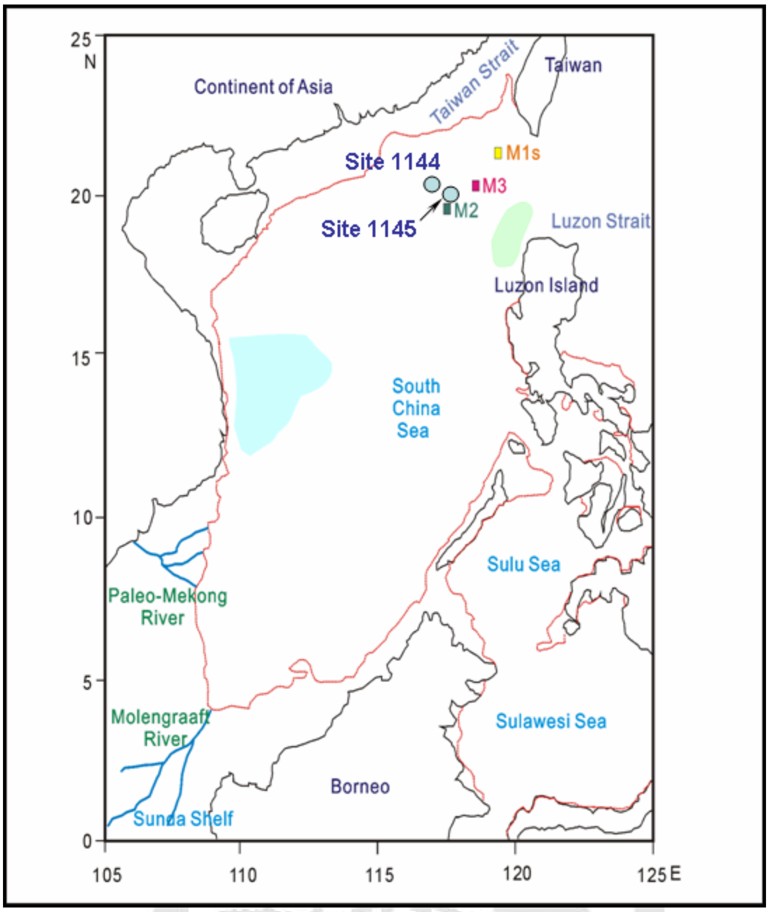

Figure 2.12 Locations of sediment traps (M1S, M2 and M3) and ODP Site 1144 and 1145 in the SCS. Red line represents 100-m isobath, showing approximately position of coastline during glacial low sea level. Mekong and Molengraaff Rivers on the (emerged) glacial Sunda Shelf are also indicated in the southwestern SCS. Modern upwelling regions occur in southeast Vietnam (blue shade area) and northwest Luzon Island (green shaded), during summer and winter time, respectively [*Shaw et al.*, 1996].

Table 2.12 Detailed information of core sediments in the South China Sea.

Site	Latitude (N)	Longitude (E)	Water depth (m)	Core type	Sample interval (cm)	Sedirate (cm/kyr)
North transect						
Site 1145	19°	1177° 38'	3175	KL	10	30-50
Site 1144	20° 31.8'	117° 25.14'	2037	KL	5-10	87
South transect						
SCS-15B	10° 19.32'	114° 10.61'	1500	G	30-40	30

KL = piston core. Sedimentation rate (sedirate) are presented.
G= gravity core

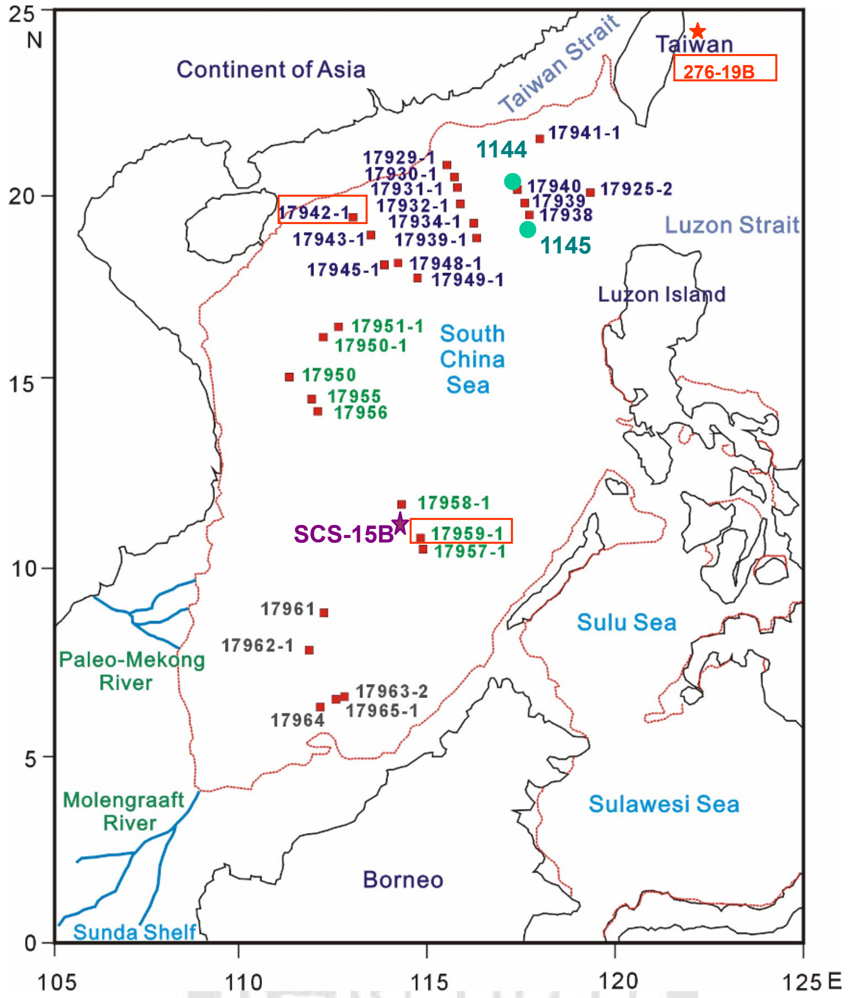

Figure 2.13 Locations of core-top sediments from the SCS and southern Okinawa Trough, as well as ODP Site 1144 and 1145, as well as SCS-15B in the SCS.

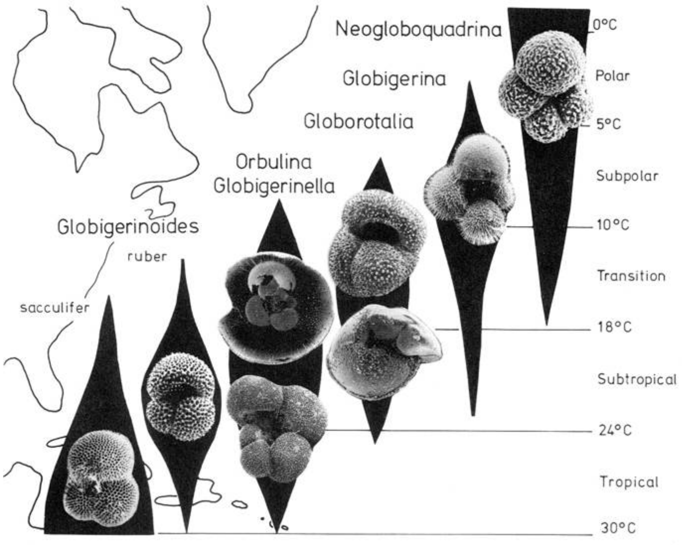

Figure 2.14 Habitat range for modern planktonic foraminifers (adapted from *Hemleben et al*., 1989)

Planktonic foraminifera live in surface oceans, which is highly dynamic environments and quickly response to the abrupt climate change. However, previous studies have indicated that foraminifers are unicellular animals, and their distributions, habitat depths and life cycles may be significantly different among species [*Hemleben et al*., 1989]. In addition, planktonic foraminifers commonly migrate vertically throughout their life cycle. For example, *G. ruber* and *G. sacculifer* spend most of their life cycles dwelling in the surface layer of tropical-subtropical oceans mainly in the mixed layer (Figure 3.6), and often live at deeper depth as they mature, and finally rise back into shallower water (Figure 3.7). Of special interest is that *G. sacculifer* grows a sac-like chamber after it completes reproduction.

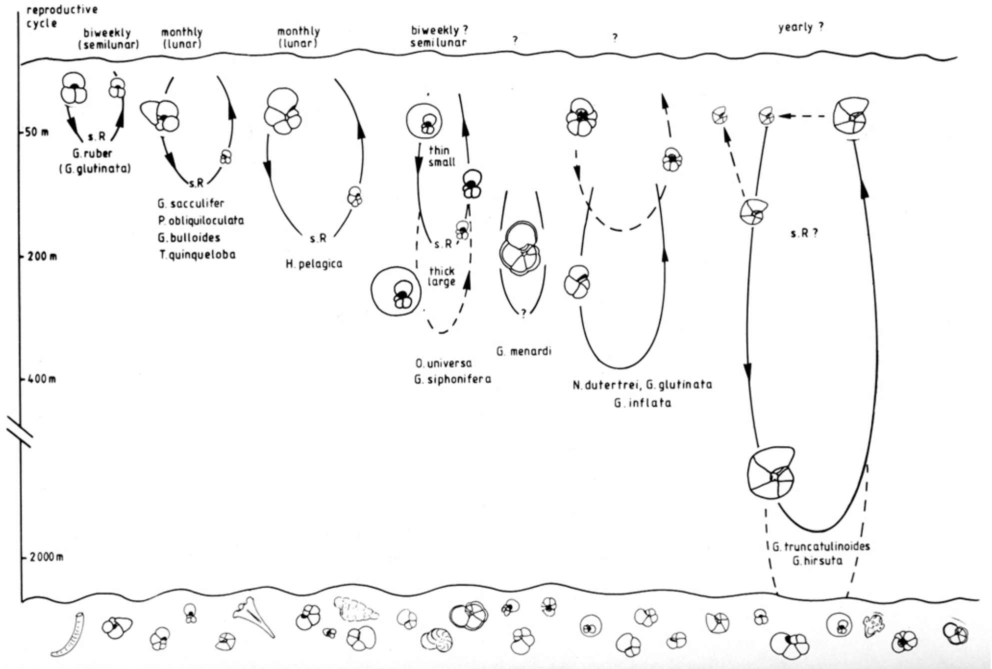

Figure 2.15 Depth habitat of modern planktonic foraminifers (adapted from *Hemleben et al*., 1989)

Table 2.13 Calcification depth of modern planktonic foraminifers (adapted from *Hemleben et al*., 1989)

Species	Calcification Depth, m
Globigerinoides ruber pink	0–25
Globigerinoides ruber white	0–50
Globigerinoides sacculifer	0–50
Globigerinoides sacculifer with sac	0–50
Globigerinella aequilateralis,	50–75
Orbulina universa thin test	50–100
Orbulina universa thick test	50–100
Globigerinoides conglobatus	50–100
Neogloboquadrina dutertrei	50–100
Pulleniatina obliquiloculata	50–100
Globorotalia inflata	100–400
Globorotalia truncatulinoides	200–500
Globorotalia crassiformis	500–800
Globorotalia hirsuta	500–800

The habitat depths of planktonic foraminifera are related to the regional variability of physical and chemical conditions in the ocean. For the SCS, calcification depth of the three planktonic species can be theoretically estimated through a systematic comparison between predicted equilibrium $\delta^{18}O_c$ and measured foraminiferal $\delta^{18}O_c$. Considerable works on S and $\delta^{18}O_{sw}$ have indicated that the two parameters are strongly affected by monsoon precipitation and freshwater input [*Lin et al*., 2003 and references therein]. The modern S-$\delta^{18}O_{sw}$ relationship, $\delta^{18}O_{sw}= -11.6+ 0.33\times S$, has been established from coastal seawater samples [*Lin et al*., 2003].

On the other hand, re-arrangement of paleotemperature equations described by *O'Neil et al*. [1969] and *Shackleton* [1974] can also be used to calculate equilibrium $\delta^{18}O_c$:

$$\delta^{18}O_c= (\delta^{18}O_{sw}-0.27)+[4.38-(4.38^2-4\times0.1\times(16.9-T))^{0.5}]/2\times0.1 \qquad (1)$$

The predicted $\delta^{18}O$ of calcite, in equilibrium with seawater, were then calculated using equation (1) and monthly mean temperature in seawater profiles. Comparison between foraminiferal $\delta^{18}O_c$ values and theoretically predicted $\delta^{18}O_c$ at various depths (Figure 3.8) allows estimating a mean calcification depth for individual species and the final compiled results are schematically drawn in Figure 3.9. The estimated species-specific calcification depths are in good agreement with known depth ranges for living planktonic species by plankton tow and trap specimens from the SCS [*Lin et al*., 2004].

2.3.2 Cleaning procedure for foraminiferal shell calcite

About 15-20 individuals (250-350 μm in size) of foraminiferal shells were hand-picked under stereoscope to minimize ontogenetic effects. These foraminiferal tests were gently crushed to facilitate removal of remnant cytoplasma from the interior of shell chamber and then a series of physical and chemical cleaning protocols modified from *Boyle and Keigwin* [1985/1986] and *Anand et al.* [2003] were applied to completely remove potential contamination phases. For crushing shell samples, foraminifera tests were ultrasonically cleaned three times with distilled water, twice with methanol and eventually rinsed with distilled water several times to remove adhering detrital grains and fine clay materials. Reduction and DTPA reagents (so called "Cd" and "Ba" cleaning methods [*Boyle and Keigwin*, 1985/1986; *Lea and Boyle*, 1993]) were used to remove Fe-Mn oxides and barite accumulation within these shells. For trap samples, more care is necessary to clean all adsorbed contamination due to the present of organic matter not generally found in down-core sediments and lengthy exposure to organic-rich materials in the collecting cups (see also *Anand et al.* [2003] and *Pak et al*., [2004]). Organic matter contents presented in the inner chambers were intensively oxidized in 50% buffered hydrogen peroxide-sodium hydroxide solution at 90°C water bath for at least 30 minutes followed by a dilute acid (0.001N HNO_3) polish to remove adsorbed metals. After weak acid leaching, distilled water were introduced again to completely remove all surface-adsorbed and residue contaminants, and finally transfer

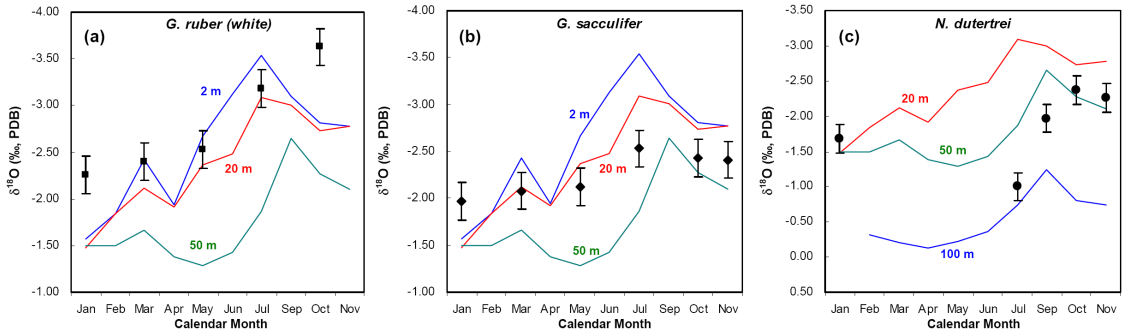

Figure 2.16 Determinations of depth habitat for the three dominant planktonic species, (a) *G. ruber* white, (b) *G. sacculifer* without sac and (c) *N. dutertrei*, in the SCS. Measured $\delta^{18}O_c$ of foraminiferal calcite is plotted against calendar month, together with predicted $\delta^{18}O_c$ in equilibrium with seawater for various water depths using T and S profiles at time of the trap deployment and relationships of S-$\delta^{18}O_{sw}$ in the SCS.

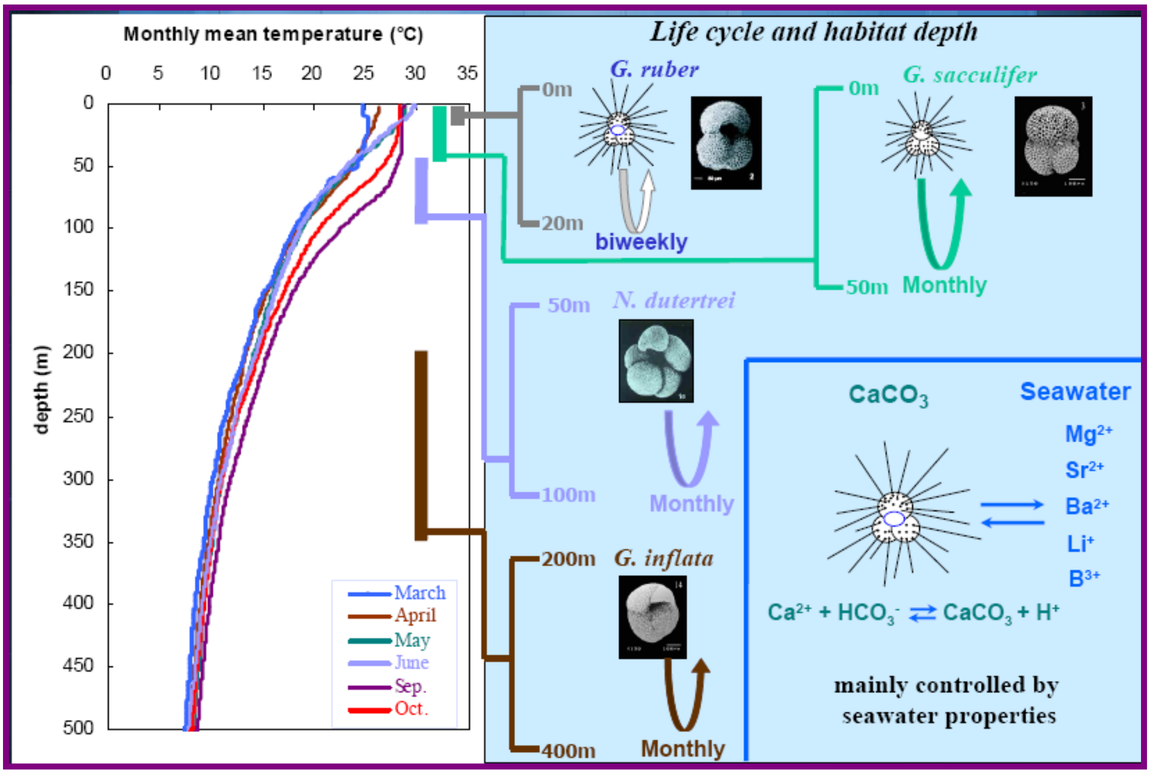

Figure 2.17 Depth habitats for the living planktonic species in the SCS used in this study.

calcite fragments into new acid-leached microcentrifuge vials prior to analysis. The remaining shell calcites were then dissolved in 0.065N HNO_3 contains internal standards of Sc and Y. All dilute nitric acids used were prepared with a Vycor sub-boiling system and other chemical reagents were purified by PFA two-bottle equipments or commercial ultrapure-grade reagents. Sample preparation procedures were processed under class-10 working bench to eliminate trace element blank derived from HEPA air-filter.

2.3.3 Efficiency of the cleaning method

Three core-top sediments from the northwestern (SO17942-1, water depth: 329 m) and the central South China Sea (SO17959-1, water depth: 1957 m), as well as from the southern Okinawa (276-19B, water depth: 727 m) were selected to evaluate the differences in the cleaning procedure between Cd (with DTPA) and Mg cleaning methods (commonly used method) for foraminiferal calcites, as well as the efficiency of this extra-cleaning step. All the core-top samples were analyzed at least twice to obtain more representative value (Figures 3.10 and 3.11).

Because the SCS ocean basin is a marginal sea, the problem of contaminations associated with detrital or continental materials (e.g., Mn oxides or Fe hydroxides) on shell chemistry from core-top sediments must be more serious than the open oceans. Preliminary results indicate much higher levels of Fe, Mn, Al in cleaned calcites without a reductive step (i.e., DTPA), and show significant decreases in these trace metal ratios after the DTPA treatment. This can be explained by effective removals of detrital sources and Fe-Mn oxides. Furthermore, Li/Ca, Zn/Ca, Ba/Ca, and U/Ca ratios also show constant and reasonable results compared to cultured (living) foraminifera, implying the DTPA treatment should be involved to obtain real signals of Li, Zn, Ba, and U in foraminifera, especially for cores collected from marginal seas. In contrast, no significant changes in Sr/Ca, B/Ca, and S/Ca ratios. For Mg/Ca ratios, slightly decreasing trends are in agreement with previous study reported by *Barker et al.* [2003].

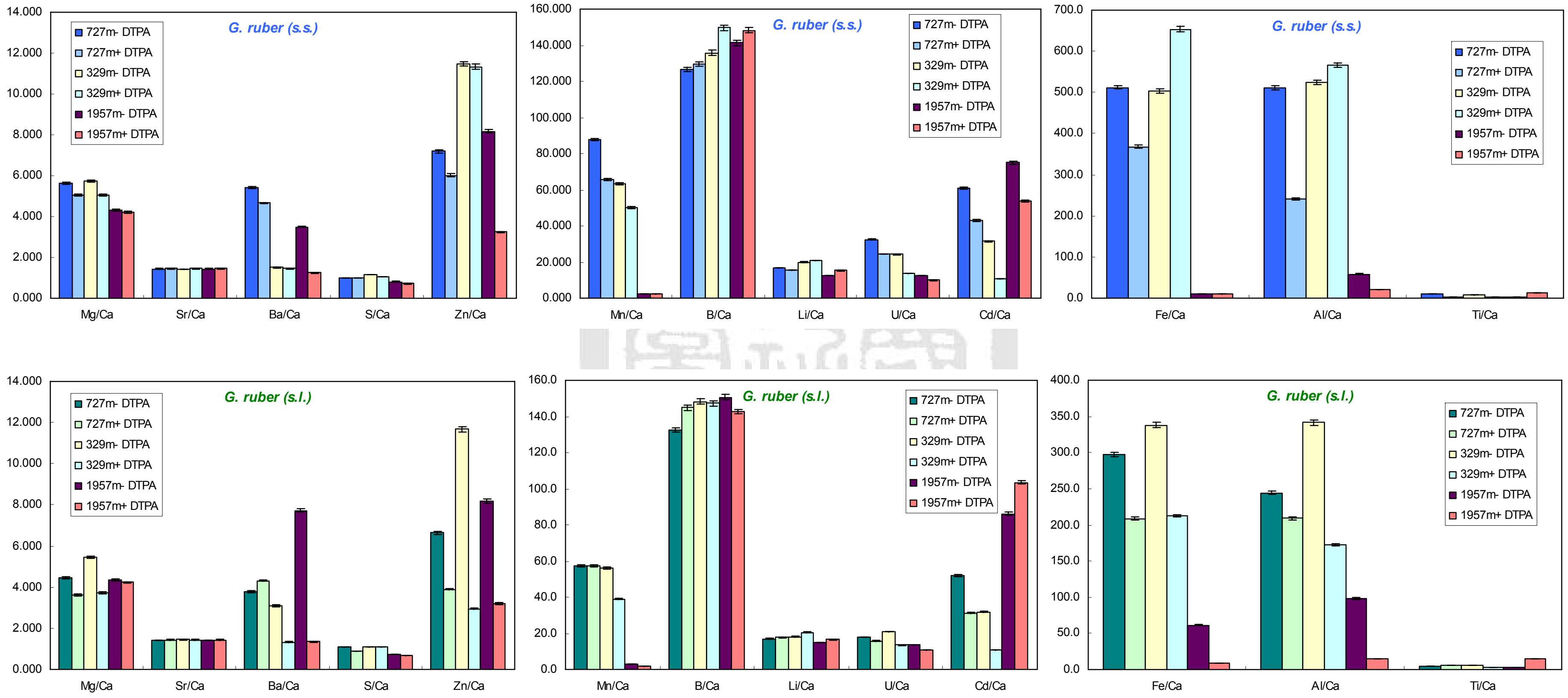

Figure 2.18 The comparisons of trace element ratios in different planktonic species with different chemical treatments (with/without DTPA). Three core-top sediments were taken from different water depths (the distance to the continent) in the South China Sea and southern Okinawa Trough. Units for Mg/Ca, Sr/Ca, S/Ca are mmol/mol, for B/Ca, Li/Ca, Mn/Ca, Ba/Ca, Zn/Ca, Al/Ca and Fe/Ca are μmol/mol, for U/Ca and Cd/Ca are nmol/mol. Error bars were presented a long-term precision (2σ).

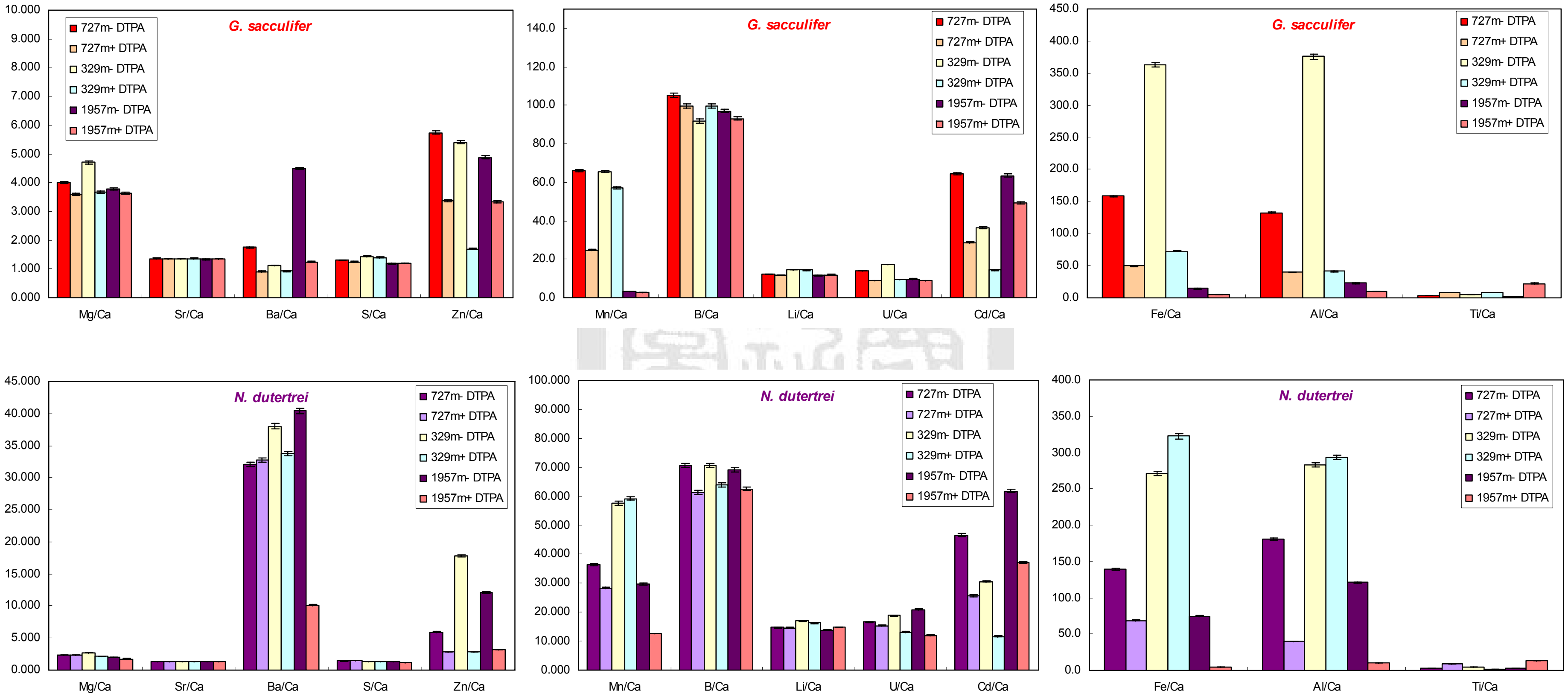

Figure2.19 (Continued) The comparisons of trace element ratios in different planktonic species with different chemical treatments (with/without DTPA). Three core-top sediments were taken from different water depths (the distance to the continent) in the South China Sea and southern Okinawa Trough. Units for Mg/Ca, Sr/Ca, S/Ca are mmol/mol, for B/Ca, Li/Ca, Mn/Ca, Ba/Ca, Zn/Ca, Al/Ca and Fe/Ca are µmol/mol, for U/Ca and Cd/Ca are nmol/mol. Error bars were presented a long-term precision (2σ).

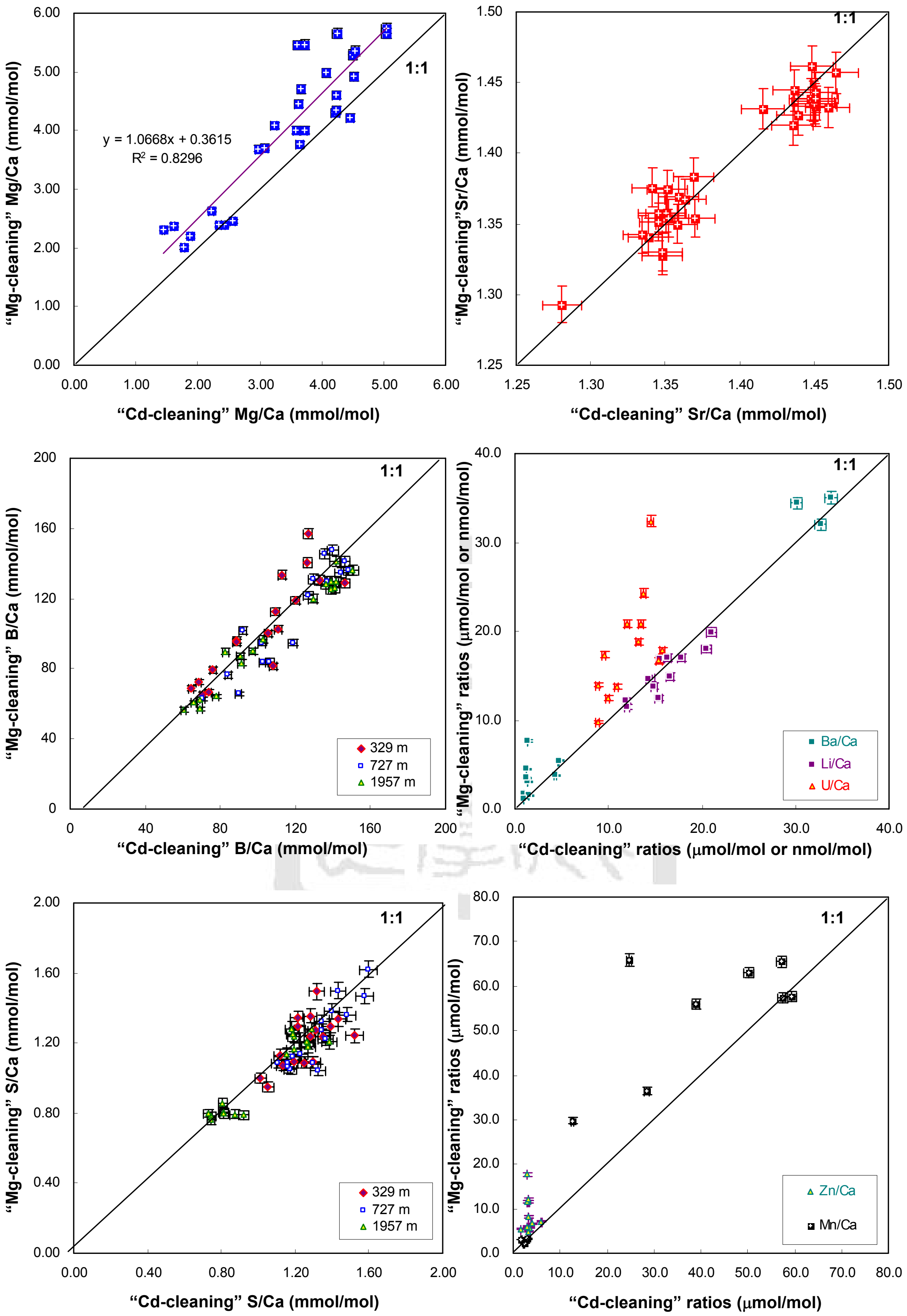

Figure 2.20 The plots of (a) Mg/Ca, (b) Sr/Ca, (c) B/Ca, (d) Ba/Ca, Li/Ca and U/Ca, (e) S/Ca, and (f) Zn/Ca and Mn/Ca ratios obtained by the use of “Mg-cleaning” (*Elderfield and Ganssen*, 2000) versus “Cd-cleaning” (*Boyle and Keigwin*, 1985/86). The primary difference between the two procedures is the use of a reductive step (i.e., DTPA) in the case of Cd-cleaning. Error bars were presented a long-term precision (2σ).

2.4 Seawater and pore water Methods

2.4.1 Sample selection and preparation

Seawater

Surface seawater samples and vertical profiles were collected from the North Equatorial Current (10°N, 140°W) in the Pacific Ocean, South China Sea, and Okinawa Trough (Figure 3.12), and have been measured for the boron and strontium isotopic compositions to understand the isotopic variations in the modern water columns. All water samples were sampled using the Glo-Flo bottles and subsequently filtered through 0.45 μm membrane filter (Nuclepore), transferred to acid-leached polypropylene containers, and then acidified to pH< 1.5 with distilled HNO_3. These valuable data can also provide an essential database and further evaluating the potential uses of boron and strontium isotopes in planktonic foraminifers as environmental proxies in the past ocean. The detailed discussion will be given in Chapter 6 and Chapter 7, for boron and strontium, respectively.

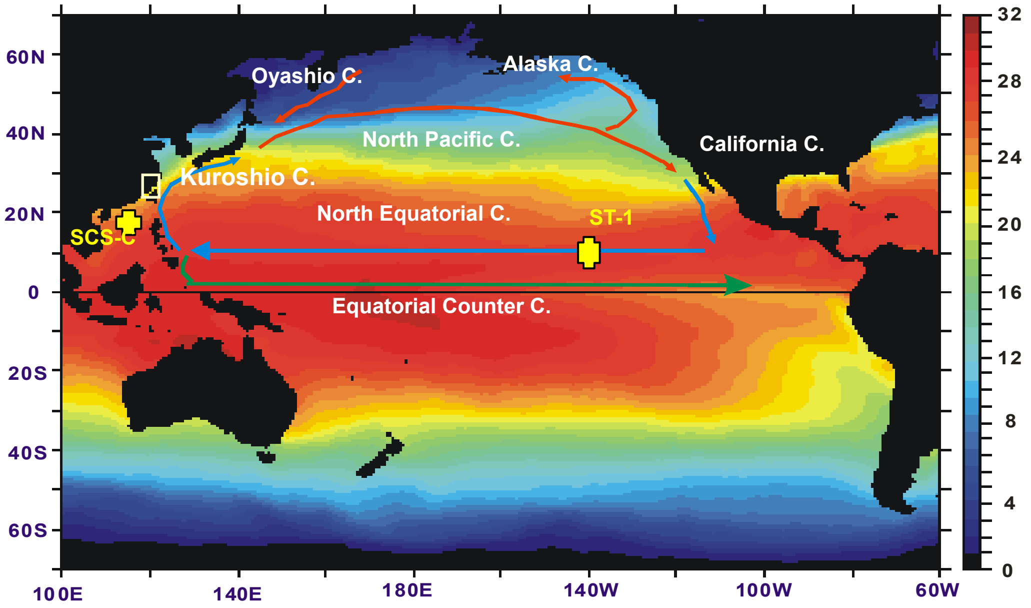

Figure 2.21 Location of seawater sampling stations used in this study.

Pore water

Pore water samples were taken from ODP Site 1202 (Leg 195, Okinawa Trough), ODP Site 1143 and 1146 (Leg 184, South China Sea) (see Figure 3.13), and were obtained by routine squeezing procedures on board JOIDES RESOLUTION using sediment sections of 5-10 cm long, which were cut immediately after core retrieval on the deck. Samples were then filtered through 0.45 μm membrane filter (Nuclepore) and acidified for laboratory analyses. Forty-one interstitial waters from ODP Site 1202 were collected with a depth resolution of 1.5 m and 20 m at intervals of 0-41.6 and 41.6-410 mbsf, respectively. For ODP Site 1143 and 1146, samples were collected with a depth resolution of 10 m and 30 m at intervals of 0-60 and 60-500 mbsf, respectively.

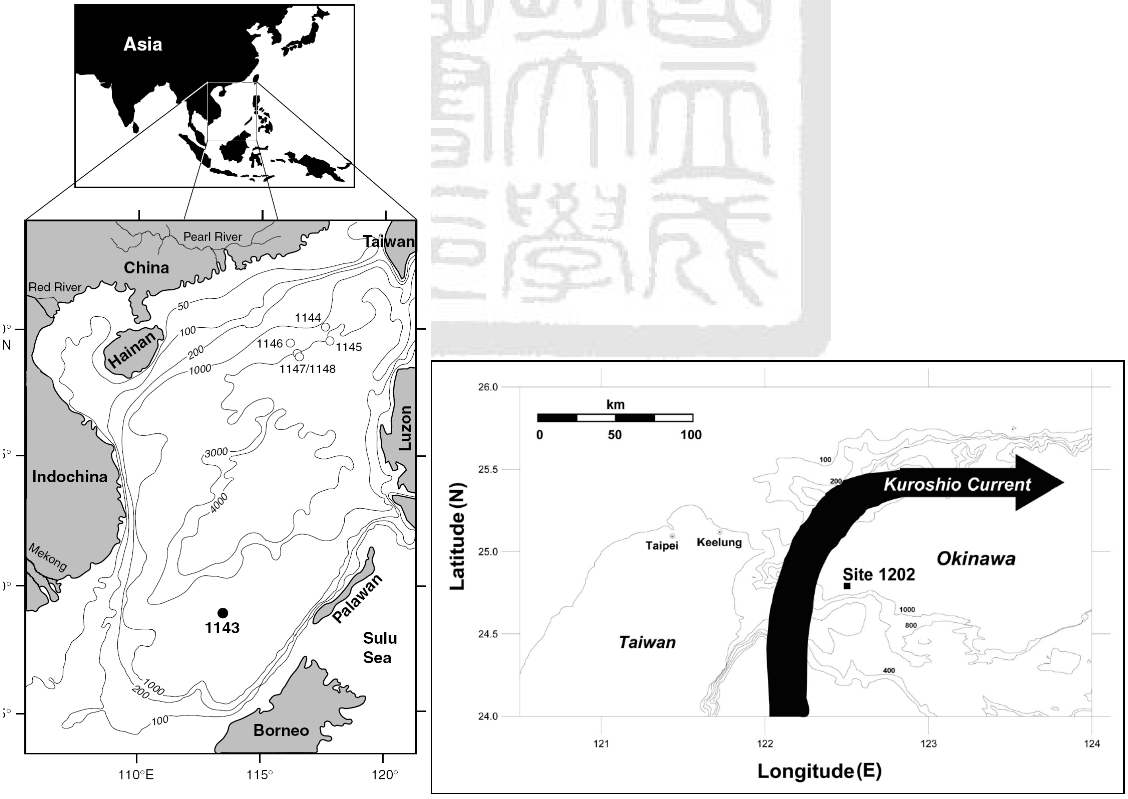

Figure 2.22 Location map showing ODP Site 1143 and 1146 in the South China Sea, and ODP Site 1202 in the southern Okinawa Trough.

2.4.2 Measurements on concentrations of major, minor and trace elements

The major ion concentration including chloride, sulfate, sodium, potassium, magnesium, and calcium were analyzed by ion chromatography installed at NCKU, with an average precision of 3-5%. Because seawater and pore water samples contain very high total dissolved solid, therefore, matrix effect must be taken into account for quantifying the concentrations of trace elements. In this study, minor and trace element concentrations were directly determined by HR-ICP-MS (Element 2) using 200-fold dilution. A series of seawater matrix-match standards prepared from certified seawater reference materials (NASS-5, salinity= 30.4, and IAPSO, salinity= 35) were used to correct for potential matrix-induced mass discrimination, and median resolution mode were applied to overcome the spectral interferences. Analytical precision and accuracy for all the elements varied between 2 to 3%. Dissolved B concentrations were determined using a curcumin colorimetric technique modified from *Grinstead and Snider* [1967] by UV-Visible spectrometer with a precision of approximately 3%, and the measured values are consistent with the results analyzed by HR-ICP-MS.

2.5 Conclusions

Retrieval of historic chemical information from biogenic carbonates (e.g., foraminifera and corals) has largely limited to Mg/Ca and Sr/Ca ratios in the past. Method presented here has extended the capability to the trace elements (e.g., Li, Cd, Ba, U, B, S, Mn), as well as B and Sr isotopes which are incorporated into skeleton carbonates. Detrital and organic materials associated with contaminants can be completely removed from pure carbonates by an intense series of the cleaning procedure. Changes in physical and chemical properties of the ocean are, therefore, recoverable through these trace element ratios and isotopic ratios in the biogenic carbonates. As for the seawater-matrix samples, a rapid and precise determination for elemental concentrations and isotopic compositions has also been developed in this study and further used to elucidate the relationship of biogenic carbonates and seawater.

As will be seen in the subsequent chapters, these methods have been applied to reconstruct the temporal changes in the surface ocean prompted by sea-surface temperature (Mg/Ca in foraminiferal calcites), oceanic pH (B/Ca, U/Ca and B isotope ratio), as well as continental inputs (Sr/Ca and Sr isotope ratio), in order to approach the physical and chemical condition of the past ocean.

References

Anand, P., Elderfield, H., Conte M. H., 2003. Calibration of Mg/Ca thermometry in planktonic foraminifera from sediment trap time series. Paleoceanography 18, 1050- 1065.

Andersson, P. S., Wasserburg, G. J., Ingri, J., Stordal M. C., 1994. Strontium, dissolved particulate loads in fresh and brackish waters: the Baltic Sea and Mississippi Delta. Earth Planet. Sci. Lett. 124, 195-210.

Barth, S., 1997. Boron isotopic analysis of natural fresh and saline waters by negative thermal ionization mass spectrometry. Chem. Geol. 143, 255-261.

Basu, A. R., Jacobsen S. B., Poreda, R. J., Dowling, C. B., Aggarwal P. K., 2001. Large groundwater strontium flux to the oceans from the Bengal Basin and the marine strontium isotope record. Science 293, 1470-1473.

Boyle, E. A., Keigwin, L. D., 1985/1986. Comparison of Atlantic and Pacific paleochemical records for the last 215, 000 years: Changes in deep ocean circulation and chemical inventories. Earth Planet. Sci. Lett. 76, 135-150.

Burke, W. H., Denison, R. E., Hetherington, E. G., Koepnick, R. B., Nelson, H. F., Otto J. B., 1982. Variations of seawater ^{87}Sr/^{86}Sr throughout Phanerozoic time. Geology 10, 516-519.

Capo, R. C., DePaolo D. J., 1992. Homogeneity of Sr Isotopes in the Oceans. EOS Transactions of the AGU 73, 272.

Elderfield, H., Ganssen, G., 2000. Reconstruction of temperature and δ^{18}O of surface ocean waters using Mg/Ca of planktonic foraminiferal calcite. Nature 405, 442-445.

Gäbler, H., Bahr, A., 1999. Boron isotopic ratio measurements with a double-focusing magnetic sector ICP mass spectrometer for tracing anthropogenic input into surface and ground water. Chem. Geol. 156, 323-330.

Grinstead, R. R., Snider, S., 1967. Modification of the curcumin method for low level boron determination. Analyst 92, 532-533.

Herbert, C. G., Johnstine, R. A. W., 2003. Mass Spectrometry Basic. p457.

Huang K.-F., You C.-F., 2007. Tracing Freshwater Plume Migration in the Estuary after a Typhoon Event using Sr Isotopic Ratios. Geophysical Research Letters 34, L02403, doi:10.1029/2006GL028253.

Kasemann, S., Meixner, A., Rocholl, A., Vennemann, T., Rosner, M., Schmitt, A. K.,

Lea, D. W., Boyle E. A., 1993. Determination of carbonate-bound barium in corals and foraminifera by isotope dilution plasma mass spectrometry. Chem. Geol. 103, 73-84.

Leeman, W. P., Vocke, R. D., Beary, E. S., Paulsen, P. J., 1991. Geochim. Cosmochim. Acta 55, 3901-3907.

Lemarchand, D., Gaillardet, J., Lewin, E., Allegre, C. J., 2000. An optimized procedure for boron separation and mass sprectrometry for river water samples. Chem. Geol. 182, 323-334.

Lin, H.-L., Wang, W.-C., Hung, G.-W., 2004. Seasonal variation of planktonic foraminiferal isotopic composition from sediment traps in the South China Sea. Mar. Micropaleontol. 53, 447-460.

Olivares, J. A., Houk, R. S., 1986. Anal. Chem. 58, 20.

O’Neil, J. R., Clayton, R. N., Mayeda, T. K., 1969. Oxygen isotope fractionation in divalent metal carbonates. The Journal of Chemical Physics 51, 5547-5558.

Pak, D. K., Lea, D. W., Kennett, J. P., 2004. Seasonal and interannual variation in Santa Barbara Basin water temperatures observed in sediment trap foraminiferal Mg/Ca. Geochem. Geophys. Geosyst. 5, doi:10.1029/2004GC000760.

Palmer, M. R., Swihart, G. R., 1996. Boron isotope geochemistry: an overview. In: Crew, E. S., Anovitz, L. M. (Eds.), Boron: Mineralogy, Petrology and Geochemistry. Mineral. Soc. Am., 33, 709-744.

Rosenthal, Y., Field, M. P., Sherrell, R. M., 1999. Precise determination of element/calcium ratios in calcareous sample using sector field inductivity coupled plasma mass spectrometry. *Anal. Chem.*, *71*, 3248-3253.

Rosner, M., ROmer, R. L., Meixner, A., 2005. Air handling in clean laboratory environments: the reason for anomalously high boron background levels. Anal. Bioanal. Chem. 382, 120-124.

Shackleton, N. J., 1974. Attainment of isotopic equilibrium between ocean water and the benthic foraminiferal genus Uvigerina: Isotopic changes in the ocean during the last glacial. Cent. Natl. Rech. Sci. Colloq. Int. 219, 203-209.

Shaw, P.-T., Chao, S.-Y., Liu, K.-K., Pai, S.-C., Liu, C.-T., 1996. Winter upwelling off Luzon in the northeastern South China Sea. J. Geophys. Res. 101, 16435–16448.

Spivack, A. J., Edmond, J. M., 1986. Determination of boron isotope ratios by thermal ionization mass spectrometry of dicesium metaborate cation. Anal. Chem. 58, 31-35.

Spivack, A. J., Edmond, J. M., 1987. Boron isotope exchange between seawater and oceanic crust. Geochim. Cosmochim. Acta 51, 1033-1043.

Tanner, S. D., Douglas, D. J., French, J. B., 1994. Appl. Spectrosc. 48, 1373.

Thomas, R., 2001. A beginner's Guide to ICP-MS Part VII: Mass Separation Devices-Double-Focusing Magnetic –Sector Technology. Spectroscopy 16, 22-24.

Thomas, R., 2002. A beginner's Guide to ICP-MS Part XII: A review of Interferences. Spectroscopy 17, 24-31.

Wiedenbeck, M., 2001. Boron and oxygen isotope composition of certified reference materials NIST SRM 610/612 and reference materials JB-2 and JR-2. Geostandards Newsletter 25, 405-416.

Winter, B. L., Clark, D. L., Johnson C. M., 1997. Late Cenozoic Sr isotope evolution of the Artic Ocean: constraints on water mass exchange with the lower latitude oceans. Deep-Sea Res. II 44, 1531-1542.

CHAPTER 3.

In situ Calibration of Mg/Ca Ratio in Planktonic Foraminiferal Shell using Time-series Sediment Trap:

A case study of intense dissolution artifact in the South China Sea

3.1 Introduction

Reconstruction of past sea surface temperatures (SSTs) in the tropical/subtropical ocean is a fundamental element for understanding the distribution of heat and moisture, as well as the evolution of the monsoon system, in the past. Moreover, it is also influential in driving long- and short-term climatic oscillations, because of the perceived importance of dynamical interaction between the atmosphere and the surface oceans in the tropics [*Lea et al.*, 2000; *Rosenthal et al.*, 2003]. The South China Sea (SCS) is located at the western equatorial Pacific, and adjacent to two major climatically sensitive areas, the Western Pacific Warm Pool (WPWP) and the Indonesian archipelago. The SCS, therefore, becomes one of the most important settings in response to seasonal variability of Asian monsoon intensity. However, the potential influence of the Asian monsoon on SST variations in the tropical ocean remains unclear and this can be investigated by high-resolution and accurate down-core records of SSTs in the SCS during the Quaternary [*Oppo and Sun*, 2005; *Steinke et al.*, 2005].

Previous studies based on laboratory and field work have highlighted that uptake of Mg by planktonic foraminifera from ambient seawater is positively correlated with water temperature (~9±1%, per °C) [*Hastings et al.*, 1998; *Lea et al.*, 1999; *Elderfield and Ganssen*, 2000; *Rosenthal and Lohmann*, 2002; *Anand et a*l., 2003]. Mg/Ca in planktonic foraminiferal calcite is, therefore, becoming a well-established temperature proxy for past surface oceans. Additionally, paired Mg/Ca and $\delta^{18}O$ measurements on foraminifera are of great merit in reconstructing both SSTs and $\delta^{18}O$ in seawater [*Rosteck et al.*, 1993; *Mashiotta et al.*, 1999]. Through this approach, the past changes in regional sea surface salinity (SSS) can be estimated directly [*Schmidt et al.*, 2004]. These results provide important information related to potential linkages of abrupt climatic changes between high latitudes and tropical regions (e.g., Heinrich events and paleo-*El Niño* or *La Niña*) in a centennial-millennial time scale [*Koutavas et al*., 2002; *Stoll et al*., 2002].

Besides temperature effects, a growing body of studies indicate that foraminiferal Mg/Ca can be altered by post-depositional dissolution [*Rosenthal and Lohmman*, 2002] and physiological processes [*Rosenthal et al*., 1997; *Bentov and Erez*, 2005; 2006]. Such artifact and bio-mineralization processes would significantly affect accurate estimates of Mg/Ca-based temperature records. The current state of the art for planktonic Mg/Ca calibrations heavily relies on culture experiments [*Nüernberg et al*., 1996; *Lea et al*., 1999; *Russell et al*., 2004] and core-top specimens [*Elderfield and Ganssen*, 2000; *Rosenthal et al*., 2000; *Dekens et al*., 2002]. Here we propose a third method to establish Mg/Ca calibration through the application of planktonic foraminifera from the modern water column, which was collected by time-series sediment traps deployed in the SCS. The trap materials will bridge the gaps between controlled laboratory culture experiments and field core-top calibrations, and can be particularly helpful to validate possible correlations between shell chemistry and natural variability of environmental factors that can be measured precisely [*Anand et al*., 2003; *Pak et al*., 2004].

In this study, we employ a particular design on sediment trap arrays, deployed at various depths in the northern SCS. This design enables us to systematically refine artifacts of partial dissolution in the SCS, and to evaluate directly any shell compositional changes in response to ambient seawater conditions. Furthermore, these results will be compared with core-top calibrations by *Hasting et al*. [2001] and *Deken et al*. [2002] to elucidate possible relationships between core-top and sediment trap data. Our main objectives are to: (1) document intra-annual (seasonal) variations of Mg/Ca and $\delta^{18}O$ in foraminiferal shells; (2) establish an in situ Mg/Ca-SST empirical equation for the SCS; (3) systematically evaluate partial dissolution effects on foraminiferal Mg/Ca in the SCS; (4) assess other environmental parameters that would affect shell Mg/Ca; (5) compare in situ empirical calibration in SCS with available equations from core-top and sediment trap materials worldwide.

3.2 Previous Paleoceanographic Studies

Since the sedimentation rates in the SCS are extremely high (30-100 cm/kyr, an order of magnitude higher than other parts of the Pacific) with widespread distribution of carbonate sediments, it provides an ideal region for high-resolution paleoceanographic reconstruction [e.g., *Wang et al.*, 1995]. Previous studies have shown growing interests in the late Quaternary oceanographic environments of the SCS, such as reconstructions of paleo-SST, productivity, deep water circulation, carbon cycles, monsoon variations, and climatic interactions between the continent and the ocean during the glacial-interglacial periods [*Thunell et al.*, 1992; *Miao et al.*, 1994; *Wang et al.*, 1999; *Pelejero et al.*, 1999; *Oppo and Sun*, 2005]. Among these studies, the determination of past temperature (T) and salinity (S) in surface ocean waters at low-latitude areas is the most essential element for understanding changes in atmosphere and ocean interaction, as well as relative Inter-Tropical Convergence Zone position in the Asian monsoon system. Thus, accurate estimates of SST and SSS in the past ocean are particularly important for a detailed evaluation of climatic sensitivity in response to solar radiation and monsoon strength variation.

Although considerable efforts have been dedicated to study the temporal paleo-SST variations in the SCS, results of marine faunal assemblage, oxygen isotope, unsaturated alkenone, and foraminiferal Mg/Ca data display a large discrepancy in temperature changes (1-6°C) from Last Glacial Maximum to late Holocene [*Wang and*

Wang, 1990; *Pelejero et al.*, 1999; *Kienast et al.*, 2001; *Chen et al.*, 2005; *Oppo and Sun*, 2005]. This partly can be attributed to a lack of understanding in oceanographic, ecological and geochemical processes affecting these temperature proxy indicators. To evaluate these potential interferences, we focus to refine geochemical processes that affect shell Mg/Ca in terms of partial dissolution, which may alter significantly the Mg/Ca ratios in planktonic foraminifera [*Brown and Elderfield*, 1996; *Rosenthal and Lohmann*, 2002].

3.3 Modern Hydrography of the SCS

The climatic variation and water mass circulation in the upper ocean of the SCS are mainly modulated by seasonal prevailing monsoons. Typically, during the summer wet season, May to October, the SCS is dominated by a warm monsoon and prevailing southwest winds. In contrast, a winter dry monsoon appears from December to February and is known to link with the Southern Oscillation Index [*Zhang et al.*, 1997]. These annually reversing monsoon winds cause a clockwise water mass circulation in summer, and then gradually switch to a reversal counterclockwise gyre during wintertime [*Wyrtki*, 1961]. Local upwelling is also forced by wind-driven circulations, such as of east Vietnam coast in summer and northwest Luzon and north Sunda shelf during the winter seasons [*Shaw et al.*, 1996; *Liu et al.*, 2002].

The modern SST distribution in summer is rather uniform (ranging from 28 to 29°C) and show a small north-south gradient. Average salinity is relatively low (approximately 33) and mainly results from fresh water inflow throughout the region. In contract, the average surface temperature is 18°C and 27°C in northern and southern SCS, respectively and shows a north-south gradient in wintertime [*Wyrtki*, 1961]. The winter SSS is relatively stable due to rather constant regional precipitation.

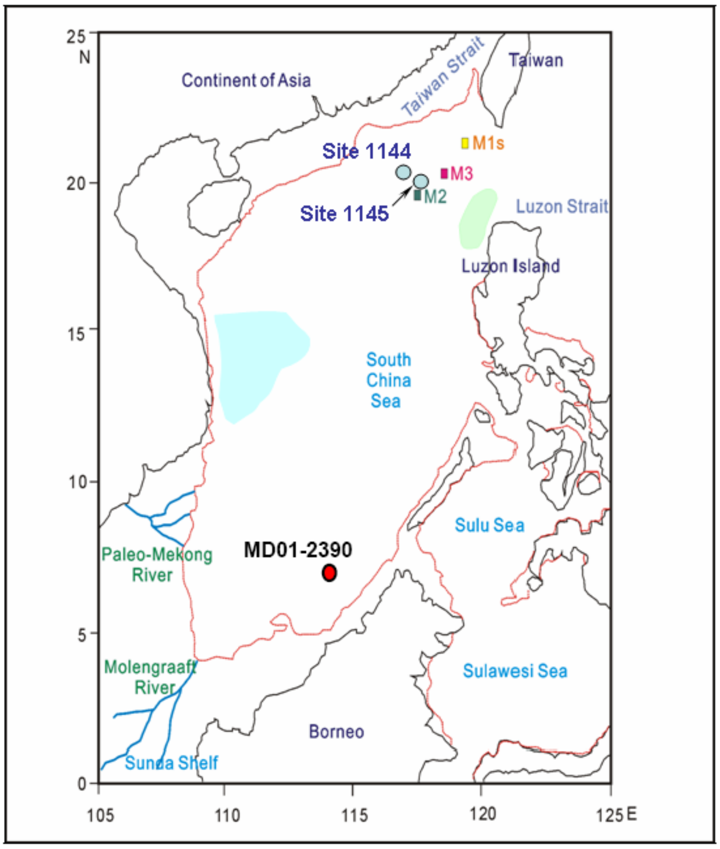

Figure 3.1 Locations of sediment traps (M1S, M2 and M3), ODP Site 1144 and 1145, as well as MD01-2390 in the SCS. Red line represents 100-m isobath, showing approximately position of coastline during glacial low sea level. Mekong and Molengraaff Rivers on the (emerged) glacial Sunda Shelf are also indicated in the southwestern SCS. Modern upwelling regions occur in the southeast Vietnam (blue shade area) and northwest Luzon Island (green shaded), during summer and winter time, respectively [*Shaw et al*., 1996].

The intermediate water in the SCS occupies depths of 250 to 1000 m, and its physical properties are quite similar to the North Pacific Intermediate Water (NPIW) [*Wyrtki*, 1961; *Nitani,* 1972]. This similarity has been attributed partly to the intrusion of NPIW, which is characterized with a salinity minimum at ~490 m. The SCS deep water is fed possibly by North Pacific Deep Water, based on hydrographic observations and T-S characteristics at 3500 m [*Nitani,* 1972]. The present-day calcite lysocline and carbonate compensation depth (CCD) in the SCS is located approximately at 3000 m and 3800 m, respectively [*Miao et al*., 1994] where calcite saturation depth ($\Omega_{calcite}<1$) is at about 2500 m [*Chou et al*., 2006]. Although sediment trap arrays in this study were deployed at shallower depth than lysocline or CCD in the SCS, *Chou et a*l. [2006] reported carbonate dissolution in shallow water based on TCO_2^{carb} measurements (i.e., excess TCO_2 produced by carbonate dissolution). Dissolution artifacts on shell Mg/Ca in the SCS will be further discussed in section 6.5.

3.4 Materials and Methods

3.4.1 Sediment Trap Deployment

Three dominant surface-dwelling species of planktonic foraminifera (*Globigerinoides ruber*, *Globigerinoides sacculifer*, and *Neogloboquadrina dutertrei*) were collected from continuous trap arrays deployed at the northern SCS (M1s, M2 and M3, see Figure 3.1 and Table 3.1 for details) to examine relationships between planktonic shell chemistry and seawater properties. Three mooring sites were selected at the northern SCS basin and these trap cups were deployed at four different depths to evaluate dissolution artifacts that may bias metal/Ca ratios. The collecting interval for each cup was set for 15-days except for those in which foraminiferal abundances were low (i.e., M1s samples), inadequate low particular flux or cup array malfunction (i.e., level 3 at M3). Operational details on trap types, deployment procedures and retrieving the trap array have been described in *Lin et al*. [2004]. Owing to the original design of the trap for radioisotope study, only discrete but representative intra-annual specimens can be taken for foraminiferal trace element/Ca ratio (TE/Ca) analyses.

3.4.2 Foraminiferal Cleaning and Analysis

About 15-20 individuals (250-350 μm in size) of foraminiferal shells were hand-picked under a stereoscope to minimize ontogenetic effects. These foraminiferal tests were gently crushed to facilitate removal of remnant cytoplasma from the interior of shell chamber and then a series of physical and chemical cleaning protocols modified from *Boyle and Keigwin* [1985/1986] and *Anand et al*. [2003] were applied to completely remove potential contamination phases. For crushing shell samples, foraminifera tests were ultrasonically cleaned three times with distilled water, twice with methanol, and finally rinsed with distilled water several times to remove adhering detrital grains and fine clay materials. Reduction and DTPA reagents (so called “Cd” and “Ba” cleaning methods [*Boyle and Keigwin*, 1985/1986; *Lea and Boyle*, 1993]) were used to remove Fe-Mn oxides and barite accumulation within these shells.

Table 3.1 Sediment trap deployments in the northern South China Sea that provided samples used in this study

Trap ID	Latitude	Longitude	Water depth (m)	Trap depth (m)	sampling date	Season
M1s	**21 30.86'N**	**119 27.87'E**	**2950**	**T2: 925** **T3: 1925** **T4: 2702**	**Dec/01, Jan/02 and Mar/02**	**Winter-Spring**
M2	**19 01.04'N**	**117 31.50'E**	**3740**	**T1: 240** **T2: 1240** **T3: 2240** **T4: 3240**	**Oct/01 and Jan/01**	**Autumn-Winter**
M3	**20 30.27'N**	**118 14.05'E**	**2626**	**T1: 597** **T2: 1126** **T3: 1726** **T4: 2326**	**May/02, July/02 and Aug/02**	**Spring-Summer**

For trap samples, more care is necessary to clean all adsorbed contamination due to the presence of organic matter not generally found in down-core sediments and lengthy exposure to organic-rich materials in the collecting cups (see also *Anand et al*. [2003] and *Pak et al*., [2004]). Organic matter presented in the inner chambers was intensively oxidized in 50% buffered hydrogen peroxide-sodium hydroxide solution in a 90°C water bath for at least 30 minutes followed by a dilute acid (0.001N HNO_3) polish to remove adsorbed metals. After weak acid leaching, distilled water was introduced again to completely remove all surface-adsorbed and residue contaminants, and finally the calcite fragments were transferred into new acid-leached microcentrifuge vials prior to analysis. The remaining shell calcites were then dissolved in 0.065N HNO_3 containing internal standards of Sc and Y. All dilute nitric acids used were prepared with a Vycor sub-boiling system and other chemical reagents were purified by PFA two-bottle equipments or commercial ultrapure-grade reagents. Sample preparation procedures were processed under class-10 working bench to eliminate the trace element blank derived from HEPA air-filter.

High-resolution ICP-MS (Finnigan Element 2) was used to measure multiple elemental ratios simultaneously at the National Cheng Kung University. The foraminiferal TE/Ca ratios were determined at the same detection mode to eliminate possible intensity bias, and to quantify intensity ratios using external matrix-matched standards adapted from *Rosenthal et al*. [1999]. In the analysis, ^{24}Mg, ^{25}Mg, ^{43}Ca, ^{44}Ca, and ^{88}Sr were determined both by low ($m/\Delta m= 300$) and medium mass resolution ($m/\Delta m= 4000$) to avoid spectral interferences. A series of matrix-matched standards were prepared from high-purity ICP standard solutions by a gravimetrical method and were standardized for TE/Ca by standard addition method. Long-term reproducibility of Mg/Ca and Sr/Ca ratios are evaluated based on routine runs of the consistency standards and matrix-matched standards, and analytical precision is ±0.44% and ±0.48% (2σ) for Mg/Ca and Sr/Ca, respectively. Internal standards of 1 ppb Sc and Y were added into sample solutions to monitor the instrumental stability (1 hr <0.5% and 8 hrs< 2.0% variations) during measurement. In addition, ^{27}Al, ^{55}Mn, and ^{56}Fe were also measured by low- and medium-resolution mode to monitor detrital contaminants, such as fine clay and Fe-Mn coatings. Al/Ca, Mn/Ca and Fe/Ca were mostly lower than 40 μmol mol^{-1}, well below thresholds for likely contamination (>100 μmol mol^{-1}). Stable oxygen and carbon isotopic data of shell calcites (250-300μm for *G. ruber* and 300-355μm for *G.*

sacculifer) separated from the same samples were adopted from *Lin et al*. [2004] to compare with measured Mg/Ca results.

3.4.3. Estimates of Habitat Mean Temperature and Salinity

The habitat mean T (T_H) and S (S_H) at which forams calcified were calculated based on modern seawater T and S profiles and the specific habitat depths of three dominant planktonic foraminifera in the SCS. To achieve this, it is necessary to obtain appropriate continuous hydrographic data and the place of calcification for individual species. Because the life cycles of the three planktonic species are about 2-4 weeks, monthly mean temperature and salinity were directly obtained using data from the CTD records during sediment trap deployment. In additions, the hydrographic grid data (117.0- 119.0°E; 19.0- 21.00°N) of monthly mean T and S (between 1994 to 1999) in the SCS were also available from the National Center for Oceanographic Research (NCOR) achieve of Taiwan to complement mean T and S data that no CTD data were collected during trap deployment.

Calcification depths of the three planktonic species can be theoretically estimated through comparisons between predicted equilibrium $\delta^{18}O_c$ and measured foraminiferal $\delta^{18}O_c$. For the SCS, considerable works on S and $\delta^{18}O_{sw}$ have been established and indicated that local relationships between two parameters were strongly affected through monsoon rain and/or freshwater input, which is characterized by changes in S-$\delta^{18}O_{sw}$ gradients during wet and dry seasons [*Su*, 2000; *Lin,* 2000], and were taken to be:

$$\delta^{18}O_{sw}= -14.58+ 0.43\times S \quad \text{for wet seasons, } r^2=0.85 \qquad (1)$$

$$\delta^{18}O_{sw}= -15.81+ 0.47\times S \quad \text{for dry seasons, } r^2=0.63 \qquad (2)$$

The rearrangements of the paleotemperature equations of *O'Neil et al*. [1969] and

Shackleton [1974] were also used for calculating the equilibrium $\delta^{18}O_c$:

$$\delta^{18}O_c = (\delta^{18}O_{sw} - 0.27) + [4.38 - (4.38^2 - 4\times0.1\times(16.9-T))^{0.5}]/2\times0.1 \qquad (3)$$

The predicted $\delta^{18}O$ of calcite in equilibrium with seawater were then calculated for various depths according to equation (3) and monthly mean temperature profiles. Based on the comparison between foraminiferal $\delta^{18}O_c$ values and theoretically predicted $\delta^{18}O_c$ at various depths (Figure 3.2), the mean calcification depths of individual species can be obtained and were listed in Table 3.2. The species-specific estimates of calcification depths in this study are in good agreement with known depth ranges for living species, estimated by using plankton tow and sediment trap specimens from the SCS [*Lin et al.*, 2004]. Base on these depth estimates, the T_H and S_H can be inferred by combining calcification depths of specific species, together with monthly mean T and S profiles, which given the most reliable habitat T and S records for the three planktonic species.

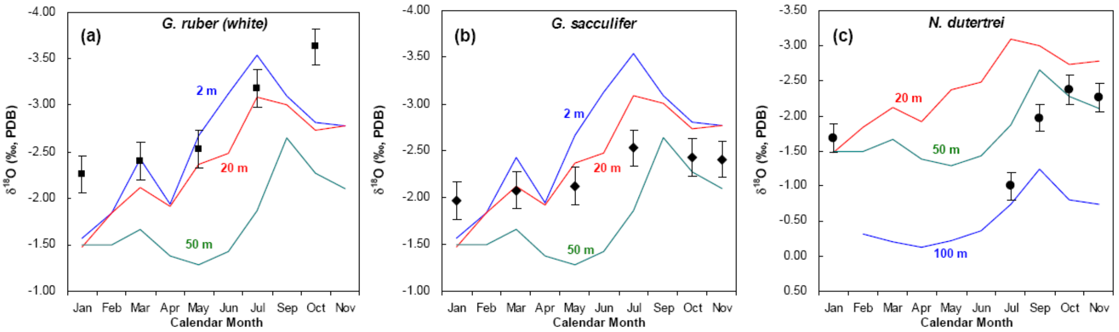

Figure 3.2 Determinations of depth habitat for the three planktonic species, (a) *G. ruber* white, (b) *G. sacculifer* without sac and (c) *N. dutertrei*, in the SCS. Measured $\delta^{18}O_c$ of foraminiferal calcite is plotted against calendar month, together with predicted $\delta^{18}O_c$ in equilibrium with seawater for various water depths using T and S profiles at time of the trap deployment and relationships of S-$\delta^{18}O_{sw}$ in the SCS.

To obtain pure temperature signals from measured shell $\delta^{18}O_c$, salinity-corrected foraminiferal $\delta^{18}O_c$ are also used for the latter comparisons with Mg/Ca ratios. The salinity correction involves subtraction from foraminiferal $\delta^{18}O_c$ and seawater $\delta^{18}O_{sw}$, which are local-scale linear relationship for the study area over the full depth range at which foraminifera were trapped. All seawater $\delta^{18}O$ was converted from standard mean ocean water (SMOW) scale to calcite Pee Dee Belemnite (PDB) unit with the correction of 0.27.

Table 3.2 Species of planktonic foraminifers in the SCS used in this study and estimations of calcification depth for individual species based on the comparison of foraminiferal $\delta^{18}O$ with calcite in equilibrium with seawater.

Planktonic species	Calcification depth, m
Globigerinoides ruber white	**0-20**
Globigerinoides sacculifer	**0-50**
Neogloboquadrina dutertrei	**50-100**

3.5 Sediment Trap Results

Foraminiferal Mg/Ca and Sr/Ca results obtained from continuous trap materials over one-year deployment period were summarized in Appendix Table A1. Mg/Ca ratio ranges from 3.244 to 5.135 mmol mol^{-1}, 2.632 to 4.185 mmol mol^{-1} and 1.689 to 2.944 mmol mol^{-1} for *G. ruber*, *G. sacculifer* and *N. dutertrei*, respectively. In addition to seasonal variability of SSTs, the observed wide ranges of Mg/Ca for intra-species could be associated with the biological activity. Planktonic foraminifera commonly migrate vertically throughout their life cycle and often live at deeper depth as they mature, which results in heterogenic distributions of Mg/Ca ratio within a signal shell and/or inter-species [*Brown and Elderfield,* 1996; *Elderfield and Ganseen,* 2000; *Eggins et al.*, 2003]. Nevertheless, species-specific Mg/Ca calibrations for individual species from the same sediment core can provide valuable information of hydrological variability of thermal structures in a water column [*Spero et al.*, 2003].

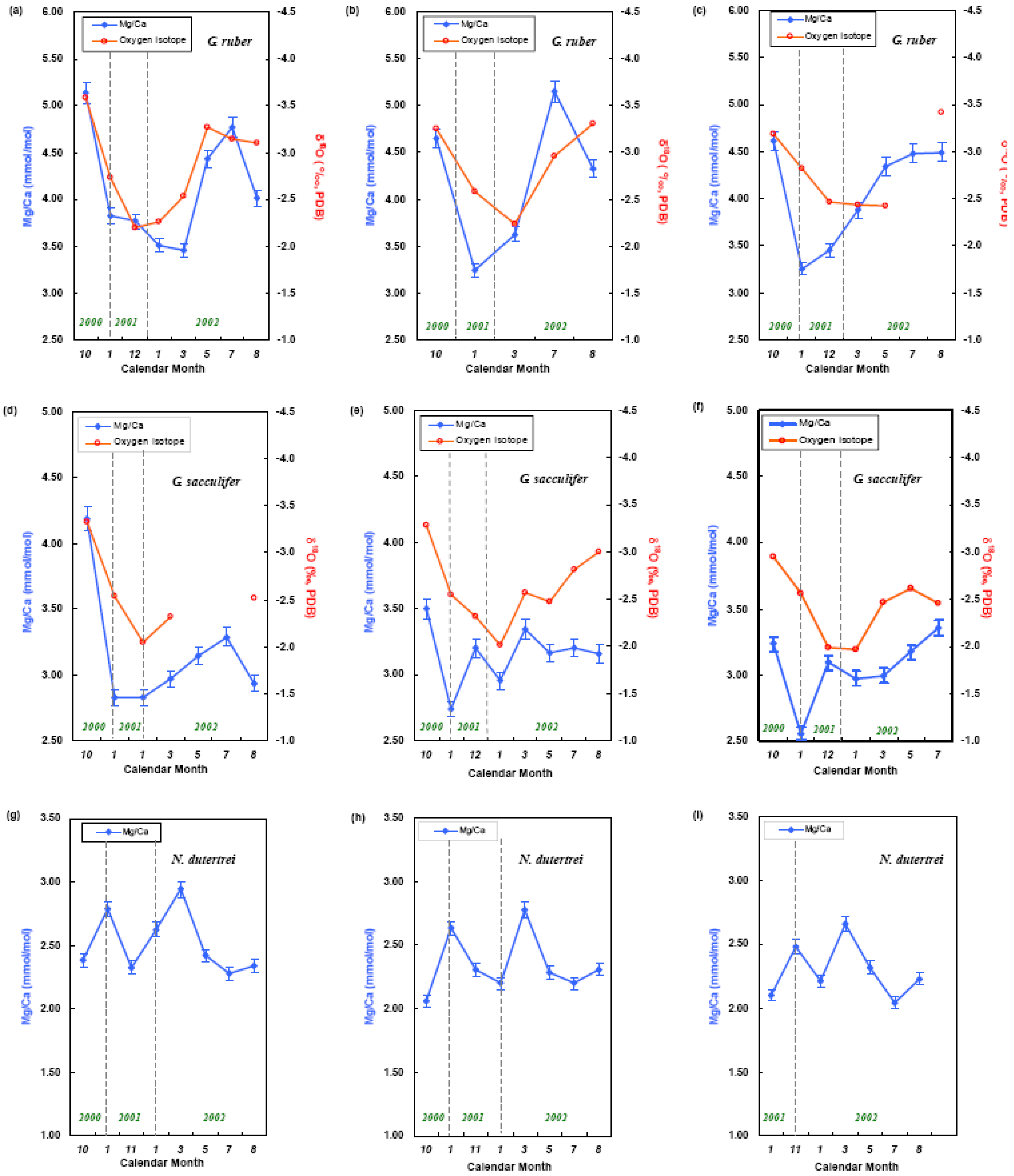

Figure 3.3 Intra-annual variations in Mg/Ca (mmol mol^{-1}) and salinity-corrected $\delta^{18}O$ (‰, PDB) of the two mixed-layer dwelling species, *G. ruber* (white) and *G. sacculifer* (without sac), as well as thermocline dwelling species- *N. dutertrei*. (a), (d) and (g) trap depths: <1000 m, (b), (e) and (h) trap depths: 1000-2000 m, (c), (f) and (i) trap depths: >2000 m. Note that the correlations between shell Mg/Ca and salinity-corrected $\delta^{18}O$ become weaker with increasing trap depth, suggesting a strong partial dissolution effect on foraminiferal Mg/Ca ratios in the SCS. For *N. dutertrei*, only Mg/Ca data is available from this study and shows a relatively small (~25%) seasonal variability relative to the other two surface dwelling species.

There are several remarkable features clearly documented in this study: (1) Strong intra-annual (seasonal) variations occur both in trapped foraminiferal Mg/Ca and $\delta^{18}O_c$ for the two planktonic species. In general, high Mg/Ca coupled with light $\delta^{18}O_c$ are observed in summer and fall months (May to October). Low Mg/Ca and heavy $\delta^{18}O_c$, on the other hand, characterize winter seasons (December to March) (Figure 3.3); (2) Deep-dwelling species showed a relatively small variation in Mg/Ca, in an order of *N. dutertrei*< *G. sacculifer*< *G. ruber* (Figure 3.3); (3) Mg/Ca is positively correlated with estimated T_H (Figure 3.4a) and shows negative relationships with $\delta^{18}O_c$ (Figure 3.4b). (4) An exponential equation fits Mg/Ca and mean habitat temperature, but shows a distinguishable difference with trap data from the Sargasso Sea (Figure 3.5); (5) Partial dissolution artifacts at various depths play an important role to alter Mg/Ca in foraminiferal calcite, even at water depths shallower than lysocline or CCD (Figure 3.6 and 3.7); (6) Foraminiferal Mg/Ca ratios were affected significantly by seawater temperature and dissolution, but potential influences by other hydrographic parameters (e.g., primary productivity and SSS) were not detected (Figure 3.9).

3.6 Discussion

3.6.1 Inter-species Foraminiferal Mg/Ca

Mg/Ca measurements of the three abundant planktonic species (*G. ruber* white, *G. sacculifer* and *N. dutertrei*) from the sediment trap in the SCS show an inter-species variability, possibly associated with calcification depths. Average Mg/Ca of *G. ruber* (white), *G. sacculifer* (w/o) and *N. dutertrei* is 4.137 mmol mol^{-1}, 3.068 mmol mol^{-1}, and 2.377 mmol mol^{-1}, respectively. The apparent difference among species is rather large compared with the potential analytical error (2σ) of ±0.005 mmol mol^{-1} for the Mg/Ca. The seawater Mg/Ca ratio does not vary under modern hydrological conditions due to the long residence times of Mg and Ca [*Broecker and Peng*, 1982]. Thus, it can be reasonably inferred that observed differences of Mg/Ca between planktonic species are mainly affected by changes in Mg partition coefficient (D_{Mg}).

Inorganic carbonate precipitation and foraminiferal culture experiment indicate that incorporation of Mg into calcite depends remarkably upon the temperature of the ambient solution [*Delaney et al*., 1985; *Oomori et al*., 1987; *Lea et al*., 1999], and can be explained by thermodynamic Mg^{2+} substitution of Ca^{2+} into the calcite crystal lattice [*Katz et al*., 1973; *Oomori et al*., 1987]. Postdepositional dissolution could play a significant role to alter foraminiferal Mg/Ca by preferential removal of Mg-enriched gametogenic calcites [*Rosenthal and Boyle*, 1993; *Brown and Elderfield*, 1996]. Other environmental factors, such as disequilibrium (or kinetic) effects, may also significantly affect Mg uptake from the ambient seawater based on the observed relationships between shell size and Mg/Ca ratios of planktonic foraminifera [*Elderfield et al*., 2002]. Moreover, there is evidence for Mg/Ca variability among different morphotypes of the same species, which might be related to differences in either growth season (e.g., *G. ruber* white vs. pink, [*Anand et al*., 2003]) or dwelling habitat (e.g., *G. ruber s.s.* and *G. ruber s.l.*, [*Steinke et al*., 2005]). In this study, we use mixed morphotypes of *G. ruber* white (i.e., *s.s.* and *s.l.*) due to sample size limitation required for precise TE/Ca determinations.

In order to eliminate possible influences of partial dissolution and disequilibrium processes, only foraminiferal Mg/Ca taken from the shallowest trap were used to assess correlations between inter-species shell Mg/Ca and depth habitat. The increases in inter-species Mg/Ca are accompanied by decreasing $\delta^{18}O_c$ and reflect a response to increased calcification temperature in the sequence *G. ruber* > *G. sacculifer* > *N. dutertrei*. This result is consistent with previous studies, which are characterized by relatively low Mg/Ca and enriched $\delta^{18}O_c$ for deep dwellers (e.g., *N. dutertrei*) compared to mixed-layer dwelling species (i.e., *G. ruber* and *G. sacculifer*) [*Fairbanks et al.*, 1982; *Rosenthal and Boyle*, 1993]. Alternatively, the offset between *G. ruber* and *G. sacculifer* is likely related to the addition of gametogenic calcite (~28%) [*Bé*, 1980] in *G. sacculifer*. Because gametogenic calcite of *G. sacculifer* is encrusted towards to the end of its life and sinks to the seafloor [*Bé and Anderson*, 1976; *Bé et al.*, 1977], the colder temperature in the deeper water would be recorded during their calcification, and, therefore, would decrease the average Mg/Ca of *G. sacculifer*. Although the inter-species differences in Mg/Ca are commonly linked to specific calcification depths of planktonic species, more recently Mg/Ca studies show a possible influence of biological processes on Mg uptakes during biomineralization of foraminiferal shells [*Bentov and Erez*, 2005; 2006].

3.6.2 Partition Coefficient for Mg

The element-to-calcium ratios in biogenic calcites depend on corresponding element-to-calcium ratios of ambient ocean water and the partition coefficients of elements between the solid carbonate and the seawater. These relationships are expressed as $(Mg/Ca)_{foram} = D_{Mg} \times (Mg/Ca)_{seawater}$, where $(Mg/Ca)_{foram}$ is a molar ratio of Mg to Ca in the foraminifera, $(Mg/Ca)_{seawater}$ is a molar ratio of Mg to Ca in seawater (assuming seawater Mg/Ca= 5.15 mol mol^{-1}, [*Broecker and Peng*, 1982]), and D_{Mg} is the partition coefficient of Mg in shell calcite. Using this relationship, we obtain D_{Mg} for all three planktonic species in the SCS. The apparent D_{Mg} values fall in a range of $0.06\text{-}0.10\times10^{-2}$ (ave. 0.08×10^{-2}), $0.05\text{-}0.08\times10^{-2}$ (ave. 0.06×10^{-2}), and $0.03\text{-}0.06\times10^{-2}$ (ave. 0.05×10^{-2}) for *G. ruber*, *G. sacculifer* and *N. dutertrei*, respectively. Again, this can be linked to depth habitats of specific life cycles for planktonic species (i.e., surface dwelling species have higher D_{Mg}, and are related to high calcification temperature or shallow habitat depth), suggesting that D_{Mg} in foraminiferal calcite is mainly a function of seawater temperature. These calculated values are consistent with estimates ($D_{Mg}\sim 0.05\times10^{-2}$) from core-top sediments [*Elderfield et al*., 2002] and culture experiments [*Nüernberg et al*, 1996]. However, these D_{Mg} values are apparently in contradiction to the inorganic experimental determination of the Mg partition [*Katz*, 1973; *Morse and Bender*, 1990], and are about two orders of magnitude lower than D_{Mg} predicted by inorganic equations (D_{Mg}= 5.3-6.2×10^{-2}), implying that biological processes exert an influence on co-precipitation of Mg in foraminifera.

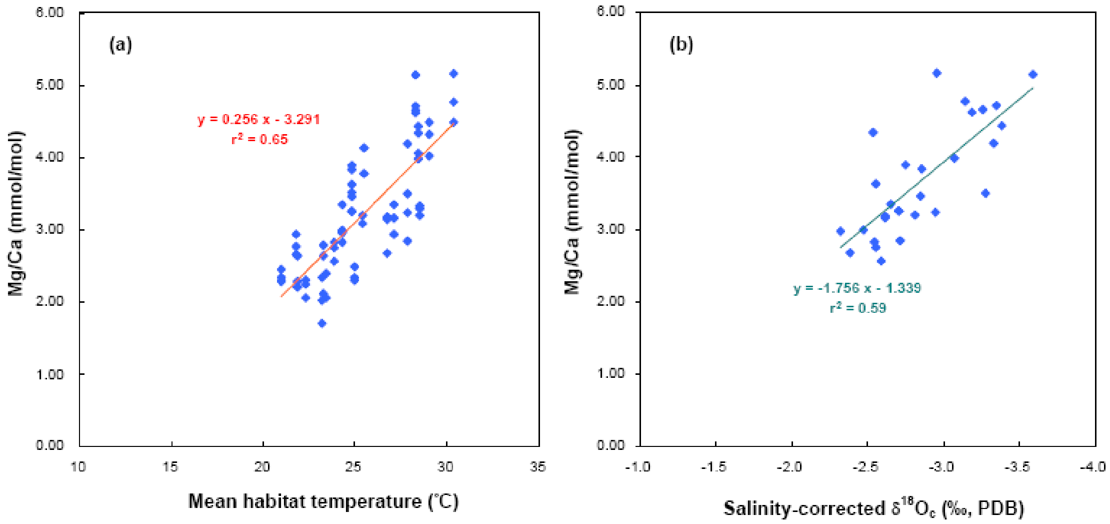

Figure 3.4 (a) Mg/Ca ratios in three planktonic foraminifera highly correlate with the mean habitat temperature (based on species-specific habitat depths and instrumental T and S), indicating a strong temperature dependency on shell Mg/Ca. Slightly scatter distribution of the data points can be attributed to the intense dissolution effect on Mg/Ca in the SCS. (b) The Plot of Mg/Ca versus salinity-corrected foraminiferal $\delta^{18}O$ (only show data with instrumental S data) also display a negative tendency, but relatively worse correlation coefficient (r^2) relative to plotting with mean habitat temperature.

3.6.3 Intra-annual Mg/Ca-$\delta^{18}O_c$ Relationship

Mg/Ca and salinity-corrected shell $\delta^{18}O_c$ data for two mixed-layer dwelling species (*G. ruber and G. sacculifer*) from the shallowest trap show a strong, but analogous intra-annual (seasonal) variation (Figure 3.3) over a ~6-7°C change (~2‰ for

G. ruber and ~1.5‰ for *G. sacculifer*) in estimated isotopic temperature. The amplitude of the seasonal Mg/Ca and $\delta^{18}O_c$ variability in *G. ruber* is significantly larger than *G. sacculifer* and *N. dutertrei*, implying that *G. ruber* grew and calcified at relatively shallower depths. This is supported by estimated habitat depth from plankton tows and sediment traps in this area [*Lin et al.,* 2004]. In general, for two mixed-layer dwelling species, high Mg/Ca values and light $\delta^{18}O_c$ occur in warm periods, and low Mg/Ca and heavy $\delta^{18}O_c$ during cold seasons. In contrast, the thermocline dweller *N. dutertrei* shows a small, but complicated Mg/Ca pattern (see Figures 3.3g-3i), possibly reflecting relative stable conditions, seasonal changes in thermocline depth or hydrographic variations by regional monsoon upwelling [*Liu et al*., 2002].

It is interesting to note that the in-phase correlation of Mg/Ca and salinity-corrected $\delta^{18}O_c$ seems to become weaker with increasing trap depth for the two mixed-layer dwellers. As $\delta^{18}O_c$ do not change significantly with trap depth, other environmental factors should have modified the primary shell Mg/Ca. Calcification of the planktonic foraminifera occurs in the upper 100 m and they descend to trap collectors after death. It takes 3 days to 2 weeks to reach collecting cups depending on the mooring depth, shell density, and sinking process during sinking in the water column. These tests are subject to chemical and physical processes in the water column. Consequently, dissolution and/or secondary overgrowth associated with diagenetic phases will cause alteration of primary Mg/Ca in the foraminiferal calcite [*Lohman*, 1995].

Although foraminiferal $\delta^{18}O_c$ has been widely used as a temperature-dependant proxy, an ontogenetic artifact can partly contribute to the discrepancy due to differences in test size used for $\delta^{18}O_c$ and Mg/Ca measurements in this study. In addition, S-$\delta^{18}O_{sw}$ correlations applied for salinity correction is not contemporaneous with actual sampling periods. The similar annual $\delta^{18}O_c$ cycles observed at various trap depths suggest that main discrepancy between Mg/Ca and $\delta^{18}O_c$ is likely caused by Mg/Ca partial dissolution artifacts. However, there is a small $\delta^{18}O_c$ variation at some collecting depths (e.g., Figure 3.3a-3c). This implies that shell $\delta^{18}O_c$ may also have been slightly altered by partial dissolution [e.g., *Wu and Berger*, 1989; *Rosenthal et a*l., 2000] or other more complicated factors.

3.6.4 In situ Mg/Ca-SST Calibration

Mg/Ca ratios in planktonic foraminiferal shells are primarily controlled by seawater temperature and result in a high correlation (r^2= 0.65) between Mg/Ca and estimated habitat temperature (Figure 3.4a). To compare with sediment trap data of *Anand et al.* [2003], we assumed that temperature sensitivity (i.e., exponential constant= 0.090) for multiple species in sediment traps in the Sargasso Sea can be applied. A temperature calibration in SCS can be described for all three species: Mg/Ca = 0.32 (±0.05) exp (0.090*T), r^2= 0.68. This calibration curve (see Figure 3.5a) deviates significantly from *Anand et al.* (2003) in the Sargasso Sea, Mg/Ca= 0.38 exp (0.090*T). A relatively larger scatter of the Mg/Ca ratio for all species has been observed in this study, and can be interpreted partly in terms of regional hydrological differences caused by seasonal monsoon and temporal changes of water masses in marginal sea. Hydrographic forcing could result in large differences in chemical properties at surface layers.

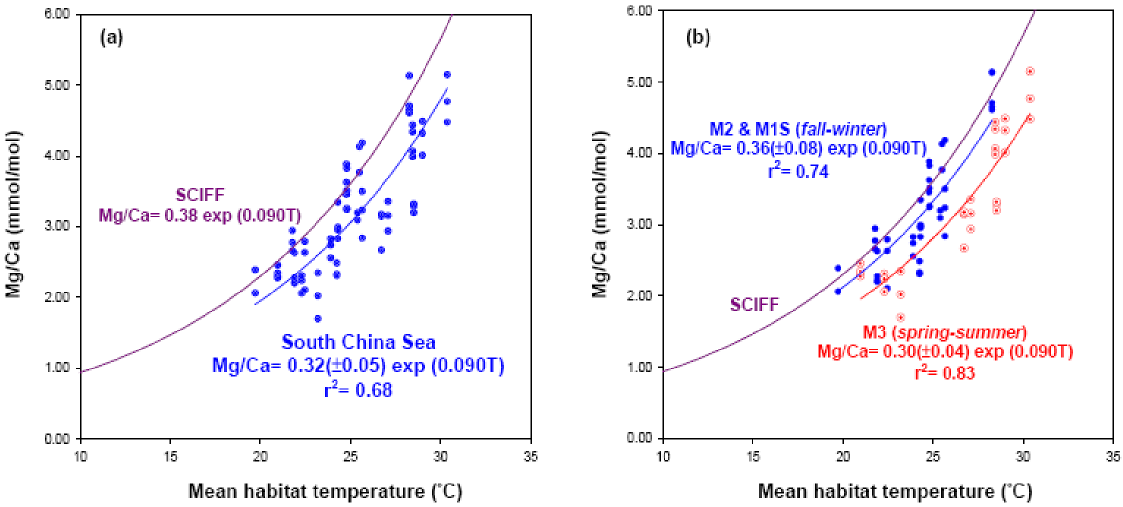

Figure 3.5 (a) Mg/Ca versus mean habitat temperature for all species in the SCS, and compare with previous calibration works from the Sargasso Sea sediment trap (Purple line) [*Anand et al.*, 2003]. All regression lines are assuming a constant exponential constant (=0.090). (b) Comparisons of seasonal variability of Mg/Ca calibration equations from two deployment periods (M2&M1S: fall-winter and M3: spring-summer).

A plot of Mg/Ca and estimated temperatures shows distinct trends between two collection periods (Figure 3.5b). The fall-winter trend (Mg/Ca= 0.36 (±0.08) exp (0.090*T), r^2= 0.74) is more close to the Mg/Ca-SST equation of *Anand et al.* [2003] than that of the spring-summer trend. The spring-summer trend (Mg/Ca= 0.30 (±0.04) exp (0.090*T), r^2= 0.83) is clearly biased toward to the low Mg/Ca ratio or the cold temperature. This most likely is a consequence of intense partial dissolution in the SCS, and a detailed discussion will be given in section 3.6.5. Besides, the species-specific calibration could not be established statistically because sample collections were conducted at different water depths and seasons, as well as the small changes in habitat temperatures for each species in the SCS. Advanced studies focused on the species-specific calibration would provide valuable information on temporal variability of thermal structures in water columns in this climate-sensitive low latitude region.

Another approach for the Mg/Ca empirical equation can be theoretically done by incorporating the dissolution term (e.g., depth or [CO_3^{2-}], *Deken et al.*, [2002]). Since there is no detectable change in Mg/Ca-derived equations from different depths during warm periods (Figure 3.6b), we further utilize the calibration curves without any dissolution correction. In contrast, in the fall-winter period, the Mg/Ca-SST equations are strongly correlated with depths (Figure 3.6a) where pre-exponent constant is a function of depth, 0.38-0.02*depth (km), r^2= 0.81. In principle, one can describe a statistical correlation between pre-exponential constant and depth for all three species as:

Mg/Ca= (0.38-0.02*water depth (km)) exp (0.090*T) for fall-winter (2)

Mg/Ca= 0.30 exp (0.090*T) for spring-summe (3)

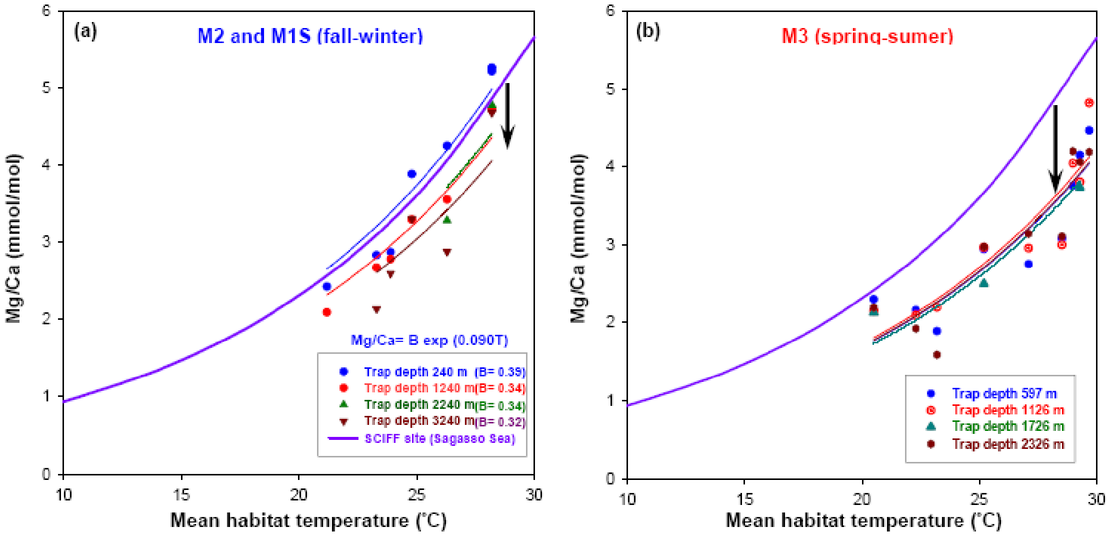

Figure 3.6 The regression curves of Mg/Ca and mean habitat temperature for various trap depths in the SCS show a strong dissolution effect on foraminiferal Mg/Ca with increasing trap depths during (a) Fall-winter period (cold/dry months), and (b) Spring-summer periods (warm/wet months). The pre-exponential constants for all regression lines are also showed in the cold season, and correlation coefficients (r^2) for all regression lines are better than 0.6.

Although the dissolution-corrected term for pre-exponential constant is derived only from limited data points (i.e., 4 trap depths), this calibration is rather reliable as its faithful reflection of water column conditions in the SCS, and high correlation coefficients (r^2>0.71) of the best-fit equations were obtained at various depths. One should be able to estimate annual SST records if average warm and cold SSTs were obtained using dissolution-corrected calibration curves established here.

3.6.5 Effect of Partial dissolution on Shell Chemistry

Earlier studies have shown that shell chemistry systematically decreases through post-depositional dissolution in un-saturated deep-water or pore fluids [*Lorens et al.*, 1977; *Rosenthal et al.*, 2000] and is thought to be influenced by preferential dissolution of high Mg calcite of the foraminiferal test. These high Mg calcites were formed at warmer temperature and partial dissolution therefore plays a major factor in shell chemistry [*Rosenthal and Boyle*, 1993; *Brown and Elderfield*, 1996].

Considerable calcium carbonate dissolution (up to 60-80%) might take place in the upper 500-1000 m water column based on excess Alkalinity signals [*Milliman et al.*, 1999]. Although recent analyses indicate that estuarine and/or coastal benthic processes [*Chen*, 2002], or a mixing of deeper waters with shallower waters [*Friis et al.*, 2006] may contribute to observed excess Alkalinity in the upper ocean, several hypothesis, including biological controls (e.g., a corrosive micro-environment due to microbial oxidation of organic matter [*Milliman et al.*, 1999]) or preferential dissolution of more soluble carbonate phases (e.g., high-Mg calcite [*Feely et al.*, 2002]), have been proposed to explain these dissolution artifacts. Consequently, similar processes may result in significant dissolution of foraminiferal shells and further modify Mg/Ca at depths well above lysocline or CCD.

The partial dissolution problem has been tackled successfully by incorporating a dissolution term using water depth, seawater [CO_3^{2-}], foraminiferal test weights [*Dekens et al.,* 2002; *Rosenthal and Lohmann,* 2002]) into calibration equations, or by applying a calcite dissolution proxy (e.g., *Globorotalia menardii* fragmentation index, MFI, or Mg/Ca and Mg/Sr in deep dwelling planktonic species [*Mekik and Fançois*, 2006]).

These methods, however, have unavoidable assumptions on the extent of dissolution. For example, the initial weight of planktonic foraminiferal species needed to be assumed to calculate dissolution weight loss. This assumption has been challenged as the initial weight could vary regionally and temporally [*Barker and Elderfield,* 2002]. In this study, we use foraminiferal shells from different trap depths to evaluate directly of regional dissolution artifacts on shell Mg/Ca. It can, therefore, provide not only the dissolution-corrected temperature equation, but also an opportunity to evaluate variability of shell chemistry with depth, which is a function of post-depositional dissolution.

The correlation coefficients (r^2) of foraminiferal Mg/Ca and T_H derived from different depths are always better than 0.64 (Figure 3.6), suggesting that our approach is suitable. The best-fit lines show strong partial dissolution in the SCS and are characterized by a gradual decrease of the pre-exponential constant from surface to deep collecting cups (Figure 3.6). Another feature is that the shallowest calibration curve (240 m) showed a similarity with species established in the Sargasso Sea [*Anand et al*., 2003]. The shallowest and the deepest (3240 m, below lysocline) traps in cold months shows ~20% decrease in Mg/Ca at the same temperature (Figure 3.6a), equivalent to 2.2°C change with ~9% sensitivity. For the warm months, because the shallowest trap depth (~600 m) is much deeper than that in cold months, a less variation of Mg/Ca is found among different deployed depths (Figure 3.6b). If we assume the empirical Mg/Ca-SST equation for the shallowest depth (240 m) is the same, the dissolution effect in warm months seems to be more intense according to the comparison between similar depths from two seasons (~10% and 25% decreases in Mg/Ca for 1240 m and 1126 m, respectively). Large differences in calibration equations for Mg/Ca at different localities and seasons emphasize the importance of in situ calibration for dissolution in various ocean basins [*Rosenthal and Lohmann*, 2002; *Deken et al.*, 2002], especially for those with distinctive water chemistry.

Particle sinking rate estimated in the SCS is ca. 300 m/day [*Lin et al.*, unpublished data]. The observed decreases of Mg/Ca thus should reflect the special variation of dissolution at various depths as these samples were collected at the same time. Among the three planktonic species, *N. dutertrei* appears to be more susceptible to dissolution and shows the strongest decrease in Mg/Ca of ~12%/km, compared to 4%/km and 5%/km for *G. ruber* and *G. sacculifer*, respectively (see Table 3.3). These percentage changes were calculated using average Mg/Ca at the shallowest and the deepest depths, and assumed linear variation at other depth. In summary, *N. dutertrei*, non-spinose thermocline dweller, is the most sensitive species to dissolution and spinose, mixed-layer dwelling species (*G. ruber* and *G. sacculifer*) are relatively resistant. This agrees well with previous observations of selective dissolution susceptibility for planktonic species in core-top samples from several transects in tropical Pacific and subtropical Atlantic [*Dekens et al*., 2002] (Table 3.3).

The foraminiferal Mg/Ca in the SCS shows a relatively strong dissolution compared with those in open oceans (Figure 3.5 and 3.6). It is possible that upwelling may play a significant role in changing the chemical composition of surface seawater through uplift of the deep subsurface, nutrient-enriched water. Several evidences show that regional upwelling forced by wind-driven circulation have occurred in the northwest Luzon and offshore Vietnam during prevailing winter and summer monsoons, respectively [*Liu et al*., 2002]. Deep water with relatively low pH is admixed upwardly with surface water and becomes more corrosive, which in turn results in intense carbonate dissolution than other marginal seas. In summertime, more corrosive surface seawaters caused by upwelling offshore Vietnam could be delivered to the northern SCS

Table 3.3 Comparison of dissolution effects on foraminiferal shell Mg/Ca as observed in specimens from core-top sediments and the sediment trap.

Species	Sample location	Mg/Ca %/km	Water depth (m)	ΔCO_3^{2-} $\mu mol\ kg^{-1}$	Reference
G. ruber	***Core-top sediment***				
	Ontong Java Plateau	-12	1600-2500	20 to 9	Lea et al. (2000)
	Ontong Java Plateau	-14	1600-4500	20 to -15	Deken et al. (2002)
	Ceaea Rise	-5	2800-4200	44 to -3	Deken et al. (2002)
	Sierra Leone Rise	-7	3100-5100	32 to -7	Deken et al. (2002)
	South China Sea	**-15**	371-2404	25 to -7	Huang et al., in preparation
	Sediment Trap				
	South China Sea	**-4**	240-3240	30 to -16	This study
G. sacculifer	***Core-top sediment***				
	Ceaea Rise	-20	3000-4700	39 to -3	Russell et al. (1994)
	Ontong Java Plateau	-5	1600-4500	20 to -15	Deken et al. (2002)
	Ceaea Rise	-7	2800-4600	44 to -3	Deken et al. (2002)
	Sierra Leone Rise	-14	3100-5100	32 to -7	Deken et al. (2002)
	Ontong Java Plateau	-12	1600-3400	20 to -3	Rosenthal et al. (2000)
	Ceaea Rise	-6	2800-4200	44 to 21	Rosenthal et al. (2000)
	Sierra Leone Rise	0	2900-5100	32 to -7	Rosenthal et al. (2000)
	South China Sea	**-15**	371-2404	25 to -7	Huang et al., in preparation
	Sediment Trap				
	South China Sea	**-5**	240-3240	30 to -16	This study
N. dutertrei	***Core-top sediment***				
	Ontong Java Plateau	-20	1600-4500	20 to -15	Deken et al. (2002)
	Ceaea Rise	-21	2800-4600	44 to -3	Deken et al. (2002)
	Sierra Leone Rise	-16	3100-5100	32 to -7	Deken et al. (2002)
	South China Sea	**-40**	371-2404	25 to -7	Huang et al., in preparation
	Sediment Trap				
	South China Sea	**-12**	240-3240	30 to -16	This study

Changes in Mg/Ca ratios of core-top sediments were calculated and expressed as percentage change pe km water depth, relative to the dissolution onset in a water depth profile. For the sediment-trap sample the percentage changes were calculated using average Mg/Ca at the shallowest and deepest wate depths. Values for ΔCO_3^{2-}(= $[CO_3^{2-}]_{in\ situ}$ − $[CO_3^{2-}]_{saturation}$, $CO_3^{2-}]_{saturation}$ were obtained based o $[CO_3^{2-}]_{saturation}$= 90 × exp [0.16(Z-4)]) were calculated using hydrographic data from nearby time-serie station [*Chou et al.*, unpublished data]. Observed trends vary intra- and inter-species, and show complicated relationship between changes in Mg/Ca and deep ocean ΔCO_3^{2-}. Note that decreases i Mg/Ca from core-top sediments in the South China Sea are much larger than sediment-trap results.

through a clockwise gyre, which may partly explain the cause of strong dissolution in warm seasons [*Wyrtki*, 1961]. Alternatively, the recent study at the SEATS time-series site in the northern SCS indicates slightly high pCO_2 (i.e., lower pH) during warm seasons relative to the cold months [*Chou et al.*, unpublished data], and provides another example for more corrosive waters in the summertime. More detailed hydrographic studies are required to evaluate this contribution further.

The Mg/Ca data presented here leads to a conclusion that Mg/Ca is strongly affected by selective partial dissolution in the SCS, even at depths well above the lysocline and calcite saturation depth (Figure 3.7). This argument is also supported by a positive covariance between trapped foraminiferal Mg/Ca and Sr/Ca (Figure 3.8), with partial dissolution reduced both shell Mg/Ca and Sr/Ca [*Brown and Elderfield*, 1996]. Additionally, preliminary weights data of shell separated from core-top sediments show a depth-related trend in weight for selected species in the SCS [*Huang et al,* in preparation].

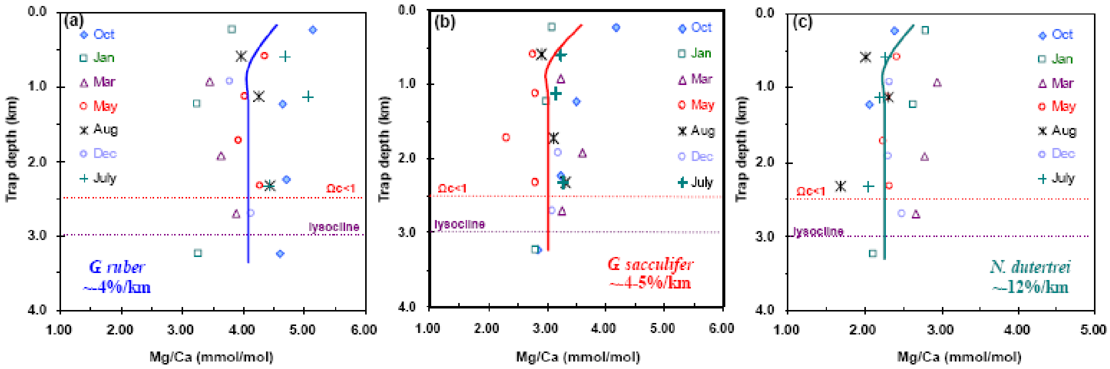

Figure 3.7 Mg/Ca data for the three species of planktonic foraminifera at various trap depths during the deployment period- (a) *G. ruber*, (b) *G. sacculifer*, and (c) *N. dutertrei*. The SCS region demonstrates the strong dissolution effect on Mg/Ca, with Mg/Ca decreasing well above the calcite lysocline (~3000 m, purple line) and calcite saturation depth (~2500 m, red line) [*Chou et al*., 2006]. Note that *N. dutertrei* is the most sensitive to dissolution (up to 12% decreases in Mg/Ca per km) and the other two surface-dwelling species (*G. ruber* and *G. sacculifer*, ~4-5%/km) are relatively resistant to the potential dissolution.

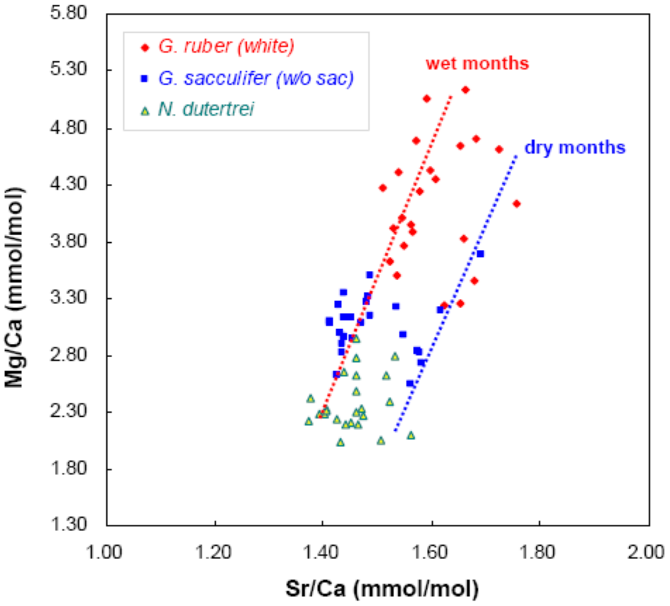

Figure 3.8 The Mg/Ca-Sr/Ca relationship of *G. ruber*, *G. sacculifer* and *N. dutertrei* from the SCS sediment traps shows a positive correlation within species, indicating shell Mg/Ca ratios are strongly affected by partial dissolution in the SCS. Seasonal variability in salinity seems to also significantly affect shell Sr/Ca, and cause an offset on Sr/Ca of those specimens collected from wet and dry seasons.

3.6.6 Other Environmental Factors on Foraminiferal Mg/Ca

Although work to date has led to an important advance in the use of foraminiferal Mg/Ca as a reliable paleothermometry, uncertainties still exist and need to be evaluated for other secondary environmental factors. These factors include shell growth rate, pH, salinity and other biological effects [*Delaney et al*., 1985; *Elderfield et al*., 1996; *Rosenthal et al*., 1997; *Lea et al*., 1999].

The $\delta^{13}C$ in foraminiferal shell is commonly in disequilibrium with ambient $\delta^{13}C$ of seawater. A considerable body of work regarding the foraminiferal $\delta^{13}C$ signal has been interpreted in terms of kinetic isotopic fractionation and incorporation of metabolic or photosynthetic CO_2 [*Spero and Williams*, 1998]. Core-top studies have also demonstrated that Mg/Ca was affected by non-equilibrium process to form correlation between $\delta^{13}C$ and size fraction [*Elderfield et al*., 2002]. *Lin et al*. [2004] reported a tight correlation between $\delta^{13}C$ (*G. ruber* and *G. sacculife*r) and integrated primary production in the northern SCS, where low $\delta^{13}C$ is associated with high nutrient level in surface water, possibly related to a prevailing winter monsoon. Consequently, $\delta^{13}C$ in planktonic foraminifera may serve as an indicator for nutrient levels in surface water of the SCS.

Lea et al. [1999] and *Russell et al*. [2004] indicate that shell Mg/Ca decreases with pH or [CO_3^{2-}] ion in *Orbulina universa* and *Globigerina bulloides* and explain this in terms of the secondary kinetic influence, high [CO_3^{2-}] leading to fast shell growth. Besides, it is evident that high [CO_3^{2-}] also leads to an increase in shell thickness and weights [*Barker and Elderfield*, 2002]. Our Mg/Ca analyses were restricted to shells within a narrow size range, 250-350 μm, to eliminate ontogenetic effect and to minimize artifacts caused by non-equilibrium processes. The observed changes in foraminiferal $\delta^{13}C$, are, therefore, primarily controlled by fertilization of surface water

[*Lin et al.*, 2004]. There is no appreciable correlation between sphere Mg/Ca and $\delta^{13}C$ (Figure 3.9a), indicating minor kinetic and nutrient level artifacts.

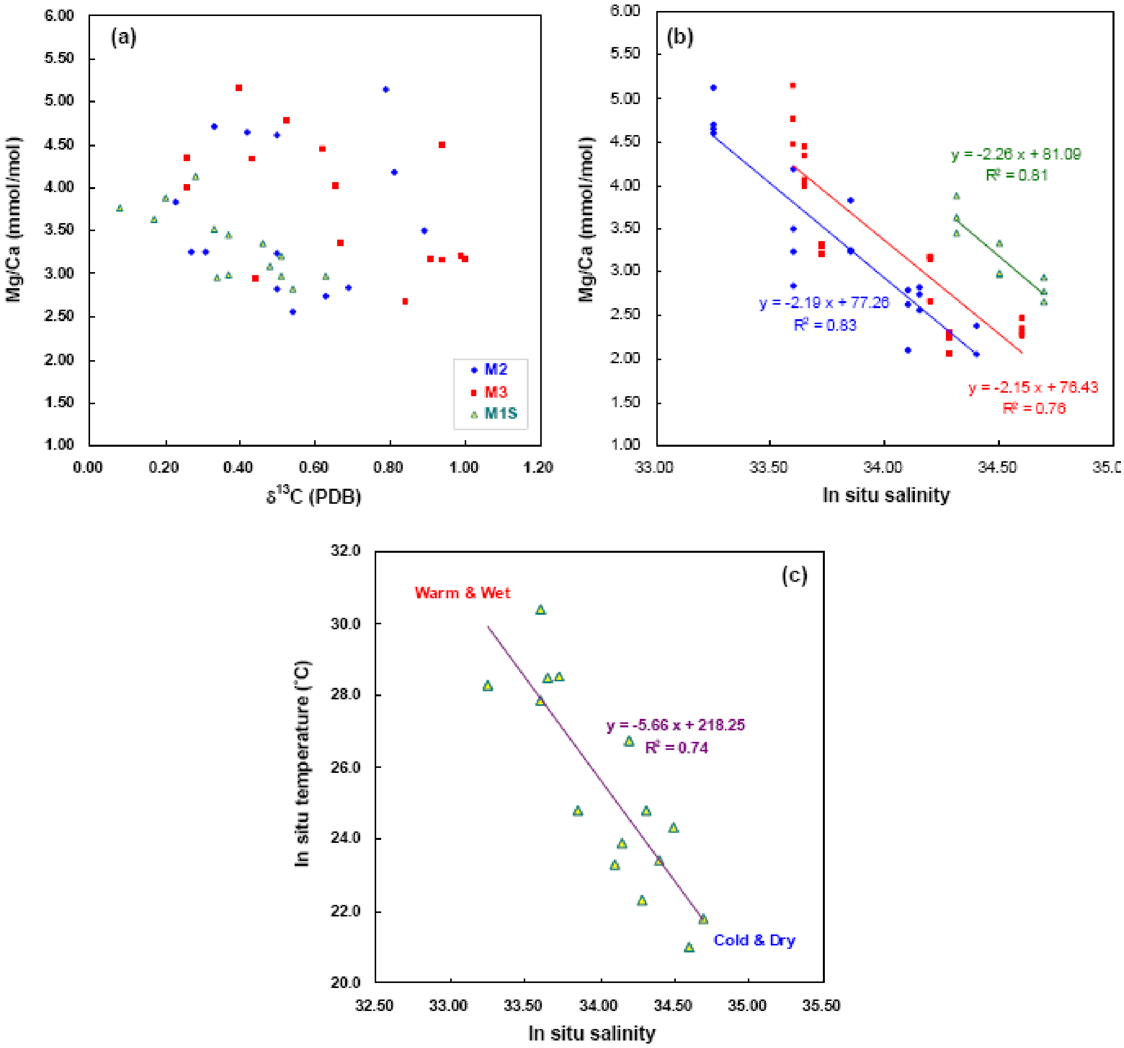

Figure 3.9 (a) Plot of foraminiferal Mg/Ca versus $\delta^{13}C$ shows no significant correlation, indicating the kinetic effect or nutrient levels of the surface water may not be main controlling factors to affect our Mg/Ca data. (b) Plot of foraminiferal Mg/Ca and in situ salinity record shows tight correlations for each deployed period, however, these tendencies inversely correlate with the culture-based observation, and can be attributed to the local relationship between salinity and temperature caused by the monsoon precipitation. (c) Modern relationship of salinity versus in situ water column temperature for the study transects.

Temperature is a conservative variable that is highly correlated with other oceanographic parameters. For instance, it correlates positively with salinity and seawater [CO_3^{2-}] in the open ocean. Yet separation of these temperature-induced artifacts in modern empirical sediment-trap is not straightforward. Salinity is another factor that may bias foraminiferal Mg/Ca ratios. Living culture experiments in the laboratory showed about +4 (±3)% Mg/Ca per psu for *O. universa* at 22°C [*Lea et al.*, 1999], suggesting a potential influence of salinity on Mg/Ca in its spherical shell. However, salinity changes are relatively small in natural systems, and errors derived from the culture experiment are rather large. Therefore, it is difficult to evaluate the salinity effect on the shell chemistry from natural or culturing samples. Besides, species difference may generate uncertainties in estimating biological response under various environmental conditions.

Modern hydrological data have shown that inputs of continental runoffs and precipitation were modulated by the East Asian Monsoon, SSS seasonal variation is 1.5-2.0 psu. Applying an empirical relationship derived from culturing experiments, it would be a ~6% or maximal to 10% variation in shell Mg/Ca between wet and dry periods. Several observations lead to a conclusion that salinity is not a dominant factor influencing foraminiferal Mg/Ca in the SCS. First of all, there is a negative correlation (see Figure 3.9b) between foraminiferal Mg/Ca and mean habitat salinity. This differs significantly from previous culture-based results. Besides, the estimated salinity effect is equal to ~40% Mg/Ca decrease per psu (e.g., $Mg/Ca= -2.19*S_H+ 77.26$ for Fall-winter months, Figure 3.9b). This can be attributed to complexity in nature, where salinity factor cannot be separated from temperature (Figure 3.9c). Furthermore, there is no discernible correlation between single species Mg/Ca and S_H, further suggests limited salinity effect on foraminiferal Mg/Ca even under large salinity variation (~1.5, 33.25-34.70) in the SCS. Future investigation should be focused on the study regarding seawater pH (or $[CO_3^{2-}]$ ion concentration) and salinity affecting shell Mg/Ca, and other species to evaluate how foraminiferal Mg/Ca response to other secondary variables.

3.7 Comparison of Existing Calibrations

To elucidate the observed differences in Mg/Ca-SST equations for *G. ruber* (white), *G. sacculifer* (w/o sac) and *N. dutertrei*, results obtained here and those core-top and trap data from literatures were compiled in Figure 3.10. For the comparisons in this section, only similar size fraction (250-350μm) data were selected to minimize any size-dependent artifacts [*Elderfield et al.*, 2002].

An inter-laboratory comparison showed a poor reproducibility of 2-3°C in temperature due to different cleaning and/or analytical procedures [*Rosenthal et al.*, 2004]. Other source of uncertainty in the application of the calibration curve produced in different laboratories is temperature estimations used for establishing the empirical calibration (i.e., calcification versus instrumental temperature) and extent of dissolution in specimens from various levels of saturation state in deep oceans. Despite such obstruction, a general consensus is merging that appropriate calibration equations can be derived, especially in view of good fits between data from multi-species and species-specific calibrations and from different laboratories.

3.7.1 Comparison of the Multi-species Calibrations

Despite difficulties in the comparison of different calibration equations, the following discussion is based on the results obtained from this study and published calibrations. For multi-species calibration, the equation derived from SCS yields a Mg/temperature relationship, $Mg/Ca= 0.32 (\pm 0.05) \exp (0.090*T)$, shows a significantly large scatter according to the wide range of the error on pre-exponential constant. It deviates slightly from that of *Anand et al.* [2003] (i.e., $Mg/Ca= 0.38 (\pm 0.02) \exp (0.090*T)$ using ten planktonic species in the Sargasso Sea. In contrast, the core-top calibration for multi-species in the North Atlantic Ocean [e.g., *Elderfield and Ganssen*, 2000] shows a pre-exponential constant of 0.65 (±0.04) (re-calculated by *Anand et al.*, [2003] and assuming temperature sensitivity of 9% for eight planktonic species), which differs significantly from those results of *Anand et al.*'s [2003] and this study (Figure 3.10). The offset in the pre-exponential constant is probably derived from different levels of dissolution in various ocean basins (Table 3.3), suggesting that dynamic dissolution may influence largely on foraminiferal Mg/Ca. Therefore, applications of sediment traps or other calcite dissolution proxies (e.g., average shell weight and MFI) should be taken into account for any potential selective dissolution even at depths shallower than CCD or lysocline.

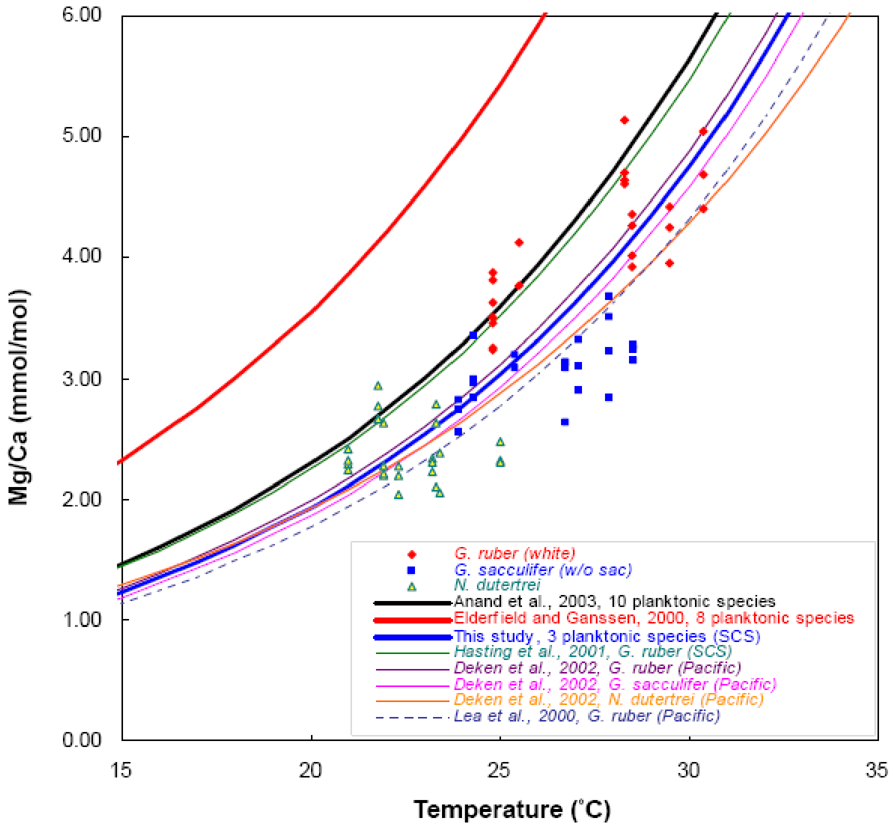

Figure 3.10 Comparisons between sediment trap *G. ruber*, *G. sacculifer* and *N. dutertrei* Mg/Ca data and Mg/Ca temperature calibration in the SCS, as well as published calibration equations for multiple species and single species. The resultant equation (Mg/Ca= 0.32* exp (0.090*T), r^2= 0.68, thick blue line) significantly differs from the other two multiple-species calibrations (solid red line, [*Elderfield and Ganssen*, 2000] and solid black line, [*Anand et al.*, 2003]), suggesting an intense dissolution effect in the SCS basin, and it also highlights the needs of the site-specific calibration for different ocean basins even well above the lysocline and saturated depth of calcite. Compared with the core-top calibrations for *G. ruber* in the SCS (solid green line, [*Hasting et al.*, 2001]) and the Pacific (solid purple line, [*Deken et a*l., 2002], and dashed blue line, [*Lea et al.*, 2000]), our equation seems to be more close to those of *Deken et al.* [2002] and *Lea et al.* [2000], indicating that all of our samples have suffered from more stronger dissolution in the study area.

3.7.2 Comparison of Species-specific Calibrations

Hasting et al. [2001] reported the first calibration equation of Mg/Ca= 0.38 exp (0.089*T) for *G. ruber* (white) using SCS core-top samples recovered only from water depth less than 2000 m. Compared to their limited data, our sediment trap data provide more extensive information on dissolution artifacts based on specimens collected from shallower and deeper than 2000 m. The trap calibration equation differs significantly from that of *Hasting et al*. [2001], but is closer to those of *Lea et al*. [2000] from the equatorial Pacific and *Dekens et al*. [2002] from the Pacific (Figure 3.10). *Hasting et al*. [2001] had explained this discrepancy in terms of less dissolution in the SCS compared to deep Pacific Ocean. However, we suggest that shell chemistry in the SCS has suffered from strong dissolution for three reasons: (1) the mentioned Mg/Ca decreases with depth; (2) covariance of Mg/Ca and Sr/Ca in planktonic foraminifera; and (3) preliminary observations in shell weight. Alternatively, this is also likely due to species difference used in this calibration study and *Hasting et al*. [2001].

It is noteworthy that no detectable discrepancy between our multi-species calibration and those of *Lea et al*. [2000] and *Dekens et al*. [2002] for *G. ruber* in the Pacific. This implies that the Mg/Ca-SST derived from multi-species (at least three planktonic species presented here) is useful to substitute for species-specific calibration while temperature variation is restricted or limited data for single species. Furthermore, it also indicates that the temperature effect on Mg uptake can be properly described and potentially applied for other un-calibrated species.

3.7.3 Comparison of Reconstructed SST Records in the SCS

The dissolution-corrected calibration equation (equation 2 and 3) established here was applied to two existing cores with available Mg/Ca in *G. ruber* (white) in the northern (ODP Leg 184 Site 1145, 3175 m) [*Oppo and Sun*., 2005] and southern SCS (MD01-2390, 1545 m) [*Steinke et al*., 2005]. The reconstructed Mg/Ca temperature for the uppermost sediments is 27.2°C and 29.0°C for northern and southern SCS, respectively, which is fairly close to modern annual mean SSTs (26.7-27.0°C and 28.7-28.9°C for northern and southern SCS, respectively). Estimated SSTs using a depth-corrected equation of *Deken et al*., [2002] is 28.0°C and 30.3°C for northern and southern SCS, respectively for Late Holocene, which is slightly higher than modern annual SST. Relatively high fluxes of *G. ruber* in summer [*Lin et al*., 2004; *Oppo and Sun*, 2005] (August to October, mean summer temperature is 28°C and 29°C in northern and southern SCS) had been proposed to interpret the discrepancy (~1.0°C) between reconstructed SST derived from *Deken et a*l. [2002]'s equation and modern annual SST. However, the reconstructed SST in the southern SCS (30.3°C) is too high to be explained by seasonal foraminifera flux variations. On the basis of the equation of *Hasting et al*. [2001], the reconstructed SST in Late Holocene for north and south SCS is 24.7°C and 28.5°C, respectively. The estimated SST of 24.7°C in Site 1145 (water depth of 3175 m) is rather unreasonable, should be due to limited recovery of sediments from depths deeper than 2000 m in the study of *Hasting et al*. [2001]. In contrast, the Late Holocene SST of 28.5°C in the southern SCS seems to agree well with modern annual mean SST and our estimation. Based on the above comparison, it can lead to a conclusion that down-core *G. ruber* may not reflect seasonal changes in foraminiferal assemblage although its flux increases in summer [*Lin et al*., 2004]. If this is correct, our trap calibration will be the most reliable method to obtain accurate SST records and highlight the importance of in situ calibration for gaining accurate SST records in the past.

3.8 Conclusions

Foraminiferal Mg/Ca ratios of three dominant planktonic species in tropical SCS collected from a series of trap arrays were analyzed. Combining with parallel measurements of shell $\delta^{18}O_c$ and $\delta^{13}C$, as well as modern hydrographic data, several conclusions can be made as follows:

1. Average Mg/Ca of inter-species foraminifera are 4.137, 3.068 and 2.377 mmol mol^{-1} for *G. ruber*, *G. sacculifer* and *N. dutertrei*, respectively and respond possibly to their habitat depths. Furthermore, the estimated apparent partition coefficient of Mg (D_{Mg}) for *G. ruber*, *G. sacculifer* and *N. dutertrei*, is 0.08×10^{-2}, 0.06×10^{-2}, and 0.05×10^{-2} respectively. These values differ significantly from the determination of inorganic calcite of $5.3\text{-}6.2\times10^{-2}$, implying biological processes exert an influence on Mg co-precipitation from ambient solution, but it does not alter its correlation with temperature.
2. A strong intra-annual variation of Mg/Ca and $\delta^{18}O_c$ occurs in surface-dwelling species. However, partial dissolution artifacts could play a significant role in modifying foraminiferal Mg/Ca, even at depths well above the lysocline or CCD in the SCS. Hence a dissolution correction is critical for optimal use of Mg/Ca in planktonic foraminifera as a paleothermometry.
3. The Mg/Ca in planktonic foraminifera is primarily governed by temperature. In situ Mg/Ca-SST calibration equation for all species in the SCS can be described as Mg/Ca = 0.32 exp (0.090*T), $r^2=0.69$. There is a significant discrepancy in calibration equations derived from fall-winter and spring-summer, and can be attributed to regional hydrological changes, possibly associated with dissolution effect driven by the East Asian Monsoon. In addition, a dissolution-corrected equation was developed using trap data from different depths. These temperature

equations are Mg/Ca= (0.38-0.02* water depth (km)) exp (0.090*T) and Mg/Ca= 0.30 exp (0.090*T) for fall-winter and spring-summer season, respectively. These equations can be applied for accurate reconstruction of mixed layer and thermocline temperatures in sediment cores.

4. Among the three dominant planktonic species in the SCS, *N. dutertrei* is the most sensitive species to dissolution (up to 12% per km) and the two surface-dwelling species of *G. ruber* and *G. sacculifer,*) are relatively resistant (~4-5%/km). This is consistent with selective dissolution susceptibility for the three planktonic species from previous core-top studies in Atlantic and Pacific.
5. Non-equilibrium processes (or kinetic effects) and salinity do not have major influence on shell Mg/Ca, but should not be entirely excluded since previous culture experiments have indicated correlations among Mg/Ca, salinity, and seawater pH (or [CO_3^{2-}]). Thus, separation of these environment factors from foraminiferal Mg/Ca is a key component in the future research to obtain accurate temperature records.
6. From a comparison of all available temperature calibration equations, there exists a significant discrepancy in core-top and trap results, and SSTs estimated for the northern and southern SCS in Late Holocene also show inconsistent results by applying these temperature empirical calibrations. Consequently, trap foraminiferal Mg/Ca presented here provide a strong support to emphasize the importance of in situ calibration work as shells from different ocean basins may have been affected by different level of dissolution or seawater chemistry. Systematical investigations are necessary to refine relationships among culture, tow, trap and core- top specimens in the SCS.

References

Anand, P., H. Elderfield, and M.H. Conte (2003), Calibration of Mg/Ca thermometry in planktonic foraminifera from sediment trap time series, *Paleoceanography*, *18*, 1050-1065.

Barker, S., and H. Elderfield (2002), Foraminiferal calcification response to glacial-interglacial changes in atmospheric CO_2, *Science*, *297*, 833-836.

Bé, A. W. H. (1980), Gametogenic calcification in a spinose planktonic foraminifera, Globogerinoides sacculifer, *Mar. Micropaleotol.*, *5*, 283-310.

Bender, M. L., R. B. Lorens, and D. F. Williams (1975), Sodium, magnesium and strontium in the tests of planktonic foraminifera, *Micropaleontology, 21*, 448-459.

Bentov, S., and J. Erez (2005), Novel observations on biomineralization processes in foraminifera and implication for Mg/Ca ratio in the shells, *Geology*, *33*, 841-844.

Bentov, S., and J. Erez (2006), Impact of biomineralization processes on the Mg content of foraminiferal shells: A biological perspective, *Geochem. Geophys. Geosyst*, *7*, doi:10.1029/ 2005GC001015.

Boyle, E. A., and L. D. Keigwin (1985/1986), Comparison of Atlantic and Pacific paleochemical records for the last 215, 000 years: Changes in deep ocean circulation and chemical inventories, *Earth Planet. Sci. Lett.*, *76*, 135-150.

Broecker, W. S., and T.-H. Peng (1982), Tracers in the Sea, Eldigio Press, New York.

Brown, S. J. and H. Elderfield (1996), Variations in Mg/Ca and Sr/Ca ratios of planktonic foraminifera caused by postdepositional dissolution: Evidence of shallow Mg-dependent dissolution, *Paleoceanography*, *11*, 543-551.

Chen, C.-T. A (2002), Shelf-vs. dissolution-generated alkalinity above the chemical lysocline, *Deep-Sea Research II*, *49*, 5365-5375.

Chen, M.-T., C.-C. Huang, U. Pflaumann, C. Waelbroeck and M. Kucera (2005), Estimating glacial western Pacific sea-surface temperature: methodological overview and data compilation of surface sediment planktonic foraminifer faunas, *Quat. Sci. Reviews*, *24*, 1049-1062.

Chou, W.-C., D.-D. Sheu, B.-S. Lee, C.-M. Tseng, C.-T. A. Chen, S.-L. Wang, and G. T.-F. Wong (2006), Depth distribution of alkalinity, TCO2, and δ13CTCO2 at SEATS time-series site in the northern South China Sea, *Deep-Sea Research II*, in press.

Deken, P. S., D. W. Lea, D. K. Pak, and H. J. Spero (2002), Core top calibration of Mg/Ca in tropical foraminifera: Refining paleotemperature estimation, *Geochem. Geophys. Geosys*t., *3*, doi: 10.1029/2001GC000200.

Delaney, M. L., A. W. H. Be, and E. A. Boyle (1985), Li, Sr, Mg and Na in foraminiferal calcite shells from laboratory culture, sediment traps and sediment cores, *Geochem. Cosmochem. Acta*, *49*, 1327-1341.

Eggins, S., P. De Deckker, and J. Marshall (2003), Mg/Ca variation in planktonic foraminifera tests: implications for reconstructing palaeo-seawater temperature and habitat migration, *Earth Planet. Sci. Lett.*, *212*, 291-306.

Elderfield, H., C. J. Bertram, and J. Erez (1996) A biomineralization model for the incorporation of trace elements into foraminiferal calcium carbonate. *Earth Planet. Sci. Lett.* 142, 409-423.

Elderfield, H., and G. Ganssen (2000), Reconstruction of temperature and $\delta^{18}O$ of surface ocean waters using Mg/Ca of planktonic foraminiferal calcite, *Nature, 405*, 442-445.

Elderfield, H., M. Vautravers, and M. Cooper (2002), The relationship between shell size and Mg/Ca, Sr/Ca, $\delta^{18}O$, and $\delta^{13}C$ of species of planktonic foraminifera, *Geochem. Geophys. Geosyst.*, *3*, doi:10.1029/ 2001GC000194.

Fairbanks, R. G., M. Sverdlove, R. Free, P. H. Wiebe, and A. W. H. Be (1982), Vertical distribution and isotopic fractionation of living planktonic foraminifera in the Panama Basin, *Nature*, *298*, 841-844.

Feely, R. A., C. L. Sabine, K. Lee, F. L. Millero, M. F. Lamb, D. Greeley, J. L. Bullister, R. M., Key, T. H. Peng, A. Kozyr, T. Ono, and C. S. Wong (2002), In situ calcium carbonate dissolution in the Pacific Ocean, *Global Biogeochem. Cysles*, *16*, doi:10.1029/2002GB001866.

Friis, K., R. G. Najjar, M. J. Follows, and S. Dutkiewicz (2006), Possible overestimation of shallow-depth calcium carbonate dissolution in the ocean, *Global Biogeochem. Cycles*, *20*, GB4019, doi:10.1029/2006GB002727.

Hastings, D. W., A. D. Russell,, and S. R. Emerson (1998), Foraminiferal magnesium in *Globeriginoides sacculifer* as a paleotemperature proxy, *Paleoceanography, 13*, 2, 161-169.

Hasting, D. W., M. Kienast, S. Steinke, A. A. Whitko (2001), A comparison of three independent paleotemperature estimates from a high resolution record of deglacial SST records in the tropical South China Sea, *EOS*, *82*, PP12B-10.

Katz, A. (1973), The interaction of magnesium with calcite during crystal growth at 25-90°C and one atmosphere, *Geochem. Cosmochem. Acta*, *37*, 1563-1586.

Jansen H. and M. J. Ahrens (2004), Carbon dissolution in the guts of benthic deposit feeders: A numerical model. *Geochem. Cosmochem. Acta*, *68*, 4077-4092.

Kienast, M., S. Steinke, K. Stattegger, S. E. Calvert (2001), Synchronous tropical South China Sea sea surface temperature change and Greenland warming during deglaciation, *Science*, *291*, 2132-2134.

Koutavas, A., J. Lynch-Stieglitz, T. M. Marchitto Jr., and J. P. Sachs (2002), El Niño-like pattern in ice age tropical Pacific sea surface temperature, *Science*, *297*, 226-230.

Lea, D. W. and E. A. Boyle (1993), Determination of carbonate-bound barium in corals and foraminifera by isotope dilution plasma mass spectrometry, *Chem. Geol., 103*, 73-84.

Lea, D. W., T. A. Mashiotta, and H.J. Spero (1999), Controls on magnesium and strontium uptake in planktonic foraminifera determined by live culturing, *Geochem. Cosmochem. Acta, 63*, 2369-2379.

Lea, D. W., D. K. Pak, and H. J. Spero (2000), Climatic impact of late Quaternary equatorial Pacific sea surface temperature, *Science, 289*, 1719-1724.

Lin, C.-F. (2000), Oxygen isotope compositions of seawaters from the South China Sea and Luzon Strait: Master thesis. National Sun Yat-Sen University, Kaohsiung, Taiwan.

Lin, H.-L., W.-C. Wang, and G.-W. Hung (2004), Seasonal variation of planktonic foraminiferal isotopic composition from sediment traps in the South China Sea, *Mar. Micropaleontol.*, 53, 447-460.

Liu, K.-K., S.-Y. Chao, P.-T. Shaw, G.-C. Gong, C.-C. Chen, and T.-Y. Tang (2002), Monsoon-forced chlorophyll distribution and primary production in the South China Sea: observations and a numerical study, *Deep-Sea Research I*, *49*, 1387-1412.

Lohamnn, G. P. (1995), A model for variation in the chemistry of planktonic foraminiferal due to secondary calcification and selective dissolution, *Paleoceanography*, *10*, 445-457.

Lorens, R. B., D. F. Williams, and M. L. Bender (1977), The early nonstructural chemical diagenesis of foraminiferal calcite, *J. Sediment. Petrol.*, *47*, 1602-1609.

Mashiotta, T. A., D. W. Lea, and H. J. Spero (1999), Glacial-interglacial changes in subantarctic sea surface temperature and δ^{18}O- water using foraminiferal Mg, *Earth Planet. Sci. Lett.*, *170*, 417-432.

Mekik, F., and R. François (2006), Tracing deep-sea calcite dissolution: Agreement between the *Globorotalia menardii* fragmentation and elemental ratios (Mg/Ca and Mg/Sr) in planktonic foraminifers, *Paleoceanography*, *21,* doi:10.1029/2006PA001296.

Miao, Q., R. C. Thunell, and D. M. Anderson (1994), Glacial- Holocene carbonate dissolution and sea surface temperatures in the South China and Sulu Seas, *Paleoceanography*, *9*, 269-290.

Morse, J. W., and M. L. Bender (1990), Partition coefficient in calcite: Examination of factors influencing the validity of experimental results and their application to natural systems, *Chem. Geol.* , *82*, 265-277.

Mortyn, P. G., H. Elderfield, P. Anand, and M. Greaves (2005), An evaluation of controls on planktonic foraminiferal Sr/Ca: Comparison of water column and core-top data from a North Atlantic transect, *Geochem. Geophys. Geosys*t., *6*, doi:10.1029/2005GC001047.

Nitani, H. (1972), Beginning of the Kuroshio, in *Kuroshio*, edited by H. Stommel and Y. Yoshida, 129-163. Univ. of Wash. Press, Seattle.

Nüernberg, D., J. Bijma, and C. Hemleben (1996), Assessing the reliability of magnesium in foraminiferal calcite as a proxy for water mass temperature, *Geochim. Cosmochim. Acta*, *60*, 803-814.

O'Neil, J. R., R. N. Clayton, and T. K. Mayeda, Oxygen isotope fractionation in divalent metal carbonates, *The Journal of Chemical Physics*, *51*, 5547-5558, 1969.

Oomori, T., H. Kameshima, Y. Maezato, and Y. Kitano (1987), Distribution coefficient of Mg2+ ions between calcite and solution at 10-50°C, *Mar. Chem.*, *20*, 327-336.

Oppo, D. W., and Y. Sun (2005), Amplitude and timing of sea-surface temperature change in the northern South China Sea: Dynamic link to the East Asian Monsoon, *Geology, 33*, 785-788.

Pak, D. K., D. W. Lea, and J. P. Kennett (2004), Seasonal and interannual variation in Santa Barbara Basin water temperatures observed in sediment trap foraminiferal Mg/Ca, *Geochem. Geophys. Geosyst.*, 5, doi:10.1029/2004GC000760.

Pelejero, C., J. O. Grimalt, S. Heilig, M. Kienast, and L. Wang (1999), High-resolution U^{k}_{37} temperature reconstructions in the South China Sea over the past 220 kyr, *Paleoceanography*, *14*, 224-231.

Rosenthal, Y. and E. A. Boyle (1993), Factors controlling the fluoride content of planktonic foraminifera: An evaluation of its paleoceanographic applicability, *Geochim. Cosmochim. Acta*, *57*, 335-346.

Rosenthal, Y., E. A. Boyle, and N. Slowey (1997), Environmental controls on the incorporation of Mg, Sr, F and Cd into benthic foraminifera shells from Little Bahama Bank: Prospects for thermocline paleoceanography, *Geochim. Cosmochim. Acta*, *61*, 3633-3643.

Rosenthal, Y., M. P. Field, and R. M. Sherrell (1999), Precise determination of element/calcium ratios in calcareous sample using sector field inductivity coupled plasma mass spectrometry, *Anal. Chem.*, *71*, 3248-3253.

Rosenthal, Y., G. P. Lohmann, K. C. Lohmann, and R. M. Sherrell (2000), Incorporation and preservation of Mg in *Globigerinoides sacculifer*: Implication for reconstructing the temperature and $^{18}O/^{16}O$ of seawater, *Paleoceanography*, *15*, 135-145.

Rosenthal, Y., and G. P. Lohman. (2002), Accurate estimation of sea surface temperatures using dissolution- corrected calibrations for Mg/Ca paleotemperature, *Paleoceanography,* *17*, 3, 1044.

Rosenthal, Y., D. W. Oppo, and B. K. Linsley (2003), The amplitude and phasing of climate change during the last deglaciation in the Sulu Sea, western equatorial Pacific, *Geophys. Res. Lett.*, *30*, doi:10.1029/2002GL016612.

Rosenthal, Y., P. Suzanne, C. H. Lear, E. Bard, S. Barker, K. Billups, M. Bryan, M. L. Delaney, D. B. deMenocal, G. S. Dwyer, H. Elderfield, C. R. German, M. Greave, and D. W. Lea (2004), Interlaboratory comparison study of Mg/Ca and Sr/Ca in planktonic foraminifera for paleoceanographic research, *Geochem. Geophys. Geosyst.*, 5, doi:10.1029/2003GC000650.

Rostek, F, G. Ruhland, F. C. Bassinot, P. J. Müller, L. D. Labeyrie, Y. Lancelot, and E. Bard (1993), Reconstructing sea surface temperature and salinity using $\delta^{18}O$ and alkenone records, *Nature*, 364, 319-321.

Russell, A. D., B. Hönisch, H. J. Spero, and D. W. Lea (2004), Effects of seawater carbonate ion concentration and temperature on shell U, Mg, and Sr in cultured planktonic foraminifera, *Geochim. Cosmochim. Acta*, *68*, 4347-4361.

Schmidt, M. W., H. J. Spero, and D. W. Lea (2004), Links between salinity variation in the Caribbian and North Atlantic thermohaline circulation, *Nature*, *428*, 160-163.

Shackleton, N. J. (1974), Attainment of isotopic equilibrium between ocean water and the benthic foraminiferal genus Uvigerina: Isotopic changes in the ocean during the last glacial, *Cent. Natl. Rech. Sci. Colloq. Int.*, *219*, 203-209.

Shaw, P.-T. (1991), The seasonal variation of the intrusion of the Phillippine Sea Water into the South China Sea, *J. Geophys. Res.*, *96*, 821-827.

Shaw, P.-T., S.-Y. Chao, K.-K. Liu, S.-C. Pai, and C.-T. Liu (1996), Winter upwelling off Luzon in the northeastern South China Sea, *J. Geophys. Res.*, *101*, 16435–16448.

Spero, H. J., J. Bijma, D. W. Lea, and B. E. Bemis (1997), Effect of seawater carbonate concentration on foraminiferal carbon and oxygen isotopes, *Nature*, *390*, 497-500.

Spero, H. J., and D. F. Williams (1998), Extracting environmental information from planktonic foraminiferal $\delta^{13}C$ data, *Nature*, *335*, 717-719.

Spero, H. J., K. M. Mielke, E. M. Kalve, D. W. Lea, and D. K. Pak (2003), Multispecies approach to reconstructing eastern equatorial Pacific thermocline hydrography during the past 360 kyr, *Paleoceanography*, *18*, doi: 10.1029/2002PA000814.

Steinke, S., H.-Y. Chiu, P.-S, Tum C.-C. Shen, L. Lowemark, H.-S. Mii,, and M.-T. Chen (2005), Mg/Ca ratios of two *Globigerinoides ruber* (white) morphotypes: Implications for reconstructing past tropical/subtropical surface water condiction, *Geochem. Geophys. Geosyst*., 6 doi:10.1029/2005GC000926.

Stott, L., K. Cannariato, R. Thunell, G. H. Haug, A. Koutavas, and S. Lund (2004), Decline of surface temperature and salinity in the western tropical Pacific Ocean in the Holocene epoch, *Nature*, *431*, 56-59,

Su, F.-H. (2000), Depth Distributions of $\delta^{18}O$ and Changes in Mixed Layer Thickness in the South China Sea: Master thesis. National Sun Yat-Sen University, Kaohsiung, Taiwan.

Thunell, R. C., Q. Miao, S. E. Calvert, and T. F. Pedersen (1992), Glacial-Holocene biogenic sedimentation patterns in the South China Sea: Productivity variations and surface water pCO_2, *Paleoceanography*, *7*, 143-162.

Wang, L., and P. Wang (1990), Late Quaternary paleoceanography of the South China Sea: Glacial-interglacial contrasts in enclosed basin, *Paleoceanography*, *5*, 77-90.

Wang, L., Sarnthein, H. Erlenkeuser, J. Grimalt, P. Grootes, S. Heilig, E. Ivanova, M. Kienast, C. Pelejero, and U. Pflaumann (1999), East Asian monsoon during the late Pleistocene: high-resolution sediment records from the South China Sea, *Mar. Geol*., *156*, 245-284.

Wang, P., L. Wang, Y. Bian, and Z. Jian (1995), Late Quaternary paleoceanography of the South China Sea: Surface circulation and carbonate cycles, *Mar. Geol*., *127*, 145-165.

Wang, P. (1999), Response of western Pacific marginal seas to glacial cycles: Paleoceanographic and sedimentological features, *Mar. Geol*., *156*, 5-39.

Wu, G., and W. H. Berger (1989), Planktonic foraminifera: Differential dissolution and the Quaternary stable isotope record in the west equatorial Pacific, *Paleoceanography*, *4*, 181-198.

Wyrtki, K. (1961), Physical Oceanography of the Southeast Asian Waters, in *Scientific Results of Marine Investigations of the South China Sea and the Gulf of Thailand, NAGA Rep*., vol. 2, 195 pp., Scripps Instit. of Oceanogr., La Jolla, Calif.

Zhang, Y., K. R. Sperber, and J. S. Boyle (1997), Climatology and interannual variation of the East Asian winter monsoon: results from the 1979–95 NCEP/NCAR reanalysis, *Monthly Weather Review*, *125*, 2605–2619.

CHAPTER 4.

Reconstructions of Paleo-SSTs and Paleo-climatic Changes in the South China Sea by using Foraminiferal Shell Chemistry

4.1 Introduction

Sea Surface Temperature (SST) is the most important variable for the Earth's climate system. It is the main factor which not only affects the circulation in atmosphere, generating winds, and transporting the heat, but also controls the water cycle and precipitation patterns in the Earth. Combining with salinity, it controls the seawater density to drive the deep-ocean circulation. Global ice volume best represents the baseline climate of the Earth, and climate records are often considered in a glacial-interglacial context. Detailed variations in the ice volume can be reconstructed by marine $\delta^{18}O$ records calibrated against direct sea level estimates by using paired Mg/Ca-SST and $\delta^{18}O$ measurements in areas of small salinity variability [*Chappell and Shackleton*, 1986; *Shackleton*, 1987; *Waelbrook et al*., 2002; *Lea et al*., 2002]. On the basis of such excellent works on the reconstruction of the long-term history of the ice volume, paired SST and $\delta^{18}O$ in planktonic foraminifera can offer very valuable information regarding the changes in regional sea surface salinity (SSS), which is mainly controlled by the precipitation-evaporation [*Mashiotta et al*., 1999].

The South China Sea provides a unique opportunity for detailed studies of abrupt climate change over glacial to interglacial timescales since its location, between the Asian continent and the Pacific Ocean, makes it rather sensitive to climate change both on land and the ocean [*Sarnthein and Wang*, 1999]. Additionally, the high sedimentation rate within the basin also allows the study of high-frequency climatic oscillations [*Wang et al*., 1999; *Oppo and Sun*, 2005]. These features enable the SCS to be one of the ideal places in response to high-frequency and dramatic climate events. Additionally, the high-resolution reconstruction can be used to resolve the phase relation among the environmental variables or between low- and high-latitude regions, and further understand the real controlling mechanisms.

Several works based on $\delta^{18}O$ and species assemblage approaches, as well as biologically produced unsaturated alkenones have been performed to study the SST record in the SCS [*Wang et al.*, 1999; *Kienast et al. 2001*; *Pelejero*, 2003]. However, these proxies can significantly be influenced by some complicated environmental factors other than the temperature effect. For example, variations in the contribution of terrestrial organic matters through time have been reported to limit the use of the molecular biomarker as a reliable paleo-temperature proxy.

In the present work, high-resolution Mg/Ca-based SST records across Termination I and the paleo-climatic variation from three sediment cores spanning the last 220kyr were integrated and compared with records from other sites in the global ocean. Furthermore, the thermal structure of the upper water column over the past 60 kyr was also reconstructed through the three planktonic species (*G. ruber*, *N. dutertrei* and *G. inflata*) which lives in different water depth. This study shows the first example to approach the real condition using the multi-proxies obtained from foraminiferal shell chemistry, and had greatly advanced in our understanding of the past climate change.

4.2 Materials and Methods

Two ODP drilling cores (ODP Site 1144 and Site 1145, located at the northern SCS) and a gravity core (276-19B, located at the central SCS) were considered in this study (Figure 4.1). The linear sedimentation rates of them range between 30-87 cm/kyr. As a general trend, sedimentation rates are high at glacials than interglacial times. The age model for all records has been adopted from previously published studies [*Wang and Chen.*, 1995; *Bühring et al.*, 2004; *Oppo and Sun*, 2005], which are based on AMS-^{14}C datings and on planktonic foraminiferal $\delta^{18}O$ data. Samples were taken at 10-cm intervals. The most detailed reconstruction is provided for Site 1145, with a time-resolution of 0.5-1.0 kyr, and ~3-4 kyr for Site 1144 and core 276-19B. The procedures and the equipment used for the determinations of trace element ratios are described in Chapter 2.

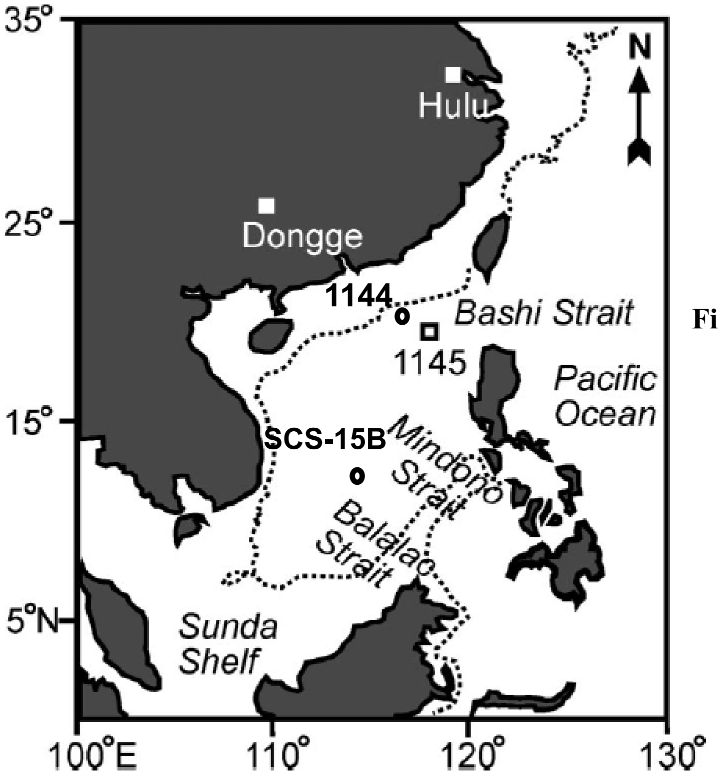

Figure 4.1 Map of the South China Sea showing the locations of cores ODP Site 1144 and Site 1145, as well as SCS-15B.

For the hydrographic setting, the SCS, on the western edge of the Western Pacific Warm Pool (WPWP), is a semi-enclosed marginal basin, and is connected to the Pacific Ocean via the Bashi Strait in the northeast and to the tropical Indo-Pacific through the Sunda Shelf in the southwest. At present, the surface circulation and hydrographic patterns are largely controlled by the seasonally reversing East Asia monsoonal regime [*Wyrtki*, 1961; *Shaw and Chao*, 1994]. The summer SST is rather uniform (28-29°C) throughout the SCS, whereas during winter, average SST is ~18°C and 27°C in the northern and southern SCS, respectively, indicating a dominant north-south gradient. Lower SSS (~33‰) during summer season reflects the generally higher precipitation or freshwater inflow, in contrast, during winter, the SSS reflects the decrease in regional precipitation combined with the inflow of higher salinity surface water masses through the Bashi Strait.

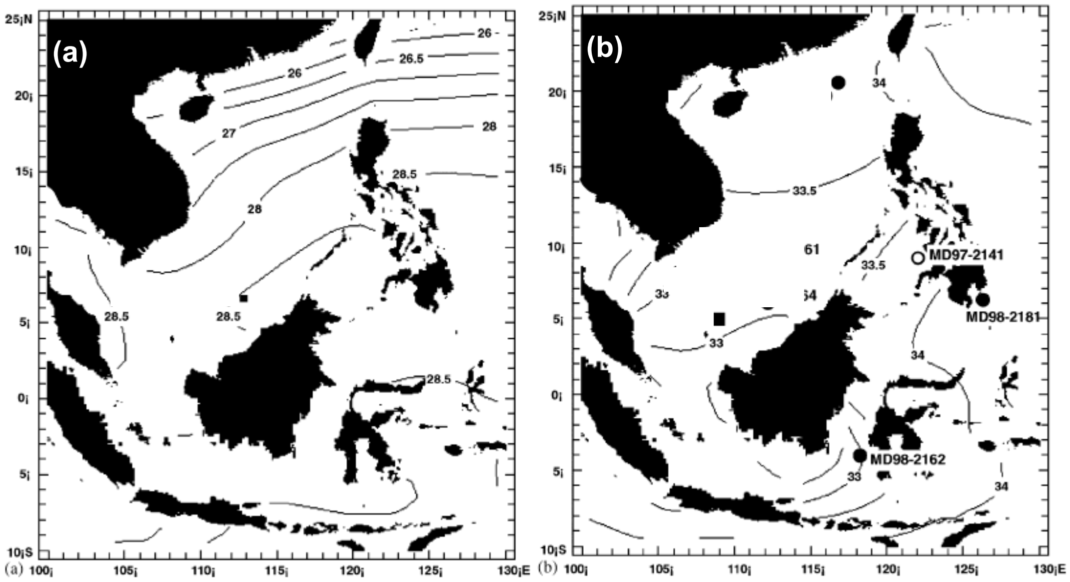

Figure 4.2 Mean annual (a) SST and (b) SSS [*Levitus and Boyer*, 1994; 1998]

4.3 Results and Discussion

4.3.1 High-resolution Mg/Ca-SST variability across Termination I

Mg/Ca ratios in *G. ruber* (white) from the ODP Site 1145 are high during the interglacial intervals and low over the glacial time, ranging from 3.58 to 2.24 mmol mol^{-1}, and inversely correlate with foraminiferal δ^{18}O. Based on the previous sediment-trap calibration, Mg/Ca= 0.32 exp (0.090*SST), in the northern SCS (*Huang et al.*, submitted), the temperature difference between the Holocene and LGM is ~4-5°C (26.8 to 22.2°C, see Figure 4.2). It is identical to the change in the reconstructed SST across Termination I reported by *Oppo and Sun* (2005).

By comparing the SST records of the SCS and adjacent Sulu Sea [*Rosenthal et al.*, 2003] with δ^{18}O records from Greenland GISP2 and Antarctica Byrd ice cores, several important features can be seen. The SST records of the marginal seas of the Pacific show a "continuous" deglacial warming, starting at around 19±1 kyr, which corresponds to the end of the Last Glacial Maximum (LGM, as defined by *Mix et al.*, 2001). There is no cessation of the deglacial warming during the Heinrich event-1 (H1, or the Antarctica Cold Reversal, ACR or the Younger Dryas, YD), and roughly half the entire deglacial warming occurs prior to the end of H1.

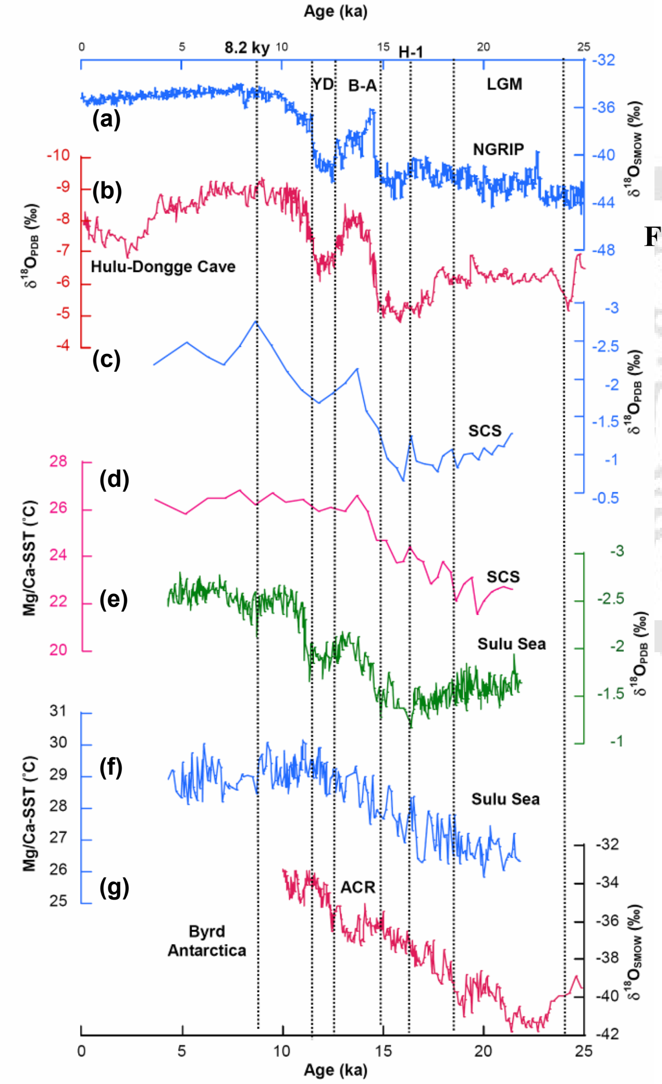

Figure 4.3 SST records characterized by a continuous warming across the deglacial without major cooling events, compared to the $\delta^{18}O$ records from ice cores in (a) Greenland NGRIP [*NGRIP Members*, 2004] and (g) Antarctica Byrd [*Blunier et al.*, 1998], as well as (b) Hulu-Dongge Cave (compilation of *Yuan et al.* [2004] and *Wang et al.* [2001]), (c) $\delta^{18}O$ data and (d) Mg/Ca-SST record of *G. ruber* in the SCS (This study), (e) $\delta^{18}O$ data and (f) Mg/Ca-SST record of *G. ruber* in Sulu Sea [*Rosenthal et al.*, 2003]. SST records are arranged North-South. Also shows the major abrupt climatic events.

The lack of any SST response during H1, the ACR, as well as YD may suggest that the deglacial warming of these regions was not affected by changes in the meridional overturning circulation (MOC), melting event of iceberg, and/or in the atmospheric circulation associated with H1 or YD. Alternatively, it is conceivable that the continuous warming trend observed in some of the lower resolution records or in cores from lower sedimentation rate sites is mainly due to unsolved SST variations or bioturbational attenuation of the signal, respectively. By using previously published high-resolution Mg/Ca-SST record in the same core [*Oppo and Sun*, 2005], like measured $\delta^{18}O$ data, it shows a "Greenland-type" deglacial pattern and a rapid warming synchronous with the Bølling-Allerød (B-A, ~15 kyr B.P.) transition in GISP2. This abrupt increase in SST is preceded by a SST minimum or a period of reduced warming during the time of H1, and is followed by a dramatic decrease in SST during the YD (~11.7 kyr B.P.). This is also supported by the variations in SST records reconstructed from faunal assemblage and $U^{k'}_{37}$ [*Pelejero et al*., 1999; *Kienast et al*., 2001; *Steinke et al*., 2001] from adjacent cores. Therefore, it is essential to obtain the high-resolution paleo-climate records to address the problems regarding abrupt climatic events.

4.3.2 Deglacial patterns in Tropical Pacific SST in ice age

Studies of El Niño-Southern Oscillation (ENSO) dynamics and impacts demonstrate that the tropical Pacific ocean-atmosphere system influences global climate on interannual to decadal time scales [*Trenberth et al*., 1998]. Furthermore, orbital perturbations of the seasonal cycle are believed to be critical determinants of the long-term behavior of ENSO [*Clement et al*., 1999]. Proxy of hydrographic records from the tropical Pacific suggest that the climate change are primarily controlled by precession periods (19-23 kyr), but the specific mechanisms and their interaction with global climate remain elusive [*Lea et al*., 2000; *Koutavas et al*., 2002]. In order to address these questions, the comparison of SST records between the western equatorial Pacific (WEP, ODP Site 1145, South China Sea) and cold tongue of the eastern equatorial Pacific (EEP, V21-30, Galapagos Island), where the largest ENSO signal occurs, were discussed in this section. Although the zonal gradient of the SST between the EEP and the WEP had been described by *Koutavas et al*. [2002], the SST history of the WEP were reconstructed by alkenone, which may be significantly influenced by variations in inputs of continental organic matters [*Muller et al*., 1998].

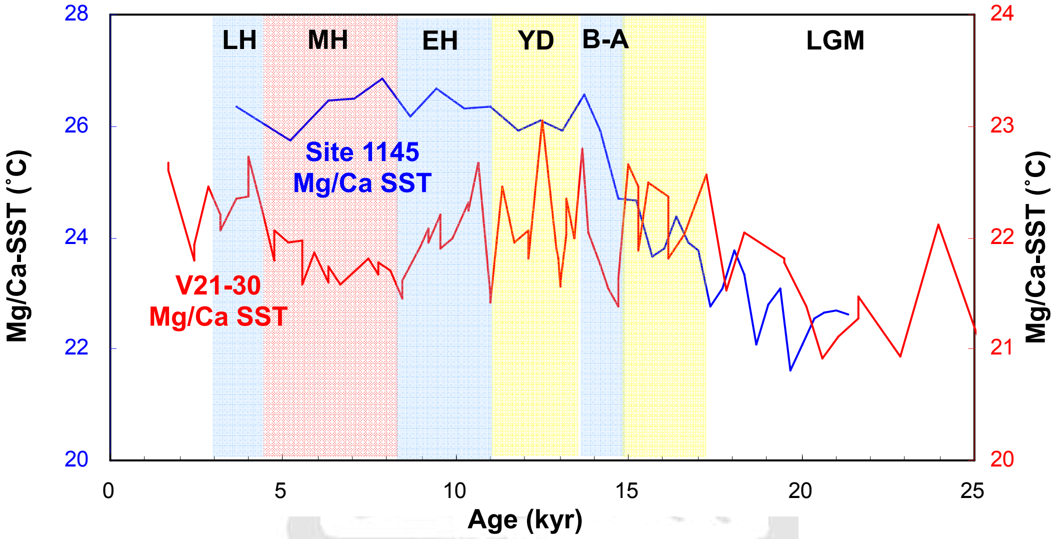

Figure 4.2 Comparison of western and eastern Pacific SST history during the last deglaciation and Holocene. Mg/Ca SST data from V21-30 (red line) and Site 1145 (blue line) are used as representative of the cold tongue and the warm pool, respectively.

To further explore the nature of the SST variability and its effect on the equatorial Pacific east-west (zonal) gradient, a comparison of the SST record between the EEP and the WEP across Termination-I has been made in Figure 4.4. Observed LGM cooling implies a relaxation of tropical temperature gradients, and shows a persistent ENSO-like pattern in the tropical Pacific. The SST pattern in the SCS shows an abrupt warming in phase with Greenland at ~14.8 kyr B.P. (B-A, Figure 4.4), whereas SST in the cold tongue dropped. This would imply an abrupt increase in the zonal SST gradient by ~2-3° C and a shift toward more La Niña-like condition at the time of the B-A warming [*Koutavas et al*., 2002]. During the YD the gradient decreased. The strongest zonal gradient is observed during the mid-Holocene (MH, 5 to 8 kyr B.P.), whereas the early-Holocene shows a decrease in east-west SST gradient, mainly because of warming in the EEP. Modeling and proxy studies found reduced mid-Holocene SSTs in the EEP, because of strengthened zonal winds and enhanced upwelling, in response to precession [*Clement et al*., 2000; *Koutavas et al*., 2002]. After the mid-Holocene, the zonal gradient decline due to a gradual cooling in the WEP and a gradual warming in the EEP. This is in disagreement with the observations of *Kienast et al*. [2001] and *Koutavas et al*. [2002], and can be attributed to the use of different materials for reconstructing SST variations. Improvements in resolution, dating, and spatial coverage of past climate records in tropical oceans are required to more accurately describe the millennial-scale climate change in the Pacific and its links with high latitudes.

4.3.3 $\delta^{18}O_{seawater}$ variations in the northern SCS across Termination I

$\delta^{18}O_{sw}$ was calculated by removing the temperature-driven component of changes in the *G. ruber* $\delta^{18}O$ record using the temperature-$\delta^{18}O_{sw}$ relationship (i.e., $\delta^{18}O_{sw} = (T - 16.5 + 4.8 * \delta^{18}O_c)/4.8 + 0.27$, [*Bemis et al*., 1998]) and subtracting the influence of ice volume taken from *Waelbroeck et al*. [2002]. Changes in the SSS can, therefore, be reconstructed using the modern $\delta^{18}O_{sw}$-S relationship, $\delta^{18}O_{sw} = 0.35*S - 11.6$ [*Lin et al*., 2003]. According to *Lea et al*. [2000] the estimated error of the $\delta^{18}O_{sw}$ data is around 0.18‰, calculated from the uncertainties in the paleothermometry, the Mg/Ca-SST calibration and the reproducibility of $\delta^{18}O_c$ and Mg/Ca measurements.

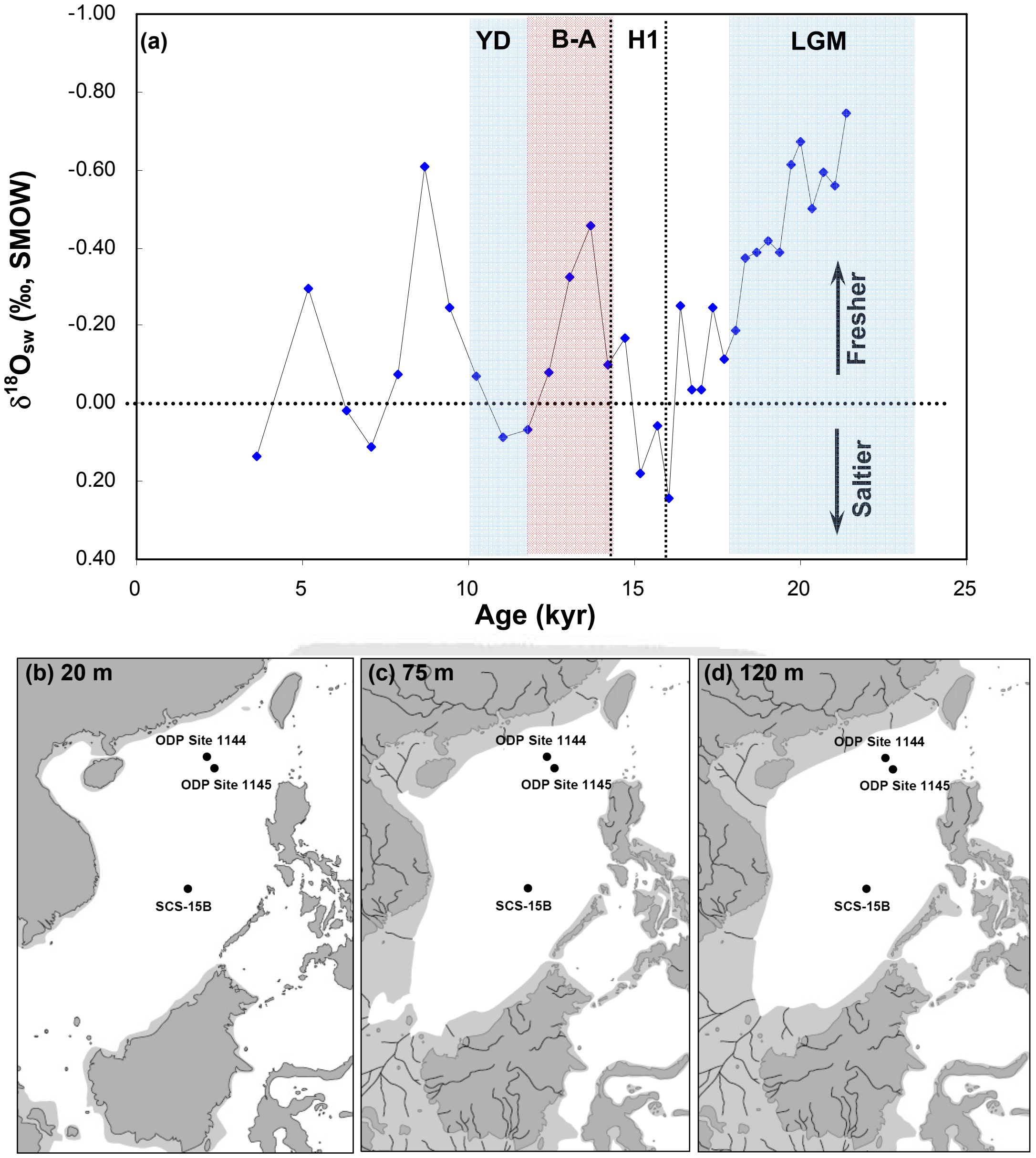

Figure 4.5 (a) Inferred paleo-$\delta^{18}O_{seawater}$ record of core Site 1145; (b)-(d) maps depicting shorelines at 20 (ca. 9 kyr), 75 (ca. 14 kyr) and 120 (ca. 20-24 kyr) below the present sea level ([*Voris*, 2000], taken from www.field museum.map).

The $\delta^{18}O_{seawater}$ record of core ODP Site 1145 reveals approximately 0.8‰ lower average $\delta^{18}O_{seawater}$ values (-0.8‰) during the LGM than during the Late Holocene (~0‰) (Figure 4.5), and the reconstructed changes in surface salinity that these may have been up to 7% lower during the glaciation, ranging from 33.5 at the late Holocene to 31.5 at the LGM. This is in agreement with previous studies from the northern and southern SCS, suggesting a regional decrease in salinity in the SCS during the glacial times [*Oppo and Sun*, 2005; *Steinke et al*., 2006], and possibly related to a reduction in δ^{18}O values of precipitation caused by a redistribution of precipitation pattern, variability in source water δ^{18}O or an increase in the amount effect [*Oppo and Sun*, 2005, and references therein]. Additionally, the variations in $\delta^{18}O_{seawater}$ seem to be correlate with the abrupt climatic events (i.e., YD, B-A and H1), which is characterized by low $\delta^{18}O_{seawater}$ values (i.e., fresher) at warm events, and high $\delta^{18}O_{seawater}$ values (i.e., saltier) at cold periods (Figure 4.5a).

In comparison with the record from the southern SCS [*Steinke et al*., 2006], the amplitude of the SSS variation in the northern SCS is significantly greater than that of the southern SCS, and reveals several of large fluctuations over the last 15 kyr B.P (Figure 4.5a). This is most likely due to differences in the surface circulation, dynamic distribution of the precipitation pattern, and land-sea contrast within the basin over the glacial-interglacial cycle (Figure 4.5b-d). In contrast, the results in the SCS are significantly different from published variations in salinity of the open oceans, which show a relatively salty condition in the tropical surface ocean [*Stoll et al*., 2004; *Schmidt et al*., 2004]. More investigations on the distribution of precipitation pattern in the tropical and subtropical oceans during the glacial-interglacial variation are necessary for resolving these questions.

4.3.4 Thermal structure of the upper ocean over the last 60 kyrs

The thermal structure (or vertical temperature gradient) of the upper layer of the ocean can provide an important clue regarding the depth of mixed layer and local wind strength. Three planktonic species with various habitat depths (*G. ruber*: 0-20 m; *N. dutertrei*: 50-100 m; and *G. inflate*: 100-400 m) were used to reconstruct the thermal structure of the water column in the SCS. The SST record of the shallow-water dwelling species (0-20 m), *G. ruber*, shows a continuous increase from the end of the LGM to the Holocene, and the temperature difference between the Holocene and LGM is ~5°C (see Figure 4.6). For deep-water dwelling species, *N. dutertrei* (<4°C) and *G. inflata* (<2°C), it reveals a much small variations in the reconstructed SST, inferring a relatively stable condition in the deep ocean during glacial-interglacial cycles. Using the SST records of *G. ruber* and *N. dutertrei*, variations in the depth of mixed layer can be qualitatively established through time. Due to the lower sampling resolution in the cores of SCS-15B and Site 1144, the detailed structure of the variations can not be further discussed in the present data, but the preliminary result seems to suggest that the upper ocean was well-mixing during the glacial periods (e.g., MIS 2), and during the interglacial time, it became more stratified because of the greater temperature gradient in the upper water column.

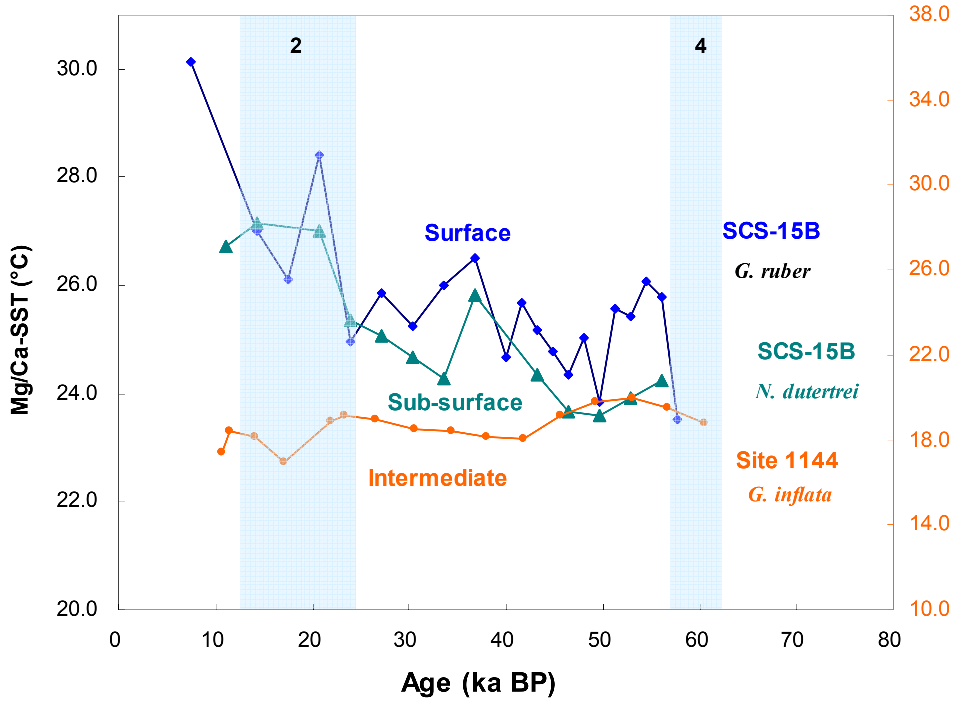

Figure 4.6 Mg/Ca-based SST records of the three planktonic species, *G. ruber*, *N. dutertrei* and *G. inflata*, indicating a larger fluctuation of the SST for the surface ocean, and a relatively stable condition in the deep ocean. Blue shaded areas represented the Marine Isotope Stage (MIS) 2 and 4.

4.3.5 Paleo-SST variation over the last 220 kyrs

The *N. dutertrei* Mg/Ca-SST estimates of core SCS-15B show a clearly glacial-interglacial periodicity over the last 220 kyr. Due to the absence of the uppermost sediments during sampling, SST variability across Termination I does not have enough time resolution to address the problems associated with high-frequency climatic events. Additionally, the records obtained from the timing of MIS-3 (57-24 kyr B.P.) seems to be altered by the bioturbation. Therefore, for core SCS-15B, it is better to focus on the time interval of the MIS 4 to MIS 7.

Figure 4.6 presents the first long-term variability in SST record in the SCS, and shows a temperature variation of ~4°C over the glacial-interglacial cycle. In comparison with *G. sacculifer* δ^{18}O, timing of the beginning of the deglacial warming based on Mg/Ca-SST leads the δ^{18}O record by ~5-6 kyr (Figure 4.7), implying that the variation in tropical SST is the main driving force for the global climate change [*Koutavas et al.*, 2002; *Visser et al.*, 2003], however, a more detailed high-resolution record is needed for confirming this argument.

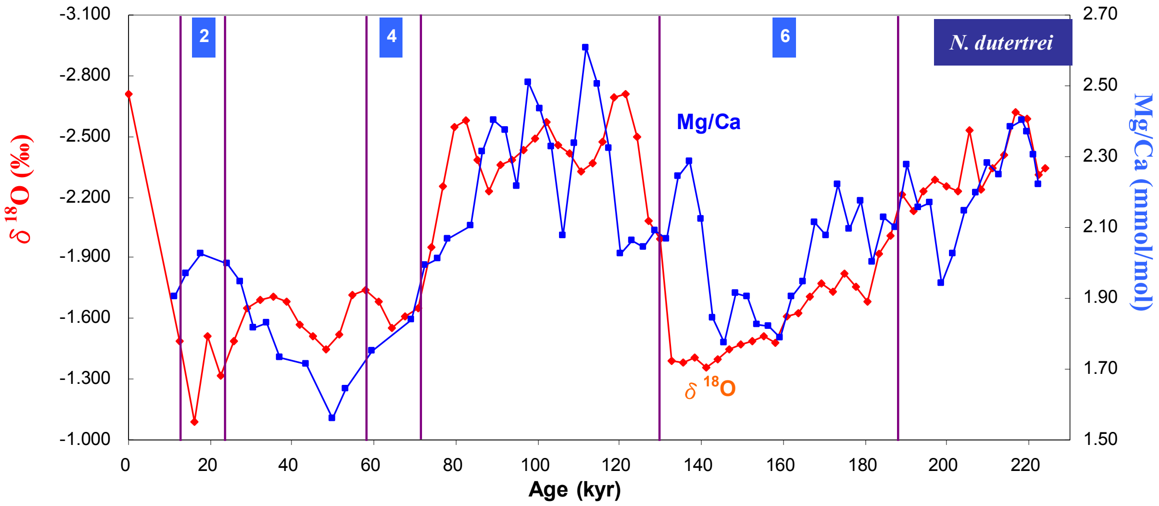

Figure 4.7 Mg/Ca-based SST records (blue line) of the planktonic species, *N. dutertrei*, and δ^{18}O of *G. sacculifer* (red line) are shown for a comparison. Numbers on the top represent the Marine Isotope Stage (MIS) 2, 4 and 6.

4.3.6 Reconstruction of continental inputs by using Ba/Ca in *N. dutertrei*

Ba/Ca in planktonic foraminifera has been reported as a reliable proxy for seawater Ba (D_{Ba}= 0.147±0.004, [*Lea and Spero*, 1990; 1994]), and already been applied to reconstruct temporal changes in past seawater Ba [*Hall and Chan*, 2004; *Plewa et al.*, 2006].

The planktonic foraminiferal Ba/Ca records of core SCS-15B reveals an interesting and approximately parallel trend similar to the Mg/Ca-based SST record, notably a high value in the interglacial period, and a low value at the glacial time (Figure 4.8). Again, due to the sampling problem, the Ba/Ca variation discussed here was only focused on MIS 4 to MIS 7. Screened Ba/Ca ratios do not correlate with corresponding Al/Ca, Mn/Ca and Ti/Ca measurements, supporting the trends in the Ba/Ca do not represent detrital contaminants and post-depositional alteration [*Lea and Boyle*, 1991].

Because changes in Ba/Ca strongly correlate with the Mg/Ca-SST, a temperature dependence on shell Ba/Ca may be firstly used to interpret the Ba/Ca variation. However, based on the culture experiments on the living planktonic foraminifera, the results lead to conclude that temperature range varying over a 7°C and salinity varying over 3‰ do not significantly influence Ba uptake [*Lea and Spero*, 1994]. Therefore, the covariation of Mg/Ca and Ba/Ca can not be ascribed to temperature effect. Instead, increased continental inputs associated glacial-interglacial changes are most likely linked to elevated Ba/Ca ratios. The Ba enrichment is believed to be the result of enhanced weathering and erosion following the glaciation [*Hall and Chan*, 2004]. Furthermore, Ba may be desorbed from shelf sediments as sea level rose [*Hanor and Chan*, 1977]. This is corroborated by the Sr isotope study in the SCS (see section 7.4.4 for details).

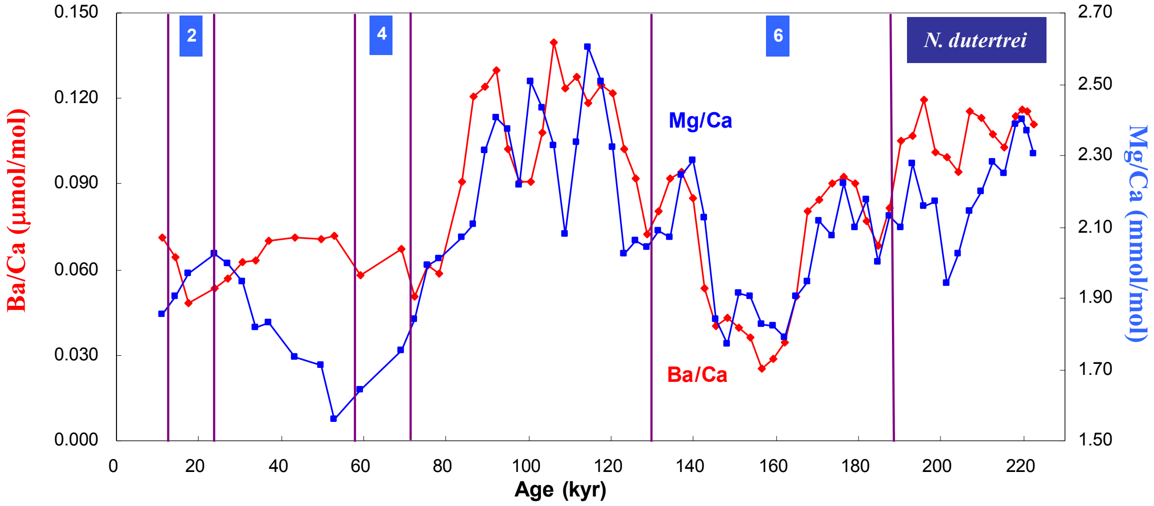

Figure 4.8 Mg/Ca-based SST records (blue line) and Ba/Ca variations (red line) of the planktonic species, *N. dutertrei*, are shown for a comparison. Numbers on the top represented the Marine Isotope Stage (MIS) 2, 4 and 6.

4.4 Conclusions

Changes in the local SST and freshwater budget over the last 22 kyrs have been reconstructed from the tropical SCS. Based on the combinations of oxygen isotopes, Mg/Ca and Ba/Ca on the planktonic foraminifera, several conclusions can be drawn: (1) The SST records of the marginal seas of the Pacific show a “continuous” deglacial warming, starting at around 19±1 kyr, which corresponds to the end of the Last Glacial Maximum. (2) Through the comparison of the east-west (zonal) SST gradient between western and eastern Pacific, a persistent ENSO-like pattern can be seen during the LGM. This is contrasted with mid-Holocene cooling suggest a La Niña-like pattern with enhanced SST gradients and strengthened trade winds. (3) Low salinity in the northern SCS during the LGM probably reflects an increase in freshwater inputs from several emerged rivers across the Sunda Shelf during glacial shelf exposure. Alternatively, an influence by the closure of the southern straits would cut off the inflow of high saline waters from the Indo-Pacific into the SCS cannot be excluded. (4) The thermal structure of the upper water column reconstructed by three different planktonic species shows a strong mixing during the LGM, and becomes more stratified during the Holocene. (5) The covariation of Mg/Ca and Ba/Ca over the last 220 kyrs indicates a periodic variation in the continental input associated with the glacial-interglacial changes.

Reference

Bemis, B. E., Spero, H. J., Bijma, J., Lea D. W., 1998. Reevaluation of the oxygen isotopic composition of planktonic foraminifer: Experimental results and revised paleotemperature equations. Paleoceanography 13, 150-160.

Blunier, T. et al., 1998. Asynchrony of Antarctica and Greenland climate change during the last glacial period. Nature 394, 739-743.

Bühring, C., Sarnthein, M., Erlenkeuser, H., 2004. Toward a high-resolution stable isotope stratigraphy of the last 1.1 m.y.: Site 1144, South China Sea, in Prell, W. L., et al., Proceedings of the Ocean Drilling Program, Scientific results, Vol. 184: College Station, Texas, Ocean Drilling Program, p. 1-29.

Chappell J., Shackleton N. J., 1986. Oxygen isotopes and sea level. Nature 324, 137-140.

Clement, A. C., Seager, R., Cane, M. A., 1999. Paleoceanography 14, 441.

Clement, A. C., Seager, R., Cane, M. A., 2000. Paleoceanography 15, 731.

Hall, J. and Chan, L.-H., 2004. Ba/Ca in *Neogloboquadrina Pachyderma* as an indicator of deglacial meltwater discharge into western Artic ocean. Paleoceanography 19, PA1017.

Hanor, J. S., Chan, L.-H., 1977. Non-conservative behavior of barium during mixing of Mississippi River and Gulf of Mexico waters. Earth Planet. Sci. Lett. 37, 242-250.

Kienast, M., Steinke, T. J. J., Stattegge, K., Calvert, S. E., 2001. Synchronous tropical South China Sea SST change and Greenland warming during deglacial. Science 191, 2132-2134.

Koutavas, A., Lynch-Stieglitz, J., Marchitto, T. M., Sachs, J. P., 2002. El Niño-Like Pattern in Ice Age

Lea, D. W., Boyle, E. A., 1990. Foraminiferal reconstruction of barium distributions in water masses of the glacial oceans. Paleoceanography 5, 719-742.

Lea, D. W., Boyle, E. A., 1991. Barium in planktonic foraminifera. Geochim. Cosmochim. Acta 55, 3321-3331.

Lea, D. W., Spero, H. J., 1994. Assessing the reliability of paleochemical tracers: Barium uptake in the shells of planktonic foraminifera. Paleoceanography 9, 44-452.

Lea, D. W., Pak, D. K., Spero, H. J., 2000. Climate impact of late Quaternary equatorial Pacific sea surface temperature variations. Science 289, 1719-1724.

Lin, I.-T., Wang, C.-H., Lin, S., 2003. Seasonal variations of oxygen isotopic compositions in the Pingtung coastal waters of Taiwan. Western Pacific Earth Science 3, 21-32.

Mashiotta, T. A., Lea, D. W., Spero H. J., 1999. Glacial-interglacial changes in subantarctic sea surface temperature and δ^{18}O- water using foraminiferal Mg. Earth Planet. Sci. Lett. 170, 417-432.

Mix, A. C., Bard, E., Schneider, R., 2001. Environmental processes of the ice age: land, oceans, glaciers (EPILOG). Quaternary Science Reviews 20, 627-657.

Muller, P. J., Kirst, G., Ruhland, G., vonStrorch, I., Rosell-Mele, A., 1998. Calibration of the alkenone paleotemperature index UK37 based on core-tops from the eatern South Atlatic and the global ocean (60˚N-60˚S), Geochim. Cosmochim. Acta 62, 1757-1772.

North Greenland Ice Core Project (NGRIP) Members., 2004. High-resolution record of Northern Hemisphere climate extending into the last interglacial period. Nature 431, 147-151.

Oppo, D. W., Sun, Y., 2005. Amplitude and timing of sea-surface temperature change in the northern South China Sea: Dynamic link to the East Asian Monsoon. Geology 33, 785-788.

Plewa, K., Meggers, H., Katern, S., 2006. Barium in sediments off northwest Afria: A tracer for paleoproductivity or meltwater events? Paleoceanography 21, PA2015.

Pelejero, C., Kienast, M., Wang, L., Grimalt, J. O., 1999. High-resolution U^{K}_{37} temperature reconstructions in the South China Sea over the past 220 kyr. Paleoceanography 14, 224-231.

Pelejero, C., 2003. Terrigenous n-alkane input in the South China Sea: high-resolution records and surface sediments. Chem. Geol. 200, 89-103.

Rickaby, R. E. M., Elderfield, H., 1999. Planktonic foraminiferal Cd/Ca: Paleonutrients or paleotemperature? Paleoceanography 14, 293-323.

Rosenthal, Y., Oppo, D. W., Linsley, B. K., 2003. The amplitude and phasing of climate change during the last deglaciation in the Sulu Sea, western equatorial Pacific. Geophysical Research Letts 30, 1428.

Sarnthein, M., Wang, P., 1999. Response of West Pacific marginal seas to global climatic change. Mar. Geol. 156, 1-3.

Schmidt, M. W., Spero, H. J., Lea, D. W., 2004. Links between salinity variation in the

Caribbian and North Atlantic thermohaline circulation, Nature, 428, 160-163.

Shackleton, N. J., 1987. Oxygen isotopes, ice volume and sea level. Quat. Sci. Rev. 6, 183-190.

Shaw, P. -T. and Chao, S. -Y., 1994. Surface circulation in the South China Sea. Deep-sea Research 41, 1663-1683.

Steinke, S., Kienast, M., Pflaumann, U., Weinelt, M., Stattegger, K., 2001. A high-resolution sea-surface temperature record from the tropical South China Sea (16,500-3,000 yr B.P.). Quaternary Research 55, 352-362.

Stott, L., Cannariato, K., Thunell, R., Haug, G. H., Koutavas, A., Lund, S., 2004. Decline of surface temperature and salinity in the western tropical Pacific Ocean in the Holocene epoch, Nature, 431, 56-59,

Trenberth, K. E., 1998. Journal Geophysical Research 103, 14291.

Visser, K., Thunell, R., Stott, L., 2003. Magnitude and timing of temperature change in the Indo-Pacific warm pool during deglaciation. Nature 421, 152-155.

Voris, H.K., 2000. Maps of Pleistocene sea levels in South East Asia: shorelines, river systems, time durations. Journal of Biogeography 27, 1153-1167.

Waelbroeck, C., Labeyrie, L., Michel, E., Duplessy, J. C., McManus, J. F., Lambeck, K., Balbon, E., Labracherie, M., 2002. Sea-level and deep water temperature changes derived from benthic foraminifera isotopic record. Quat. Sci. Rev. 21, 295-305.

Wang, L., Sarnthein, M., Erlenkeuser, H., Grimalt, J., Grootes, P., Heiling, S., Ivanova, E., Kienast, M., Pelejero, C., Pflaumann, U., 1999. East Asian monsoon climate during the Late Pleistocene: high-resolution sediment records from the South China Sea. Mar. Geol. 156, 245-284.

Wang, C.-H., Chen M.-P., 1990. Upper Pleistocene oxygen and carbon isotopic changes of core SCS-15B at the South China Sea. *J. Southeast Asian Earth Sciences* **4**, 243-246.

Wang, Y. J. et al., 2001. A high-resolution absolute-dated late Pleistocene monsoon record from Hulu Cave, China. Science 294, 2345-2348.

Wyrtki, K., 1961. Physical Oceanography of the Southeast Asian Waters, in *Scientific Results of Marine Investigations of the South China Sea and the Gulf of Thailand, NAGA Rep.*, vol. 2, 195 pp., Scripps Instit. of Oceanogr., La Jolla, Calif.

Yuan D. et al., 2004. Timing, duration, and transitions of the last interglacial monsoon. Science, 304, 575-578.

CHAPTER 5.

Reconstruction of changes in surface water pCO_2 in tropical South China Sea using foraminiferal multi-proxies approach

5.1 Introduction

The tropical ocean is generally identified as a major player both for controlling global climate and regulating the atmospheric carbon dioxide (pCO_2) concentration [*Lea et al.*, 2000; *Hönisch and Hemming*, 2005]. Under current efforts, the geographical distribution of CO_2 uptake and release in the modern ocean has been understood [*Takahashi et al.*, 2002; *Feely et al.*, 2004]. However, most of these studies shed important light only on the open ocean regimes, and little is known about the roles of coastal and marginal seas in the global carbon cycle. Their role could exert a profound effect on the global carbon cycle by linking the terrestrial, oceanic, and atmospheric carbon reservoirs [*Thomas et al.*, 2004]. Thus, knowledge of the role of greenhouse gases in climate forcing is needed for obtaining a better understanding of the ocean's contribution in response to changes in atmospheric CO_2 in the past.

The South China Sea (SCS) is located in the western equatorial Pacific, and adjacent to two major climatically sensitive areas, the Western Pacific Warm Pool (WPWP) and the Indonesian archipelago. Therefore, it has become an important setting in understanding the response to the variability of the East Asian monsoon (EAM) and abrupt climate change. Based on measured seawater pCO_2 and mass balance calculations, *Chen et al.* [2006] suggested that the SCS is a potential CO_2 source in the warm season (i.e., prevailing summer monsoon) and a weak CO_2 sink during the cold season. With these facts taken together, the SCS is likely a very weak CO_2 source or in equilibrium with atmospheric CO_2 in the modern situation [*Chen et al.*, 2006]. In contrast, during the last glaciation, decreased seasonality associated with reduced summer insolation would favor a shift of climate state toward development of a stronger winter monsoon in the SCS relative to the modern condition [*Wang et al.*, 1999], and may result in a significant CO_2 sink relative to atmosphere in this tropical marginal sea.

This argument agrees well with the estimation of seawater pCO_2 record based on marine sedimentary $\delta^{13}C_{org}$ in the SCS covering the last 220 kyr [*Kienast et al.*, 2001].

Proxies of carbonate system parameters allow us to reconstruct changes in the distribution of carbon species in the surface and deep oceans, and provide constraints necessary to evaluate the different mechanisms proposed to account for atmospheric CO_2 fluctuations. Boron isotopic compositions in foraminifera have been established to estimate changes in oceanic pH and pCO_2 for glacial-interglacial and long-term time scales of the Earth history [*Spivack et al.*, 1993; *Sanyal et al.*, 1997; *Palmer et al.*, 1998; *Sanyal and Bijma*, 1999; *Pearson and Palmer*, 2000; *Palmer and Pearson*, 2003; *Hönisch and Hemming*, 2005]. The principle of B and B isotope as a pH proxy is based on the proportions of two dissolved B species (i.e., $B(OH)_3$ and $B(OH)_4$-). In seawater they are highly pH-dependentbecause of the selective incorporation of $B(OH)_4^-$ into marine carbonates (*Hemming and Hanson*, 1992):

$$CaCO_3 + B(OH)_4^- = Ca(HBO_3)+HCO_3^-+H_2O$$

More recently, *Yu et al.* [2007] suggests that B/Ca ratios in foraminifera could provide another reliable approach for reconstructing seawater pH and pCO_2 in the past oceans. They show that the partition coefficient (K_D) of B/Ca has a strong species-specific dependence on calcification temperature, which, in principle, can be corrected for using shell Mg/Ca thermometry. Consequently, paired Mg/Ca and B/Ca measurements are especially of great worth in estimating variations in K_D through time which could be translated to seawater pH or pCO_2 by combing them with other carbonate system parameters (e.g., alkalinity).

Uranium exists in seawater as a group of carbonate complexes (mainly tricarbonato complex, $UO_2(CO_3)_3^{4-}$, [*Djogic et al.*, 1986; *Clark et al.*, 1995]) in which the relative abundance of each complex depends on seawater carbonate ion concentration ($[CO_3^{2-}]$). This fundamental knowledge led to the suggestion that U substitutes as a uranyl carbonate complex into aragonites or calcites. More recently, by applying X-ray absorbance, luminescence, and Raman techniques, *Reeder et al.* [2000] confirmed this suggestion and further explained that the relatively less U in calcite compared to U in aragonite may be possibly due to the change in coordination chemistry required to incorporate U into calcite. A growing body of evidences from the culture experiments also demonstrated that foraminiferal U/Ca ratio is mainly controlled by changes in seawater $[CO_3^{2-}]$ or pH [*Russell et al.*, 1994, 1996, 2004], which suggests that foraminiferal U/Ca has potential to provide information about changes in the ocean's carbonate concentration.

Here we present the core-top empirical calibrations of foraminiferal B/Ca and Mg/Ca for the three abundant planktonic species (*Globigerinoides ruber* white, *Globigerinoides sacculifer* and *Neogloboquadrina dutertrei*) in the SCS to further understand the biological and environmental controls on these elemental proxies. Applying the in situ empirical calibrations, we have reconstructed the SST and pH (or pCO_2) changes across Termination I. Using the multi-proxy approach (i.e., foraminiferal Mg/Ca, B/Ca, and U/Ca ratios in *G. ruber* white), we assessed the regional and temporal changes in the CO_2 flux between ice core records (i.e., atmosphere) and the tropical marginal sea, to further constrain the potential role of the tropical marginal sea.

5.2 Materials and Methods

5.2.1 Sediment locations

The sediment samples studied correspond to the upper centimeter (0-1 cm) of a suite of box core tops in the SCS (from 300 to 2500 m water depth) obtained during the R/V SONNE cruise in April-June 1994 ([*Sarnthein et al.*, 1994]; Figure 5.1). The sedimentation rates of these cores range between 5 to 50 cm/kyr [*Pelejero et al.*, 1999, and referenced therein]. The upper sediment sections average approximately 20 to 200-year records without taking into account for bioturbation. These SCS core-top sediments were used to investigate the temperature and pH effects on K_D and B/Ca in the three dominant planktonic foraminiferal species. The core-top materials provide an ideal sample/data set for evaluating the incorporation of trace elements into foraminiferal shell calcites and have been successfully used for calibrating with the modern seawater hydrography [*Rosenthal et al.*, 1997; *Rickaby and Elderfield*, 1999; *Elderfield and Ganssen*, 2000].

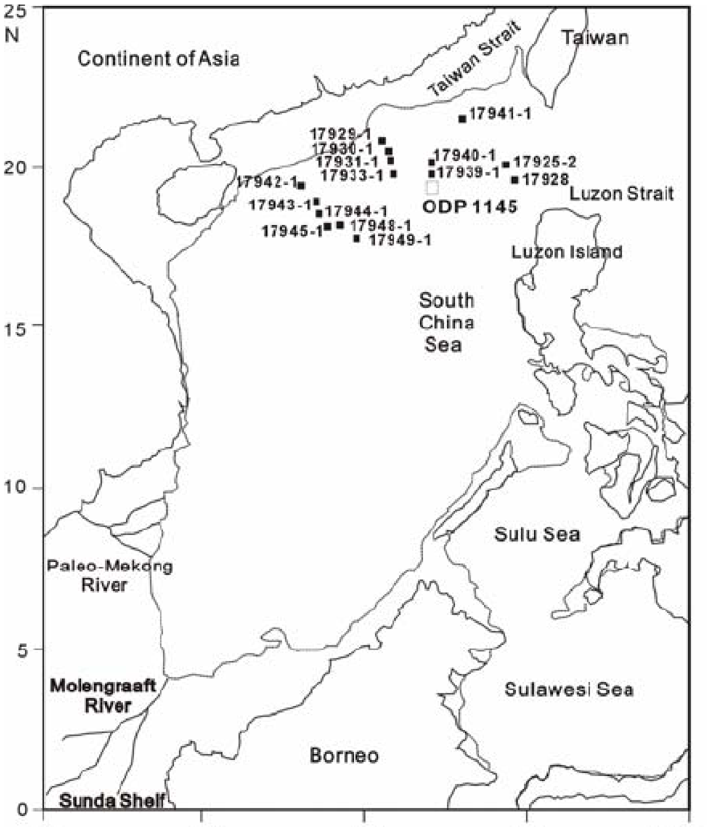

Figure 5.1 The locations of core-top sediments (solid squares) in the South China Sea for the in situ calibration. Also show the location of our down-core record from ODP Site 1145 (open square) used in this study. Gray line represents 100-m isobath, showing approximately position of coastline during glacial low sea level. Mekong and Molengraaftf Rivers on the (emerged) glacial Sunda Shelf are also indicated in the southwestern SCS [*Wang et al.*, 1999].

Down-core *G. ruber* (white) samples of ODP Site 1145 (19°N, 117°38’E, 3175 m water depth, Figure 5.1) in the northern SCS were hand-picked at 10 cm intervals from 0.4 to 4.0 m composition depth (across Termination I, 3.6-21.4 kyr) [*Shipboard Scientific Party*, 2000]. The age model of Site 1145 for the record extending back to ca. 16 kyr is based on four accelerator mass spectrometry (AMS) ^{14}C dates converted to calendar age and four age assignments between 20 and 60 kyr tie the northern SCS record to terrestrial records established by *Oppo and Sun* [2005]. Accumulation rates, averaging 10 cm/kyr, are assumed constant between the tie points.

5.2.2 Modern hydrographic properties

The modern hydrographic distributions of summer SST in the SCS are quite uniform (ranging from 28-29°C) and show a small north-south temperature gradient. The average surface salinity is relatively low (approximately 33 per salinity unit, psu), which mainly results from high fresh water inflows throughout the region. Winter SST in SCS is significantly influenced by two distinct water masses- warm Kuroshio Surface Water (~25°C) and colder Oyashio Waters (~18°C) [*Shaw et al.*, 1991]. The surface temperature ranges from 18°C in the north to 27°C in southern SCS and shows a greater north-south temperature gradient than during summer time [*Wyrtki*, 1961]. The winter SSS is relatively stable due to the lesser change in the regional precipitation.

For the core-top calibration, temperature (T) and salinity (S) were obtained using one-degree latitude-longitude grid World Ocean Atlas 1998 dataset. The World Ocean Atlas 1998 was produced by the National Oceanographic Data Center (NODC) Ocean Climate Laboratory. Mean habitat depths for the three abundant planktonic species were estimated following the method of *Huang et al.* [2007], and then used to calculate mean habitat T and S, as well as other hydrographic data for each species. Total dissolved inorganic carbon (DIC), total alkalinity (ALK), together with nutrient levels (i.e., PO_4^{3-} and SiO_3) were obtained from the South East Asia Time-series Study (SEATS) hydrographic station nearby the studied core-top sites [*Chou et al.*, 2007]. The total boron concentration ($[B]_{tot}$) in seawater was calculated from S using $[B]_{tot}$ (µmol/kg) = 416*S (psu)/35. The carbonate system parameters were then calculated using CO2SYS.xls (Ver. 12) (after [*Lewis and Wallace*, 1998; *Pelletier et al.*, 2005]). K_1 and K_2 were selected according to *Mehrback et al.* [1973] refit by *Dickson and Millero* [1987], K_B^* and K_{SO4} were based on *DOE* [1994] and *Dickso*n [1990], respectively.

5.2.3 Foraminiferal cleaning method

About 25-30 individuals of foraminiferal samples were hand-picked (250-300 µm, 300-355 µm and 300-355 µm for *G. ruber* white, *G. sacculife*r without sac-like chamber and *N. dutertrei*, respectively) using stereoscope and weighed by a six-place microbalance (precision= 1 µg) before cleaning for analysis. The foraminiferal tests were gently crushed to facilitate removal of remnant cytoplasm from the interior of shell chamber and then completely removed of contamination phases by a series of physical and chemical cleaning protocols modified from *Boyle and Keigwin* [1985/1986] and *Rosenthal et al.* [1997]. For crushing foraminifera tests, samples were ultrasonically cleaned three times with distilled water, twice with methanol and eventually rinsed with distilled water several times to remove adhering detrital grains and fine clay materials.

Reduction, DTPA and oxidation reagents, often called the “Cd” and “Ba” cleaning methods [*Boyle and Keigwin*, 1985/1986; *Lea and Boyle*, 1993; *Rosenthal et al.*, 1997], were used to effectively remove Fe-Mn oxides, barite accumulations and organic coatings within the shells because large amounts of continental materials exist in the SCS sediments. After weak acid leaching (with 0.001N HNO_3), distilled water were introduced again to completely remove all surface-adsorbed and residue contaminants, and finally transfer calcite fragments into new acid-leached microcentrifuge vials prior to analysis. The cleaned shell calcites were then dissolved in 0.065N HNO_3. All dilute nitric acids and other chemical reagents used for cleaning procedures were prepared from commercial ultrapure-grade reagents (BASELINE, SEASATR). Sample preparation procedures were processed under laminar flow bench to avoid any metal contamination. A comparison of the ”Cd-cleaning” and “Mg-cleaning” methods showed a negligible effect on B/Ca, but significantly reduced Fe, Mn, and Ti concentrations in the shells, which can strongly bias the shell U/Ca due to U incorporation into Mn overgrowths [*Russell et al*., 1994; 2004].

5.2.4 Foraminiferal shell chemistry analysis

Cleaned samples were dissolved and analyzed for B, Mg, U, and Ca using a modification of methods described previously in *Rosenthal et al*. [1999]. Multiple elemental ratios (Mg/Ca, B/Ca, and U/Ca) of samples were simultaneously measured using a high-resolution ICP-MS (HR-ICP-MS, Finnigan Element XR) at Rutgers University. The analytical precision (2σ) was 0.44% (Mg/Ca), 1.10% (B/Ca), 2.38% (U/Ca) based on repeated analysis of a matrix-matched consistency standard. Additionally, ^{27}Al, ^{55}Mn, and ^{56}Fe had been also measured by low- ($m/\Delta m= 300$) and medium-resolution ($m/\Delta m= 4000$) setting to monitor detrital contaminants, such as fine clay and Fe-Mn coatings. Al/Ca, Mn/Ca and Fe/Ca were mostly well below thresholds for likely contamination (>100 μmol mol^{-1}), and trace element data in the foraminifera with Fe/Ca and Mn/Ca ratios higher than this criteria were excluded in this study, especially for U/Ca.

Precise and accurate determinations of B/Ca ratios are plagued both by high B blanks and a significant memory effect as observed by *Al-Ammar et al.* [1999]. In this study, we developed an on-line purification system (Boron-specific resin, Amberlite IRA 743, Sigma) to remove any B from the double distilled water, which we found to be the main B blank source in the laboratory. Besides, the use of PFA spray chamber and nebulizer were also minimized the potential contaminations from glass materials. The B blank is less than 3% of the natural foraminiferal samples and displays a relatively stable blank contribution during the analysis. Isotopic data were collected on a Finnigan MAT 253 mass spectrometer, and the precision of the measurements is better than 0.09‰ for $\delta^{18}O$, as determined by replicate analyses of NBS-19 and laboratory standards [*Oppo and Sun*, 2005].

5.3 Results

5.3.1 Core-tops Mg/Ca and B/Ca

A core-top transect in the northern SCS exhibits a significant depth-related decrease in test weight for all three species (Figure 5.2c). Over the depth range of 300 to 2500 meters the size-normalized test weight (for the size fraction of 250-300μm) of *G. ruber* decreases from 18.3 to 8.1 μg, of *G. sacculifer* from 28.2 to 15.0 μg (300-350μg) and of *N. dutertrei* 26.5 to 13.7 μg (300-350μg). Concomitantly, Mg/Ca ratios in the three planktonic species also decrease with depth (Figure 5.2a). Over this depth interval, Mg/Ca in *G. ruber* decreases from 3.63 to 4.76 mmol mol^{-1}, in *G. sacculifer* from 2.84 to 3.40 mmol mol^{-1} and in *N. dutertrei* from 0.96 to 2.15 mmol mol^{-1}. The differences in Mg/Ca among the three species are consistent with their preferred depth habitat with the highest ratios observed in the mixed layer species of *G. ruber* and the lowest ratios in the thermocline dweller *N. dutertrei* [*Anand et al.*, 2003; *Huang et al.*, 2007]. Similarly, B/Ca also exhibits inter-specific variability with decreasing ratios from G. *ruber*

(119-142 μmol mol^{-1}), *G. sacculifer* (81-87 μmol mol^{-1}), and *N. dutertrei* (55-81 μmol mol^{-1}). Possibly, this can be linked to depth habitats of specific life cycles for planktonic species. In the surface ocean, high sea surface temperature and basic oceanic pH value, in principal, would result in higher B/Ca values in the foraminiferal calcite. Thus, the surface-dwelling species should have higher B/Ca than the deep dwellers, in the sequence of *G. ruber* > *G. sacculifer* > *N. dutertrei*, which agrees well with the B/Ca ratios in the three planktonic species in the SCS. Additionally, unlike Mg/Ca, none of the three species shows a significant, depth-related decrease in B/Ca (r^2< 0.32, Figure 5.2b and Table 5.1).

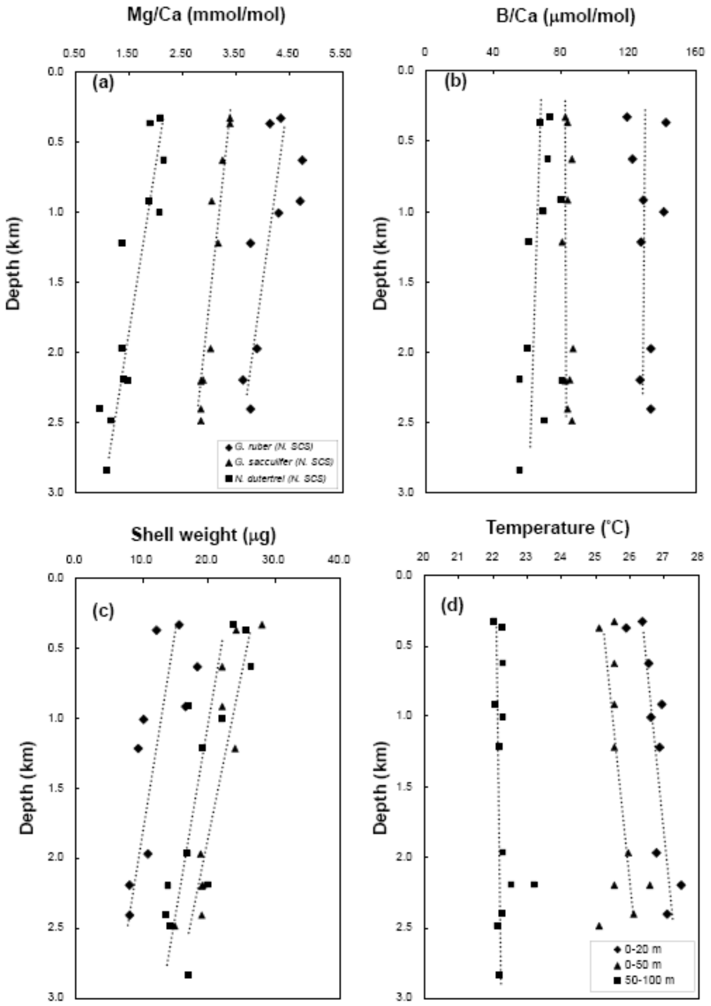

Figure 5.2 (a) Mg/Ca ratios for the three planktonic species versus depths, showing s an obvious decrease with increasing depths. (b) B/Ca ratios for the three planktonic species versus depths, showing no significant change in shell B/Ca ratio with depths. (c) Average shell weight for the three planktonic species versus depths, showing a depth-related decrease with increasing depths. (d) Annual mean temperatures of 0-20 m, 0-50 m and 50-100 m in the SCS, corresponding to the calcification depths for *G. ruber*, *G. sacculifer* and *N. dutertrei* in the SCS

5.3.2 Down-core record from the South China Sea

Elemental ratios were obtained from samples used by *Oppo and Sun* [2005] in their study of ODP site 1145 in the SCS. Our down-core record of Mg/Ca in *G. ruber* (250-300 μm) shows an increase from ~2.6 mmol mol^{-1} during the last glacial maximum (LGM) to ~3.4 mmol mol^{-1} during the late Holocene, associated with 1.5‰ negative shift in the $\delta^{18}O$ composition of the planktonic foraminifera. The Mg/Ca data are consistent with the published deglacial Mg/Ca record from this site [*Oppo and Sun*, 2005]. Concomitantly, the B/Ca ratio decreases from 170 to 124 μmol/mol during the transition from the LGM to Holocene. Paired U/Ca measurements show an LGM-Holocene decrease from 8.91 to 6.24 nmol mol^{-1}.

5.4 Discussion

5.4.1 Dissolution effects on Mg/Ca and B/Ca

In our northern SCS transect, the core top depth increases with increasing distance from the basin's margins. The overlying surface conditions change concomitantly, with SST and pH (and hence $B(OH)_4^-/HCO_3^-$) increasing along the trend of increasing water depth. The increase in SST and pH along this transect are, however, very limited; SST varies by less than 2°C from the shallowest to deepest cores. Surface water pH varies by less than 0.01 or the equivalent of 3 μmol kg^{-1} in $[CO_3]$ ion concentration, based on the modern regional relationship between surface pCO_2 and SST [*Chen et a*l., 2006]. This small change implies that the observed depth-related decrease in test size-normalized weight is due to the effect of post-depositional dissolution on the foraminiferal tests [*Rosenthal et al.*, 2000; *Rosenthal and Lohmann, 2002*] rather than variations in the initial test weight [*Barker and Elderfield*, 2002]. The decrease in average test weight for all three species is highly correlated with the core-tops depth ($r^2 > 0.53$, Table 5.1).

Furthermore, the trend of shell weight versus CO_3^{2-*} for *G. ruber* (slope= 0.08) is slightly higher than the weight-loss slope of 0.06 μg per a change in ΔCO_3 (μmol kg^{-1}) from the Sierra Leone Rise [*Rosenthal and Lohmann*, 2002]. In contrast, the decrease in shell weight per a change in ΔCO_3 for *G. sacculifer* (slope= 0.13) and *N. dutertrei* (slope= 0.10) are significantly lower than the weight-loss slope of 0.30±0.05 μg per a change in ΔCO_3 (μmol kg^{-1}) [*Broecker and Clark*, 2001]. However, the extent of dissolution is difficult to directly compare only by the slopes because of the difference in selected size fraction among these studies, and the depths of core-top sediments (300-2500 m) in the SCS are much shallower than previous studies (~2700 to 5300 m). The dissolution effect is also evident by the significant decrease in Mg/Ca ratios in all three planktonic species with depth, even though SST increases slightly from the shallowest to deepest cores. This corollary is also supported by the significant correlation between Mg/Ca and test-weight data, observed in our depth transect for all three species ($r^2 > 0.52$, see Table 5.1).

Table 5.1 Summary of correlation of shell weight, core-top depth, Mg/Ca and B/Ca ratios in the three planktonic species from this study.

	core depth			**shell weight**			**Mg/Ca**			**B/Ca**		
	G. ruber	*G. sacculifer*	*N. dutertrei*	*G. ruber*	*G. sacculifer*	*N. dutertrei*	*G. ruber*	*G. sacculifer*	*N. dutertrei*	*G. ruber*	*G. sacculifer*	*N. dutertrei*
core depth	1	1	1	**0.53**	**0.79**	**0.67**	**0.52**	**0.92**	**0.80**	*0.01*	*0.08*	*0.17*
shell weight				1	1	1	**0.86**	**0.78**	**0.65**	*0.22*	*0.31*	*0.00*
Mg/Ca							1	1	1	*0.05*	*0.06*	*0.30*
B/Ca										1	1	1

In contrast with Mg/Ca, B/Ca ratios in all three planktonic species show no significant trend with depths (Figure 5.2b). This and the lack of significant correlation between B/Ca and test weight suggest that unlike Mg/Ca, B/Ca ratios in tests of these three species of planktonic foraminifera is not altered by post-depositional dissolution. This finding is consistent with a recent core top calibration from the North Atlantic [*Yu* *et al.*, 2007] and is also with the lack of positive covariance between B/Ca and test weight in the down-core record of ODP Site 806 from the Ontong-Java Plateau in the western equatorial Pacific [*Wara et al.*, 2003]. In that record, B/Ca is inversely correlated with test weight (i.e., highest B/Ca is found in tests with lowest weights, which apparently reflect greater dissolution intensity). These consistent lines of evidence suggest that post-depositional dissolution of planktonic foraminifera does not alter their test's B/Ca composition as it so happens with Mg/Ca. Our conclusion about minimal dissolution effects on B/Ca underscores the importance of the primary controls, i.e., temperature and pH.

5.4.2. Core tops calibration of planktonic foraminiferal B/Ca

In order to examine our empirical K_D-T relationship we further evaluated if the B/Ca in the foraminiferal shell is in equilibrium with seawater [$B(OH)_4^-/HCO_3^-$], modern surface hydrographic (i.e., T and S) and carbonate parameters (i.e., pH and HCO_3^-, [*Chou et al.*, 2007]) (Figure 5.3a). Calcification depths for each species were used to calculate [$B(OH)_4^-/HCO_3^-$] in surface seawaters, and then compared with the theoretical seawater [$B(OH)_4^-/HCO_3^-$] based on K_D-T and measured B/Ca. Figure 5.3b shows that B/Ca in the three planktonic species is rather close to equilibrium with seawater [$B(OH)_4^-/HCO_3^-$], thus suggesting that B/Ca in planktonic foraminifera can faithfully record the ambient seawater pH.

The positive correlation between B/Ca and Mg/Ca found in a down core record from the Ontong Java Plateau [*Wara et al.*, 2003] suggested that temperature, in addition to the pH, might have a significant effect on B/Ca ratios in planktonic foraminifera. The exact relationship between the two variables was, however, not defined in that study. More recently, based on Atlantic core tops calibration, *Yu et al.*

[2007] estimated the temperature dependence of the K_D for boron in three planktonic foraminifera. The latter study also demonstrated that Mg/Ca measurements could be used for correcting the temperature effect on the K_D, thereby allowing the estimation of paleo-pH from paired B/Ca and Mg/Ca measurements. It remains, however, to be determined how applicable is their calibration to other ocean basins. Below we follow the methodology of *Yu et al.* [2007] to obtain a K_D from a suit of core tops in the northern South China Sea.

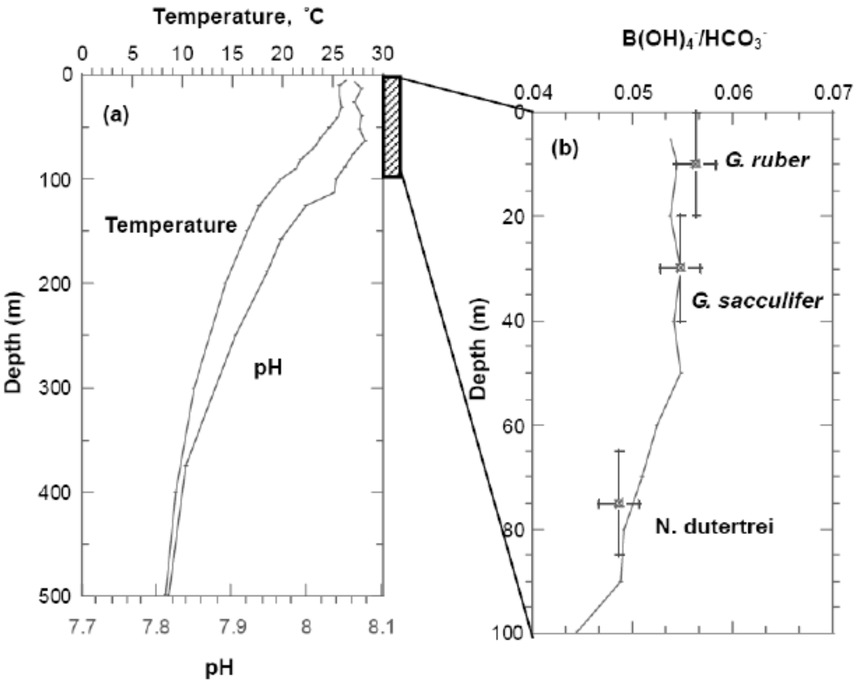

Figure 5.3 (a) Seawater temperature and pH profiles above the water depth of the upper 500 m in the South China Sea. (b) A comparison of seawater $[B(OH)_4^-]/[HCO_3^-]$ calculated from modern seawater T, pH and carbonate parameters and estimated seawater $[B(OH)_4^-]/[HCO_3^-]$ based on measured B/Ca in three planktonic species and the species-specific K_D-T relations, suggesting an equilibrium between foraminiferal B/Ca ratios and seawater $[B(OH)_4^-]/[HCO_3^-]$.

Following *Yu et al.* [2007] the partition coefficient of B in calcitic foraminifera is defined as:

$$K_D = \frac{[HBO_3^{2-}/CO_3^{2-}]_{CaCO_3}}{[B(OH)_4^-/HCO_3^-]_{seawater}} = \frac{[B/Ca]_{CaCO_3}}{[B(OH)_4^-/HCO_3^-]_{seawater}}$$

where $[B/Ca]_{CaCO3}$ is the measured B/Ca ratio in planktonic foraminifera and

$[B(OH)_4^-/HCO_3^-]_{seawater}$ is the ratio of borate to bicarbonate ion in seawater. In the modern ocean, $[B(OH)_4^-/HCO_3^-]_{seawater}$ is proportional to seawater pH (i.e., as an increase in $[B(OH)_4^-]$ and a decrease in $[HCO_3^-]$ with increasing seawater pH).

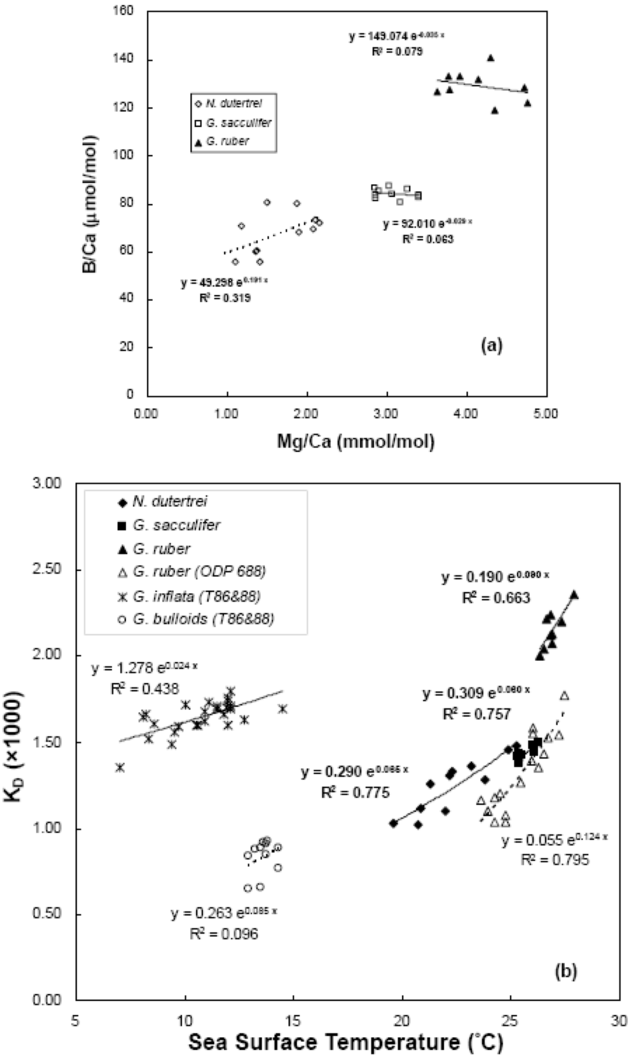

Figure 5.4 (a) A plot of foraminiferal B/Ca and Mg/Ca for the three selected planktonic species in the core-top sediments of this study. The large amounts of scatter for each species are primitively affected by strong partial dissolution on Mg/Ca in the South China Sea core-top sediments. (b) a plot of K_D of B/Ca with calcification temperature (dissolution-corrected Mg/Ca-SST for this study), indicating a strong temperature dependency on foraminiferal B/Ca (solid symbols, solid triangle rhombus- *G. ruber*; solid square- *G. sacculife*r; Solid rhombus- *N. dutertrei*), and also shows a comparison of the present data and previous study (open symbols) [*Yu et al.*, 2007]. Data were fitted by an exponential mode due to better correlation coefficients and based on the theoretically thermodynamic temperature equation.

We use paired B/Ca and Mg/Ca measurements to estimate the temperature dependence on K_D in the SCS samples. A plot of B/Ca vs. Mg/Ca shows relatively weak correlations for all three species (Figure 5.4a). This is likely because of the effect of dissolution on the seafloor on Mg/Ca ratios. To circumvent this problem, we calculate the dissolution-corrected Mg/Ca-temperature calibrations for the SCS, following the methodology outlined in *Rosenthal and Lohmann* [2002]. Based on the trend discussed above (Figure 5.2), we determine the pre-exponential constant (B) for the three planktonic species as a function of the average test weight, using a temperature sensitivity (A) of 0.095 for all the three species (based on [*Rosenthal and Lohmann*, 2002; *Anand et al*., 2003]). The species-specific calibrations are:

1) *G. ruber* $_{(250\text{-}300\ \mu m)}$, Mg/Ca= (0.010 wt + 0.212) exp (0.095T)
2) *G. sacculifer* $_{(300\text{-}350\ \mu m)}$, Mg/Ca= (0.005 wt + 0.159) exp (0.095T)
3) *N. dutertrei* $_{(300\text{-}350\ \mu m)}$, Mg/Ca= (0.009 wt + 0.009) exp (0.095T)

The empirical K_Ds were calculated from the observed B/Ca data and surface water $[B(OH)_4^-]$ and $[HCO_3^-]$ concentrations as estimated from the annual mean surface water salinity, pH, and ALK data available for the northern SCS [*Chen et al*., 2006; *Chou et al*., 2007]. The SCS calibration yields different temperature-K_D relationships for each of the three planktonic foraminiferal species (Figure 5.4b). All three calibrations show, however, significant positive correlations between the K_Ds and Mg/Ca-based SSTs. The K_D of *G. ruber* exhibits a temperature sensitivity of +9% per °C, which significantly differs from 6-6.5% changes per °C of *G. sacculifer* and *N. dutertrei*. The temperature sensitivity of K_D in *G. ruber* suggested from our calibration is consistent, within the experimental uncertainties, with the results of *Yu et al*. [2007]. Likewise, the results of that study also demonstrate significant inter-specific variability in the temperature dependence of K_D of boron in planktonic foraminifera. There is, however, a significant difference in the absolute values of the K_D obtained for *G. ruber* (white) from the SCS and the eastern equatorial Atlantic data (ODP 668B, [*Yu et al.*, 2007]). Notably, the SCS *G. ruber* K_D varies between about 0.0020 and 0.0025 for a temperature range of ~26-28°C, whereas those derived from the equatorial Atlantic calibration varies between 0.0010 and 0.0015 for the temperature range of 24.5 and 27°C (Figure 5.4b). This apparent discrepancy raises the possibility of an additional control on foraminiferal B/Ca, such as regional sea surface temperature and pH.

5.4.3 Estimation of pH and pCO$_2$ from Foraminiferal B/Ca

Following the method outlined in *Yu et al.* [2007], we use the K_D-T relationship obtained from our core tops calibration, and the Mg/Ca-derived SST record to convert the measured foraminiferal B/Ca record at ODP Site 1145 to $[B(OH)_4^-/HCO_3^-]$ ratios in the surface water. Subsequently, records of surface water pH and pCO$_2$ are reconstructed by combining the $[B(OH)_4^-/HCO_3^-]$ with estimates of total alkalinity (ALK) derived from seawater $\delta^{18}O$ ($\delta^{18}O_{sw}$) [*Oppo and Sun*, 2005].

Sea surface temperatures in the SCS, estimated from Mg/Ca (using the calibration of: Mg/Ca= 0.32 exp (0.090*SST)) show ~4.6°C increase during the last deglaciation, from 22.2°C at the LGM to 26.8°C during the late Holocene. This estimate is in excellent agreement with a previous Mg/Ca-based SST reconstruction from the same core [*Oppo and Sun*, 2005] and alkenone based SST estimates from other cores in the northern SCS [*Kienast et al.*, 2003]. Note that the dissolution-corrected equation (i.e., Eq. 1) is not appropriate to use in this case because variations in average shell weights of down-core sediments also reflect changes in initial shell weights associated with seawater $[CO_3^{2-}]$ and nutrient levels at glacial-interglacial periods). B/Ca ratios do not covary with SST, but rather show a decrease from 170 μmol mol^{-1} at the LGM to 124 μmol mol^{-1} in thee late Holocene (Figure 5.5). The lack of positive covariance with SST, suggests that changes in surface water pH (due to changing atmospheric pCO$_2$) rather than temperature, exert the dominant control on the foraminiferal B/Ca variability during the deglaciation. This corollary is significantly different than those implied by the positive correlation between B/Ca and Mg/Ca in down core records from the Ontong Java Plateau [*Wara et al.*, 2003] and the North Atlantic Ocean [*Yu et al.*, 2007].

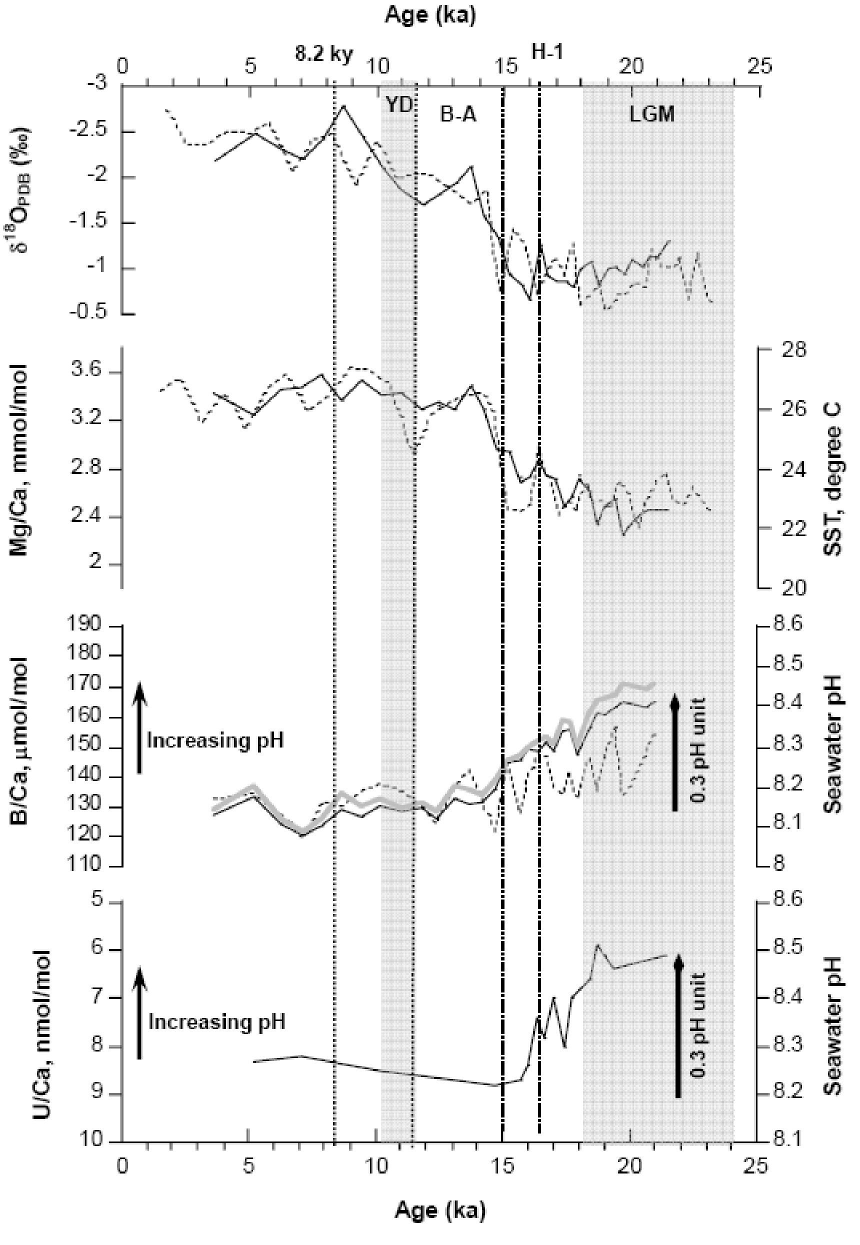

Figure 5.5 (a) *G. ruber* $\delta^{18}O$ from Site 1145. Solid and dashed lines show $\delta^{18}O$ data from the present study and *Oppo and Sun*. [2005], respectively. (b) Solid line, Site 1145 Mg/Ca and Mg/Ca-derived SST records in this study; dashed line: data adopted from *Oppo and Sun*. [2005]. (c) Black line shows a B/Ca-based seawater pH record attained by assuming ALK vary as a function of salinity and modern ALK-S relationship is constant through time; gray line represents a B/Ca-based seawater pH record attained by constant ALK at 2240 µeq/kg; dashed line represents the foraminiferal B/Ca variability through time. (d) U/Ca and U/Ca-derived pH records using the U/Ca-pH equation of *Russell et al.* [2004].

Following the method outlined in *Yu et al.* [2007], we use the K_D-T relationship obtained from our core tops calibration, and the Mg/Ca-derived SST record to convert the measured foraminiferal B/Ca record at ODP Site 1145 to $[B(OH)_4^-/HCO_3^-]$ ratios in the surface water. Subsequently, records of surface water pH and pCO_2, are reconstructed by combining the $[B(OH)_4^-/HCO_3^-]$ record with estimates of total alkalinity (ALK) (Appendix Table A2). Two models are used to estimate changes in seawater ALK. First, down-core variations in ALK are estimated from surface salinity, as derived from seawater $\delta^{18}O$ ($\delta^{18}O_{sw}$) and using the modern ALK-S relationship in the SCS. Changes in the SCS surface seawater $\delta^{18}O_{sw}$ are calculated from paired $\delta^{18}O$ and Mg/Ca using the equation of $\delta^{18}O_{sw} = (T - 16.5 + 4.8 * \delta^{18}O_c)/4.8 + 0.27$ [*Bemis et al.*, 1998]. Assuming that in the SCS the modern relationships of $\delta^{18}O_{sw} = 0.35*S - 11.6$ [*Lin et al.*, 2003] and $ALK = 75.8*S - 347.4$ [*Chou et al.*, 2007] is applicable to the past 25ky we then estimate the changes in ALK. Secondly, a constant ALK concentration of 2240 μeq kg^{-1} is applied for the entire record. The reconstructed record suggests that surface salinity in this site increased from about 31.5 at the LGM to 33.5 in the late Holocene, in agreement with previous studies of northern and southern SCS [*Oppo and Sun*, 2005; *Steinke et al.*, 2006]. This change in surface salinity implies that surface ALK was an approximately 150 μmol kg^{-1} lower during the LGM than at present. Comparison of the two model calculations indicates that the uncertainty in ALK estimates, as expressed in the difference between the ALK estimates, leads to an error of <0.04 in pH and ~7 ppmv in pCO_2 estimates (see Figure 5.5c). The reconstructed pH and pCO_2 using different models are in good agreement. The reconstructed record of salinity for Site 1145 suggests that it was ~7% lower during the LGM, which would correspond to a decrease in ALK of ~ 150 μmol kg^{-1}. Although it is still not clear whether ALK can be attained in the northern SCS, true variation in ALK probably lies between the two models.

5.4.4 Uncertainties in estimating pH and pCO_2

Because the down-core records of pH and pCO_2 were reconstructed from seawater $[B(OH)_4^-/HCO_3^-]$, $\delta^{18}O_{sw}$ (from $\delta^{18}O_c$) and ALK (as a function of salinity or constant ALK), it is important to evaluate the sensitivity for changing these parameters in estimation of pH and pCO_2. Using the CO_2sys.xls (Ver. 12, [*Pelletier et al.*, 2005]) and dissociation constants described in Section 5.2.2, we can obtain the average uncertainty in pH and pCO_2 from error propagations of seawater $[B(OH)_4^-/HCO_3^-]$ and estimated ALK. The average errors in seawater $[B(OH)_4^-/HCO_3^-]$ are ±0.001 mol mol^{-1} (corresponding to ±0.010 units in pH and ±10 μatm in pCO_2) caused by K_D (from Mg/Ca-SST) and B/Ca in foraminifera. The average errors in ALK are ±51 μeu kg^{-1} (corresponding to ±0.006 units in pH and ±3 μatm in pCO_2) caused by Mg/Ca and $\delta^{18}O_{cc}$ (assumed $\delta^{18}O_w$-S and ALK-S). The uncertainty of the T and S is ±0.5C (corresponding to ±0.008 units in pH and ±5 μatm in pCO_2) and ±0.60 psu corresponding to ±0.008 units in pH and ±4 μatm in pCO_2), respectively. Combining uncertainties in T, S, ALK and seawater $[B(OH)_4^-/HCO_3^-]$ result in an overall error of pH and pCO_2 is ±0.02 units and ±20 μatm, respectively.

5.4.5 Comparison with U/Ca-derived pH estimates

Foraminiferal U/Ca ratios in *G. ruber* (white) from Site 1145 in the SCS show a significant variation of 6.2- 8.9 nmol mol^{-1}. In general, high U/Ca can be observed during the interglacial intervals and low U/Ca are found during the glacial time. This is identical to the glacial-Holocene difference in U/Ca of *G. sacculifer* from cores CP6001-4 (Caribbean) and EN066-17GGC (eastern equatorial Atlantic), showing that U/Ca ratios in glacial planktonic species, *G. ruber* and *G. sacculifer*, was approximately 25% lower than Holocene values, corresponding to difference of 80 to 110 μmol kg^{-1} in

$[CO_3^{2-}]$ [*Russell et al.*, 1996]. In the SCS core, mean U/Ca in Holocene *G. ruber* is ~30% higher than mean U/Ca from glacial specimens, indicating a relatively larger variation in surface pH (or pCO_2) than both the Atlantic and Caribbean cores over the glacial-interglacial cycles. Although the correlation of U/Ca and Mg/Ca in down-core samples of *G. ruber* shows a positive linear relationship ($r^2= 0.53$), no temperature dependence on shell U/Ca can be observed based on previous studies in cultured and core-top planktonic foraminifera [*Russell et al.*, 1994, 2004]. Glacial-interglacial changes (~1-2‰) in regional salinity may be taken into account for U/Ca variations, however, more detailed investigations on the effect of salinity on shell U/Ca are necessary to further understand its potential influence.

The utility of foraminiferal U/Ca in *G. ruber* (white) at Site 1145 can provide additional evidence to test the approach of B/Ca-derived pH by independently calculating seawater pH according to the U/Ca-pH relationship in cultured planktonic foraminifera [*Russell et al.*, 2004]. Although there is no available empirical U/Ca-pH equation for *G. ruber*, the first approach at calculating seawater pH has been made by using the *O. universa* U/Ca-pH exponential relationship, $U/Ca= 2.20*10^5 \exp(-1.23* pH)$, taken from *Russell et a*l. [2004]. Figure 5.6 shows a comparison of the pH dependence on shell U/Ca between down-core *G. ruber* U/Ca in this study, $U/Ca= 1.20*10^5 \exp(-1.16* pH)$, and *O. universa* from culturing experiments [*Russell et al.*, 2004]. The similar slope suggests that two planktonic species, *G. ruber* and *O. universa*, have the same pH sensitivity. However, the significant offset between these two species imply the need for species-specific calibration to obtain the accurate oceanic pH values. Because the sediment cores of the SCS have large amounts of continental inputs, U/Ca may be strongly affected by U incorporation into Mn oxides and secondary carbonates. However, there is no positive correlation observed in all sections of Site 1145, and therefore the potential influence of Mn overgrowths can be ruled out.

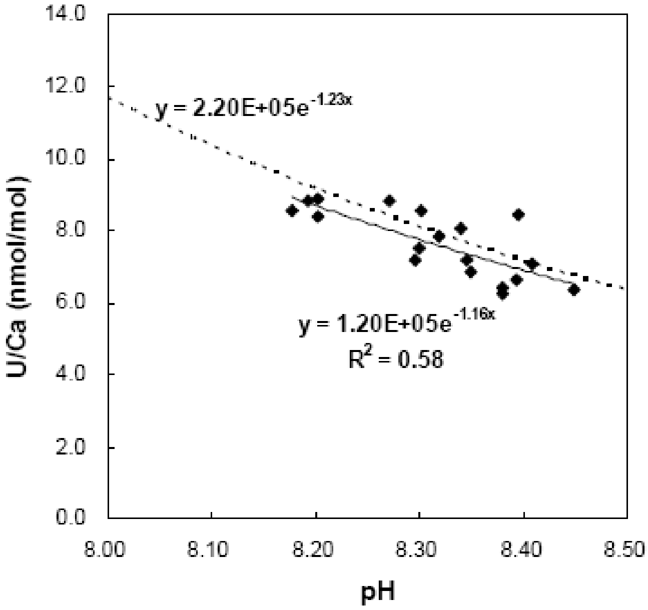

Figure 5.6 A comparison of the U/Ca-pH relationship between down-core foraminiferal U/Ca in *G. ruber* presented here and *O. universa* from the culturing experiment [*Russell et al.*, 2004]. Solid line shows a best regression of down-core U/Ca and B/Ca-derived pH. Dashed line indicates a dependence of culturing shell U/Ca in *O. universa* on seawater pH [*Russell et al.*, 2004].

5.5 Paleoceanographic Implication

5.5.1 Paleo-pH variability in the northern SCS across Termination I

Changes in surface-ocean pH in the SCS across Termination I were estimated using paired Mg/Ca and B/Ca ratios measured in *G. ruber* (white) from Site 1145 in the northern SCS, and had been shown in Figure 5c. The calculated pH value during Late Holocene (~3 ka B.P.) is 8.13±0.02, which is slightly higher than modern annual mean seawater pH of ~ 8.07 at depths of 0-20 m [*Chou et al.*, 2006]. This difference could be linked to an abrupt increase in atmospheric CO_2 concentration and ocean acidification over the past several decades caused by anthropogenic CO_2 increases in the oceans (e.g., [*Chen et al.*, 2006]).

During the last deglaciation, seawater pH values gradually increased from Late Holocene to the LGM (3-22 ka BP). The oceanic pH record shows high values at the glacial intervals and low during the interglacial times. The pH contrast in the northern SCS reveals a change of 0.30 (±0.02, error propagations were calculated based on Section 5.4.4) across Termination I (Figure 5.5c). In addition, the reconstruction of seawater pH records derived from U/Ca ratio in *G. ruber* over the past 22 ka indicates that the change in seawater pH is around 0.3 pH units (Figure 5.5d). The difference in absolute values of reconstructed pH between foraminiferal B/Ca- and U/Ca-based estimations can be attributed to differences in cultured planktonic species used for obtained the U/Ca-pH relationship.

Using the above multi-proxy approach, it can further confirm that the oceanic pH variation in the SCS is significantly larger than those previously determined glacial-interglacial pH differences of 0.18 (±0.03) from eastern equatorial Atlantic [*Hönisch and Hemming*, 2005] and 0.2 (±0.1) from Southern Ocean [*Sanyal et al*., 1995] based on *G. sacculifer* δ^{11}B data, as well as more recently, 0.15 units in Southern Ocean using B/Ca in subsurface-dwelling planktonic foraminifera [*Yu et al*., 2007]. A larger LGM-Late Holocene pH difference in the northern SCS is most likely due to the fact that the regional primary productivity were enhanced by the prevailing winter monsoon at the glacial periods, especially during the LGM. This speculation is in a good agreement with published productivity records in the SCS such as results of alkenone concentrations [*Kienast et al*., 2001] and the chlorin accumulation rate [*Higginson et al*., 2003]. High productivity caused by an increase in regional dust supply and upwelling during the glacial intervals could stimulate the activity of photosynthesis in the surface ocean, which in turn resulted in an increase in oceanic pH value (or a dramatic reduction of sea surface pCO_2). Therefore, the variability in the efficiency of biological bump through time likely played a significant role in accounting for abrupt changes in surface oceanic pH, especially for those climate-sensitive marginal seas.

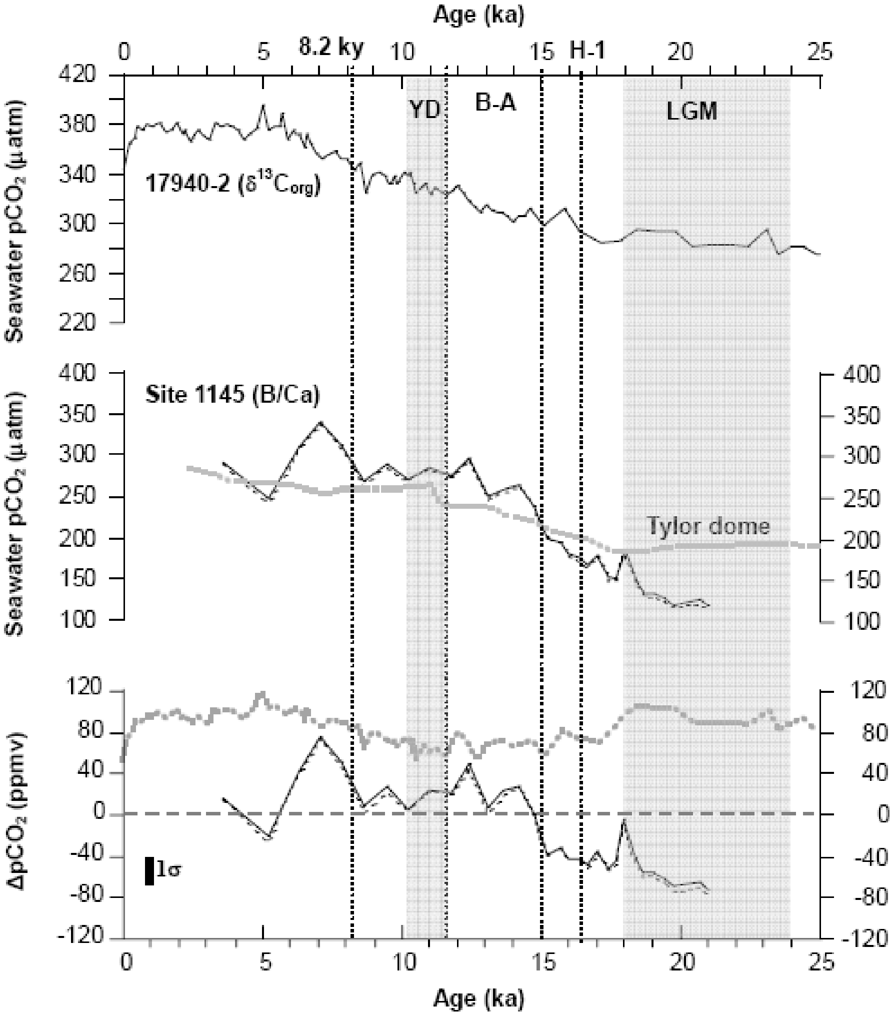

Figure 5.7 (a) Past oceanic pCO_2 records based on the sedimentary $\delta^{13}C_{org}$ in the northern SCS over the past 21,000 yr B.P. (b) Seawater pCO_2 records reconstructed from G. ruber B/Ca ratios across Termination I. Note that the thick gray dashed line shows the variation of atmospheric pCO_2 concentration recorded in air bubbles in Tylor dome, Antarctica. Thin gray line (in fig. 7b and 7c) represents a B/Ca-based seawater pCO_2 record attained by constant ALK at 2240 μeq/kg. (c) Calculated ΔpCO_2 ($=pCO_{2seawater}-pCO_{2atmosphere}$) in the northern SCS. When $\Delta pCO_2>0$ indicates that the ocean serves as a source for CO_2 relative to the atmosphere; $\Delta pCO_2<0$ indicates that the ocean is a sink relative to the atmosphere. Error bar is also shown based on the estimations of uncertainties in section 5.4.4.

5.5.2 Past surface-ocean pCO_2 records in the SCS

Fig. 6 illustrates the reconstructed pCO_2 data collected in this study, as well as the atmospheric pCO_2 record of the Tylor Dome ice core in the Antarctica and seawater pCO_2 estimates from marine sedimentary $\delta^{13}C_{org}$ in the northern SCS (Figure 5.7a, [*Kienast et al.*, 2001]). The pCO_2 value of the late Holocene is ~283±20 ppmv (Figure 5.7b), similar to the pre-industrial atmospheric pCO_2 value (280 μatm). This is in an agreement with the modern situation in the SCS, showing a weak CO_2 source or nearly equilibrium between aqueous and atmospheric pCO_2 in the SCS [*Chen et al.*, 2006].

In comparison with paleo-pCO_2 records reconstructed from marine sedimentary $\delta^{13}C_{org}$ (assuming 0% terrigenous C_{org} contribution) in the northern SCS [*Kienast et al.*, 2001], a significant discrepancy in the absolute values of pCO_2 can be clearly observed for the last 22 ka (see Figure 5.7). *Kienast et al.* [2001] has suggested that the SCS is a considerable CO_2 sink during glacial times and alternatively, a strong source during interglacial times. However, the SCS pCO_2 estimates in the Late Holocene (or the pre-industrial period) suggest that sea surface pCO_2 values were persistently higher than atmospheric CO_2 concentration recorded in trapped air by around 100 ppm. This is in conflict with the current understanding of the SCS oceanography, showing the near ocean-atmosphere equilibrium is reached in the modern SCS [*Chen et al.*, 2006; *Chou et al.*, 2005]. The possible interpretation is most likely due to the contribution of the terrestrial organic matter to the bulk C_{org} throughout the records. An admixture of only 10-15% terrestrial C_{org} ($\delta^{13}C_{org}$ ca. -26‰) would decrease the CO_2 concentration estimates from supersaturated to equilibrium values [*Kienast et a*l., 2001]. Therefore, the influences of the C_{org} flux in the SCS should have a profound effect on the estimation of absolute pCO_2 from marine $\delta^{13}C_{org}$. Based on the above discussion, we suggest that our pCO_2 approach seems to be more appropriate and reliable than $\delta^{13}C_{org}$-based pCO_2 records in the SCS.

The calculated pCO_2 values in the northern SCS reveals that the LGM surface pCO_2 (~130±20 ppmv) was approximately 150 ppmv lower than the Holocene (~284±20 ppmv) (Figure 5.7b). The amplitude of the seawater pCO_2 variability is much larger than a ~90 ppmv change in atmospheric CO_2 observed in high-latitude ice cores. As discussed in Section 5.5.1, enhanced primary productivity in the SCS during the

LGM could be attributed to this rapid change in surface-ocean pCO_2. Additionally, the nature of pCO_2 in the surface ocean shows more variability than atmospheric gas records (Figure 5.7b). This is probably related to well-mixed and near homogeneous nature of the atmospheric gases.

The difference (ΔpCO_2) between the calculated surface-ocean and atmospheric CO_2 values has been shown in Figure 5.7c, and provides a clear pattern regarding the role of the surface SCS as a CO_2 source or sink relative to atmosphere through time. Several scenarios of seawater pCO_2 variations can be observed in the northern SCS. Our B/Ca-based pCO_2 records indicate a rapid increase in surface-ocean CO_2 concentration relative to a slow increase in atmospheric CO_2 at the interval from the LGM (~21.4 ka B.P.) to the start of the Younger Dryas (YD, ~11.7 ka B.P.). At the time of ~15 ka B.P., correlates with the Bølling-Allerød (B-A) transition, seems to be an important turning point that the condition of the ΔpCO_2 in the northern SCS dramatically change from a significant CO_2 sink ($\Delta pCO_2<0$, during the interval of ~21.4 to 15 ka B.P.) toward a near equilibrium or CO_2 source compared to the atmosphere ($\Delta pCO_2=0$, from ~15 ka B.P. to present day). The interval of ~6 to 8 ka B.P., following the 8.2 ka cooling event, is marked by surface-ocean pCO_2 that is substantially higher (ΔpCO_2~+80 ppmv) than those in the contemporaneous atmosphere. Because the overall uncertainty in ΔpCO_2 values from other contributing variables (temperature, salinity, ALK and seawater $[B(OH)_4^-/HCO_3^-]$) is about ±20 ppmv, so that the relatively high CO_2 levels in surface SCS during the interval of ~8.2 to 6 ka B.P. Further studies are needed to reconstruct more high-resolution seawater pH or pCO_2 records in order to better constrain the potential influence of such abrupt climatic events (such as YD and B-A) on the regulation of Earth’s climate system through the ocean-atmosphere interaction.

5.6 Conclusions

Results from core-top sediments in the South China Sea demonstrate that B/Ca ratios in the three planktonic foraminiferal species are strongly affected by seawater temperature and pH. Species-specific foraminiferal B/Ca ratios from core-top sediments are in equilibrium with ambient seawater [$B(OH)_4^-/HCO_3^-$] in response to their habitat depths in the modern water column, indicating shell B/Ca can be used as a reliable paleo-pH proxy by applying the dissolution-corrected Mg/Ca-derived SST and K_D of B/Ca. Furthermore, in comparison with the previous study in north Atlantic, a significantly different relationship between K_D and seawater temperature for *G. ruber* (white) can be observed, and B/Ca ratios in foraminiferal shell calcites are not affected by partial dissolution even at such a strong dissolution region.

Using a multi-proxy approach in planktonic foraminifera, the pH and pCO_2 reconstructions at Site 1145 indicate that the variability of surface-ocean pCO_2 shows a more variability than atmospheric CO_2 records, and the ocean-atmosphere CO_2 flux has substantially changed with time in the SCS. The pCO_2 (or pH) in glacial surface waters was approximately 150 ppmv lower (or 0.3 pH units higher) than the Holocene. This amplitude in surface-water pCO_2 is significantly larger than changes in atmospheric pCO_2 recorded in the ice cores (~ 90 ppmv), and changes estimated from elevated glacial pH based on boron isotopes in the eastern equatorial Atlantic [*Sanyal and Bijma*, 1999; *Hönisch and Hemming*, 2005] and B/Ca ratios in Southern Ocean [*Yu et al.*, 2007]. This observation indicates that this area was a strong CO_2 sink to the atmosphere at the LGM, and presumably reflects a significant increase in regional primary productivity in the north SCS during the LGM.

References

Anand, P., Elderfield, H., Conte M. H., 2003. Calibration of Mg/Ca thermometry in planktonic foraminifera from sediment trap time series. Paleoceanography 18, 1050- 1065.

Al-Ammar, A., Gupta, R. K., Barnes, R. M., 1999. Elimination of boron memory effect in inductively coupled plasmas-mass spetrometry by addition of ammonia. Spectrochim. Acta Part B 54, 1077-1084.

Barker, S., Elderfield, H., 2002. Foraminiferal calcification response to glacial-interglacial changes in atmospheric CO_2. Science, 297, 833-836.

Bemis, B. E., Spero, H. J., Bijma, J., Lea D. W., 1998. Reevaluation of the oxygen isotopic composition of planktonic foraminifer: Experimental results and revised paleotemperature equations. Paleoceanography 13, 150-160.

Boyle, E. A., Keigwin, L. D., 1985/1986. Comparison of Atlantic and Pacific paleochemical records for the last 215, 000 years: Changes in deep ocean circulation and chemical inventories. Earth Planet. Sci. Lett. 76, 135-150.

Chen, C.-T. A., Wang, S.-L., Chou, W.-C., Sheu, D. D., 2006. Carbonate chemistry and projected future changes in pH and CaCO3 saturation of the SCS. Marine Chem. 101, 277-305.

Chou, W. C., Sheu, D. D., Chen, C.-T. A., Wang, S. L., Tseng, C. M., 2005. Seasonal variability of carbon chemistry at the SEATs time series site, northern South China Sea between 2002 and 2003. T. A. O. 16, 445-465.

Clark, D., Hobart, D. E., Neu, M. P., 1995. Actinide carbonate complexes and their importance in actinide environmental chemistry. Chem. Rev., 95, 25-48.

Dickson, A. G., Millero, F. J., 1987. A comparison of the equilibrium constants for the dissociation of carbonic acid in seawater media. Deep Sea Res. Part A 34, 1733-1743.

Dickson, A. G., 1990. Thermodynamics of the dissociation of boric-acid in synthetic seawater from 273.15-k to 318.15k. Deep Sea Res. Part A 37, 755-766.

Djogic, R., Sipos, L., Branica, M., 1986. Characterization of uranium (VI) in seawater. Limnol. Oceanogr. 31, 1122-1131.

Elderfield, H., Ganssen G., 2000. Reconstruction of temperature and $\delta^{18}O$ of surface ocean waters using Mg/Ca of planktonic foraminiferal calcite. Nature 405, 442-445.

Feely, R. A., Sabine, C. L., Lee, K., Berelson, W., Kleypas, J., Fabry, V. J., Millero, F. J., 2004. Impact of anthropogenic CO_2 on the $CaCO_3$ system in the oceans. Science 305, 362-366.

Hemming, G. N., Hanson, G. N., 1992. Boron isotopic composition and concentration in modern carbonates. Geochim. Cosmochim. Acta 56, 537-543.

Higginson, M. J., Maxwell, J. R., Altabet, M. A., 2003. Nitrogen isotope and chlorine paleoproductivity records from the northern South China Sea: Remote vs. local forcing of millennium- and orbital-scale variability. Marine Geol. 201, 223-250.

Hönisch, B., Hemming, N. G., 2005. Surface ocean pH response to variations in pCO_2 through two full glacial cycles. Earth Planet. Sci. Lett. 236, 305-314.

Huang, K.-F., You, C.-F., Lin, H.-L., Shieh, Y. T., 2007. In situ calibration of Mg/Ca ratio in planktonic foraminiferal shell using time-series sediment trap: A case study of intense dissolution artifact in the South China Sea. (Submitted to Geochem. Geophys. Geosyst).

Kienast, M., Calvert, S. E., Pelejero, C., Grimalt, J. O., 2001. A critical review of marine sedimentary $\delta^{13}C_{org}$-pCO_2 estimates: New palaeo-records from the South China Sea and a revisit of the other low-latitude $\delta^{13}C_{org}$-pCO_2 records. Global Biogeochem. Cycles 15, 113-127.

Kienast, M., Hanebuth, T. J., Pelejero, C., Steinke, S., 2003. Synchrononeity of meltwater pulse 1a and the Bøiling warming: New evidence from the South China Sea. Geology 31, 67-70.

Lea, D. W., Boyle E. A., 1993. Determination of carbonate-bound barium in corals and foraminifera by isotope dilution plasma mass spectrometry. Chem. Geol. 103, 73-84.

Lea, D. W., Pak, D. K., Spero, H. J., 2000. Climate impact of late Quaternary equatorial Pacific sea surface temperature variations. Science 289, 1719-1724.

Lewis, E., Wallace, D. W. R., 1998. Program developed for CO_2 system calculations, Rep. ORNL/CDIAC-105, Carbon Dioxide Ind. Anal. Cent. Oak Ridge Natl. Lab. U. S. Dept. of Energy, Oak Ridge, Tenn.

Leeman, W. P., Vocke, R. D., Beary, E. S., Paulsen, P. J., 1991. Geochim. Cosmochim. Acta 55, 3901-3907.

Lemarchand, D., Gaillardet, J., Lewin, E., Allegre, C. J., 2002. An optimized procedure for boron separation and mass sprectrometry for river water samples. Chem. Geol. 182, 323-334.

Lin, I.-T., Wang, C.-H., Lin, S., 2003. Seasonal variations of oxygen isotopic compositions in the Pingtung coastal waters of Taiwan. Western Pacific Earth Science 3, 21-32.

Mehrbach, C., Culberso, C. H., Hawley, J. E., Pytkowic, R. M., 1973. Measurement of apparent dissociation-constants of carbonic-acid in seawater at atmospheric- pressure. Limnol. Oceanogr. 18, 897-907.

NODC (Levitus) World Ocean Atlas 1998. Provided by the NOAA/OAR/ESRL PSD, Boulder, Colorado, USA.

O'Neil, J. R., Clayton, R. N., Mayeda, T. K., 1969. Oxygen isotope fractionation in divalent metal carbonates. The Journal of Chemical Physics 51, 5547-5558.

Oppo, D. W., Sun, Y., 2005. Amplitude and timing of sea-surface temperature change in the northern South China Sea: Dynamic link to the East Asian Monsoon. Geology 33, 785-788.

Pak, D. K., Lea, D. W., Kennett, J. P., 2004. Seasonal and interannual variation in Santa Barbara Basin water temperatures observed in sediment trap foraminiferal Mg/Ca. Geochem. Geophys. Geosyst. 5, doi:10.1029/2004GC000760.

Palmer, M. R., Swihart, G. R., 1996. Boron isotope geochemistry: an overview. In: Crew, E. S., Anovitz, L. M. (Eds.), Boron: Mineralogy, Petrology and Geochemistry. Mineral. Soc. Am., 33, 709-744.

Palmer, M. R., Pearson, P. N., Cobb, S. J., 1998. Reconstructing past ocean pH-depth profiles. Science 282, 1468-1471.

Palmer, M. R., Pearson, P. N., 2003. A 23,000-year record of surface water pH and pCO_2 in the western Equatorial Pacific Ocean. Science 300, 480-482.

Pearson, P. N., Palmer, M. R., 2000. Atmospheric carbon dioxide concentrations over the past 60 million years. Nature 406, 695-699.

Pelejero, C., Grimalt, J. O., Heilig, S., Kienast, M., Wang, L., 1999. High resolution U^k_{37}-temperature reconstructions in the South China Sea over the last 220 kyrs. Paleoceanography 14, 224-231.

Pelletier, G. E., Lewis, E., Wallace, D., 2005. A calculator for the CO_2 system in seawater for Microsoft Excel/VBA, report, Wash. State Dept. of Ecol., Olympia.

Reeder, R. J., Nugent, M. L., Lamble, G. M., Tait, C. D., Morris, D. E., 2000. Uranyl incorporation into calcite and aragonite: XAFS and luminescence studies. Environ. Sci. Technol. 34, 638-644.

Rosenthal, Y., Boyle, E. A., Slowey. N., 1997. Environmental controls on the incorporation of Mg, Sr, F and Cd into benthic foraminifera shells from Little Bahama Bank: Prospects for thermocline paleoceanography. Geochim. Cosmochim. Acta 61, 3633-3643.

Rosenthal, Y., Field, M. P., Sherrell, R. M., 1999. Precise determination of element/calcium ratios in calcareous sample using sector field inductivity coupled plasma mass spectrometry. *Anal. Chem.*, *71*, 3248-3253.

Rosenthal, Y., Lohmann, G. P., Lohmann, K. C., Sherrell, R. M., 2000. Incorporation and preservation of Mg in *Globigerinoides sacculifer*: Implication for reconstructing the temperature and $^{18}O/^{16}O$ of seawater. Paleoceanography 15, 135-145.

Rosenthal, Y., Lohman, G. P., 2002. Accurate estimation of sea surface temperatures using dissolution- corrected calibrations for Mg/Ca paleotemperature. Paleoceanography 17, 3, 1044.

Russell, A. D., Emerson, S. R., Nelson, B. K., Erez, J., Lea, D. W., 1994. Uranium in foraminiferal calcite as a recorder of seawater uranium concentrations. Geochim. Cosmochim. Acta 58, 671-681.

Russell, A. D., Emerson, S., Mix, A. C., Peterson, L. C., 1996. The use of foraminiferal U/Ca as an indicator of changes in seawater U content. Paleoceanography 11, 649-663.

Russell, A. D., Hönisch, B., Spero, H. J., Lea, D. W., 2004. Effects of seawater carbonate ion concentration and temperature on shell U, Mg, and Sr in cultured planktonic foraminifera. Geochim. Cosmochim. Acta 68, 4347-4361.

Sanyal, A., Hemming, N. G., Hanson, G. N., Broecker, W. S., 1995. Evidence for a higher pH in the glacial ocean from boron isotopes in foraminifera. Nature 373, 234-236.

Sanyal, A., Hemming, N. G., Broecker, W. S., Hanson, G. N., 1997. Changes in pH in the eastern equatorial Pacific across stage 5-6 boundary based on boron isotopes in foraminifera. Global Biogeochem. Cycles 11, 125-133.

Sanyal, A., Bijma, J., 1999. A comparative study of the northwest Africa and eastern equatorial Pacific upwelling as a source of CO_2 during glacial periods based on boron isotope paleo-pH estimation. Paleoceanography 14, 753-759.

Shackleton, N. J., 1974. Attainment of isotopic equilibrium between ocean water and the benthic foraminiferal genus Uvigerina: Isotopic changes in the ocean during the last glacial. Cent. Natl. Rech. Sci. Colloq. Int. 219, 203-209.

Shaw, P.-T., 1991. The seasonal variation of the intrusion of the Phillippine Sea Water into the South China Sea. J. Geophys. Res. 96, 821-827.

Spivack, A. J., You, C.-F., Smith, H. J., 1993. Foraminiferal boron isotope ratios as a proxy for surface ocean pH over the past 21 Myr. Nature 363, 149-151.

Steinke, S., Chiu, H.-Y., Yu, P.-S., Shen, C.-C., Erlenkeuser, H., Löwemark, L., Chen, M.-T., 2006. On the influence of sea level and monsoon climate on the southern South China Sea freshwater budget over the last 22,000 years. Quaternary Science Reviews 25, 1475-1488.

Takahashi, T. et al., 2002. Global sea-air CO_2 flux based on climatological surface ocean pCO_2, and seasonal biological and temperature effects. Deep-Sea Research II 49, 1601-1622.

Thomas, H., Bozec, Y., Elkalay, K., de Baar, H. J. W., 2004. Enhanced open ocean storage of CO_2 from shelf sea pumping. Science 304, 1005-1008.

Wang, L., Sarnthein, M., Erlenkeuser, H., Grimalt, J., Grootes, P., Heiling, S., Ivanova, E., Kienast, M., Pelejero, C., Pflaumann, U., 1999. East Asian monsoon climate during the Late Pleistocene: high-resolution sediment records from the South China Sea. Mar. Geol. 156, 245-284.

Wara, M. W., Delaney, M. L., Bullen, T. D., Ravelo, A. C., 2003. Possible roles of pH, temperature, and partial dissolution in determinating boron concentration and isotopic composition in planktonic foraminifera. Paleoceanography 18, doi:10.1029/2002PA000797.

Wyrtki, K., 1961. Physical Oceanography of the Southeast Asian Waters, in *Scientific Results of Marine Investigations of the South China Sea and the Gulf of Thailand, NAGA Rep*., vol. 2, 195 pp., Scripps Instit. of Oceanogr., La Jolla, Calif.

Yu, J., Elderfield, H., Hönisch, B., 2007. B/Ca in planktonic foraminifera as a proxy for surface seaawater pH. Paleoceanography 22, doi:10.1029/2006PA001347.

CHAPTER 6.

Boron Isotopic Composition in the Planktonic Foraminifera and Seawater: Calibration and Paleo-application

6.1 Introduction

The element boron (B) has two stable isotopes, ^{10}B and ^{11}B, with relative abundance of 19.9% and 80.1%, respectively [*Nuclides and Isotopes*, 1996], leading to an ^{11}B/^{10}B ratio of about 4 in most natural materials. The mass difference of ~ 10% makes B isotopic system become a potential tool to unravel mechanisms that cause mass-dependent fractionation in natural samples. It was well-known that marine system constitutes a major reservoir for B [*Ishikawa and Nakamura*, 1993]. Sources of B include seawater (~39.5‰), adsorbed B (~-15‰), lattice-bound B (~-5‰, [*Spivack and Edmond*, 1987]), and marine carbonates (~20‰, [*Vengosh et al.*, 1991]).

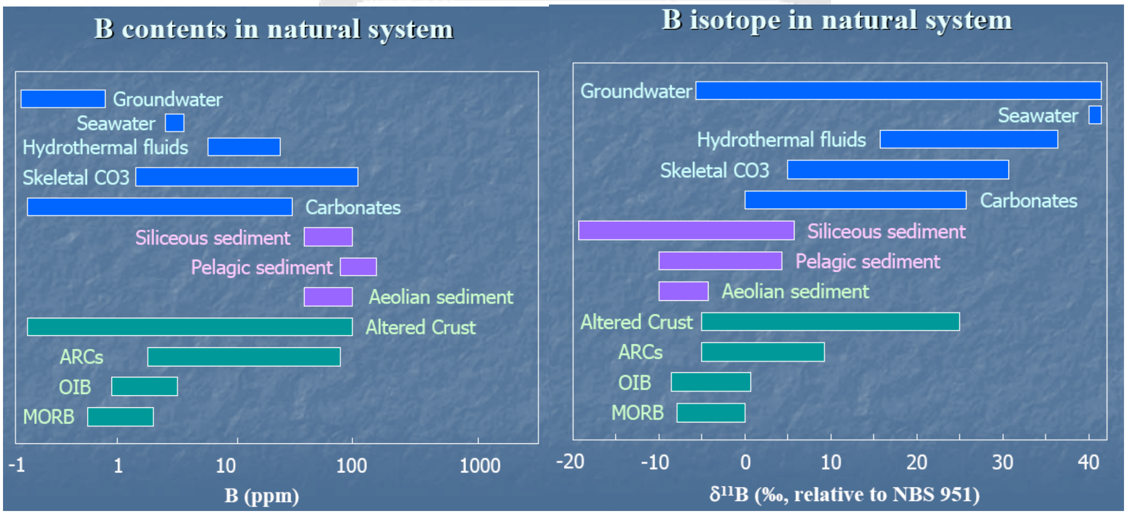

Figure 6.1 Comparisons of B and δ^{11}B values in natural samples (modified after [Palmer and Swihart, 1996])

The potential of B as a useful tracer has recently become apparent due to it is highly volatile, particularly at elevated temperature (e.g., [*You et al.*, 1996a, b]), and its high solubility in aqueous fluids, high magmatic incompatibility, as well as relatively large isotopic fractionation (ca. 70‰, Figure 6.1). In the subduction zone, its geochemical behavior can be used as tracers for the deep fluids [*Brumsack and Zuleger*, 1992]. Furthermore, it has been shown that the B isotope signature can reflect the recycling of subducted materials and altered oceanic crust at convergent margins [*You et al.*, 1993a, b; Ishikawa and Nakamura, 1993; *You et al.*, 1994, see Figure 6.2].

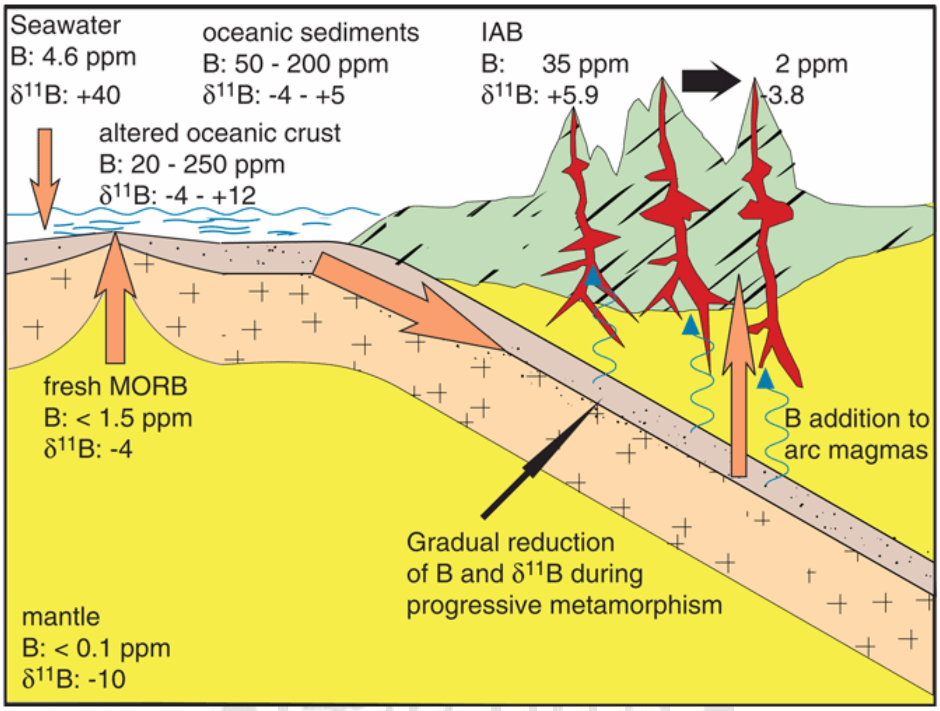

Figure 6.2 The B isotopic compositions of various reservoirs in the subduction zone.

The dominant dissolved species of B in seawater are $B(OH)_3$ and $B(OH)_4^-$ (p*K*= 8.830 at 25°C, [*Hershey et al.*, 1986]). The relative proportion of these two species is a function of pH and can be given by the equilibrium reaction:

$$B(OH)_3 + H_2O = B(OH)_4^- + H^+$$

In principle, p*K* increases with increasing temperature, i.e., the $B(OH)_4^-/B(OH)_3$ decreases with increasing temperature. For the fluids with ionic strength greater than that of seawater, the $B(OH)_4^-/B(OH)_3$ decreases with increasing ionic strength [*Hemming and Hanson*, 1992]. At low pH values, $B(OH)_3$ is the dominant species, conversely, at high pH, virtually all of the B is in the $B(OH)_4^-$ species (Figure 6.3a).

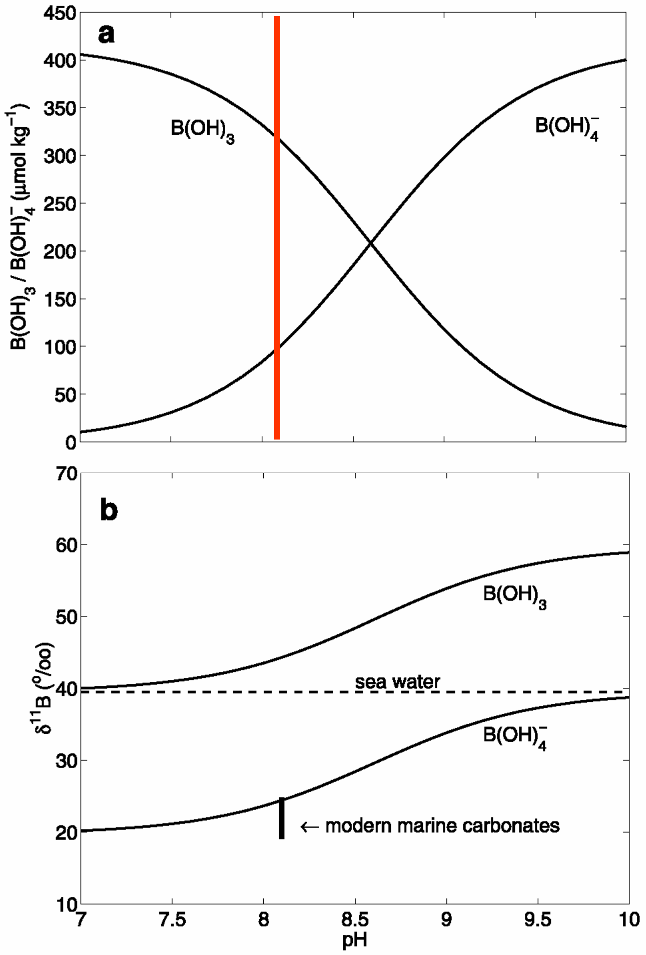

Figure 6.3 Distributions of (a) boron-species $B(OH)_3$ and $B(OH)_4^-$, and (b) boron isotopic composition versus pH in aqueous solutions (after [*Hemming and Hanson*, 1992]). Note that the red line presents modern seawater pH (~8.2), and the $\delta^{11}B$ of modern carbonates fall into the theoretical line of $B(OH)_4^-$ species.

Because ^{11}B preferentially enters the trigonal $B(OH)_3$-species (probably BO_3^{3-} in minerals) and ^{10}B enters tetrahedral $B(OH)_4^-$-species (probably BO_4^{5-} in minerals). The isotope exchange between these two species is given by:

$$^{10}B(OH)_3 + {}^{11}B(OH)_4^- = {}^{11}B(OH)_3 + {}^{10}B(OH)_4^-$$

where K= 1.0194 at 25°C [*Kakihana et al.*, 1977]. The temperature effect on the K value is rather small (K= 1.0206 at 0°C and K= 1.0177 at 60°C). Figure 6.3 shows the theoretical distribution of boron species and the isotope exchange reaction as a function of pH for seawater.

In the past the applications of B and B isotopes in the fields of Earth Sciences were mainly limited by problems with separation B from major matrix without influencing its isotopic composition, and the low analytical precision of mass spectrometric techniques [*Vengosh et al.*, 1989; *Hemming and Hanson*, 1992]. Therefore, to obtain meaningful results, it is imperative that sample preparation is performed properly and the high-precision measurement of B isotopes is needed to be developed.

Recently, due to the advances in analytical technologies, interest has been raised in bringing boron isotopes into geosciences, oceanography as well as environmental sciences [*Gallardet and Allègre*, 1995; *Barth*, 1997; *Sanyal et al.*, 1997; *Gäbler and Bahr*, 1999; *Pearson and Palmer*, 2000; *Lemarchand et al.*, 2000; *Rose et al.,* 2000; *Barth*, 2000; *Hogan and Blum*, 2003; *Hönisch and Hemming*, 2004]. Among these researches, boron isotopic compositions in foraminifera have been proposed as a reliable paleo-pH or pCO_2 proxy in the past ocean. The principle of the use of foraminiferal B isotope is based on the pH-dependence on the proportion of the two dissolved B species, and the preferential incorporation of $B(OH)_4^-$ into marine carbonates (Figure 6.3a). Combining with other environmental proxies (e.g., alkalinity, which can be obtained by a combination of foraminiferal $\delta^{18}O$-based sea surface salinity (SSS) records and the relationship between SSS-alkalinity), changes in oceanic pH or pCO_2 for glacial-interglacial cycles and longer time-scale variation can be reconstructed to further understand the mechanisms that control the Earth's climate [*Spivack et al.*, 1993; *Sanyal et al.*, 1997; *Palmer et al.*, 1998; *Sanyal and Bijma*, 1999; *Palmer and Pearson*, 2003; *Hönisch and Hemming*, 2005].

Although a growing body of paleoceanographic records has been established during the past decade, however, a more precise determination on B isotopes is still necessary to be achieved due to a fairly small B isotopic variability in fossil foraminifera (i.e., less than 3‰ during the glacial-interglacial cycle). The main goal of this chapter is to develop high-precision B isotopic analyses and effectively chemical separation for various types of natural samples. To achieve this, a variety of reference materials (e.g., NIST SRM 951), international seawater standards (i.e., NASS-5 and IAPSO) and well-mixed core-top planktonic foraminifera, as well as modern corals are used to control the whole analytical procedure for B isotopic analyses.

6.2 Reagents and Laboratory Equipment

Water

The water used in this study was de-ionized and purified with a mixed-bed resin and filtered by new generation Milli-Q water system (Millipore®, 18.2 MΩ). The specific water purification chain comprises a series combination of purification technologies: [1] Elix 10 system, making up of a pretreatment filter, a reverse osmosis membrane and an electro-deionization module; [2] Mili-Q Element System, to remove any remaining trace contaminants; [3] Q-Gard B1 containing boron specific ion exchange resin (Amberlite IRA 743) and mixed-bed ion exchange resin, effectively remove B and Si. The boron concentration of this ultrapure water is less than 13 ppt (ng/L).

Nitric and hydrochloric acid

Reagent grade 65% HNO_3 (Merck®) and 33% HCl (Merck®) were purified by doubly or triply sub-boiling distillation and Vycor sub-boiling system at NCKU. For HCl, two-bottle technique was also applied to reduce the B blank after the sub-boiling due to its highly volatile behavior. The prepared HNO_3 and HCl usually have a concentration of 12.5-13.2 M and 6.4-6.8 M, respectively, and their B content were comparable to commercial ultrapure-grade reagents (BASELINE, SEASTAR®). The boron concentrations of these two prepared acids are less than 20 ppt (ng/L), and the different molarities of acids were prepared by dilution with ultrapure water.

Other organic and inorganic reagents

All organic solvents (ethanol, methanol, and mannitol) were of commercial high purity grade. In order to reduce the boron blank in the chemical procedure, all these reagents were further purified through the column chemistry or two-bottle system. D (-) -Mannitol (high-purity grade, Merck®), (CH_2OH-$(CHOH)_4$-CH_2OH), were directly purified by the boron specific anion resin Amberlite IRA 743 (20-50 mesh, Sigma®); Ethanol (Analytical grade, 99.7-100%, Merck®) was purified by the two-bottle technique at < 50°C; High-purity graphite (99.9999%, Alfa Aesar®, ~200 mesh) is added to a mixture of 80% ethanol and 20% H_2O to obtain a solution corresponding to 13 mg/g graphite slurry. Organic reagent blanks were lower than 0.5 ppb (ng/mL), and their contribution can be negligible given the amount of boron used in the experiments.

CsOH solution was made by analytical grade (Sigma®) CsOH with ultrapure water, and then purified by the boron specific anion resin Amberlite IRA 743; NH_4OH, 0.3M, was made by two-bottle system and was purified by exchanging with Amberlite IRA 743; NaOH, 0.5M, solution was purified by exchanging with Amberlite IRA 743; NaCl powder was dissolved in water to obtain 0.6M solution and adjusted to pH= 8 by additions of 0.5M B-free NaOH.

Beaker, bottle and ware

Precaution must be taken to use only Teflon- and polypropylene (PP)-ware during the entire sample preparation. Because common laboratory glassware usually contain significant amounts of boron that can be easily leached by acidic sample solutions, it should be avoided the use of any glass container. The use of HNO_3 is to be avoided when cleaning beakers due to potential isobaric interferences at mass 42 and mass 308 (CNO^- or Cs_2CNO^+) during the N-TIMS and P-TIMS measurements. The Teflon- and PP-ware and Savillex® beaker cleaning were conducted with 6N HCl on a hot bath of <100°C. The equipments were then rinsed with water for three times to remove HCl and stored in acid-leached plastic boxes.

6.3 Column Chemistry

6.3.1 The characteristics of Amberlite IRA 743 resin

In previous studies on B isotopes in natural samples, the extraction of B from other elements was mainly accomplished by anion exchange resin, Amberlite IRA 743 (also called XE-23) produced by Rohm and Hass Co.. The resin consists of an N-methylglucamine group fixed on a polystyrenic backbone. The tertiary amine is a weak base with a $pK_A \sim 7$ [*Pinon et al.*, 1968]. Consequently, the resin behaves as an anion exchanger at pH< 7. Based on the study of *Pinon et al.* [1968], B is strongly adsorbed onto the alcohol groups of glucamine for pH values from neutral to base, following the reaction:

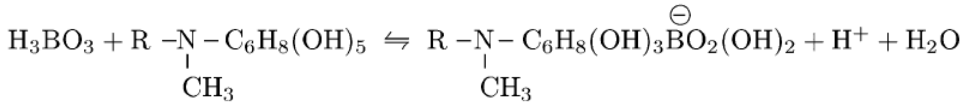

$$H_3BO_3 + R-\underset{CH_3}{\underset{|}{N}}-C_6H_8(OH)_5 \rightleftharpoons R-\underset{CH_3}{\underset{|}{N}}-C_6H_8(OH)_3\overset{\ominus}{B}O_2(OH)_2 + H^+ + H_2O$$

A theoretical capacity of Amberlite IRA 743 is ~5.7 mg B/mL, which is given by Rohm and Hass Co.. *Pinon et al.* [1968] demonstrated that the capacity of B for Amberlite IRA 743 depends on the B contents of the exchanging solution and showed a linear relationship. They proposed a B capacity of 4.9 mg B/mL for a diluted solution, and up to 15 mg B/mL for boron solution of 0.7 M. *Kiss* [1988] and *Leeman et al.* [1991] reported similar B capacity of ~6.4 mg B/mL (or 0.6 meq/mL).

6.3.2 Chemical Procedure

Two different boron extraction procedures established by the US [*Hemming and Hanson*, 1994], modified from *Kiss*. [1988] and *Leeman et al*. [1991]) and France [*Lemarchand et al*., 2002] groups have been widely applied to the natural water and carbonates samples. The main difference between two groups are that the US group preferred to use 0.3M NH_4OH to condition the column and remove cations, in contrast, the France group used 0.5M NaOH and H_2O to condition the column and 0.6M NaCl to remove cations based on their detailed evaluation of the efficiency on the removal of anions (see Table 6.1 and 6.2 for details). In this study, both of the B separation methods were investigated and further evaluated the limitation for these two methods. All sample handling was performed in the Class 10 laminar flow clean box.

Table 6.1 Cleaning, loading and elution steps for the "Ammonia" method (modified from *Hemming and Hanson*, [1994])

Step	Reagent	Amount (µL)	Flow rate (µL/min)	Purpose
1	water	100	80	wet beads
2	0.1N HCl	667	30	clean column
3	water	100	40	condition
4	0.3M NH4OH	50	40	condition
5	water	100	40	condition
6	sample	0-500	15	sample introduction
7	water	100	40	remove cations
8	0.3M NH4OH	50	40	remove cations
9	water	100	40	remove cations
10	0.1N HCl	1000	30	elute boron

For the "Ammonia" protocol (i.e., followed by *Hemming and Hanson* [1994]), boron specific anion resin Amberlite IRA 743 (20-50 mesh, Sigma®) was loaded into the acid-leached Teflon-tubing (0.08-mm I.D.; 0.15-mm O.D.). The column was connected to 0.15-mm-I.D. peristaltic pump tubing and the flow rate (from 10 to 80 μL/min) for each step was adjusted by peristaltic pump. For most samples, 30-cm of beads is adequate. Prior to sample introduction, DIW water and 0.1N HCl passed the columns for cleaning, and 0.3M NH_4OH and DIW were used to condition the columns. Acidic water samples or carbonate samples (dissolved in 0.2N HCl) were dried (avoid completely drying the samples) under the hot plate at <50°C and taken up in water adjusted to pH= 8.2 by the addition of B-free NH_4OH, and loaded onto the ion-exchange column. After sample loading, remaining cations retained in the columns were removed by DIW and 0.3M NH_4OH, and then boron was eluted by 0.1N HCl. All the cleaning, loading and elution steps for boron separation using Amberlite IRA 743 from carbonate samples and natural waters were presented in Table 6.1. Boron isotopic analyses for $Cs_2BO_2^+$ P-TIMS and BO_2^- N-TIMS were described in section 2.2 of Chapter 2.

Table 6.2 Boron extraction procedure for the "NaOH" method (after *Lemarchand et al.* [2002]).

Step	Reagent	Amount (μL)	Flow rate (μL/min)	Purpose
1	water	2 × bed volume	50	wet beads
2	0.1N HCl	2 × bed volume	50	clean column
3	water	2 × bed volume	50	clean column
4	0.5M NaOH	2 × bed volume	50	condition
5	water	10 × bed volume	50	condition
6	sample	0-500	30	sample introduction
7	water	5 × bed volume	50	remove cations
8	0.6M NaCl pH=8	5 × bed volume	50	remove cations
9	water	5 × bed volume	50	remove cations
10	0.1N HCl	10 × bed volume	50	elute boron

As for the "NaOH" protocol (i.e., followed by *Lemarchand et al.* [2002]), the bed volume for this procedure are 50, 10 and 10 μL in order to reduce the elution volume from 500 to 40 μL. Prior to sample introduction, columns were cleaned up with 0.1N HCl, DIW and 0.5M NaOH, and then conditioned with ultrapure water. The pH of the loaded solution can be as low as 5.5, but should not exceed 9 due to the potential precipitation of hydroxides or carbonate species. After sample loading, the columns were washed by DIW, 0.6M NaCl and DIW to remove cations and anions, and then boron was eluted by 0.1N HCl. The detailed boron extraction procedure using Amberlite IRA 743 for carbonates and natural waters were listed in Table 6.2. Boron isotopic analyses for $Cs_2BO_2^+$ P-TIMS and BO_2^- N-TIMS were described in section 2.2 of Chapter 2.

6.3.3 Removal of organic matter

The organic matter could originate from the sample itself or from the slight breakdown of the resin, and usually leads to a decrease of signal intensity and results in isobaric interference during TIMS analyses. Based on the recently developed technique of microsublimation ([*Gaillardet et al.*, 2001, modified from *Birck et al.* [1997]], boron can be successfully separated from organic matter. This procedure is mainly based on the physical behavior of boron for sublimation at temperature higher than its sublimation point (~70°C).

The final elution volume of 0.1N HCl is immediately transferred into the cap of a 5 mL Savillex® conical beaker, and rapidly and tightly screwed with V-shape condenser tubes in the upside down position. The beakers were completely wrapped in an Al foil to ensure heat conduction, and sited on its cap onto a hot plate at a constant temperature of 98°C for 12 hours. The temperature control is crucial for this experiment due to lower recovery resulted from the lower temperature. For 5 mL Savillex vials, the maximum volume of the initial droplet is limited to <55 μL. Furthermore, the microsublimation technique was also further applied to extract B from freshwater-matrix samples and biogenic carbonates (i.e., corals) (see below).

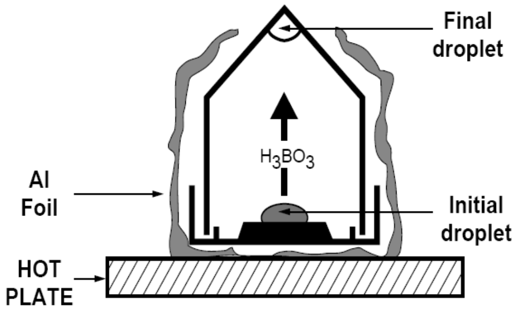

Figure 6.4 Schematic picture of B purification by the "microsublimation" technique. This method was firstly developed for Os purification [*Birck et al.*, 1997], and further modified by *Gaillardet et al.* [2001]. (adopted from *Gaillardet et al.* [2001])

6.4 Results and Discussion

6.4.1 Boron recovery study

The yield of the boron recovery is quantified by "standard calibration curve "method. The efficiency of the boron extraction procedure is tested by the elution curves, and by evaluating the total chemical procedure recovery yield for both "Ammonia" and "NaOH" protocols (a 50-μL column). The boron recovery yield for these two procedures ranges from 99.5% to 100.3% (presented in Figure 6.5a and 6.5b) based on two duplicated results for each procedure. This indicates that the chemical procedures presented here are rather highly stable and any isotopic fractionation caused by low chemical yield can therefore be eliminated.

6.4.2 Boron isotopic composition of seawater

International seawater standards, NASS-5 (S=30.1‰ , National Research Council Canada®) and IAPSO (S=35‰, OSIL®), as well as natural seawater samples collected from Taiwan Strait were used to evaluate the reproducibility of the seawater-matrix sample. Because of the higher ionization efficiency, N-TIMS technique was selected to directly analyze B isotopic compositions of these seawater samples. 1 μL seawater

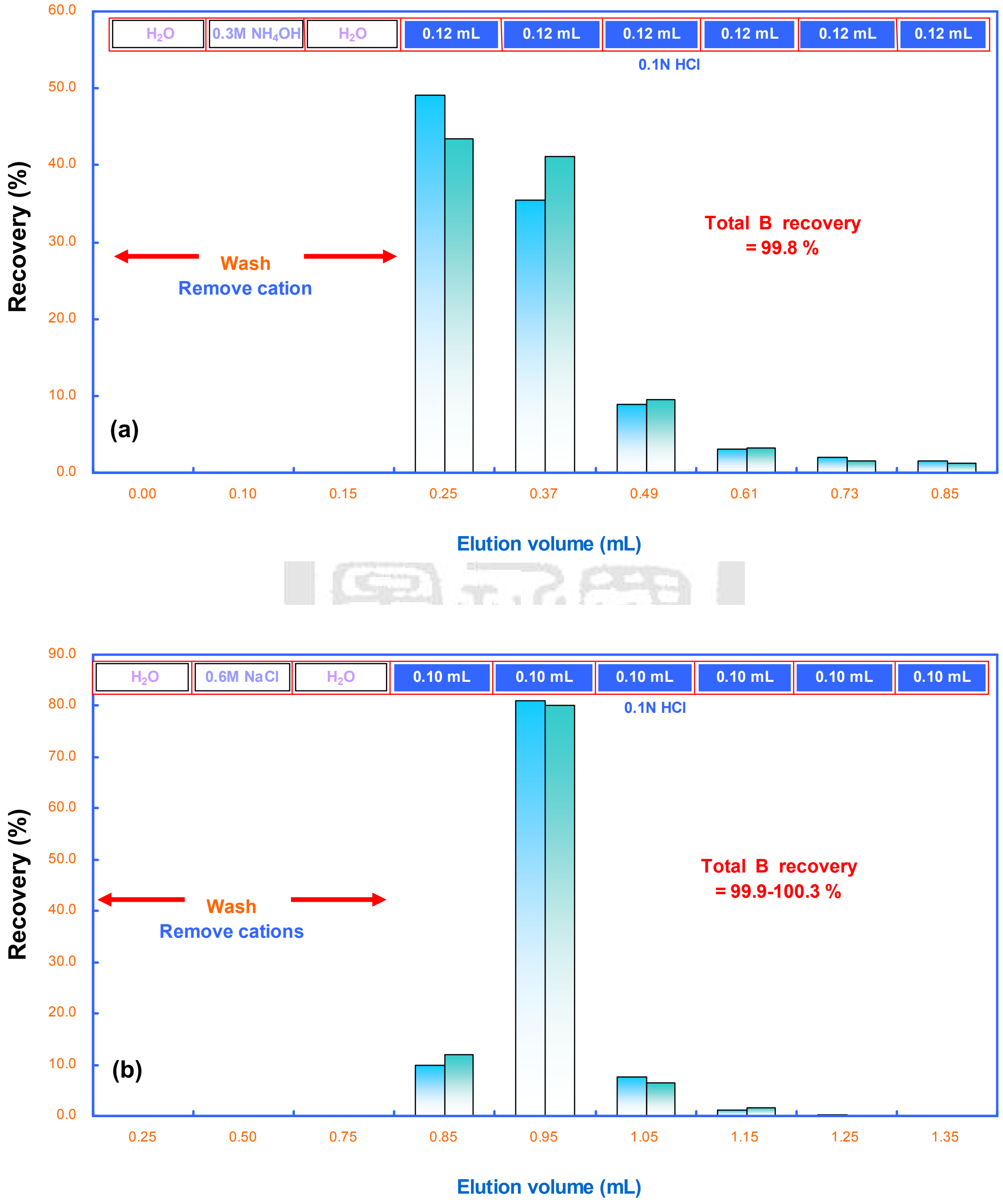

Figure 6.5 Elution of B with 0.1N HCl from boron-specific resin Amberlite IRA 743 using (a) “Ammonia” and (b) “NaOH” method. The excellent yields for the two different chemical separations can be achieved in this study.

containing ~4.5 ng was directly loaded onto ingle Re filament for the N-TIMS technique (see section 2.2 for the analytical method in detail) without any chemical separation, and the results of B isotope analyses for seawaters are presented in Table 6.3 and Figure 6.6. For international seawater standards, the mean δ^{11}B value of NASS-5 and IAPSO is 38.6±0.3‰ (n=12) and 39.5±0.2‰ (n=5), respectively. The slightly lighter δ^{11}B value of NASS-5 possibly can be attributed to the influence of freshwater inputs (~+10‰ for the globally average riverine δ^{11}B, [*Lemarchand et al*., 2000]) around the coastal region. For natural seawater samples (542-18B, S=34.8‰), the mean seawater δ^{11}B value (39.6±0.3‰,) is in consistent with IAPSO and worldwide seawater δ^{11}B isotopic composition (+39.5‰, [*Spivack and Edmond*, 1987]).

Table 6.3 External reproducibility of B isotope measurements on seawater standards.

	Seawater $^{11}B/^{10}B$		Seawater $\delta^{11}B$ (‰, NBS 951)
NASS-5			
Jun-04	**4.1594**	**0.00006**	**38.7**
Jun-04	**4.1600**	**0.00008**	**38.9**
Aug-04	**4.1589**	**0.00005**	**38.6**
Oct-04	**4.1597**	**0.00004**	**38.8**
Nov-04	**4.1596**	**0.00009**	**38.8**
Jan-05	**4.1607**	**0.00004**	**39.0**
Jan-05	**4.1576**	**0.00010**	**38.2**
Mar-05	**4.1605**	**0.00011**	**39.0**
Mar-05	**4.1586**	**0.00012**	**38.5**
Aug-05	**4.1581**	**0.00012**	**38.4**
Dec-05	**4.1581**	**0.00008**	**38.4**
Feb-06	**4.1584**	**0.00008**	**38.5**
Mean	**4.1591**		**38.6**
STD	**0.0010**		**0.3**
2σ (‰)	**0.48**		
SE (‰)	**0.14**		**38.6±0.3 ‰**
IAPSO			
Jun-05	**4.1620**	**0.00007**	**39.4**
Jun-05	**4.1630**	**0.00008**	**39.6**
Aug-05	**4.1623**	**0.00005**	**39.4**
Oct-05	**4.1635**	**0.00008**	**39.7**
Jan-06	**4.1614**	**0.00006**	**39.2**
Mean	**4.1624**		**39.5**
STD	**0.0008**		**0.2**
2σ (‰)	**0.39**		
SE (‰)	**0.18**		**39.5±0.2 ‰**

Table 6.4 External reproducibility of B isotope measurements on natural seawaters.

Date	Seawater $^{11}B/^{10}B$		Seawater $\delta^{11}B$ (‰, NBS 951)
Jun-02	4.1624	0.00005	39.5
Jun-02	4.1648	0.00005	40.1
Jun-02	4.1634	0.00005	39.7
Aug-02	4.1635	0.00005	39.7
Aug-02	4.1612	0.00004	39.2
Aug-02	4.1622	0.00005	39.4
Oct-02	4.1637	0.00005	39.8
Oct-02	4.1644	0.00004	40.0
Jan-03	4.1608	0.00006	39.1
Jan-03	4.1628	0.00005	39.6
Jan-03	4.1634	0.00011	39.7
Mar-03	4.1631	0.00004	39.6
Mean	4.1630		39.6
STD	0.0012		0.3
2σ (‰)	0.57		
SE (‰)	0.17		39.6±0.3 ‰

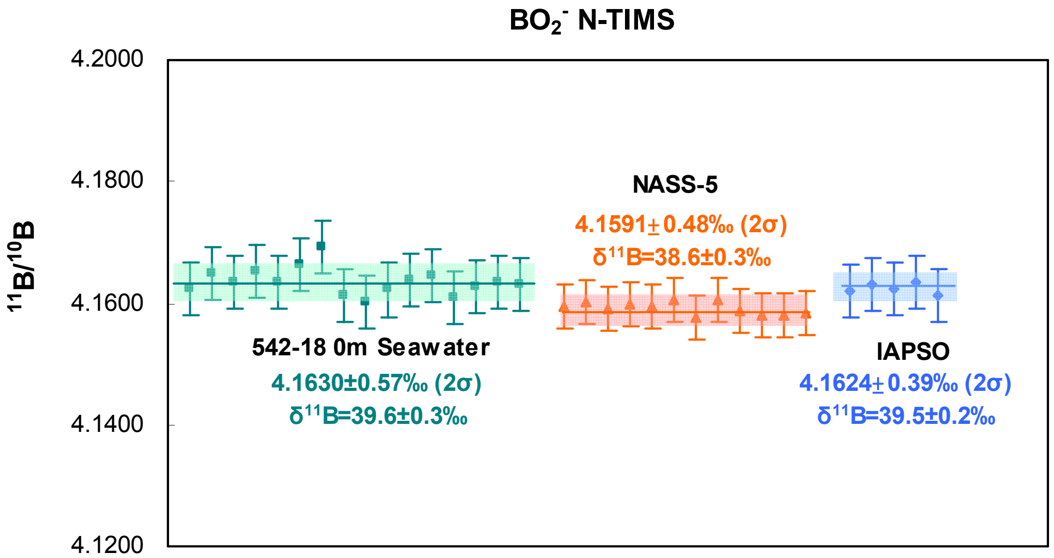

Figure 6.6 Long-term repeatability of seawater-matrix samples, 542-18B, NASS-5 and IAPSO. Error bars show a $2\sigma_m$ errors (in-run precision) based on cycle averages. The mean $^{11}B/^{10}B$ ratios are indicated by the solid line together with the 2SD range represented by the shade area.

6.4.3 Boron isotopic composition of pore fluid

In order to obtain real $\delta^{11}B$ signals from foraminiferal shells, it is imperative to evaluate the potential influence of diagenetic processes (i.e., sediment-pore water interaction) occurred on the seafloor after the burial of foraminiferal shell. Although previous studies reported that the use of the cleaning procedure can effectively remove most of the contaminants (e.g., Mn overgrowth and secondary calcite) [*Boyle and Keigwin*, 1986/85], however, the effect of cleaning procedure on foraminiferal δ^{11}B has yet to be evaluated until now. The boron and boron isotopic compositions of pore fluids obtained from ODP Site 1143 and 1146 (located at the SCS), as well as ODP Site 1202 (located at the southern Okinawa Trough) were therefore used to understand the main controlling factors and provide insights into their potential influences on pore water chemistry.

Possible causes for B and δ^{11}B variations in pore waters

Boron and δ^{11}B are sensitive tracers for sedimentary diagenesis that might influence pore water geochemistry [*Deyhle et al.*, 2001], as well as fluids processes at convergent margins [*Brumsack and Zuleger*, 1992; *You et al.*, 1993a; *You et al.*, 1995; *Kopf et al.*, 2000; *Deyhle and Kopf*, 2001]. Possible mechanisms that affect B and B isotope signatures in pore waters are briefly summarized as follow: (1) De-sorption of exchangeable B in clays, resulting in elevated B with low δ^{11}B. In other words, adsorption of B will decrease B and cause heavier δ^{11}B in fluids [*You et al.*, 1993a, b]; (2) Mixing of fluids with different sources along high-porosity intervals affect B and δ^{11}B differently, depended on P-T conditions and local tectonic settings [*Deyhle et al.*, 2004]; (3) Involvement of deep generated fluids. The B and δ^{11}B in deep-seated fluids are rather variable and depend on lithology, regional fractures and shear zones. Elevated B and heavy B isotopes are reported in Naikai and Barbados Ridge Complex [*You et al.*, 1993a, b; *Deyhle et al.*, 2001]. However, the δ^{11}B in pore waters is more negative (<35 $^{o}/_{oo}$) in forearc environments (e.g. Japan Trench, [*Deyhle and Kopf*, 2002]); (4) Alteration of volcanic products shift δ^{11}B in fluids toward positive direction [*Palmer* *and Swihart*, 1996]; (5) Carbonate precipitation leads to low B and high $\delta^{11}B$ due to preferential uptake of tetrahedral borate, $^{10}B(OH)_4^-$; (6) ^{10}B uptake into B-bearing minerals (e.g. tourmaline, borosilicate) decrease B and increase $\delta^{11}B$. The B and $\delta^{11}B$ in residual fluids depend on the original sources, metamorphic or magmatic [*Palmer and Swihart*, 1996]; (7) Opal-A to Opal-CT transition reduces B significantly [*Brumsack and Zuleger*, 1992]; (8) Illitization of smectite, starts at ~60-70°C and reaches advanced levels at ~120-150°C, decrease B and elevate $\delta^{11}B$ in fluids [*Weaver*, 1989; *Williams et al.*, 2001]. Based on the above possible controlling factors, B and B isotopic signatures can be used to further discuss the natural variability in these two geologically-differentiated settings, South China Sea and Okinawa Trough.

Leg 195 ODP Site 1202 (Okinawa Trough)

The B contents in pore fluids at Site 1202 are, in general, slightly elevated relative to seawater (Figure 6.7a). This phenomenon was explained as a result of organic matter decomposition lead to release of B [*You et al.*, 1993a, b]. In the uppermost 40 mbsf, B varies largely ranging between 200 to 1200 μM. This partly is a result of fluid advection along the sandy horizons. Two distinct low B layers (50% seawater) are observed at 16.1 and 41.6 mbsf (see Figure 6.7a), reflecting other sources and/or fresh water addition. Gas hydrate dissociation is a possible candidate for causing low B in pore waters [*Kastner et al.*, 1995; *Sample and Kopf*, 1995; *Kopf et al.*, 2000]. Other likely fresh water sources are clay dehydration water (e.g., smectite-illite transformation) and continental inputs. It is, however, difficult to distinguish the two mechanisms without further oxygen isotopic information [*Fitts and Brown*, 1999]. Further down-core, significant elevation of B (585 μM at 176 mbsf) was detected at 150-200 mbsf. At depths greater than 250 mbsf, B remains constant with average seawater value.

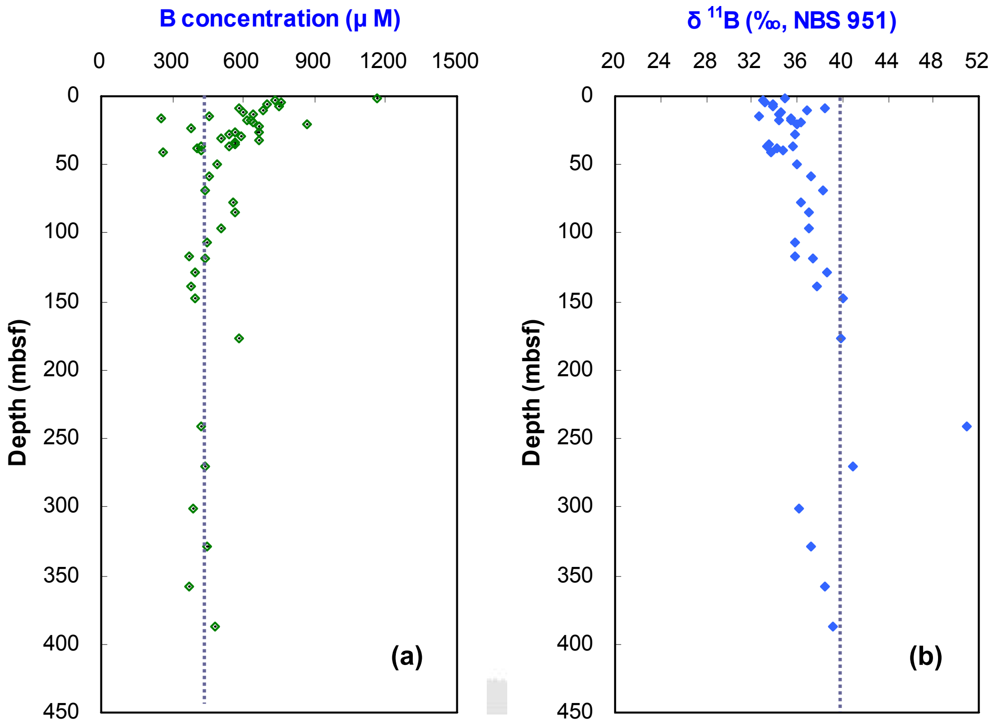

Figure 6.7 Depth profiles of (a) B concentration and (b) δ^{11}B in pore fluids at Site 1202. The vertical dashed line represents seawater B content of 420μM and δ^{11}B of 39.5‰. Also shows lithologic facies and the occurrences of sandy and ash layers (after [*Shipboard Scientific Party 2002*]).

The B isotopes show an interesting correlation with that of dissolved B down-core (Figure 6.7b). In general, the Site 1202 pore fluids are characterized by slightly lower δ^{11}B values than seawater. Similar to the dissolved B pattern, degradation of organic matter in the upper sedimentary column releases significant amounts of B enriched in ^{10}B [*Brumsack and Zuleger*, 1992; *You et al.*, 1993a; *You et al.*, 1996]. Between 40 and 120 mbsf, δ^{11}B remains low, possibly were affected by clay de-sorption [*Spivack et al.*, 1987] and ash alteration [*Brumsack and Zuleger*, 1992]. Near the sandy horizons, δ^{11}B becomes more negative, suggesting mixing of fluids with low isotopic compositions. δ^{11}B increases gradually between 120 and 230 mbsf. At depths greater than 150 m, δ^{11}B becomes significantly heavier than seawater up to 50.9‰ (Figure 4b). These enhanced B isotopic signatures coincide with the occurrence of sandy turbidites at 230-280 mbsf, however, no significant changes in dissolved B occurred. Below 280 mbsf, δ^{11}B decreases toward the seawater value.

Figure 6.8 shows a correlation plot of δ^{11}B versus 1/B in pore fluids at Site 1202, and de-sorption of the clay-rich sediment is thought to be the main source of B in Site 1202, resulting in elevated B contents with low δ^{11}B values. Other mechanisms including precipitation of carbonates, interaction with terrigenous materials, and low-temperature ash alteration may also affect the B and δ^{11}B in pore waters.

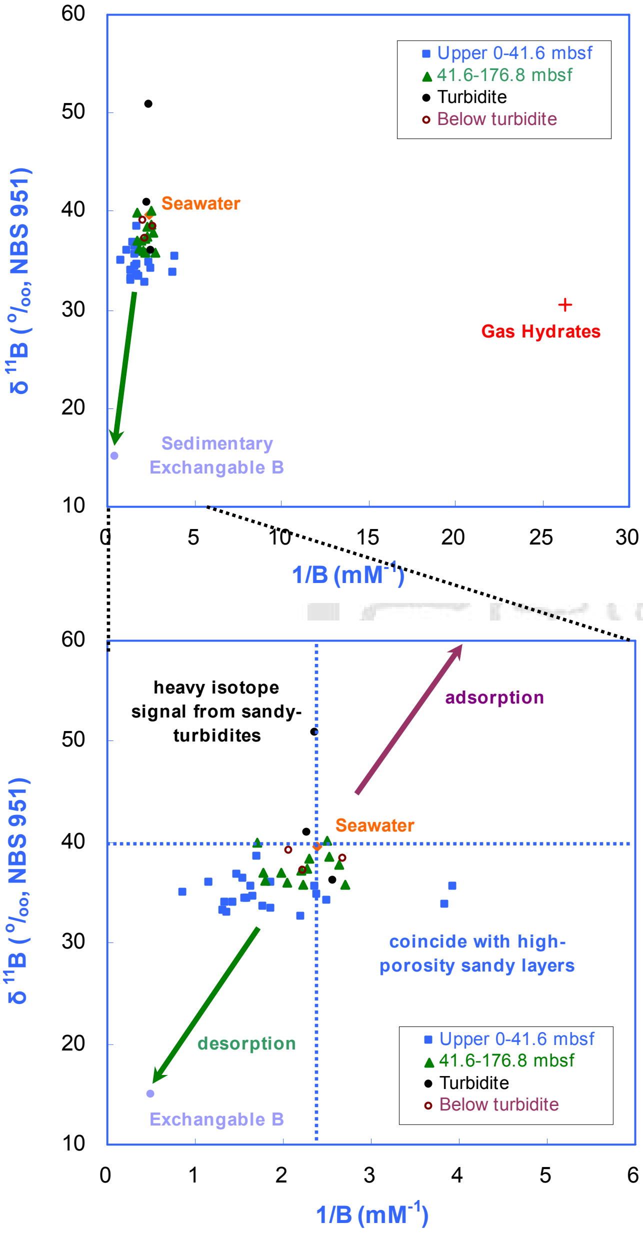

Figure 6.8 Correlation plot of δ^{11}B versus 1/B in pore waters at Site 1202. The sketch illustrates three possible fluid sources: [1] seawater ([B]= 420 μM and δ^{11}B= 39.5‰, *Spivack and Edmond*, (1987)); [2] exchangeable B ([B]= 2000 μM and δ^{11}B= 15‰, *Kopf et al.* (2000)); and [3] gas hydrates ([B]= 38 μM and δ^{11}B= 30.6‰, *Zuleger et al*, unpublished data).

Leg 184 ODP Site 1143 and 1146 (South China Sea)

Unlike the pore waters at Site 1202 in the southern Okinawa Trough, the B contents in pore fluids at Site 1143 and 1146 in the SCS do not show a significant enrichment at shallower depths relative to seawater. In the uppermost 100 mbsf, B varies slightly ranging between 350 to 450 μM. Between 100 and 450 mbsf, relative low B contents were possibly caused by clay de-sorption [*Spivack et al.*, 1987] and ash alteration [*Brumsack and Zuleger*, 1992]. Two distinguishable low B layers (less than 50% of seawater [B]) are found at 140 and 201 mbsf (see Figure 6.9), possibly reflecting the intense adsorption of the volcanic ash. The elevated δ^{11}B values reinforce the likelihood of the alteration of volcanic products [*Palmer and Swihart*, 1996] (see Figure 6.10).

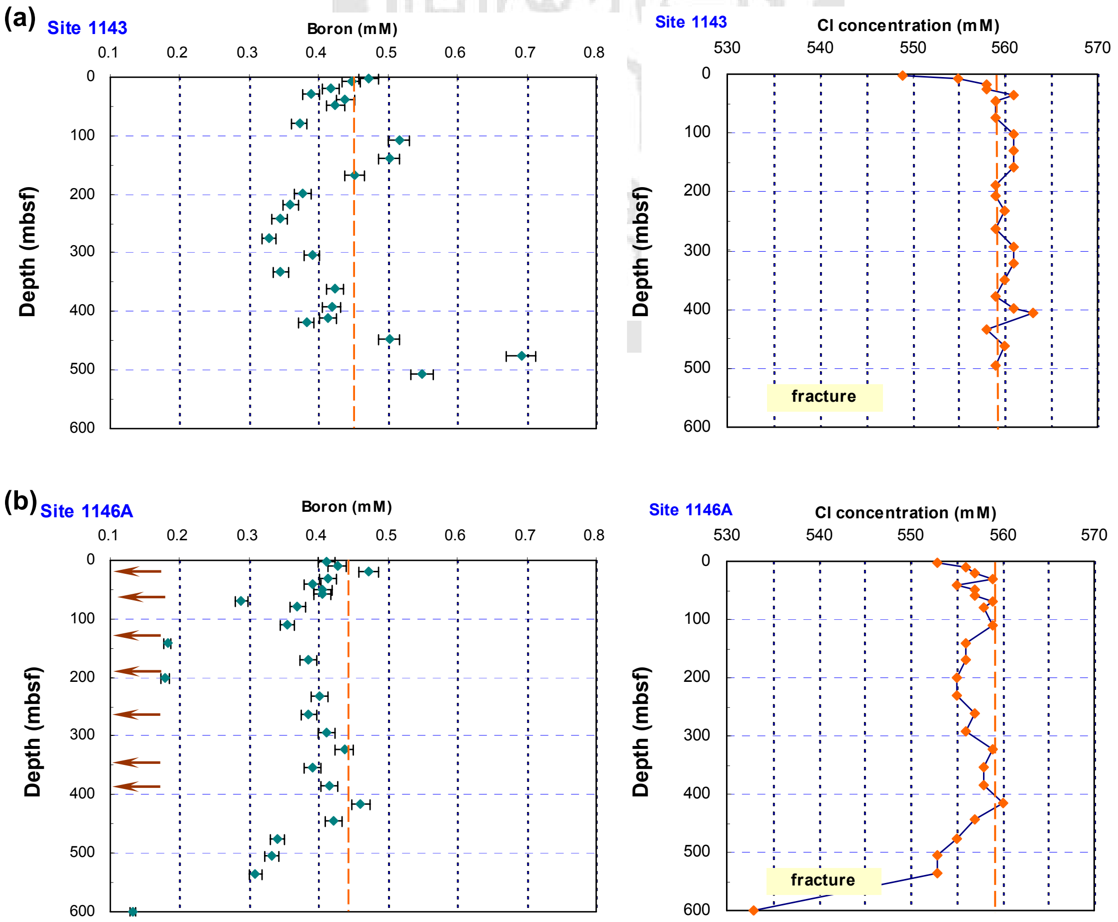

Figure 6.9 Depth profiles of B and Cl contents in pore fluids at (a) Site 1143 and (b) Site 1146. The vertical red dashed line represents seawater B content of 420μM and seawater Cl content of 559 mM. Also shows the occurrences of the volcanic ash layers at Site 1146 (after [*Shipboard Scientific Party 1999*]).

Below 450 mbsf, the B distributions display an opposite excursion for these two sites, showing a gradually increases at Site 1143 and a decrease at Site 1146. This can be thought to result mainly from fluid advections or fresh water additions along the fractures.

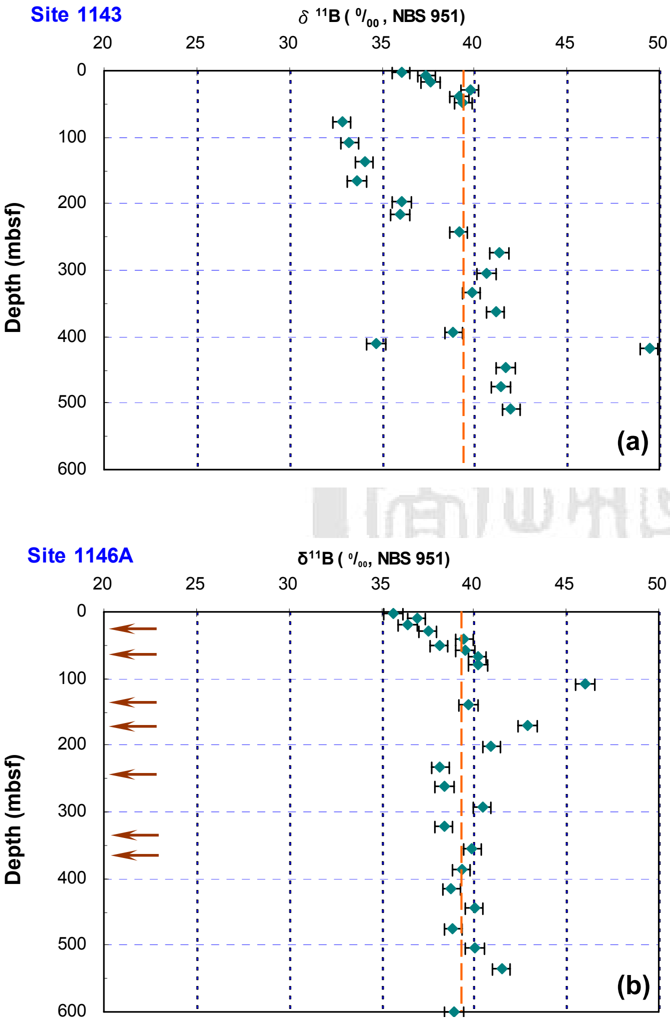

Figure 6.10 Depth profiles of B isotopic compositions in pore fluids at (a) Site 1143 and (b) Site 1146. The vertical red dashed line represents pressure-corrected seawater δ^{11}B content of 39.5‰. Also shows the occurrences of the volcanic ash layers at Site 1146 (after *Shipboard Scientific Party 1999*).

The B isotopes show an interesting correlation with that of dissolved B down-core (Figure 6.10). In general, the Site 1143 and 1145 pore fluids are characterized by slightly lower δ^{11}B values than seawater at surface layers. Degradation of organic matter in the upper sedimentary column releases significant amounts of B enriched in ^{10}B [*Brumsack and Zuleger*, 1992; *You et al.*, 1993a; *You et al.*, 1996].

Between 100 and 300 mbsf, δ^{11}B remains low at Site 1143, were mainly affected by clay de-sorption [*Spivack et al*., 1987], and significantly high δ^{11}B occurs at Site 1146, possibly reflecting the ash alteration [*Brumsack and Zuleger*, 1992]. At depths greater than 300 m, δ^{11}B becomes more fluctuated at Site 1143. In contrast, at Site 1146, it shows no significant change in pore water δ^{11}B relative to the seawater value (Figure 6.10). All of these isotopic excursions are most likely controlled by admixing with different sources of deep fluids containing various [B] and δ^{11}B. The end-members of these deep fluids (e.g., dehydration water vs. gas hydrate water) could change significantly in various geological settings and geochemical processes [*Kopf et al*., 2002].

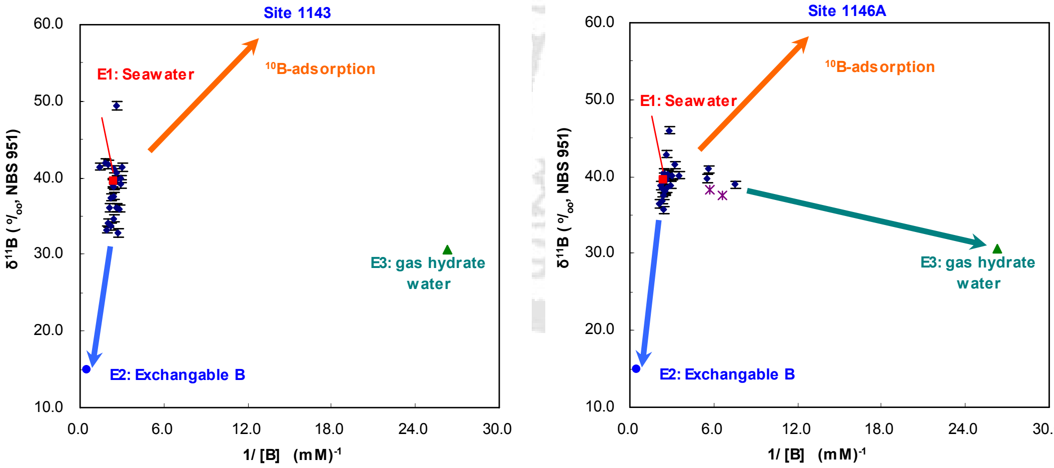

Figure 6.11 Correlation plot of δ^{11}B versus 1/B in pore waters at Site 1143 and 1146. The sketch illustrates three possible fluid sources: [1] seawater ([B]= 420 μM and δ^{11}B= 39.5‰, *Spivack and Edmond*, [1987]); [2] exchangeable B ([B]= 2000 μM and δ^{11}B= 15‰, *Kopf et al*. [2000]); and [3] gas hydrates ([B]= 38 μM and δ^{11}B= 30.6‰, *Zuleger et al*, unpublished data).

Figure 6.11 shows the correlation plots of δ^{11}B versus 1/B in pore fluids at Site 1143 and 1146, and the de-sorption of the clay-rich sediment is thought to be the main source of B at the both sites, resulting in elevated B contents with low δ^{11}B values. For the Site 1146, the B and $\delta^{11}B$ seems to be affected by the potential end-member of gas hydrate water ([B]= 38 μM and $\delta^{11}B$= 30.6‰, *Zuleger et al*, unpublished data). This is consistent with previous study reported by *Zhu et al.* [2003]. They observed a slight decrease in the Cl concentration and substantial increases in methane concentrations, as well as evidences of stable carbon isotope at the same site, and concluded the present of gas hydrates at Site 1146. Other mechanisms including precipitation of carbonates, interaction with terrigenous materials, and low-temperature ash alteration may also affect the B and $\delta^{11}B$ in pore waters.

6.4.4 Boron isotopic composition of biogenic carbonates

Boron isotopic compositions in biogenic carbonates (i.e., foraminiferal and corals) have been successfully and widely applied to reconstruct oceanic pH in short-term and long-term timescale [*Sanyal et al*., 1995; *Hemming et al*., 1998; *Pearson and Palmer*, 1999; *Pearson and Palmer*, 2000; *Palmer and Pearson*, 2003; *Pelejero et al*., 2004]. However, caution should be taken due to the potential secular isotopic variation of seawater B [*Lemarchand et al*., 2000]. Other limitations arise from isotopic fractionation between foraminiferal species, shell size and dissolution effects [*Sanyal et al*., 1996; *Sanyal et al*., 2001; *Hönisch and Hemming*, 2004]. Sample selection and careful analysis are therefore critical. In this study, the analytical method and sample preparation were firstly described. Additionally, replicated analyses and strict data acceptance criteria improve the analytical precision in order to obtain the reliable results for the paleo-pH reconstructions.

Sample selection

For studying the $\delta^{11}B$/pH variations related to past atmospheric pCO_2 changes, the ideal core location must be shallow enough to reduce the risk of dissolution, which can substantially bias the δ^{11}B in foraminifera. Additionally, a detailed SEM examination can also provide information about the real preservation of foraminiferal shells [*Hönisch and Hemming*, 2004]. In this study, mono-specific, size-specific foraminiferal samples (*G. sacculifer* without sac-like chamber, 350-500 μm) from a well-preserved core-top sediment, 276-19B (24°19.90'N；122°40.12'E, water depth: 727 m) were selected to evaluate the replicated B isotopic analyses using the N-TIMS technique. Besides, modern coral samples (Porities *spp.*) collected from Lutao Island were used to test the potential application of the P-TIMS technique on biogenic carbonates.

Sample preparation and isotopic analyses

For the biogenic carbonates (i.e., *G. sacculifer* and Porities *spp.*), samples were crushed and bleached with 4-6% sodium hypochlorite to remove organic matter. Containers remained open during the entire bleaching process so that produced CO_2 could escape. After 24 hours in bleach the samples were repeatedly rinsed with B-free waters, ultrasonicated and centrifuged to remove soluble salt and any adsorbed B. Finally, samples were dissolved in 2N ultrapure HCl. The microsublimation technique was then applied to extract the B from pure calcium carbonates without any column separation (Amberlite IRA 743). The microsublimation not only provides a more effective method for extracting B, but also eliminates the use of chemical reagents that contain B. The recoveries of this technique for carbonate samples were directly examined through a comparison between column chemistry and microsublimation. Figure 6.12 shows an excellent reproducibility of δ^{11}B in foraminiferal shell calcites and coral samples for the N-TIMS and P-TIMS. Furthermore, the results are also in a good agreement with the data obtained from column chemistry, indicating that the microsublimation can be successfully applied to the carbonate samples. Although the P-TIMS has a better analytical precision, at least 100 ng B (or 25 mg $CaCO_3$, ~200 individuals of foraminiferal calcite) is needed to obtain a stable signals. Therefore, the N-TIMS technique is more suitable for natural samples with low B level.

By comparing with previous calibration work reported by *Hönisch and Hemming* [2004], the mean δ^{11}B value of *G. sacculifer* (300-500 μm) is 20.34±0.4‰, and corresponding to seawater pH of 7.95±0.15, which is similar to the modern seawater pH of 0-50 m (pH= 8.0) around Taiwan. The average coralline δ^{11}B (24.43±0.2‰) in the Lutao Island also falls within the δ^{11}B value of the modern coral, and comparable with previous studies [*Hemming et al*., 1998; *Pelejero et al*., 2004]. This preliminary result demonstrates that both of P-TIMS and N-TIMS techniques combining with the microsublimation method can provide the most powerful tool to precisely determine δ^{11}B in foraminifera and corals, and thus provide insights into the possible linkage between surface seawater pH (or aqueous pCO_2) and atmospheric CO_2 concentration.

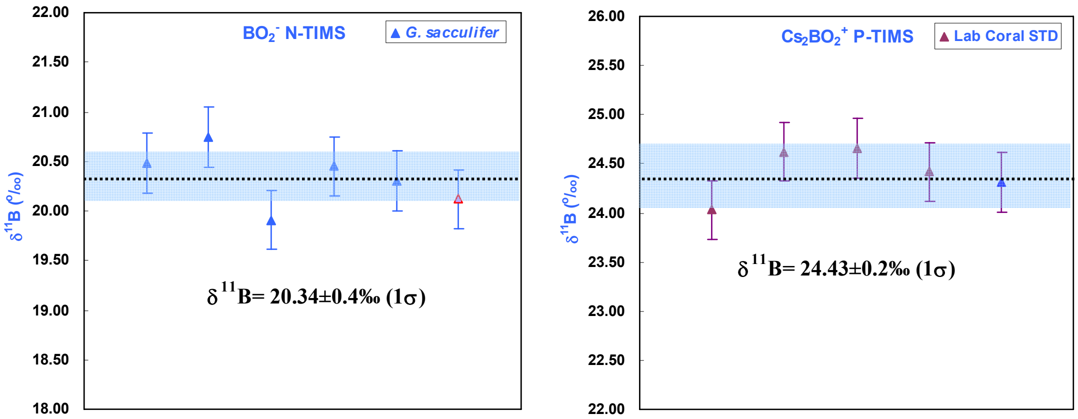

Figure 6.12 Repeatability of B isotope ratios for (a) *G. sacculifer* (250-350μm) and (b) Porities *spp.* using the microsublimation technique without any further chemical separation. Note that foraminiferal samples were measured by N-TIMS technique and coral samples were determined by P-TIMS technique. Red and blue symbols shown in (a) and (b), respectively, represent a result obtained by the whole column chemistry using B-specific resin Amberlite IRA 743.

6.5 Conclusions

The B isotopic analyses presented here have been successfully developed, and extend its potential applications for various natural samples, including seawaters, pore waters and biogenic carbonates. Combining with P-TIMS or N-TIMS technique, together with the new microsublimation, a rapid, highly-reliable and high-precision analytical method for B isotopes can be used to determine different types of natural samples. For the natural seawaters, δ^{11}B shows a rather homogeneous distribution in the open ocean (δ^{11}B= 39.5‰), but slightly negative δ^{11}B value can be determined in the coastal ocean. This can be thought to be resulted mainly from the influence of riverine inputs (averaged δ^{11}B= +10‰) with substantially lighter δ^{11}B relative to seawater.

B and δ^{11}B in pore fluids collected from the southern Okinawa Trough and South China Sea show a complicated distribution pattern with depths, indicating distinct geochemical processes or admixtures of fluids with various source end-members of B were involved in different geological settings. Because of the large variability of B (200-2000 μM) and δ^{11}B (+32-+51‰) in pore fluids, the approach using foraminiferal δ^{11}B to estimate pH into long-term and short-term timescale needs to be interpreted cautiously due to potential influences of diagenetic processes that reacted with the surrounding sediment pore waters.

This study also indicates that the recovery yields of B extraction by microsublimation is close to 100%, and shows that a precise determination of B isotopic ratios is possible for coral skeletons and foraminiferal shells. This advance would offer an opportunity to evaluate the empirical calibration of δ^{11}B/pH, and further refine the relationship between surface water pCO_2 and atmospheric CO_2 level in short-term and long-term timescales.

References

Barth, S., 1997. Boron isotopic analysis of natural fresh and saline waters by negative thermal ionization mass spectrometry. Chem. Geol. 143, 255-261.

Barth, S., 2000. Geochemical and boron, oxygen, and hydrogen isotopic constraints on the origin of salinity in groundwaters from the crystalline basement of the Alpine Foreland. Applied Geochem. 15, 937-952.

Birck, J. L., Roy Barman, M., Capmas, F., 1997. Re-Os isotopic measurements at the femtomole level in natural samples. Geostandard Newsletter: The Journal of Geostandards and Geoanalysis 21, 19-27.

Boyle, E. A., Keigwin, L. D., 1985/1986. Comparison of Atlantic and Pacific paleochemical records for the last 215, 000 years: Changes in deep ocean circulation and chemical inventories. Earth Planet. Sci. Lett. 76, 135-150.

Brumsack, H., Zuleger, E., 1992. Boron and boron isotopes in pore waters from ODP Leg 127, Sea of Japan. Earth Planet Sci. Lett. 113, 427-433.

Deyhle, A., Kopf, A., Eisenhauer, A., 2001. Boron systematics of authigenic carbonates: A new approach to identify fluids processes in accretionary prisms. Earth Planet. Sci. Lett. 187, 191-205.

Deyhle, A., Kopf, A., 2001. Deep fluids and ancient pore waters at the backstop: Stable isotope systematics (B, C, O) of mud-volcano deposits on the Mediterranean Ridge accretionary wedge. Geology 29, 1031-1034.

Deyhle, A., Kopf, A., 2002. Strong B enrichment and anomalous δ^{11}B in pore fluids from the Japan Trench forearc. Marine Geol. 183, 1-15.

Deyhle, A., Kopf, A., Frape, S., Hesse, R., 2004. Evidence for fluid flow in the Japan Trench forearc using isotope geochemistry (Cl, Sr, B): Results from ODP Site 1150. The Island Arc 13, 258-270.

Fitts, T. G., Brown, K. M., 1999. Stress induced smectite dehydration remifications for patterns of freshening fluid expulsion in the N. Barbados accretionary wedge. Earth Planet. Sci. Lett. 172, 179-197.

Gäbler, H., Bahr, A., 1999. Boron isotopic ratio measurements with a double-focusing magnetic sector ICP mass spectrometer for tracing anthropogenic input into surface and ground water. Chem. Geol. 156, 323-330.

Gaillardet, J., Allegre, C. J., 1995. Boron isotopic composition of corals: Seawater or diagenesis record? Earth Planet Sci. Lett. 136, 665-676.

Gaillardet, J., Lemarchand, D., Go¨pel, C., Manhe`s, G., 2001. Evaporation and sublimation of boric acid: application for boron purification from organic rich solutions. Geostand. Newsl. 25 Ž1., 67–75.

Hemming, N. G., Hanson, G. N., 1992. Boron isotopic composition and concentration in modern carbonates. Geochim. Cosmochim. Acta 56, 537-543.

Hemming, N. G., Hanson, G. N., 1994. A procedure for the analysis of boron by thermal ionization mass spectrometry. Chem. Geol. 114, 147-156.

Hemming N. G., Guilderson T. P., Fairbanks R. G., 1998. Seasonal variations in the boron isotopic composition of a coral: A productivity signal? Global Biogeochem. Cy. 12, 581–586.

Hönisch, B., Hemming, N. G., 2004. Ground-truthing the boron isotope-paleo-pH proxy in planktonic foraminifera shells: Partial dissolution and shell size effects. Paleoceanography 19, doi:10.1029/2004PA001026.

Hönisch, B., Hemming, N. G., 2005. Surface ocean pH response to variations in pCO_2 through two full glacial cycles. Earth Planet. Sci. Lett. 236, 305-314.

Hershey, J. P., Fernandez, M., Milne, P. J., Millero, F. J., 1986. The ionization of boric acid in NaCl, Na-Ca-Cl, and Na-Mg-Cl solution at 25˚C. Geochim. Cosmochim. Acta 50, 143-148.

Ishikawa, T., Nakamura, E., Boron isotope systematics of marine sediments. Earth Planet. Sci. Lett. 117, 567-580.

Kakihana, H., Kotoka, M., Shohei, S., Nomura, M., Okamota, M., 1977. Fundamental studies on the ion-exchange separation of boron isotopes. Bull. Chem. Soc. Jpn. 50, 158-163.

Kastner, M., Kvenvolden, K. A., Whiticar, M. J., Camerlenghi, A., Lorenson, T. D., 1995. Relation between pore fluids chemistry and gas hydrates associated with bottom simulating reflectors at thr Cascadia Margin, Site 889 and Site 892. Proceeding of the ODP, Sci. Results 146, 175-187.

Kiss, E., 1988. Ion exchange separation and spectrophotometric determination of boron in geological materials. Anal. Chim. Acta 211, 243–256.

Kopf, A., Deyhle, A., Zuleger, E., 2000. Evidence for deep fluid circulation and gas hydrate dissociation using boron and boron isotopes of pore fluids in forearc sediments from Costa Rica (ODP Leg 170). Marine Geol. 167, 1-28.

Kopf, A., Deyhle, A., 2002. Back to the roots: boron geochemistry of mud volcanoes and its implications for mobilization depth and global B cycling. Chem. Geol. 192, 195-210.

Leeman, W.P., Vocke, R.D., Bearly, E.S., Paulsch, P.J. P., 1991. Precise boron isotopic analysis of aqueous samples ion exchange extraction and mass spectrometry. Geochim.

Cosmochim. Acta 55, 3901–3907.

Lemarchand, D., Gaillardet, J., Lewin, E., Allegre, C. J., 2000. The influence of rivers on marine boron isotopes and implications for reconstructing past ocean pH. Nature 408, 951-954.

Lemarchand, D., Gaillardet, J., Lewin, E., Allegre, C. J., 2002. An optimized procedure for boron separation and mass sprectrometry for river water samples. Chem. Geol. 182, 323-334.

Palmer, M. R., Swihart, G. R., 1996. Boron isotope geochemistry: an overview. In: Crew, E. S., Anovitz, L. M. (Eds.), Boron: Mineralogy, Petrology and Geochemistry. Mineral. Soc. Am., 33, 709-744.

Palmer, M. R., Pearson, P. N., Cobb, S. J., 1998. Reconstructing past ocean pH-depth profiles. Science 282, 1468-1471.

Palmer, M. R., Pearson, P. N., 2003. A 23,000-year record of surface water pH and pCO_2 in the western Equatorial Pacific Ocean. Science 300, 480-482.

Pearson, P. N., Palmer, M. R., 1999. Middle Eocene seawater pH and atmospheric carbon dioxide concentrations. Science 284, 1824-1826.

Pearson, P. N., Palmer, M. R., 2000. Atmospheric carbon dioxide concentrations over the past 60 million years. Nature 406, 695-699.

Pelejero, C. et al., 2004. Preindustrial to modern interdecadal variability in coral reef pH. Science 309, 2204-2207.

Pinon, F., Deson, J., Rosset, R., 1968. Proprie´te´s de la re´sine e´changeuse d'ions spe´cifique du bore amberlite XE 243. Bull. Soc. Chim. Fr. 8Ž535., 3454–3461.

Rose, E. F., Chaussidon, M., France-Lanord, C., 2000. Fractionation of boron isotopes during erosion processes : The example of Himalayan rivers. Geochim. Cosmochim. Acta 64, 397-408.

Salisbury, M. H., Shinohara, M., Richter, C., 2002. Site 1202. *Proceeding of the ODP,* Init. Reports 195.

Sample, J. C., Kopf, A., 1995. Occurrences and geochemistry of syntectonic carbonate cements and veins from ODP Leg 146: Implications for hydrogeologica evolution of the Cascadia margin. Proceeding of the ODP, Sci. Results 146, 137-150.

Sanyal, A., Hemming, N. G., Hanson, G. N., Broecker, W. S., 1995. Evidence for a higher pH in the glacial ocean from boron isotopes in foraminifera. Nature 373, 234-236.

Sanyal, A., Hemming, N. G., Broecker, W. S., Lea, D. W., Spero, H. J., Hanson, G. N., 1996. Oceanic pH control on the boron isotopic composition of foraminifera: Evidence from culture experiments. Paleoceanography 11, 513-517.

Sanyal, A., Hemming, N. G., Broecker, W. S., Hanson, G. N., 1997. Changes in pH in the eastern equatorial Pacific across stage 5-6 boundary based on boron isotopes in foraminifera. Global Biogeochem. Cycles 11, 125-133.

Sanyal, A., Bijma, J., 1999. A comparative study of the northwest Africa and eastern equatorial Pacific upwelling as a source of CO_2 during glacial periods based on boron isotope paleo-pH estimation. Paleoceanography 14, 753-759.

Sanyal, A., Bijma, J., Spero, H. J., Lea, D. W., 2001. Empirical relationship between pH and the boron isotopic composition of Globigerinoides sacculifer: Implications for the boron isotope paleo-pH proxy. Paleoceanography 16, 515-519.

Spivack, A. J., Edmond, J. M., 1986. Determination of boron isotope ratios by thermal ionization mass spectrometry of dicesium metaborate cation. Anal. Chem. 58, 31-35.

Spivack, A. J., Edmond, J. M., 1987. Boron isotope exchange between seawater and oceanic crust. Geochim. Cosmochim. Acta 51, 1033-1043.

Spivack, A. J., Palmer, M. R., Edmond, J. M., 1987. The sedimentary cycle of the boron isotopes. Geochim. Cosmochim. Acta 51, 1939-1949.

Spivack, A. J., You, C.-F., Smith, H. J., 1993. Foraminiferal boron isotope ratios as a proxy for surface ocean pH over the past 21 Myr. Nature 363, 149-151.

Vengosh, A., Chivas, A. R., McCulloch, M. T., 1989. Direct determination of boron and chlorine isotopic compositions in geological materials by negative thermal-ionization mass spectrometry. Chem. Geol. 79, 333-343.

Vengosh, A., Chivas, A. R., McCulloch, J. M., Stainsky, A., Kolodny, Y., 1991. Boron isotope geochemistry of Australian salt lakes. Geochim. Cosmochim. Acta 55, 2591-2606.

Weaver, C. E., 1989. Clays, Muds, and Shales. Development in Sedimentology 44. Elsevier.

Williams, L. B., Hervig, R. L., Holloway, J. R., Hutcheon, I., 2001. Boron isotope geochemistry during diagenesis. Part I. Experimental determination of fractionation during illization of smectite. Geochim. Cosmochim. Acta 65, 1769-1782.

You, C.-F., Spivack, A. J., Smith, J. H., Gieskes, J. M., 1993a. Mobilization of boron in convergent margins: Implications for the boron geochemical cycle. Geology 21, 207-210.

You, C.-F., Gieskes, J. M., Chen, R. F., Spivack, A. J., Gamo, T., 1993b. Iodide, bromide, manganese, boron, and dissolved organic carbon in interstitial of organic carbon-rich marine sediments: Observations in Nankai accretionary prism. Proceeding of the ODP, Init. Reports 131, 165-174.

You, C.-F., Morris, J. D., Gieskes, J. M., Rosebauer, R., Zheng, S. H., Xu, X., Ku, T.-L., Bischoff, J. L., 1994. Mobilization of Be in sedimentary column at convergent margins. Geochim. Cosmochim. Acta 58, 4887-4897.

You, C.-F., Chan, L.-H., Spivack, A. J., Gieskes, J. M., 1995. Lithium, boron, and their isotopes in sediments and pore waters of Ocean Drilling Program Site 808, Nankai Trough: implications for fluid expulsion in accretionary prisms. Geology 23, 37-40.

You, C.-F., Spivack, A. J., Gieskes, J. M., Martin, J. B., Davisson, M. L., 1996. Boron contents and isotopic compositions in pore waters: a new approach to determine temperature induced artifacts- geochemical implications. Marine Geol. 129, 351-361.

You, C.-F., Castillo, P. R., Gieskes, J. M., Chan, L. H., Spivack, A. J., 1996. Trace element behavior in hydrothermal experiments: Implications for fluid processes at shallow depths in subduction zones. Earth Planet Sci. Lett. 140, 41-52.

Zhu, Y., Huang, Y., Matsumoto, R., Wu, B., 2003. Geochemical and stable isotopic compositions of pore fluids and authigenic siderite concretions for Site 1146, ODP Leg 184: Implication for gas hydrate. Proceeding of the ODP, Sci. Results 184.

CHAPTER 7.

Strontium Isotopic Composition in the Planktonic Foraminifera and Seawater: Calibration and Paleo-application

7.1 Introduction

The element strontium (Sr) has four isotopes, ^{84}Sr (0.56%), ^{86}Sr (9.86%), ^{87}Sr (7.00%) and ^{88}Sr (82.58%), and ^{87}Sr is the only Sr isotope that is affected by radioactive decay from ^{87}Rb ($T_{1/2}$= 4.88 × 10^{10} year, β^--decay). Because Sr isotopes are not fractionated by any natural chemical or biological processes, the ^{87}Sr/^{86}Sr ratio in natural samples is, therefore, mainly controlled by the Rb/Sr ratios during the formation of minerals or rocks and the age.

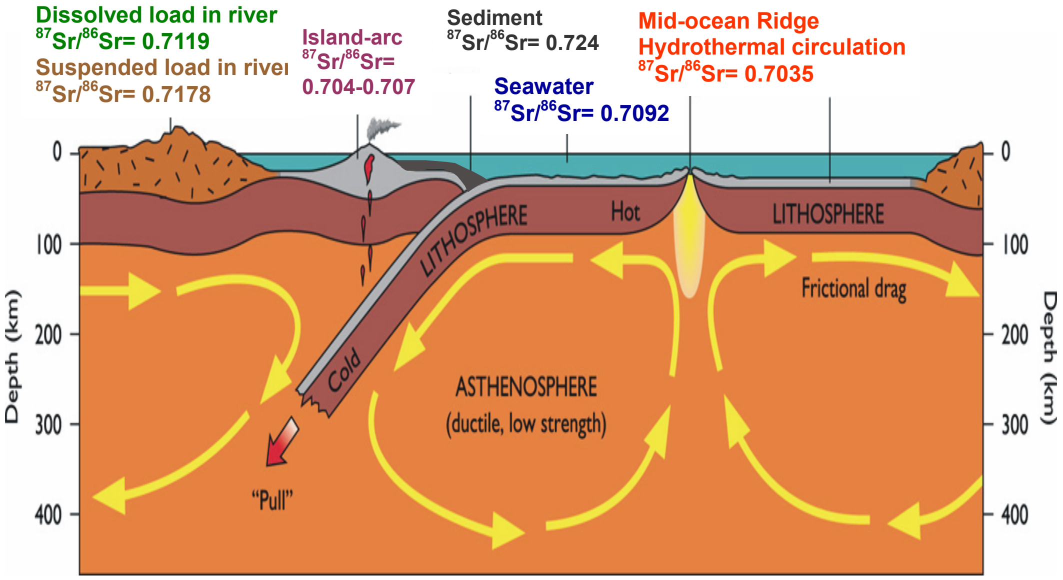

Figure 7.1 Sr isotopic compositions of several major reservoirs in the Earth system.

The global marine Sr isotopic mass balance is shown in Table 7.1 and the three main sources of Sr delivered to the oceans are: [1] Continental flux (i.e., River and groundwater inputs) with a high ^{87}Sr/^{86}Sr ratio of 0.7116 [*Palmer and Edmond*, 1989; *Galy et al.*, 1999]; [2] Hydrothermal flux (i.e., high-temperature and low-temperature hydrothermal alterations) with a low ^{87}Sr/^{86}Sr ratio of 0.7116 [*Palmer and Edmond*, 1989; *Richter et al.*, 1992]; [3] Benthic flux (i.e., buffering effect of carbonate diagenesis) with a ^{87}Sr/^{86}Sr ratios of 0.7084 [*Palmer and Edmond*, 1989]. The seawater ^{87}Sr/^{86}Sr ratio at any one time is mainly controlled by the relative amount of Sr from these three main sources (Figure 7.1).

Table 7.1 The global marine Sr isotopic budget. The total mass of Sr in seawater is 1.25 × 10^{17} mol.

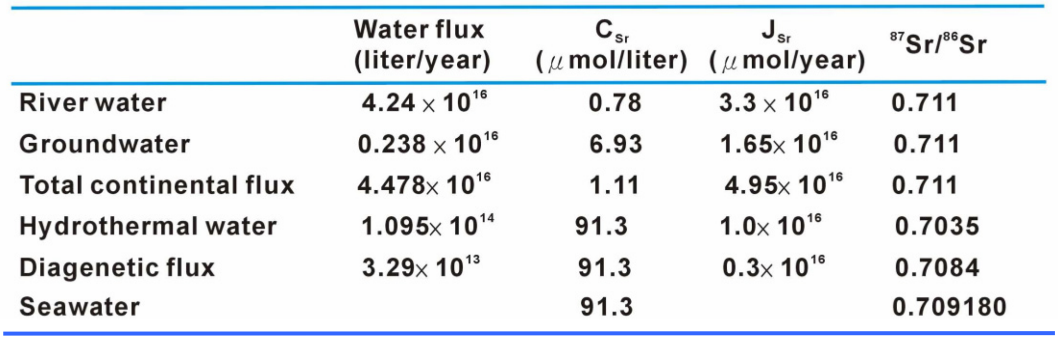

	Water flux (liter/year)	C_{Sr} (μmol/liter)	J_{Sr} (μmol/year)	$^{87}Sr/^{86}Sr$
River water	4.24×10^{16}	0.78	3.3×10^{16}	0.711
Groundwater	0.238×10^{16}	6.93	1.65×10^{16}	0.711
Total continental flux	4.478×10^{16}	1.11	4.95×10^{16}	0.711
Hydrothermal water	1.095×10^{14}	91.3	1.0×10^{16}	0.7035
Diagenetic flux	3.29×10^{13}	91.3	0.3×10^{16}	0.7084
Seawater		91.3		0.709180

Note that river values from Galy et al. [1999]; Groundwater values from Basu et al. [2001]; Hydrothermal and Diagenetic values from Palmer and Edmond [1989]

The $^{87}Sr/^{86}Sr$ isotope ratio of marine sediment has long been used as a proxy in isotopic stratigraphy, global climate change and chemical weathering studies [*Broecker and Peng*, 1982; *Burke and Denison*, 1982; *Raymo*, 1991; *Ingram and Sloa*n, 1992; *Andersson et al*., 1994; *Huh and Edmond*, 1998]. Variations of $^{87}Sr/^{86}Sr$ ratio in seawater has followed by a gradually increase over the last 40 Ma (*Hess et al*., 1986), and it evolves into an approximately linear increase for the last 2.5 Ma [*Hodell et al*., 1990]. These rapid increases in seawater $^{87}Sr/^{86}Sr$ are primarily attributed to enhanced erosion rates of continental rocks with a high $^{87}Sr/^{86}Sr$ ratio, and possibly associated with the uplifts of the Himalayas and the Tibetan Plateau, following the India-Asia continental collision [*Jacobsen*, 1988; *Capo and Depalo*, 1990; *Richter et al*., 1992].

Within the long-term variation of seawater $^{87}Sr/^{86}Sr$, some finer structures have been observed on the timescale of 0.5-1.0 Ma or even less [*Dia et al*., 1991; *Clemens et al*., 1993], which is much shorter than the residence time of Sr in the ocean (~2 Ma, *Basu et al*. [2001]). *Dia et al*. [1991] found small variations of ~20 ppm in the $^{87}Sr/^{86}Sr$ ratio recorded in foraminiferal shells over the past 300 kyrs, an seem to follow a cycle close to the 100-kyr periodicity (i.e., Eccentricity) seen for a number of other climate-related variations. Additionally, a high-resolution seawater ^{87}Sr/^{86}Sr record spanning the past 450 kyr also showed that seawater ^{87}Sr/^{86}Sr ratio coincides with changes in continental ice volume from SPECMAP oxygen isotope records [*Clemens et al.*, 1993]. This apparently suggests that there was less chemical weathering in arid glacial periods than in more humid interglacials, and was most likely controlled by variations in the global riverine Sr flux, and thus by weathering rates. However, more recently, *Henderson* et al. [1994] concluded that these cycles were caused by an analytical artifact according to the duplicated results of Pacific core V28-238, that used in the study of *Dia et al.* [1991] (see Figure 7.2).

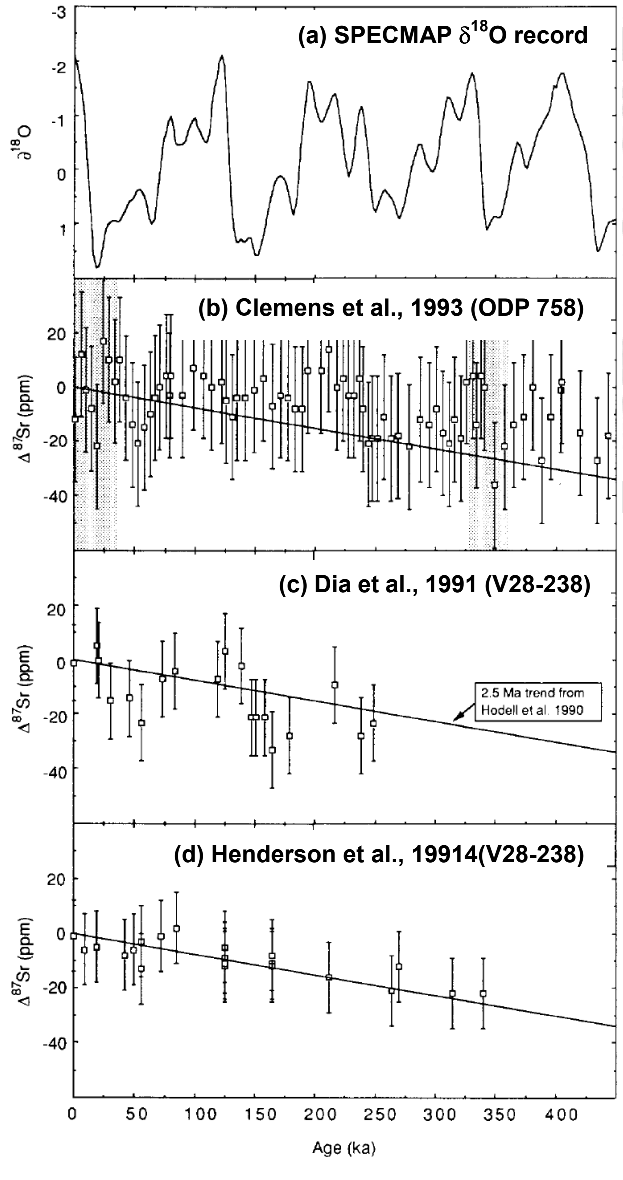

Figure 7.2 (a) SPECMAP δ18O curve [*Imbrie et al.*, 1984]. (b)- (d) Comparisons of reconstructed seawater Sr isotope ratios from *Clemens et al.* [1993], *Dia et al.* [1991] and *Henderson et al.* [1994], respectively. All errors are reported 2 s.d. external reproducibility and are: (b) 23 ppm; (c) 14 ppm; and (d) 13 ppm. All data are adjusted to an NBS 987 value of 0.710233, and Δ^{87}Sr (ppm)= {(^{87}Sr/^{86}Sr in sample /0.709158)-1}×10^{6}.

In this study, new and very high-precision $^{87}Sr/^{86}Sr$ measurements on seawater and planktonic foraminifera have been developed and further calibrated the Sr isotope fractionation between seawater and foraminiferal shells. Furthermore, several possible artifacts in the measurements of $^{87}Sr/^{86}Sr$ ratios were also investigated, including: [1] the potential influence of the adhering clay and [2] the isotopic variability in different planktonic species, in order to systematically evaluate the potential use of foraminiferal $^{87}Sr/^{86}Sr$.

7.2 Reagents and Laboratory equipment

Chemical reagents

The preparation of ultra-cleaned water, nitric and hydrochloric acids used in this study have been described in the section 6.2. The Sr and Rb concentrations of Millipore ultrapure water is less than 0.004 ppt [*Kano and Darbouret*, 1999]. For the Lab-purified HNO_3 and HCl, the blanks of Sr and Rb are less than 1 ppt, which is similar to the levels of Seastar® ultrapure HNO_3 and HCl.

Beaker, bottle and ware

During the entire sample preparation, only Teflon- and PP-wares were used to store or transfer sample solutions. The Teflon bottles and the Savillex PFA beakers were firstly soaked with 1N HCl or 1N HNO_3 over night prior to clean with ultrapure HNO_3 gas leaching in the cleaning system housed at NCKU. This special equipment was made by high-purity quartz and plastic materials to avoid any potential contamination. 6N HNO_3 were heating to boiling and then produce highly concentrated HNO_3 gas to leach the surface of the PFA wares in the quartz container at least for 6 hours. The PP-wares cleaning were conducted with 3N HNO_3 (or HCl) on a hot water bath of <100°C. All of the Teflon- and PP-wares were then rinsed with water for three times to make sure there is no HCl or HNO_3 solution left in the wares.

7.3 Column chemistry

7.3.1 The characteristics of Sr-spec resin

The extraction chromatographic materials Sr-spec (particle size 50-100 μm, see Figure 7.3) was obtained from Eichrom®. This resin consists of the crown ether di-tertbutyl-cis-dicyclohexano-18-Crown-6 in 1-octanol sorbed on the inert support Amberchrom CG-71ms [*Horwitz et al.*, 1991; *Horwitz et al.*, 1992].

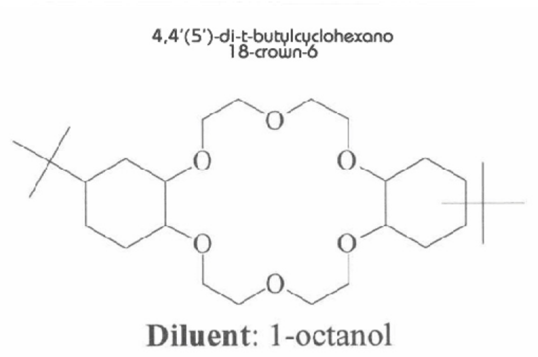

Figure 7.3 The chemical structure of crown ether, di-tertbutyl-cis-dicyclohexano-18-Crown-6.

Figure 7.4 shows the acid dependency of distribution coefficient, *k'* for Sr, as well as other alkali (Na, K, and Cs) and alkaline earth metals (Rb, Ca, Ba and Ra) on Sr-spec resin [*Horwitz et al.*, 1992]. The uptake of Sr by Sr-spec increases with increasing nitric acid concentration. For example, at 8N nitric acid, *k'* is approximately 90, and it falls to less than 1 at concentrations less than 0.05N. Another important feature is that the alkali and alkaline earth metals show much lower affinity for the resin than Sr across the concentration range of nitric acid, especially for Ca and Na. This would make Sr-spec resin more appropriate to be used to extract Sr from seawater-matrix or calcium carbonates. Besides, an efficient separation of Sr, Ba, Pb and Ra from natural samples could be performed with Sr-spec resin [*Deniel and Pin*, 2001]. By comparing with the total exchange capacity of Sr-spec resin (~9 mg/mL), a 0.1 mL seawater contains major ions (Na, Mg, Ca and Sr) of ~0.65 mg (without considering the differences in *k'* for these elements), which is less than 10% of the total capacity.

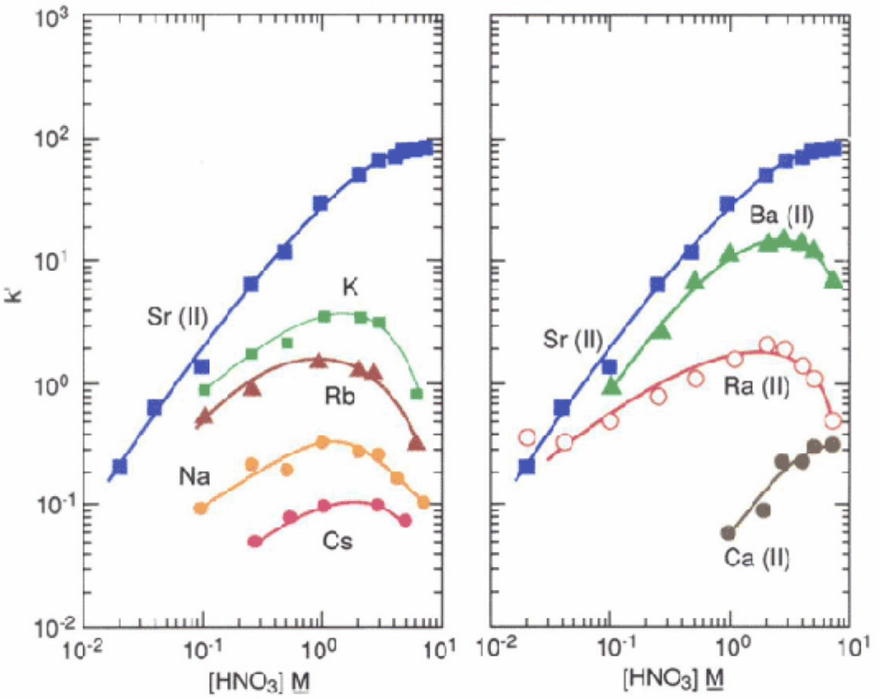

Figure 7.4 Acid dependency of *k'* for various concentration of nitric acid [*Horwitz et al.*, 1992]

7.3.2 Chemical procedure

The Sr separation procedure used in thus study was modified from the Sr column described by *Deniel and Pin* [2001]. All sample handling was performed in the Class 10 laminar flow clean box. PP-column (2.5 mL reservoir and 10cm long, 1cm i.d. BioRad®) with porous PE-frits at the bottom and on the top were used for the separation experiment. A small amount of Sr-spec in ultrapure water was loaded onto the columns, resulting in a ca. 1 mL bed volume. To avoid memory effects, new Sr-spec was used each sample whereas the columns were thoroughly cleaned with 6N HCl after each run.

A detailed chemical separation step was given in Table 7.2, and the Sr separation method has already been fully evaluated and shown in section 7.4. The Sr fraction was then evaporated to dryness on a hot plate with a constant temperature of ~80-85°C. For the seawater samples (0.1~0.2 mL), a proportion corresponding to 700-1400 ng Sr was loaded with highly dilute HCl onto a double outgassed Ta filament for high-precision mass spectrometric measurements.

Table 7.2 Cleaning, loading and elution steps for the Sr-spec resin in this study.

Step	Reagent	Amount (mL)	Flow rate (μL/min)	Purpose
1	water	10 × bed volume	500	wet beads and clean column
2	0.05N HNO_3	3 × bed volume	500	clean column
3	water	3 × bed volume	500	clean column
4	3N HNO_3	3 × bed volume	500	condition
5	sample	0.1~0.2	500	sample introduction
6	3N HNO_3	6 × bed volume	500	remove cations (e.g., Rb, Ca)
7	0.05N HNO_3	7 × bed volume	500	elute Sr

7.4 Results and Discussion

7.4.1 Sr recovery study

The recovery yield of the Sr is quantified by “standard calibration curve” method, and the efficiency of the Sr extraction is tested by the elution curves, and by evaluating the total chemical yield for the above Sr extraction technique. Because natural samples with large amounts of Ca and Na, like seawaters and carbonates, can dramatically affect Sr recoveries by Sr-spec resin, replicated results and introductions of different amounts (e.g., 0.1 mL vs. 0.2 mL seawater) of samples can be used to further test the recovery yield. Figure 7.5 shows excellent Sr and Ba recovery yields and repeatability, strongly suggesting that the Sr-spec resin can be successfully applied for samples with high Ca and Na contents.

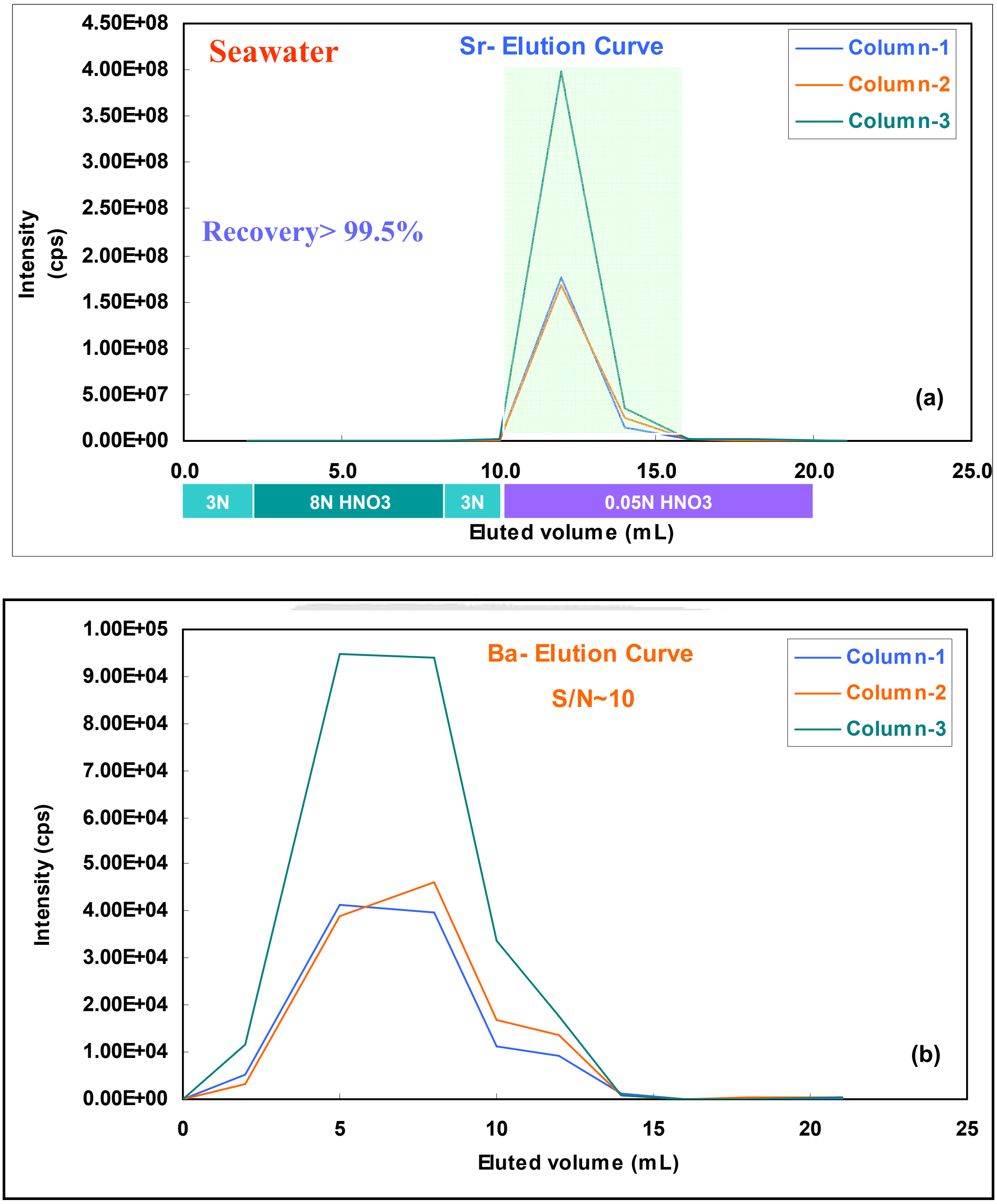

Figure 7.5 Elution curves of (a) Sr and (b) Ba for the natural seawaters by using Sr-spec resin.

7.4.2 Sr isotopic composition of seawater

Modern hydrological context of sampling station

To study the dynamic distribution of the Sr isotopic composition (Sr IC) in surface waters, samples were collected from several stations located at the South China

Sea (SCS, SEATs St-C, 18°N, 115°30'E, 2003-August), North Equatorial Current (NEC, ST-1, 12°N, 140°W, Figure 7.6), southern Okinawa Trough (SOT, S-1, S-3 and S-6, 2003-April), and Kao-Ping Estuary (KPE, Figure 7.7). Immediately after sampling through the Glo-Flo bottles, water samples were filtered through 0.45-μm membrane, transferred to acid-leached PP containers and then acidified to pH<1.5 with ultra-pure distilled HNO_3 (Sr blank <1 pg) on board. In land-based laboratory, Sr purification was performed under class 10-100 clean benches at NCKU. Sr isotope ratios were measured on a Thermo-Fisher Scientific TRITON TI at NCKU using the P-TIMS technique described in section 2.2.5. Data of potential temperature (θ) and salinity (S) were obtained from the National Center for Ocean Research (NCOR) to identify the water masses and can be further used to constrain the Sr ICs of oceanic water masses.

In the following discussion, ^{87}Sr/^{86}Sr ratios are expressed as ppm deviation from a seawater standard (STD).

$$\Delta^{87}Sr = \left(\frac{\left(\dfrac{^{87}Sr}{^{86}Sr} \right)_{sample}}{\left(\dfrac{^{87}Sr}{^{86}Sr} \right)_{STD}} - 1 \right) \times 10^{6} \qquad (ppm)$$

where STD represents the present-day seawater value of the deep North Pacific Ocean. The measured ^{87}Sr/^{86}Sr value of this seawater standard is 0.709180± 03 ppm in our laboratory.

In the SOT, the surface layer is primarily occupied by the Kuroshio Current (KC). Based on the θ-S plot reported by *Chen et al.* [1995], six water masses, Kuroshio Surface Water (SW), North Pacific Typical Water (NPTW, or KC), Kuroshio Intermediate Water (IW), East China Sea Surface Water (ECSW), Coastal Water (CW) and Taiwan Strait Water (TSW) are mixing in this area. These water masses may bring different sources of ^{87}Sr/^{86}Sr and eventually affect seawater Sr isotopic signatures.

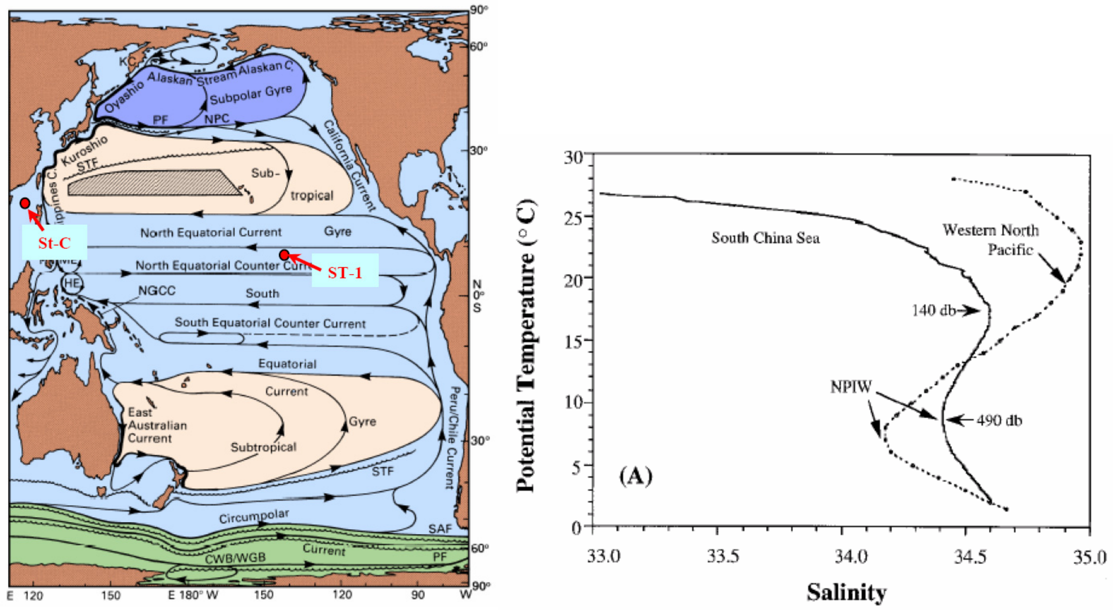

Figure 7.6 (a) Sampling locality of seawater samples from the SCS (St-C) and NEC (ST-1). (b) The typical θ-S diagram of water masses around Taiwan [*Alibo and Nozaki*, 2000].

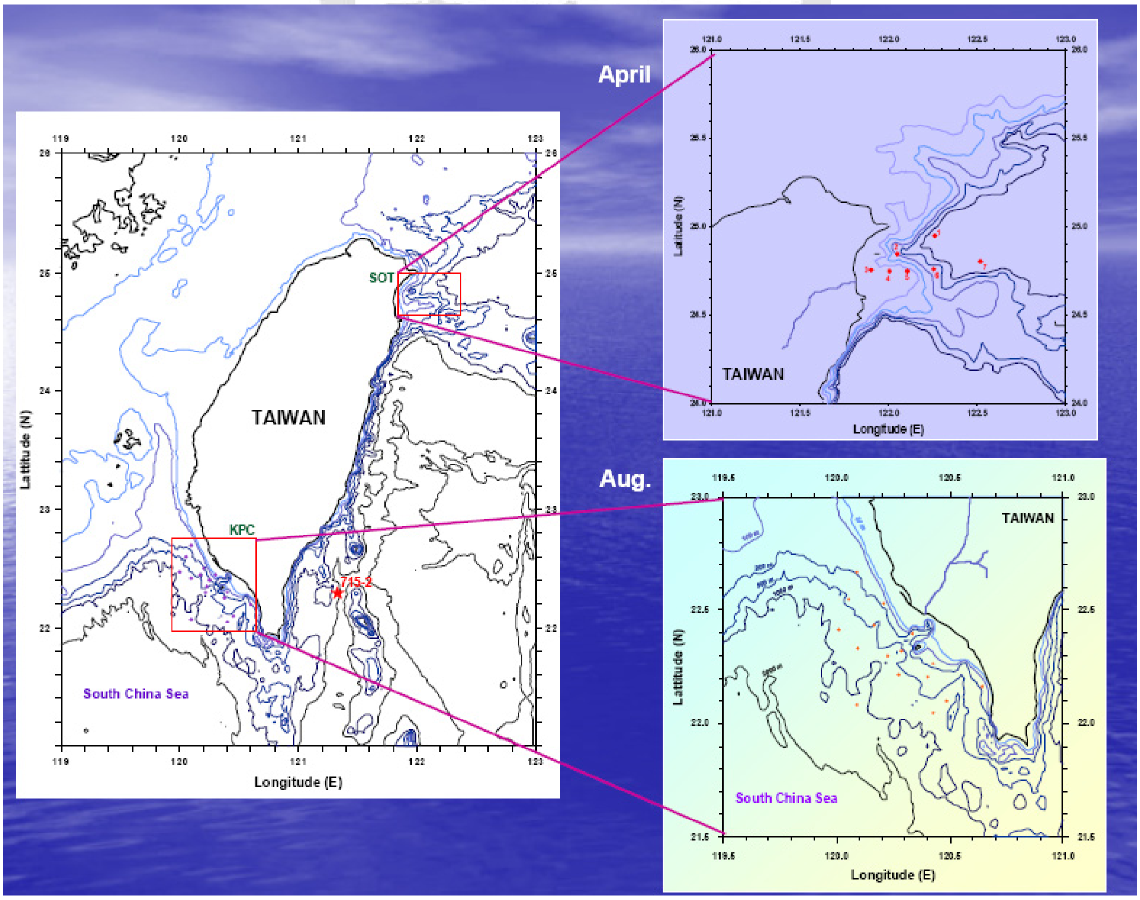

Figure 7.7 Sampling sites of surface seawaters in the SOT and KPE.

In the SCS, the climatic variation and water mass circulation in the upper ocean of the SCS are mainly modulated by seasonal prevailing monsoons. Typically, during the summer monsoon season, the SCS is dominated by prevailing southwest winds. In contrast, the SCS is dominated by prevailing northeast winds during the winter monsoon season. These annually reversing monsoon winds cause a clockwise water mass circulation in summer, and then gradually switch to a reversal counterclockwise gyre during wintertime [*Wyrtki*, 1961]. On the basis of the θ-S diagram, the subsurface salinity maximum (S=34.9) is marked at depth of around 140 m because of the influence of the KC (or North Pacific Typical Water, NPTW). The salinity minimum (S=34.4 in the SCS and S= 34.2 in the Western North Pacific, [*Nitani et al*., 1972; *Alibo and Nozaki*., 2000]) at water depth of ~490 m can be observed. This is most likely due to the intrusion of North Pacific Intermediate Water (NPIW) [*Li et al*., 1998; *Chu et al*., 1998]. The intermediate water in the SCS occupies depths of 250 to 1000 m, and its physical properties are quite similar to the NPIW [*Wyrtki*, 1961; *Nitani,* 1972]. This similarity has been attributed partly to the intrusion of NPIW, which is characterized with a salinity minimum at ~490 m. The SCS deep water is fed possibly by North Pacific Deep Water, based on hydrographic observations and T-S characteristics at 3500 m [*Nitani,* 1972; *Broecker et al*., 1986].

Surface water spatial distribution at the KPE is complex due to intense regional mixing of different sources, which exhibits a strong seasonal variability. In the wet summer season, the three dominant water masses near the KPE coastal region are Kao-ping River Water (KPRW), South China Sea Surface Water (SCSSW), and the KC. The KPRW (Δ^{87}Sr= 5547ppm), which carries a large amount of continental runoff with salinity close to 0, occupies predominantly the surface layer. The SCSSW (Δ^{87}Sr= 43.7 ppm, as inferred from the reference site, SEATs St-C), which transports water from the

SCS to the KPE, is influenced strongly by a clockwise eddy due to the prevailing southwest winds.

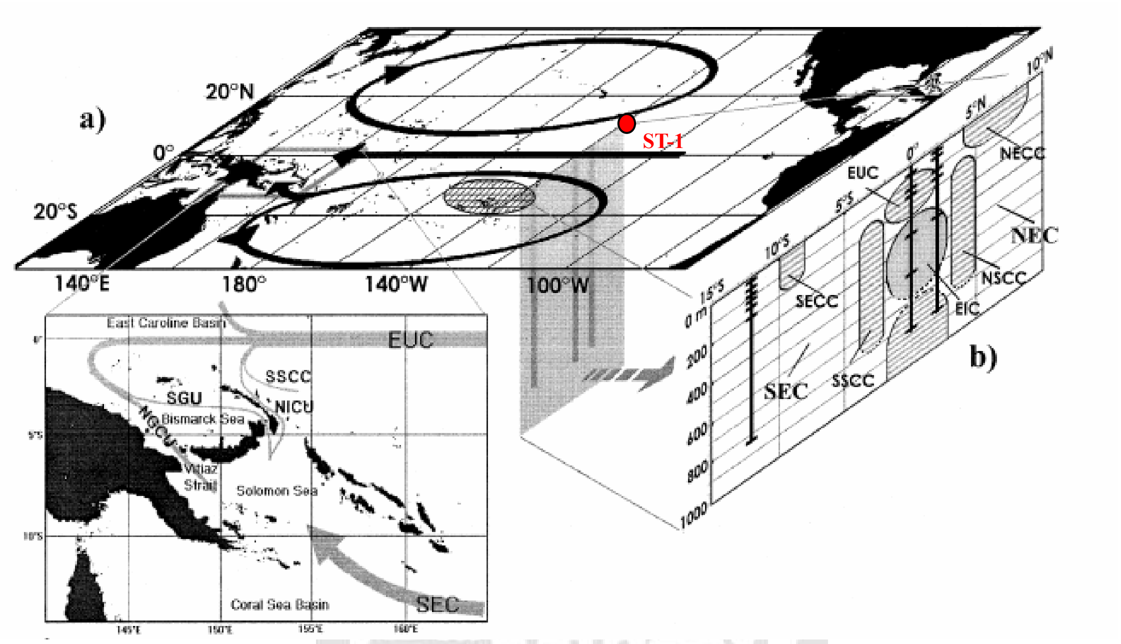

Figure 7.8 (a) Map of the central Pacific. The main structures of the surface circulation are presented by black arrows. Sampling station (ST-1) in the NEC is also shown by the red dot. (b) Details of the 140˚W section [*Tomczak and Godfrey*, 1994; *Lacan and Jeandel*, 2001].

As for the NEC station (ST-1), the major features of the circulation of the north equatorial Pacific are (1) a large anti-cyclonic gyres with axes along 20˚N and (2) the equatorial system (Figure 7.8). The NEC is the originated current of the NPTW (or KC). The NEC flows westward between 12-13˚N, and break into two branches, northward current- Kuroshio Current and southern current- Mindanao Current, near the Luzon island. Although the KC originates from the NEC, the chemical composition between the KC and NEC may be significantly different due to the exchange with volcanic materials from the Luzon Arc (e.g., seawater Nd and Sr isotopes).

Surface distribution of seawater Sr isotopic composition

Of special interest is that the surface seawater Sr ICs show non-homogeneous and dynamic distributions around the KPE and the SOT. $\Delta^{87}Sr$ in the coastal surface layers are highly variable, ranging from 12.7 to 64.9 ppm and from 20 to 48 ppm in the KPE and the SOT region, respectively. A large variability in $\Delta^{87}Sr$ in the KPE compared to the SOT should be related to the relatively higher contribution of freshwater plume or the intense water-sediment interaction in the KPE after a typhoon event [*Huang and You*, 2007]. For the seawater $\Delta^{87}Sr$, little attention has been paid until now because of the insufficient analytical precision (~±15 ppm, 2σ, [*Henderson et al.*, 1994]) and the relatively small variation (<50 ppm) in the seawater $^{87}Sr/^{86}Sr$ ratio. Through this new and extremely high precision (±4 ppm, 2σ) $^{87}Sr/^{86}Sr$ measurements on seawater samples, it should be able to revisit the Sr isotopic fractionation in the natural processes.

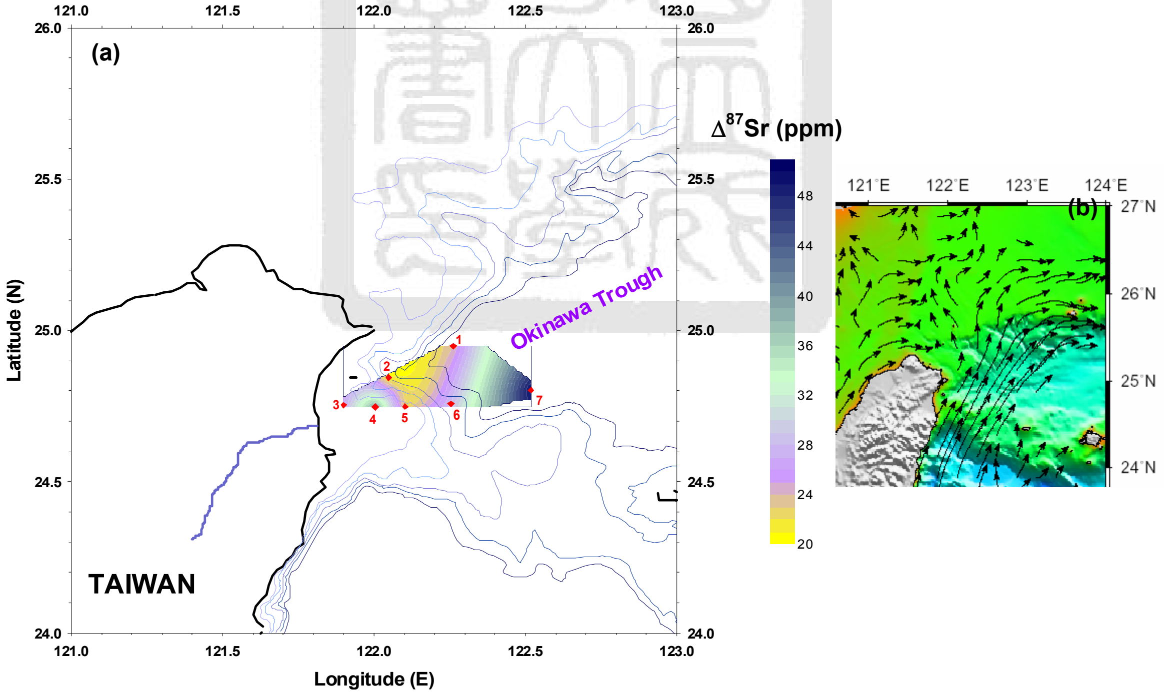

Figure 7.9 (a) Surface distribution of seawater Sr isotopic composition in the SOT. (b) Composite current vectors of the surface ocean [*adopted from NCOR*].

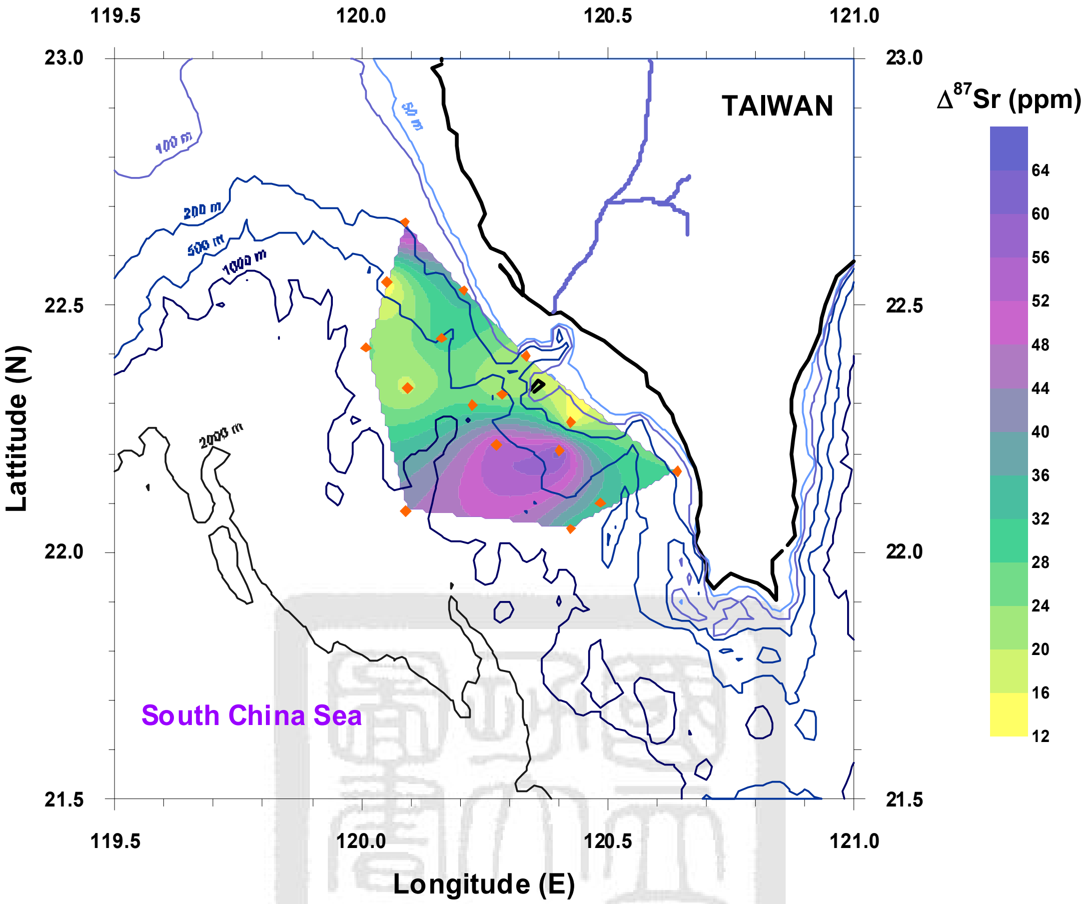

Figure 7.10 Surface distribution of seawater Sr isotopic composition in the KPE.

Vertical profile of seawater Sr isotopic composition

Several vertical profiles of the seawater Sr isotope have been shown in Figure 7.11. In the following discussion, the Sr profile in the NEC can be used as a reference station. This is because it locates at the Central Pacific, and no significant influence of continental inputs can affect the seawater ^{87}Sr/^{86}Sr (Figure 7.11a). At the station ST-1, the more radiogenic ^{87}Sr/^{86}Sr signature can be seen at three different water depths. For the surface layer of water column, it may be primarily caused by an accumulation of eolian dust with high ^{87}Sr/^{86}Sr ratio. At depth of 140 m and 350 m, another two enriched

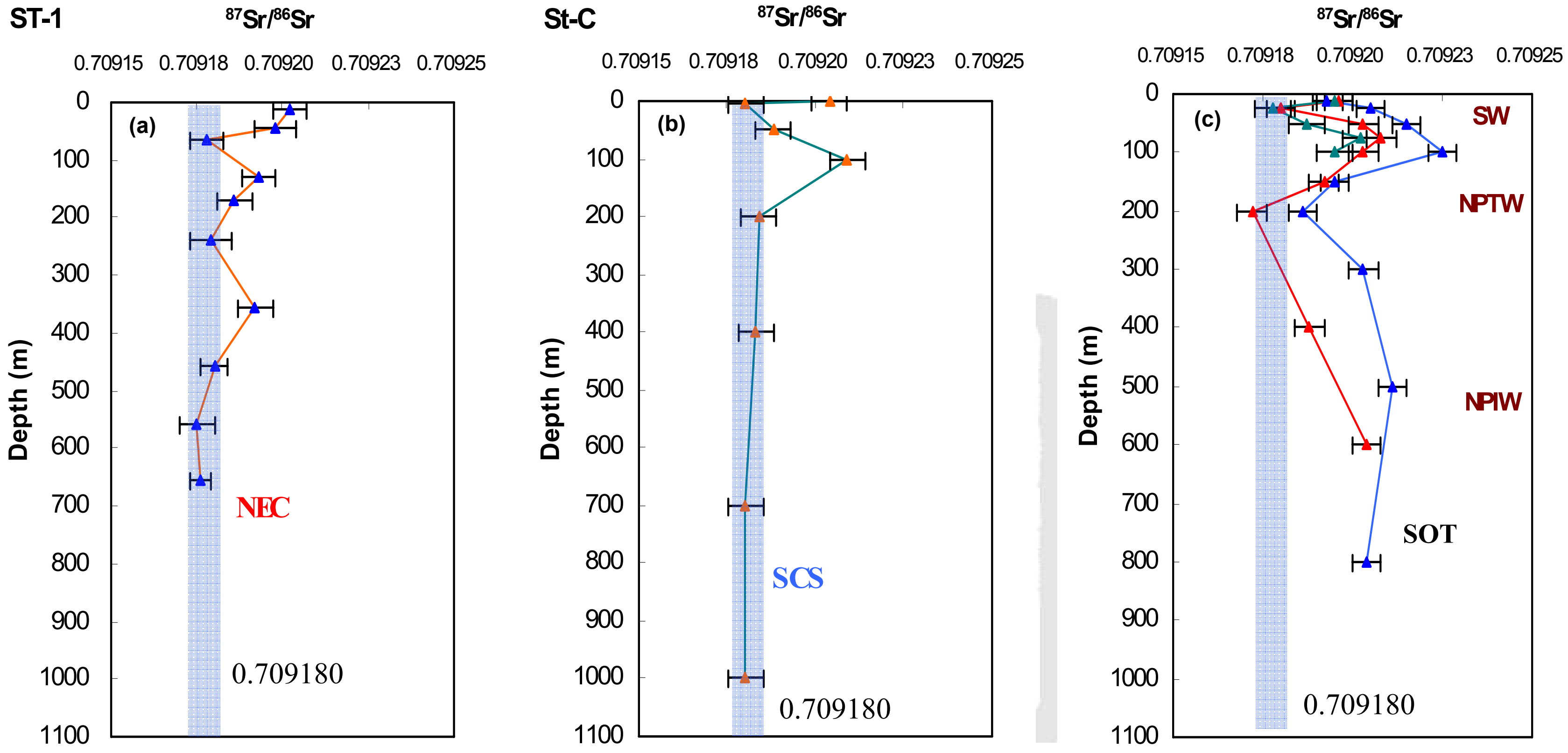

Figure 7.11 Vertical profiles of seawater ^{87}Sr/^{86}Sr ratios in the (a) NEC, (b) SCS and (c) SOT regions. Blue shaded area is an average value of the ^{87}Sr/^{86}Sr ratio (0.709180±0.000003) in the deep ocean. All errors are reported 2 s.d. external repeatability and are 4 ppm.

^{87}Sr water mass were observed. Because there is only very few data available for seawater Sr isotopes, therefore, the hypothesis and mechanism still needs to be confirmed by the more detailed investigations in the modern ocean. Like ST-1, the SCS station, St-C (Figure 7.11b), shows a more radiogenic Sr isotopic signature at the surface and the depth of 120-140 m, suggesting that water masses with the similar pathway might have a similar pattern of the seawater Sr isotope. For the peak at depth of ~350 m seen in the ST-1, it needs an enough sampling resolution to make a comparison. At the SOT stations, the vertical profiles of seawater Sr isotopes show a rather similar pattern among these stations, but slightly differ from the ST-1 and St-C. Again, this can only rely on the intense investigations on the seawater Sr isotopic ratios for various water masses.

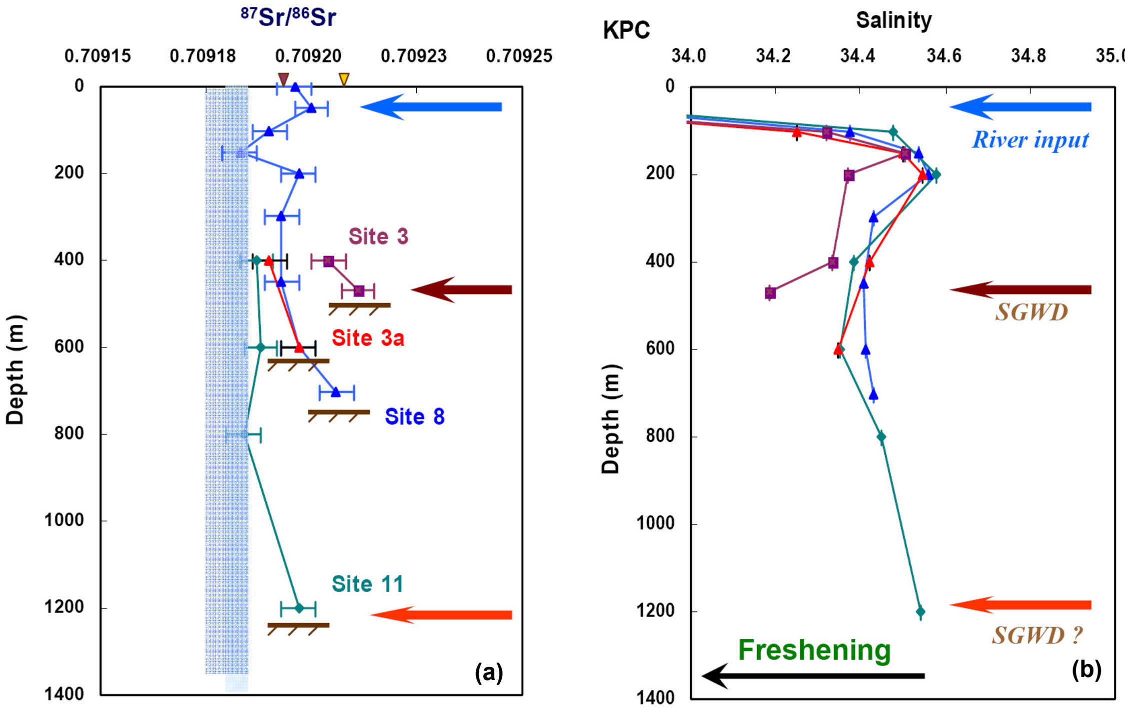

Figure 7.12 (a) Vertical profiles of seawater Sr isotopes along the Kao-ping submarine canyon. (b) The vertical changes in salinity along the Kao-ping Canyon. Blue shaded area is an average value of the ^{87}Sr/^{86}Sr ratio (0.709180±0.000003) in the deep ocean. All errors are reported 2 s.d. external repeatability and are 4 ppm. Blue, brown and red arrow indicates the water masses were influenced by river water, shallow and deep submarine groundwater discharge, respectively.

In contrast to previous ${}^{87}Sr/{}^{86}Sr$ measurements in seawaters [e.g., *Capo and DePaolo*, 1992; *Winter et al.*, 1997], the Sr ICs in the KPE and the central SCS were not distributed homogeneously in wet season. Vertical transect along the KPC, stations 3, 3a, 8 and 11, clearly depict unique characteristics of water masses in KPE (Figure 7.12a and 7.13). For the upper most 100 m, Sr ICs show more radiogenic (>20 ppm) signals than the deep SCS. This phenomenon can be explained in terms of heavy Sr addition due to continental inputs. At 100-150 m, Sr ICs display large discrepancies in station 8 and SCS-C, possibly caused by Kuroshio Current intrusion in summer [*Qu et al.*, 2000]. The detected Sr ICs anomalous distributions make it a novel tracer for monitoring water mass migration in coastal zone.

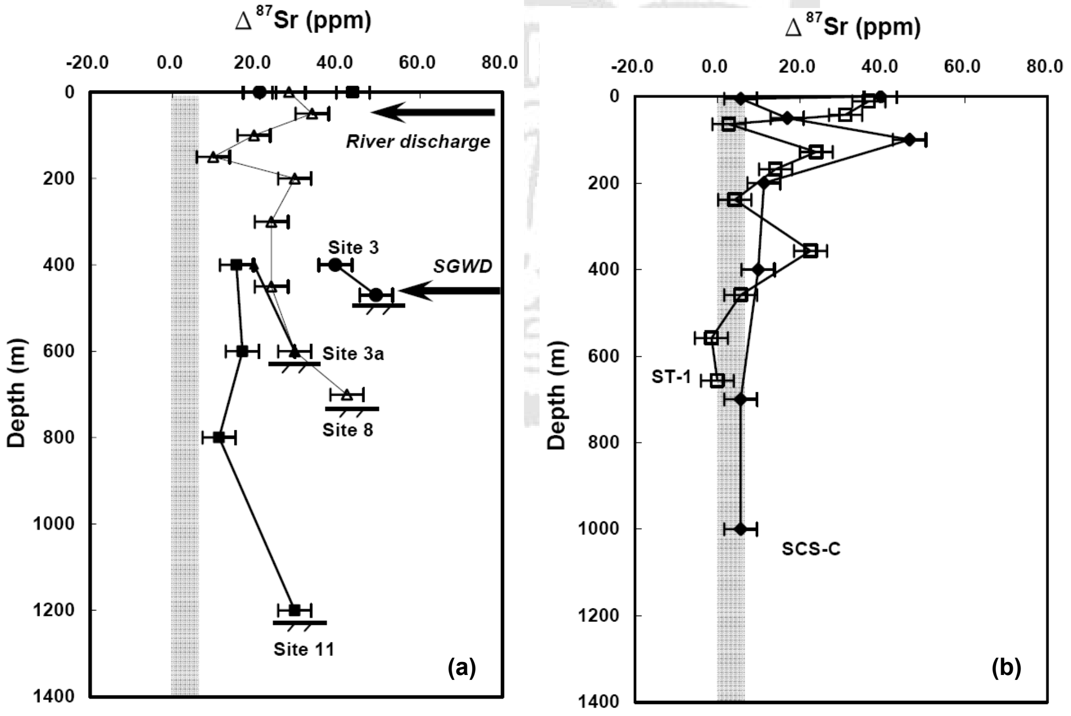

Figure 7.13 (a) Vertical profiles of seawater $\Delta^{87}Sr$ along the Kao-pings submarine canyon. (b) A comparison of the NEC ST-1 and SCS St-C stations. Gray shaded area is an average value of the ${}^{87}Sr/{}^{86}Sr$ ratio (0.709180±0.000003, or $\Delta^{87}Sr = 0$) in the deep ocean. All errors are reported 2 s.d. external repeatability and are 4 ppm.

An interesting correlation between Sr ICs and relative distance from the river mouth occurred at 300-700 m, where ${}^{87}Sr/{}^{86}Sr$ becomes less radiogenic with increasing distance from the estuary. At station 11, Δ^{87}Sr is similar to the deep water in the central SCS, suggesting negligible continental inputs. At depths greater than 800 m, theoretically, Sr ICs should be closed to the deep SCS or NPIW. The Δ^{87}Sr at 1200 m has, however, ~20 ppm higher than these deep waters. Contribution via SGWD at depth (>1000 m, e.g., offshore New Jersey; [*Robb*, 1984]) is likely to have occurred. Alternatively, more intense interactions associated with bottom re-suspension caused slightly heavy Sr ICs.

There are two ^{87}Sr-enriched layers along the KPC at 400-600 m and 1200 m, respectively (Figure 7.13a). In particular, Δ^{87}Sr at 400-600 m shows the largest enrichment in station 3, ~30-40 ppm. At stations 3a and 8, the Sr ICs were at least 20 ppm higher than station 11. This scenario is consistent with that a greater proportion of continental freshened water addition in the near estuary stations. This means that flood events associated with typhoon affected SGWD activity 50 km offshore. This agrees well with previous δ^{18}O and salinity results [*Lin et al.*, 2003], which found characterized light δ^{18}O and low salinity at the same layers. The Sr ICs, salinity (Figure 7.12b) and δ^{18}O suggest strong SGWD from aquifers in Pingtung Plain, which served as freshened waters sources at depth near the KPC. This study demonstrates that SGWD may discharge freshwater directly and continually into the coastal zone apart from brackish water recycle [*Moore et al.*, 1996]. In addition, NPIW occupied at 400-1500 m at the northern SCS may have modified Sr ICs in the KPE. The Δ^{87}Sr, however, displays little difference at depth below 400 m in station 11 and SCS-C (Figure 7.13b), where strong NPIW influence were rule out.

7.4.3 Sr isotopic composition of planktonic foraminifera

To investigate inter-species variations and the correlation between the seawater

Δ^{87}Sr profile and foraminiferal Δ^{87}Sr, three planktonic species, *P. obiliqulata*, *N. dutertrei* and *G. inflata*, were picked from two depth intervals of ODP Site 1144 sediments, corresponding to ~114.5 (MIS 5e) and 139 kyr old (MIS 6), respectively. Samples from the core-top sediments were also selected to test if the foraminiferal Δ^{87}Sr equilibrate with ambient seawater Δ^{87}Sr. Besides, because Site 1144 sediments contain large amounts of detrital materials than other cores collected from the open ocean, the effect of two different cleaning procedures (labeled "clean" and "unclean") was also investigated using these three planktonic species from the core-top sediment of Site 1144. In this study, cleaned samples were treated by "Cd "cleaning method.

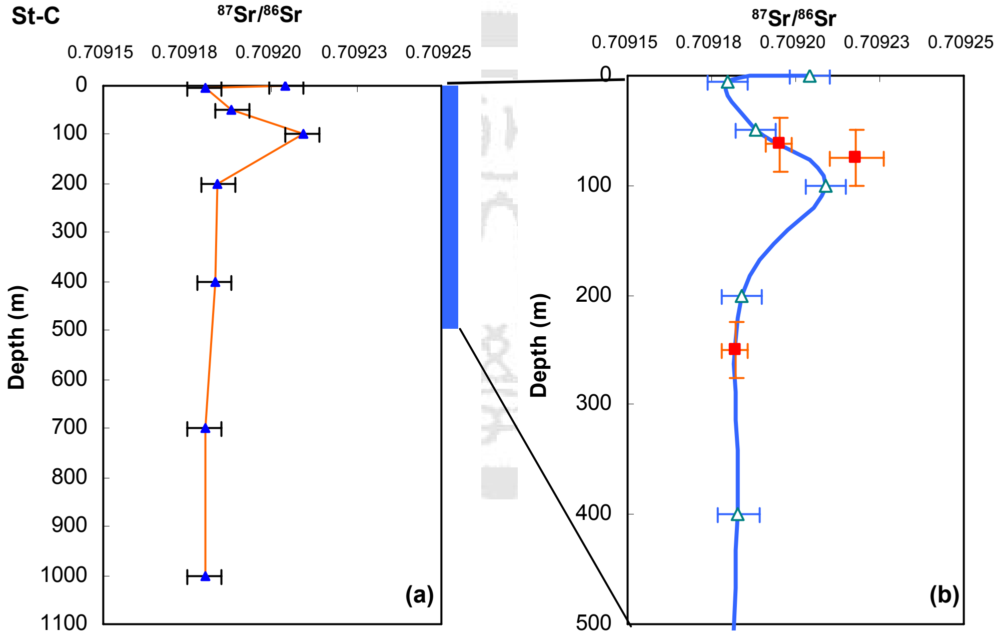

Figure 7.14 (a) Vertical profiles of seawater ^{87}Sr/^{86}Sr in the SCS station St-C. (b) A comparison between seawater ^{87}Sr/^{86}Sr and foraminiferal ^{87}Sr/^{86}Sr. Blue line and open trigonal symbols are presented the Sr isotopic distribution of upper 500 m in the SCS. Red squares are indicated the Sr isotopes of three planktonic species. Errors on the Sr isotopes are reported 2 s.d. external precision based on three duplicated data.

Measured ^{87}Sr/^{86}Sr ratios on three planktonic foraminifera are equal to the surrounding seawater (Figure 7.14), indicating that foraminiferal calcite is precipitated in equilibrium with seawater ^{87}Sr/^{86}Sr. This is the first result to demonstrate that foraminiferal ^{87}Sr/^{86}Sr can faithfully record seawater Sr isotopes, thus highlighting foraminiferal $^{87}Sr/^{86}Sr$ can be used as a seawater $^{87}Sr/^{86}Sr$ proxy. The $^{87}Sr/^{86}Sr$ ratio of *P. obliquiloculata* (0.709194±0.000004) presented here are also in a good agreement with published data ($^{87}Sr/^{86}Sr$= 0. 709188±0.000007, after correcting for the value of NBS 987) reported by *Henderson et* al. [1994], but different species have their own $^{87}Sr/^{86}Sr$, which is associated with their habitat depths. Conclusively, this preliminary result shows a species dependency, but is independent of pre-cleaning method (Figure 7.15).

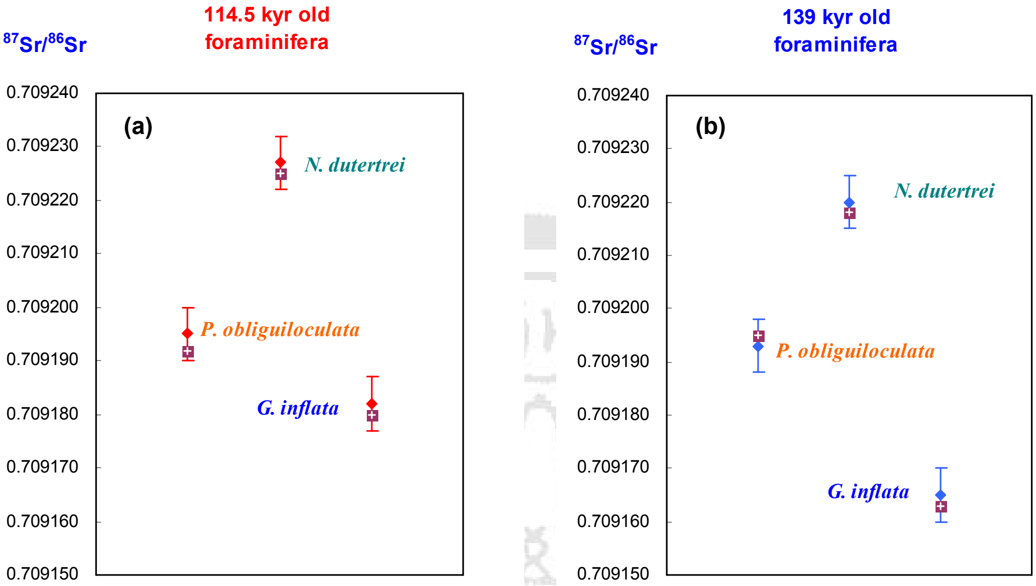

Figure 7.15 $^{87}Sr/^{86}Sr$ ratios in various species of planktonic foraminifers from (a) ~115kyr (MIS 5) and (b) ~139 kyr (MIS 6) samples demonstrating a dependence of the $^{87}Sr/^{86}Sr$ ratio on species. All errors are reported 2 s.d. external repeatability and are 4 ppm.

7.4.4 Glacial-interglacial changes in seawater $^{87}Sr/^{86}Sr$ ratios

The 100-kyr cycle of the seawater $^{87}Sr/^{86}Sr$ variation has been seen both in the Pacific and Indian oceans [*Dia et al.*, 1991; *Clemens et al.*, 1993], and have been characterized by glacial-interglacial fluctuations accompanied by glacio-eustatic changes in sea level and changes in continental erosion arising from varying low-latitude rainfall and river discharge. Although more recent study had pointed out that these cycles were caused by the analytical artifact [*Henderson et al.*, 1994], the results presented here can provide a most reliable seawater $^{87}Sr/^{86}Sr$ record based on the very high precision analytical technique for Sr isotopes. Additionally, the studying region, SCS, is a climate-sensitive marginal sea, which could be sensitive to climatic variability and further testify the hypothesis of the effect of sea-level changes on high-frequency $^{87}Sr/^{86}Sr$ variations [*Dia et al.*, 1991; *Clemens et al.*, 1993].

As the precision of Sr isotope analysis has been improved, it is possible to determine variations in $^{87}Sr/^{86}Sr$ of seawater over the ocean history. To evaluate the structure in the past 220 kyr (two glacial-interglacial cycles) of the seawater $^{87}Sr/^{86}Sr$ ratio, 15 samples of *N. dutertrei* (350-500 μm, ~30 individuals) from core SCS-15B in the central SCS (see Figure 7.16).

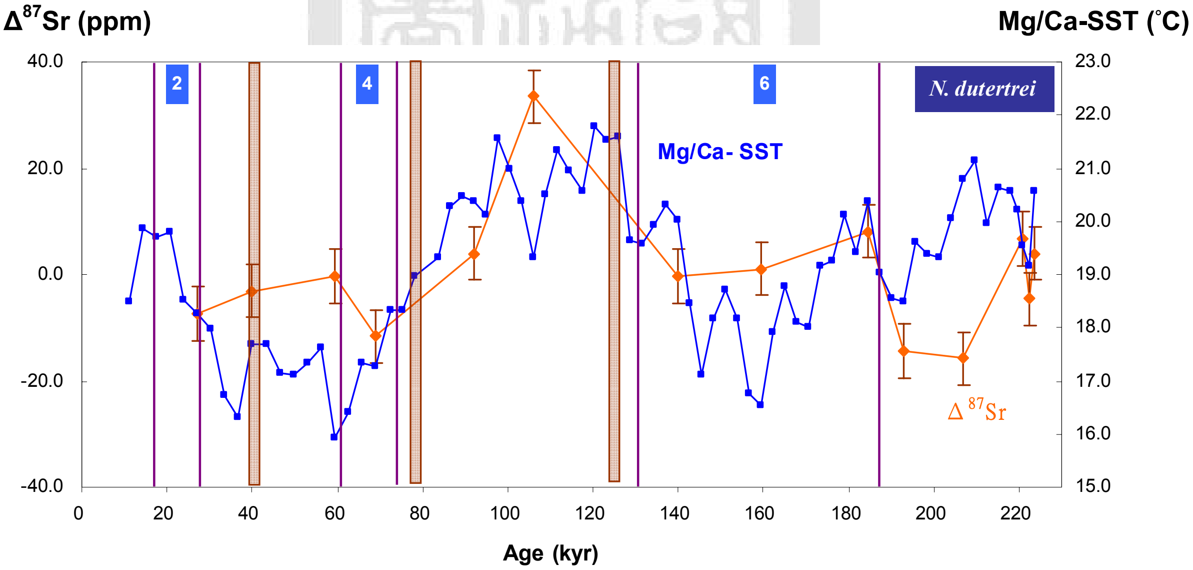

Figure 7.16 Mg/Ca-based SST records (blue line) and seawater $^{87}Sr/^{86}Sr$ variations (red line) reconstructed from the planktonic species, *N. dutertrei*, are shown for a comparison. Numbers on the top represented the Marine Isotope Stage (MIS) 2, 4 and 6. All errors are reported 2 s.d. external reproducibility and are 4 ppm.

A small, but significant variation of about 40 ppm in the $^{87}Sr/^{86}Sr$ ratio, and the amplitudes of the seawater $\Delta^{87}Sr$ in the SCS are ~2 times higher than the open ocean (~20 ppm). This is most likely due to the effect of amplification in the marginal sea. The main feature of seawater $\Delta^{87}Sr$ in the SCS are characterized by high $\Delta^{87}Sr$ values at interglacial intervals and low Δ^{87}Sr values during glacial times (Figure 7.16). The main reason to interpret these observations should be related to the variability in continental weathering inputs with glacial-interglacial fluctuations. During the interglacial period, an enhanced chemical weathering caused by a warm and humid climate condition can provide more continental inputs (with high ^{87}Sr/^{86}Sr) to the coastal ocean [*Dia et al*., 1991; *Clemens et al*., 1993], and then deliver into the marginal sea. On the other hand, *Stoll and Schrag*. [1998] had hypothesized that at the glacial time, more Sr could be released from exposed coral reefs in the continental shelf after the diagenetic process, and hence increase the seawater Sr/Ca ratio [*Stoll et al*., 1999]. However, this would not significant alter the seawater Sr isotope because the Sr isotopic composition in corals also nearly equilibrate with seawater ^{87}Sr/^{86}Sr.

7.5 Conclusions

This study provides the first detailed observations of Sr ICs in surface and vertical profiles near KPE in southern Taiwan. Combining results of Sr ICs, T, S and δ^{18}O, we have found that Sr ICs are distributed rather complicated and in-homogeneously both in vertical (Δ^{87}Sr variation >40 ppm) and surface (>50 ppm) distributions after a heavy flood event, as well as two reference sites in the central SCS and NEC. In the Kao-ping river-sea system, the surface Sr ICs were affected by mixing of three end-members water masses: two episodic continental runoffs with radiogenic Sr ICs and a modified SCSSW. The two radiogenic sources were most likely resulted from: (1) unusual inputs of radiogenic Sr due to typhoon disturbance in the upper stream (i.e., top soils or ambient rocks), (2) intense water/sediment interaction in seawater column in response to heavy rainfalls, and (3) normal river discharge plume into the coastal zone. These observations agree with salinity and δ^{18}O studies, but Sr ICs warrant much higher sensitivity compared with other conventional tracers. Vertical Δ^{87}Sr profiles along the Kao-ping canyon show large isotopic variations in the upper most 200 m, possibly were affected by continental runoffs and local seawater masses. Below 200 m, Sr ICs gradually become radiogenic while decreasing distance toward river mouth and reflect relatively high contribution of terrestrial inputs. Two radiogenic Sr layers occurred at 400-600 m and 1200 m, were attributed to influence of SGWD after typhoon event. Future works on Sr ICs in various water masses are necessary for a systematic evaluation of Sr ICs applications as a novel tracer to monitoring water mass migration and dynamic mixing in the coastal zones.

Sr isotopic composition in planktonic foraminifera shows a species dependency, but is independent of pre-cleaning method, and is in equilibrium with ambient seawater Sr isotopes. The results presented here strongly suggest that the use of foraminiferal Sr isotopes for reconstructing seawater ^{87}Sr/^{86}Sr ratios with time. A small, but significant variation of about 40 ppm in the seawater ^{87}Sr/^{86}Sr can be found in the SCS, and seems to follow a cycle to the previously reported 100-kyr cycle. This periodicity can be linked to one of the prominent cycles in the Earth's orbital parameters, which are known to modulate the patterns of solar insolation and climate. On this short timescale these changes are most likely be controlled by variations in the riverine Sr input, and thus by weathering rates.

References

Anand, P., Elderfield, H., Conte M. H., 2003. Calibration of Mg/Ca thermometry in planktonic foraminifera from sediment trap time series. Paleoceanography 18, 1050- 1065.

Al-Ammar, A., Gupta, R. K., Barnes, R. M., 1999. Elimination of boron memory effect in inductively coupled plasmas-mass spetrometry by addition of ammonia. Spectrochim. Acta Part B 54, 1077-1084.

Alibo, D. S., Nozaki, Y., 2000. Dissolved rare earth elements in the South China Sea: Geochemical characterization of the water masses. J. Geophys. Res. 105, C12, 28771-28783.

Andersson, P. S., Wasseerburg, G. J., Ingri, J., Stordal, M. C., 1994. Strontium, dissolved particulate loads in fresh and brackish waters: the Baltic Sea and Mississippi Delta. Earth Planet. Sci. Lett. 124, 195-210.

Barker, S., Elderfield, H., 2002. Foraminiferal calcification response to glacial-interglacial changes in atmospheric CO_2. Science, 297, 833-836.

Barth, S., 1997. Boron isotopic analysis of natural fresh and saline waters by negative thermal ionization mass spectrometry. Chem. Geol. 143, 255-261.

Barth, S., 2000. Geochemical and boron, oxygen, and hydrogen isotopic constraints on the origin of salinity in groundwaters from the crystalline basement of the Alpine Foreland. Applied Geochem. 15, 937-952.

Basu, A. R., Jacobsen, S. B., Poreda, R. J., Dowling, C. B., Aggarwal, P. K., 2001. Large groundwater strontium flux to the oceans from the Bengal Basin and the marine strontium isotope record. Science 293, 1470-1473.

Bé, A. W. H., 1980. Gametogenic calcification in a spinoso planktonic foraminifer Globigerinoides sacculifer (Brady). Mar. Micropaleont. 5, 283-310.

Bé, A. W. H., 1982. Biology of planktonic foraminifera. In: Foraminifera: Notes for a short course. Studies in Geology Vol. 6. Broadhead TW (ed) Univ. Tenn. Knoxville 51-92.

Bé, A. W. H., Hemleben, C., Anderson, O. R., Spindler, M., Hacunda, J., Tunitivate-Choy, S., 1977. Laboratory and field observation of living planktonic foraminifera. Micropaleont. 23, 155-179.

Bemis, B. E., Spero, H. J., Bijma, J., Lea D. W., 1998. Reevaluation of the oxygen isotopic composition of planktonic foraminifer: Experimental results and revised paleotemperature equations. Paleoceanography 13, 150-160.

Bentov, S., Erez, J., 2005. Novel observations on biomineralization processes in foraminifera and implications for Mg/Ca ratio in the shells. Geology 33, 841-844.

Bentov, S., Erez, J., 2006. Impact of biomineralization processes on the Mg content of foraminiferal shells: A biological perspective. Geochem. Geophys. Geosys. 7, doi:10.1029/2005GC001015.

Birck, J. L., Roy Barman, M., Capmas, F., 1997. Re-Os isotopic measurements at the femtomole level in natural samples. Geostandard Newsletter: The Journal of Geostandards and Geoanalysis 21, 19-27.

Boyle, E. A., Keigwin, L. D., 1985/1986. Comparison of Atlantic and Pacific paleochemical records for the last 215, 000 years: Changes in deep ocean circulation and chemical inventories. Earth Planet. Sci. Lett. 76, 135-150.

Boyle, E. A., 1988. The role of vertical chemical fractionation in controlling late Quaternary atmospheric carbon dioxide. J. Geophys. Res. 15701-15714.

Broecker, W. S., Peng T.-H. , 1982. Tracers in the Sea, Eldigio Press, New York.

Broecker, W. S., Patzert, W. C., Toggweiler, J. R., Stuiver, M., 1986. Hydrography, chemistry, and radioisotopes in the southeastern Asian basins. J. Geophys. Res. 91, 14345- 14354.

Broecker, W. S., 1997. Thermohaline circulation, the Achilles heel of our climate system: Will man-made CO2 upset the current balance? Science 278, 1582-1588.

Brumsack, H., Zuleger, E., 1992. Boron and boron isotopes in pore waters from ODP Leg 127, Sea of Japan. Earth Planet Sci. Lett. 113, 427-433.Boyle, E. A., Keigwin, L. D., 1982. Deep circulation of the North Atlantic over the last 200,000 years: Geochemical evidence. Science 218, 784-787.

Burke, W. H. Denison, R. E., 1982. Variation of seawater ^{87}Sr/^{86}Sr throughout Phanerozoic time. Geology 10, 516-519.

Chen, C.-T. A., Wang, S.-L., Chou, W.-C., Sheu, D. D., 2006. Carbonate chemistry and projected future changes in pH and CaCO3 saturation of the SCS. Marine Chem. 101, 277-305.

Capo, R. C., DePaolo, D. J., 1990. Seawater strontium isotopes variation from 2.5 million yearsto present. Science 249, 51-55.

Capo, R. C., DePaolo D. J., 1992. Homogeneity of Sr Isotopes in the Oceans. EOS Transactions of the AGU 73, 272.

Chen, C.-T. A., Ruo, R., Pai, S. C., Li, C. T., Wong, G. T. F., 1995. Exchange of water masses between the East China Sea and the Kuroshio off northeastern Taiwan. Cont. Shelf Research 15, 19-39.

Chu, P. C., Fan, C., Lozano, C. J., Kerling, J. L., 1998. An airborne expendable bathy-thermography survey of the South China Dea, May, 1995. J. Geophys. Res. 103, 21637-21652.

Clemens, S. C., Farrell, F. W., Gromet L. P., 1993. Synchronous changes in seawater strontium isotope composition and global climate. Nature 363, 607-610.

Chou, W. C., Sheu, D. D., Chen, C.-T. A., Wang, S. L., Tseng, C. M., 2005. Seasonal variability of carbon chemistry at the SEATs time series site, northern South China Sea between 2002 and 2003. T. A. O. 16, 445-465.

Clark, D., Hobart, D. E., Neu, M. P., 1995. Actinide carbonate complexes and their importance in actinide environmental chemistry. Chem. Rev., 95, 25-48.

Cuffey, K. M., Vimeux, F., 2001. Covariation of carbon dioxide and temperature from Vostok ice core after deuterium-excess correction. Nature 412, 523-527

Deniel, C., Pin, C., 2001. Single-stage method for the simultaneous isolation of lead and strontium from silicate samples for isotopic measurements. Anal. Chim. Acta 426, 95-103.

Deyhle, A., Kopf, A., Eisenhauer, A., 2001. Boron systematics of authigenic carbonates: A new approach to identify fluids processes in accretionary prisms. Earth Planet. Sci. Lett. 187, 191-205.

Deyhle, A., Kopf, A., 2001. Deep fluids and ancient pore waters at the backstop: Stable isotope systematics (B, C, O) of mud-volcano deposits on the Mediterranean Ridge accretionary wedge. Geology 29, 1031-1034.

Deyhle, A., Kopf, A., 2002. Strong B enrichment and anomalous δ^{11}B in pore fluids from the Japan Trench forearc. Marine Geol. 183, 1-15.

Deyhle, A., Kopf, A., Frape, S., Hesse, R., 2004. Evidence for fluid flow in the Japan Trench forearc using isotope geochemistry (Cl, Sr, B): Results from ODP Site 1150. The Island Arc 13, 258-270.

Dia, A. N., Cohen, A. S., O'Nions, R. K. Shackleton N. J., 1991. Seawater Sr- isotope variations over the last 300ka and global climate change. Nature 356, 786-789.

Dickson, A. G., Millero, F. J., 1987. A comparison of the equilibrium constants for the dissociation of carbonic acid in seawater media. Deep Sea Res. Part A 34, 1733-1743.

Dickson, A. G., 1990. Thermodynamics of the dissociation of boric-acid in synthetic seawater from 273.15-k to 318.15k. Deep Sea Res. Part A 37, 755-766.

Djogic, R., Sipos, L., Branica, M., 1986. Characterization of uranium (VI) in seawater. Limnol. Oceanogr. 31, 1122-1131.

DOE., 1994. Handbook of methods for the analysis of the various parameters of the carbon dioxide system in seawater. Version 2. Dickson, A. G., and Goyet, C., editors.

ORNL/CDIAC-74.

Elderfield, H., Ganssen G., 2000. Reconstruction of temperature and δ^{18}O of surface ocean waters using Mg/Ca of planktonic foraminiferal calcite. Nature 405, 442-445.

Emiliani, C., 1955. Pleistocene temperatures. J. Geol. 63, 538-578.

Epstein, S., Buchsbaum, R., Lowenstam, H. A., Urey, H. C., 1953. Revised carbonate-water temperature scale. Bull. Geol. Soc. Am. 64, 1315-1326.

Erez, J., 2003. The source of ions for biomineralization in foraminifera and their implications for paleoceanographic proxies. Reviews in mineralogy and Geochemistry 54, Biomineralization, 115-149.

Falkowski, P. G. et al., 2000. The global carbon cycle: A test of our knowledge of earth as a system. Science 290, 291-296.

Feely, R. A., Sabine, C. L., Lee, K., Berelson, W., Kleypas, J., Fabry, V. J., Millero, F. J., 2004. Impact of anthropogenic CO_2 on the $CaCO_3$ system in the oceans. Science 305, 362-366.

Fischer, H., Wahlen, M., Smith, J., Mastroianni, D, Deck, B., 1999. Ice core records of atmospheric CO2 around the last three glacial terminations. Science 283, 1712-1714.

Fitts, T. G., Brown, K. M., 1999. Stress induced smectite dehydration remifications for patterns of freshening fluid expulsion in the N. Barbados accretionary wedge. Earth Planet. Sci. Lett. 172, 179-197.

Gäbler, H., Bahr, A., 1999. Boron isotopic ratio measurements with a double-focusing magnetic sector ICP mass spectrometer for tracing anthropogenic input into surface and ground water. Chem. Geol. 156, 323-330.

Gaillardet, J., Allegre, C. J., 1995. Boron isotopic composition of corals: Seawater or diagenesis record? Earth Planet Sci. Lett. 136, 665-676.

Gaillardet, J., Lemarchand, D., Go¨pel, C., Manhe`s, G., 2001. Evaporation and sublimation of boric acid: application for boron purification from organic rich solutions. Geostand. Newsl. 25 Ž1., 67–75.

Galy, A., France-Lanord, C., Derry, L. A., 1999. The strontium isotopic budget of Himalayan rivers in Napal and Bangladesh. Geochim. Cosmochim. Acta 63, 1905-1925.

Grossman, E. L., 1987. Stable isotopes in modern benthic foraminifera: A study of vital effect. J. Foramin. Res. 17, 48-61.

Huh, Y., Edmond, J. M., 1998. On the interpretation of the oceanic variations in ^{87}Sr/^{86}Sr recorded in marine limestones. Proc. Indian Acad. Sci. 107, 293-305.

Hedley, R. H., Adam, C. G., 1978. Foraminifera. Vol. 3. Academic Press, London.

Hemleben, C., Spindler, M., Anderson, O. R., 1989. Modern Olanktonic Foraminifera.

Spring-Verlag, New York.

Hemming, N. G., Hanson, G. N., 1992. Boron isotopic composition and concentration in modern carbonates. Geochim. Cosmochim. Acta 56, 537-543.

Hemming, N. G., Hanson, G. N., 1994. A procedure for the analysis of boron by thermal ionization mass spectrometry. Chem. Geol. 114, 147-156.

Hemming N. G., Guilderson T. P., Fairbanks R. G., 1998. Seasonal variations in the boron isotopic composition of a coral: A productivity signal? Global Biogeochem. Cy. 12, 581–586.

Henderson, G. M., Martel, D. J., O'Nions R. K., Shackleton, N. J., 1994. Evolution of seawater ^{87}Sr/^{86}Sr over the past 400 ka: the absence of glacial/interglacial cycles. Earth Planet. Sci. Lett. 128, 643-651.

Hershey, J. P., Fernandez, M., Milne, P. J., Millero, F. J., 1986. The ionization of boric acid in NaCl, Na-Ca-Cl, and Na-Mg-Cl solution at 25°C. Geochim. Cosmochim. Acta 50, 143-148.

Hess, J., Bender, M. L., Schilling, J-G., 1986. Evolution of the ratio of strontium-87 to strontium-86 in seawater from Cretaceous to present. Science 231, 979–984.

Higginson, M. J., Maxwell, J. R., Altabet, M. A., 2003. Nitrogen isotope and chlorine paleoproductivity records from the northern South China Sea: Remote vs. local forcing of millennium- and orbital-scale variability. Marine Geol. 201, 223-250.

Hodell, D. A., Mead, G. A., Mueller, P. A., 1990. Variations in the strontium isotopic composition of seawater (8Ma to present) implications for chemical weathering rates and dissolved fluxes to the oceans. Chem. Geol. 80, 291-307.

Hönisch, B., Hemming, N. G., 2004. Ground-truthing the boron isotope-paleo-pH proxy in planktonic foraminifera shells: Partial dissolution and shell size effects. Paleoceanography 19, doi:10.1029/2004PA001026.

Hönisch, B., Hemming, N. G., 2005. Surface ocean pH response to variations in pCO_2 through two full glacial cycles. Earth Planet. Sci. Lett. 236, 305-314.

Horwitz, E. P., Dietz, M. L., Fisher, D. E., 1991. Anal. Chem. 63, 522.

Horwitz, E. P., Chiarizia, R., Dietz, M. L., Solvent Extr. Ion Exch. 10, 313

Huang K.-F., You C.-F., 2007. Tracing Freshwater Plume Migration in the Estuary after a Typhoon Event using Sr Isotopic Ratios. Geophysical Research Letters 34, L02403, doi:10.1029/2006GL028253.

Huang, K.-F., You, C.-F., Lin, H.-L., Shieh, Y. T., 2007. In situ calibration of Mg/Ca ratio in planktonic foraminiferal shell using time-series sediment trap: A case study of intense dissolution artifact in the South China Sea. (Submitted to Geochem. Geophys. Geosyst).

Ingram, B. L., Sloan D., 1992. Strontium isotopic composition of estuarine sediments as Paleosalinity and Paleoclimate Indicator. Science 255, 68-72.

Ishikawa, T., Nakamura, E., Boron isotope systematics of marine sediments. Earth Planet. Sci. Lett. 117, 567-580.

Kakihana, H., Kotoka, M., Shohei, S., Nomura, M., Okamota, M., 1977. Fundamental studies on the ion-exchange separation of boron isotopes. Bull. Chem. Soc. Jpn. 50, 158-163.

Kano, I., Darbouret, D., 1999. Ultrapure water for boron and silica sensitive laboratory Applications. The R $ D Notebook, Millipore.

Kastner, M., Kvenvolden, K. A., Whiticar, M. J., Camerlenghi, A., Lorenson, T. D., 1995. Relation between pore fluids chemistry and gas hydrates associated with bottom simulating reflectors at thr Cascadia Margin, Site 889 and Site 892. Proceeding of the ODP, Sci. Results 146, 175-187.

Kienast, M., Calvert, S. E., Pelejero, C., Grimalt, J. O., 2001. A critical review of marine sedimentary $\delta^{13}C_{org}$-pCO_2 estimates: New palaeo-records from the South China Sea and a revisit of the other low-latitude $\delta^{13}C_{org}$-pCO_2 records. Global Biogeochem. Cycles 15, 113-127.

Kienast, M., Hanebuth, T. J., Pelejero, C., Steinke, S., 2003. Synchrononeity of meltwater pulse 1a and the Bøiling warming: New evidence from the South China Sea. Geology 31, 67-70.

Kiss, E., 1988. Ion exchange separation and spectrophotometric determination of boron in geological materials. Anal. Chim. Acta 211, 243–256.

Kohler-Rink, S., Kuhl, M., 2000. Microsensor studies of photosynthesis and respiration in large symbiotic foraminifera. The physico-chemical microenvironment of Marginopora vertebralis, Amphistegina lobifera and Amphisorus hemprichii. Mar. Biol.137, 473-486.

Kohler-Rink, S., Kuhl, M., 2001. Microsensor studies of photosynthesis and respiration in large symbiont bearing foraminifera, Amphistegina lobifera and Amphisorus hemprichii. Ophelia 55, 111-122.

Kopf, A., Deyhle, A., Zuleger, E., 2000. Evidence for deep fluid circulation and gas hydrate dissociation using boron and boron isotopes of pore fluids in forearc sediments from Costa Rica (ODP Leg 170). Marine Geol. 167, 1-28.

Kopf, A., Deyhle, A., 2002. Back to the roots: boron geochemistry of mud volcanoes and its implications for mobilization depth and global B cycling. Chem. Geol. 192, 195-210.

Kuile, B., Erez, J., 1987. Uptake of inorganic carbon and internal carbon cycling in symbiont-bearing benthic foraminifera. Mar. Biol. 94, 499-510.

Lacan F., Jeandel, C., 2001. Tracing papua New Guinea imprint on the central Equatorial Pacific Ocean using neodymium isotopic compositions and Rare Earth Element patterns. Earth Planet. Sci. Lett. 186, 497-512.

Langer, M. R., 1992. Biosynthesis of glycosaminoglycans in foraminifera: a review. Mar. Micropaleont. 19, 245-255.

Lea, D. W., Boyle E. A., 1993. Determination of carbonate-bound barium in corals and foraminifera by isotope dilution plasma mass spectrometry. Chem. Geol. 103, 73-84.

Lea, D. W., 1999. Trace elements in foraminiferal calcite. Modern Foraminifera, 259-277. Hemming, G. N., Hanson, G. N., 1992. Boron isotopic composition and concentration in modern carbonates. Geochim. Cosmochim. Acta 56, 537-543.

Lea, D. W., Pak, D. K., Spero, H. J., 2000. Climate impact of late Quaternary equatorial Pacific sea surface temperature variations. Science 289, 1719-1724.

Leeman, W.P., Vocke, R.D., Bearly, E.S., Paulsch, P.J. P., 1991. Precise boron isotopic analysis of aqueous samples ion exchange extraction and mass spectrometry. Geochim. Cosmochim. Acta 55, 3901–3907.

Lemarchand, D., Gaillardet, J., Lewin, E., Allegre, C. J., 2000. The influence of rivers on marine boron isotopes and implications for reconstructing past ocean pH. Nature 408, 951-954.

Lemarchand, D., Gaillardet, J., Lewin, E., Allegre, C. J., 2002. An optimized procedure for boron separation and mass sprectrometry for river water samples. Chem. Geol. 182, 323-334.

Lewis, E., Wallace, D. W. R., 1998. Program developed for CO_2 system calculations, Rep. ORNL/CDIAC-105, Carbon Dioxide Ind. Anal. Cent. Oak Ridge Natl. Lab. U. S. Dept. of Energy, Oak Ridge, Tenn.

Lin, H.-L., Wang, W.-C., Hung, G.-W., 2004. Seasonal variation of planktonic foraminiferal isotopic composition from sediment traps in the South China Sea. Mar. Micropaleontol. 53, 447-460.

Li, L., Nowlin, W. D., Lilan, S., 1998. Anticyclonic rings from the Kuroshio in the South China Sea. Deep Sea Res. Part I 45, 1469-1482.

Lin, I.-T., Wang, C.-H., Lin, S., 2003. Seasonal variations of oxygen isotopic compositions in the Pingtung coastal waters of Taiwan. Western Pacific Earth Science 3, 21-32.

Mehrbach, C., Culberso, C. H., Hawley, J. E., Pytkowic, R. M., 1973. Measurement of apparent dissociation-constants of carbonic-acid in seawater at atmospheric-pressure. Limnol. Oceanogr. 18, 897-907.

Moore, W. S., 1996. Large groundwater inputs to coastal waters revealed by 226Ra enrichments. Nature 380, 612-614.

Morse, J. W., Bender, M. L., 1990. Partition coefficients in calicite: Examination of factors influencing the validity of experimental results and their application to natural systems. Chem. Geol. 82, 265-277.

Mucci, A., Morse, J. W., 1990. Chemistry of low-temperature abiotic calcites: experimental studies on coprecipitation, stability and fractionation. Aquatic Sci. 2, 217-254.

Nitani, H., 1972. Beginning of the Kuroshio, in Kuroshio, edited by H. Stommel and Y. Yoshida, pp. 129-163. Univ. of Wash. Press, Seattle.

NODC (Levitus) World Ocean Atlas 1998. Provided by the NOAA/OAR/ESRL PSD, Boulder, Colorado, USA.

Olivares, J. A., Houk, R. S., 1986. Anal. Chem. 58, 20.

O'Neil, J. R., R. N. Clayton, and T. K. Mayeda, Oxygen isotope fractionation in divalent metal carbonates, *The Journal of Chemical Physics*, *51*, 5547-5558, 1969.

Oppo, D. W., Sun, Y., 2005. Amplitude and timing of sea-surface temperature change in the northern South China Sea: Dynamic link to the East Asian Monsoon. Geology 33, 785-788.

Ortiz, J. D., Mix, A. C., Rugh, W., 1996. Deep-dwelling planktonic foraminifera of the northeastern Pacific Ocean reveal environmenta; control of oxygen and carbon isotopic disequilibria. Geochim. Cosmochim. Acta 60, 4509-4523.

Pak, D. K., Lea, D. W., Kennett, J. P., 2004. Seasonal and interannual variation in Santa Barbara Basin water temperatures observed in sediment trap foraminiferal Mg/Ca. Geochem. Geophys. Geosyst. 5, doi:10.1029/2004GC000760.

Palmer, M. R., Edmond, J. M., 1989. The strontium isotope budget of the modern ocean. Earth Planet. Sci. Lett. 92, 11-26.

Palmer, M. R., Swihart, G. R., 1996. Boron isotope geochemistry: an overview. In: Crew, E. S., Anovitz, L. M. (Eds.), Boron: Mineralogy, Petrology and Geochemistry. Mineral. Soc. Am., 33, 709-744.

Palmer, M. R., Pearson, P. N., Cobb, S. J., 1998. Reconstructing past ocean pH-depth profiles. Science 282, 1468-1471.

Palmer, M. R., Pearson, P. N., 2003. A 23,000-year record of surface water pH and pCO_2 in the western Equatorial Pacific Ocean. Science 300, 480-482.

Pearson, P. N., Palmer, M. R., 1999. Middle Eocene seawater pH and atmospheric carbon dioxide concentrations. Science 284, 1824-1826.

Pearson, P. N., Palmer, M. R., 2000. Atmospheric carbon dioxide concentrations over the past 60 million years. Nature 406, 695-699.

Pelejero, C., Grimalt, J. O., Heilig, S., Kienast, M., Wang, L., 1999. High resolution U^k_{37}-temperature reconstructions in the South China Sea over the last 220 kyrs. Paleoceanography 14, 224-231.

Pelejero, C. et al., 2004. Preindustrial to modern interdecadal variability in coral reef pH. Science 309, 2204-2207.

Pelletier, G. E., Lewis, E., Wallace, D., 2005. A calculator for the CO_2 system in seawater for Microsoft Excel/VBA, report, Wash. State Dept. of Ecol., Olympia.

Petit, J. R. et al., 1999. Climatic and atmospheric history of the past 420,000 years from the Vostok ice core, Antarctica. Nature 399, 429-436.

Pinon, F., Deson, J., Rosset, R., 1968. Proprie´te´s de la re´sine e´changeuse d'ions spe´cifique du bore amberlite XE 243. Bull. Soc. Chim. Fr. 8Ž535., 3454–3461.

Qu, T., Mitsudera, H., Yamagata, T., 2000. Intrusion of the North Pacific waters into the South China Sea. J. Geophys. Res. 105, 6415-6424.

Raven, J. A., Falkowski, P. G., 1999. Oceanic sinks for atmospheric CO_2. Plant. Cell and Environment 22, 741-755.

Raymo, M. E., 1991. Geochemical evidence supporting T. C. Chamberlin's theory of glaciation. Geology 19, 344-347.

Reeder, R. J., Nugent, M. L., Lamble, G. M., Tait, C. D., Morris, D. E., 2000. Uranyl incorporation into calcite and aragonite: XAFS and luminescence studies. Environ. Sci. Technol. 34, 638-644.

Richter, F. M., Rowley, D. R., DePaolo, D. J., 1992. Sr isotope evolution of seawater: the role of tectonics. Earth Planet. Sci. Lett. 109, 11-23.

Robb, J. M., 1984. Spring sapping on the lower continental slope, offshore New Jersey. Geology 12, 278-282.

Rohling, E., Cooke, S., 1999. Stable oxygen and carbon isotopes in foraminiferal carbonate shells. Modern Foraminifera, 239-258.

Rose, E. F., Chaussidon, M., France-Lanord, C., 2000. Fractionation of boron isotopes during erosion processes : The example of Himalayan rivers. Geochim. Cosmochim. Acta 64, 397-408.

Rosenthal, Y., Boyle, E. A., Slowey. N., 1997. Environmental controls on the incorporation of

Mg, Sr, F and Cd into benthic foraminifera shells from Little Bahama Bank: Prospects for thermocline paleoceanography. Geochim. Cosmochim. Acta 61, 3633-3643.

Rosenthal, Y., Field, M. P., Sherrell, R. M., 1999. Precise determination of element/calcium ratios in calcareous sample using sector field inductivity coupled plasma mass spectrometry. *Anal. Chem.*, *71*, 3248-3253.

Rosenthal, Y., Lohmann, G. P., Lohmann, K. C., Sherrell, R. M., 2000. Incorporation and preservation of Mg in *Globigerinoides sacculifer*: Implication for reconstructing the temperature and $^{18}O/^{16}O$ of seawater. Paleoceanography 15, 135-145.

Rosenthal, Y., Lohman, G. P., 2002. Accurate estimation of sea surface temperatures using dissolution- corrected calibrations for Mg/Ca paleotemperature. Paleoceanography 17, 3, 1044.

Russell, A. D., Emerson, S. R., Nelson, B. K., Erez, J., Lea, D. W., 1994. Uranium in foraminiferal calcite as a recorder of seawater uranium concentrations. Geochim. Cosmochim. Acta 58, 671-681.

Russell, A. D., Emerson, S., Mix, A. C., Peterson, L. C., 1996. The use of foraminiferal U/Ca as an indicator of changes in seawater U content. Paleoceanography 11, 649-663.

Russell, A. D., Hönisch, B., Spero, H. J., Lea, D. W., 2004. Effects of seawater carbonate ion concentration and temperature on shell U, Mg, and Sr in cultured planktonic foraminifera. Geochim. Cosmochim. Acta 68, 4347-4361.

Salisbury, M. H., Shinohara, M., Richter, C., 2002. Site 1202. *Proceeding of the ODP,* Init. Reports 195.

Sample, J. C., Kopf, A., 1995. Occurrences and geochemistry of syntectonic carbonate cements and veins from ODP Leg 146: Implications for hydrogeologica evolution of the Cascadia margin. Proceeding of the ODP, Sci. Results 146, 137-150.

Sanyal, A., Hemming, N. G., Hanson, G. N., Broecker, W. S., 1995. Evidence for a higher pH in the glacial ocean from boron isotopes in foraminifera. Nature 373, 234-236.

Sanyal, A., Hemming, N. G., Broecker, W. S., Lea, D. W., Spero, H. J., Hanson, G. N., 1996. Oceanic pH control on the boron isotopic composition of foraminifera: Evidence from culture experiments. Paleoceanography 11, 513-517.

Sanyal, A., Hemming, N. G., Broecker, W. S., Hanson, G. N., 1997. Changes in pH in the eastern equatorial Pacific across stage 5-6 boundary based on boron isotopes in foraminifera. Global Biogeochem. Cycles 11, 125-133.

Sanyal, A., Bijma, J., 1999. A comparative study of the northwest Africa and eastern equatorial

Pacific upwelling as a source of CO_2 during glacial periods based on boron isotope paleo-pH estimation. Paleoceanography 14, 753-759.

Sanyal, A., Bijma, J., Spero, H. J., Lea, D. W., 2001. Empirical relationship between pH and the boron isotopic composition of Globigerinoides sacculifer: Implications for the boron isotope paleo-pH proxy. Paleoceanography 16, 515-519.

Sigman, D. M., Boyle, E. A., 2000. Glacial/interglacial variations in atmospheric carbon dioxide. Nature 407, 859-869.

Shackleton, N. J., 1974. Attainment of isotopic equilibrium between ocean water and the benthic foraminiferal genus Uvigerina: Isotopic changes in the ocean during the last glacial, Cent. Natl. Rech. Sci. Colloq. Int. *219*, 203-209.

Shackleton, N. J., Opdyke, N. D., 1973. Oxygen isotope and paleomagnetic stratigraphy of equatorial Pacific core V28-238: oxygen isotope temperatures and ice volumes on a 105 and 106 years scale. Quarter. Res. 3, 39-55.

Shackleton, N. J., 1974. Attainment of isotopic equilibrium between ocean water and the benthic foraminiferal genus Uvigerina: Isotopic changes in the ocean during the last glacial. Cent. Natl. Rech. Sci. Colloq. Int. 219, 203-209.

Shackleton, N. J., 1977. ^{13}C in Uvigerina: tropical rainforest history and the equatorial Pacific carbonate dissolution cycles, in Fate of Fossil Fuel CO_2 in the oceans, Plenum, New York, 401-427.

Shannon, 1976. Revised effective ionic radii. Acta crystallog. A32, 751-767.

Shaw, P.-T., 1991. The seasonal variation of the intrusion of the Phillippine Sea Water into the South China Sea. J. Geophys. Res. 96, 821-827.

Speer, J. A., 1983. Crystal chemistry and phase relations of orthorhombic carbonates, in carbonates: Mineralogy and Chemistry, (ed R. J. Reeder), Mineralogical society of America, Washington, D. C., 145-190.

Spivack, A. J., Edmond, J. M., 1986. Determination of boron isotope ratios by thermal ionization mass spectrometry of dicesium metaborate cation. Anal. Chem. 58, 31-35.

Spivack, A. J., Edmond, J. M., 1987. Boron isotope exchange between seawater and oceanic crust. Geochim. Cosmochim. Acta 51, 1033-1043.

Spivack, A. J., Palmer, M. R., Edmond, J. M., 1987. The sedimentary cycle of the boron isotopes. Geochim. Cosmochim. Acta 51, 1939-1949.

Spivack, A. J., You, C.-F., Smith, H. J., 1993. Foraminiferal boron isotope ratios as a proxy for surface ocean pH over the past 21 Myr. Nature 363, 149-151.

Spero, H. J., Parker, S. L., 1985. Photosynthesis in the symbiotic planktonic foraminifer

Orbulina universa and its potential contribution to oceanic primary productivity. J. Foram. Res. 15, 273-281.

Spero, H. J., 1988. Ultrastructural examination of chamber morphogenesis and biomineralization in the planktonic foraminifera Orbulina universa. Mar. Biol. 99, 9-20.

Spero, H. J., Lea, D. W., 1993. Intraspecific stable isotope variability in the planktonic foraminifera Globigerinoides sacculifer: results from laboratory experiments. Mar. Micropaleont. 22, 221-234.

Spero, H. J., Lea, D. W., 1996. Experimental determination of stable isotope variability in Globigerina bulloides: implications for paleoceanographic reconstructions. Mar. Micropaleont. 28, 231-246.

Spero, H. J. et al., 1997. Effect of seawater carbonate concentration on foraminiferal carbon and oxygen isotopes. Nature 390, 497-500.

Steinke, S., Chiu, H.-Y., Yu, P.-S., Shen, C.-C., Erlenkeuser, H., Löwemark, L., Chen, M.-T., 2006. On the influence of sea level and monsoon climate on the southern South China Sea freshwater budget over the last 22,000 years. Quaternary Science Reviews 25, 1475-1488.

Stoll, H. M., Schrag, D. P., 1998. Effects of Quaternary sea level cycles on strontium in seawater. Geochim. Cosmochim. Acta 62, 1107-1118.

Stoll, H. M., Schrag, D. P., Clemens S. C., 1999. Are seawater Sr/Ca variations preserved in Quaternary foraminifera ? Geochim. Cosmochim. Acta 63, 3535-3547.

Takahashi, T. et al., 2002. Global sea-air CO_2 flux based on climatological surface ocean pCO_2, and seasonal biological and temperature effects. Deep-Sea Research II 49, 1601-1622.

Tanner, S. D., Douglas, D. J., French, J. B., 1994. Appl. Spectrosc. 48, 1373.

Trenberth, K. E. et al., 1998. J. Geophys. Res. 103, 14291.

Thomas, R., 2001. A beginner's Guide to ICP-MS Part VII: Mass Separation Devices-Double-Focusing Magnetic –Sector Technology. Spectroscopy 16, 22-24.

Thomas, R., 2002. A beginner's Guide to ICP-MS Part XII: A review of Interferences. Spectroscopy 17, 24-31.

Thomas, H., Bozec, Y., Elkalay, K., de Baar, H. J. W., 2004. Enhanced open ocean storage of CO_2 from shelf sea pumping. Science 304, 1005-1008.

Tomczak, M., Godfrey, J. S., 1994. Regional Oceanography: An introduction. Pergamon, Oxford, p. 422.

Urey, H. C., 1947. The thermodynamic properties of isotopic substances. J. Chem. Soc.

562-581.

Vengosh, A., Chivas, A. R., McCulloch, M. T., 1989. Direct determination of boron and chlorine isotopic compositions in geological materials by negative thermal-ionization mass spectrometry. Chem. Geol. 79, 333-343.

Vengosh, A., Chivas, A. R., McCulloch, J. M., Stainsky, A., Kolodny, Y., 1991. Boron isotope geochemistry of Australian salt lakes. Geochim. Cosmochim. Acta 55, 2591-2606.

Wang, L., Sarnthein, M., Erlenkeuser, H., Grimalt, J., Grootes, P., Heiling, S., Ivanova, E., Kienast, M., Pelejero, C., Pflaumann, U., 1999. East Asian monsoon climate during the Late Pleistocene: high-resolution sediment records from the South China Sea. Mar. Geol. 156, 245-284.

Wara, M. W., Delaney, M. L., Bullen, T. D., Ravelo, A. C., 2003. Possible roles of pH, temperature, and partial dissolution in determinating boron concentration and isotopic composition in planktonic foraminifera. Paleoceanography 18, doi:10.1029/2002PA000797.

Weaver, C. E., 1989. Clays, Muds, and Shales. Development in Sedimentology 44. Elsevier.

Weiner, S., Erez, J., 1984. Organic matrix of the shell of the foraminifer. Heterostegina depressa. J. Foramin. Res. 14, 206-212.

Wiedenbeck, M., 2001. Boron and oxygen isotope composition of certified reference materials NIST SRM 610/612 and reference materials JB-2 and JR-2. Geostandards Newsletter 25, 405-416.

Williams, L. B., Hervig, R. L., Holloway, J. R., Hutcheon, I., 2001. Boron isotope geochemistry during diagenesis. Part I. Experimental determination of fractionation during illization of smectite. Geochim. Cosmochim. Acta 65, 1769-1782.

Winter, B. L., Clark, D. L., Johnson C. M., 1997. Late Cenozoic Sr isotope evolution of the Artic Ocean: constraints on water mass exchange with the lower latitude oceans. Deep-Sea Res. II 44, 1531-1542.

Wyrtki, K., 1961. Physical Oceanography of the Southeast Asian Waters, in *Scientific Results of Marine Investigations of the South China Sea and the Gulf of Thailand, NAGA Rep*., vol. 2, 195 pp., Scripps Instit. of Oceanogr., La Jolla, Calif.

You, C.-F., Spivack, A. J., Smith, J. H., Gieskes, J. M., 1993a. Mobilization of boron in convergent margins: Implications for the boron geochemical cycle. Geology 21, 207-210.

You, C.-F., Gieskes, J. M., Chen, R. F., Spivack, A. J., Gamo, T., 1993b. Iodide, bromide, manganese, boron, and dissolved organic carbon in interstitial of organic carbon-rich marine sediments: Observations in Nankai accretionary prism. Proceeding of the ODP, Init. Reports 131, 165-174.

You, C.-F., Morris, J. D., Gieskes, J. M., Rosebauer, R., Zheng, S. H., Xu, X., Ku, T.-L., Bischoff, J. L., 1994. Mobilization of Be in sedimentary column at convergent margins. Geochim. Cosmochim. Acta 58, 4887-4897.

You, C.-F., Chan, L.-H., Spivack, A. J., Gieskes, J. M., 1995. Lithium, boron, and their isotopes in sediments and pore waters of Ocean Drilling Program Site 808, Nankai Trough: implications for fluid expulsion in accretionary prisms. Geology 23, 37-40.

You, C.-F., Spivack, A. J., Gieskes, J. M., Martin, J. B., Davisson, M. L., 1996. Boron contents and isotopic compositions in pore waters: a new approach to determine temperature induced artifacts- geochemical implications. Marine Geol. 129, 351-361.

You, C.-F., Castillo, P. R., Gieskes, J. M., Chan, L. H., Spivack, A. J., 1996. Trace element behavior in hydrothermal experiments: Implications for fluid processes at shallow depths in subduction zones. Earth Planet Sci. Lett. 140, 41-52.

Yu, J., Elderfield, H., Hönisch, B., 2007. B/Ca in planktonic foraminifera as a proxy for surface seaawater pH. Paleoceanography 22, doi:10.1029/2006PA001347.

Zeebe, R. E., Wolf-Gladrow, D. A., 2001. CO2 in seawater: Equilibrium, kinetics, isotopes. Elsevier Oceanography Series 65. Elsevier. p. 346.

Zhu, Y., Huang, Y., Matsumoto, R., Wu, B., 2003. Geochemical and stable isotopic compositions of pore fluids and authigenic siderite concretions for Site 1146, ODP Leg 184: Implication for gas hydrate. Proceeding of the ODP, Sci. Results 184.

APPENDIX-1

Supplimentary Data

Table A1. Chemical data for *G. ruber* (white) from SCS sediment traps and modern hydrological parameters

Species	Date	Size (μm)	depth (km)	$\delta^{18}O_c$ (‰)	$\delta^{18}O_{sw}$ [a]	Salinity-corrected $\delta^{18}O_c$ [b]	$\delta^{13}C$ (‰)	Mg/Ca (mmol/mol)	Sr/Ca (mmol/mol)	Average T [c]	Average S [d]
G. ruber	Oct/00	250-350	0.240	-3.87	-0.90	-2.97	0.79	5.135	1.663	28.27	33.25
	Oct/00	250-350	1.240	-3.54	-0.23	-3.31	0.42	4.648	1.654	28.27	33.25
	Oct/00	250-350	2.240	-3.63	-0.23	-3.40	0.33	4.705	1.683	28.27	33.25
	Oct/00	250-350	3.240	-3.47	-0.23	-3.24	0.50	4.609	1.724	28.27	33.25
	Jan/01	250-350	0.240	-2.76	-0.02	-2.74	0.23	3.825	1.658	24.80	33.85
	Jan/01	250-350	1.240	-2.61	-0.02	-2.59	0.31	3.244	1.624	24.80	33.85
	Jan/01	250-350	3.240	-2.61	-0.02	-2.59	0.27	3.256	1.653	24.80	33.85
	Dec/01	250-350	0.925	-2.20	_	_	0.08	3.768	1.548	25.50	_
	Dec/01	250-350	2.702	-2.46	_	_	0.28	4.129	1.757	25.50	_
	Jan/02	250-350	0.925	-2.26	_	_	0.33	3.509	1.536	24.80	_
	Mar/02	250-350	0.925	-2.53	0.14	-2.67	0.37	3.454	1.678	24.79	34.31
	Mar/02	250-350	1.925	-2.24	0.14	-2.38	0.17	3.625	1.524	24.79	34.31
	Mar/02	250-350	2.702	-2.43	0.14	-2.57	0.20	3.882	1.566	24.79	34.31
	May/02	250-350	0.597	-3.38	-0.09	-3.29	0.62	4.357	1.607	28.46	33.65
	May/02	250-350	1.126		-0.09			4.016	1.544	28.46	33.65
	May/02	250-350	1.726	-3.07	-0.09	-2.98	0.26	3.926	1.528	28.46	33.65
	May/02	250-350	2.326	-2.53	-0.09	-2.44	0.26	4.274	1.511	28.46	33.65
	July/02	250-350	0.597	-3.27	-0.11	-3.16	0.53	4.691	1.571	30.38	33.60
	July/02	250-350	1.126	-3.09	-0.11	-2.98	0.40	5.056	1.591	30.38	33.60
	July/02	250-350	2.326	_	-0.11	_	_	4.414	1.540	30.38	33.60
	Aug/02	250-350	0.597	-3.10	-0.08	-3.02	0.66	3.955	1.563	29.46	33.67
	Aug/02	250-350	1.126	-3.31	-0.08	-3.23	0.44	4.248	1.579	29.46	33.67
	Aug/02	250-350	2.326	-3.41	-0.08	-3.33	0.94	4.429	1.596	29.46	33.67

[a] $\delta^{18}O_{sw}$ were calculated from modern S-δ^{18}Osw relationship [*Lin et al*., 2003] and habitat mean salinity. [b] salinity-corrected $\delta^{18}O_c$ were obtained from measured $\delta^{18}O_c$ and estimated δ^{18}Osw. [C] Average T: Habitat mean temperature used in this study was estimated from in situ seawater temperature and habitat depth for each species. [d] Average S: Habitat mean salinity used in this study.

Table A1. (Continued) Chemical data for *G. sacculifer* (w/o sac) from SCS sediment traps and modern hydrological parameters

Species	Date	Size (μm)	depth (km)	$\delta^{18}O_C$ (‰)	$\delta^{18}O_{sw}$[a]	Salinity-corrected $\delta^{18}O_c$[b]	$\delta^{13}C$ (‰)	Mg/Ca (mmol/mol)	Sr/Ca (mmol/mol)	Average T[c]	Average S[d]
G. sacculifer	Oct/00	250-350	0.240	-3.46	-0.11	-3.35	0.81	3.685	1.691	27.86	33.60
	Oct/00	250-350	1.240	-3.41	-0.11	-3.30	0.89	3.499	1.488	27.86	33.60
	Oct/00	250-350	2.240	-3.08	-0.11	-2.97	0.50	3.234	1.536	27.86	33.60
	Oct/00	250-350	3.240	-2.85	-0.11	-2.74	0.69	2.836	1.574	27.86	33.60
	Jan/01	250-350	0.240	-2.30	0.08	-2.38	0.50	2.827	1.578	23.90	34.15
	Jan/01	250-350	1.240	-2.31	0.08	-2.39	0.63	2.739	1.580	23.90	34.15
	Jan/01	250-350	3.240	-2.35	0.08	-2.43	0.54	2.555	1.561	23.90	34.15
	Dec/01	250-350	1.925	-2.32	_	-2.32	0.51	3.199	1.616	25.40	_
	Dec/01	250-350	2.702	-1.99	_	-1.99	0.48	3.092	1.469	25.40	_
	Jan/02	250-350	0.925	-2.05	_	-2.05	0.54	2.829	1.434	24.30	_
	Jan/02	250-350	1.925	-2.01	_	-2.01	0.34	2.955	1.456	24.30	_
	Jan/02	250-350	2.702	-1.97	_	-1.97	0.63	2.972	1.549	24.30	_
	Mar/02	250-350	0.925	-1.92	0.20	-2.12	0.51	2.970	1.438	24.31	34.50
	Mar/02	250-350	1.925	-2.25	0.20	-2.45	0.46	3.343	1.438	24.31	34.50
	Mar/02	250-350	2.702	-2.07	0.20	-2.27	0.37	2.993	1.431	24.31	34.50
	May/02	250-350	0.597	_	0.10	_	_	3.091	1.414	26.72	34.20
	May/02	250-350	1.126	-2.35	0.10	-2.45	0.91	3.136	1.438	26.72	34.20
	May/02	250-350	1.726	-2.12	0.10	-2.22	0.84	2.632	1.426	26.72	34.20
	May/02	250-350	2.326	-2.35	0.10	-2.45	1.00	3.133	1.452	26.72	34.20
	July/02	250-350	0.597	_	-0.07	_	_	3.239	1.430	28.53	33.73
	July/02	250-350	1.126	-2.89	-0.07	-2.82	0.99	3.144	1.488	28.53	33.73
	July/02	250-350	2.326	_	-0.07	_	_	3.277	1.481	28.53	33.73
	Aug/02	250-350	0.597	-2.52	-0.09	-2.43	0.44	2.903	1.434	27.10	33.66
	Aug/02	250-350	1.726	-3.00	-0.09	-2.91	0.94	3.103	1.411	27.10	33.66
	Aug/02	250-350	2.326	-2.46	-0.09	-2.37	0.67	3.316	1.483	27.10	33.66

Table A1. (Continued) Chemical data for *N. dutertrei* from SCS sediment traps and modern hydrological parameters

	Date	**Size (μm)**	**depth (km)**	**Mg/Ca (mmol/mol)**	**Sr/Ca (mmol/mol)**	**Average T**^{c}	**Average S**^{d}
N. dutertrei	Oct/00	250-350	0.240	2.387	1.524	23.42	34.40
	Oct/00	250-350	1.240	2.059	1.508	23.42	34.40
	Jan/01	250-350	0.240	2.789	1.533	23.30	34.10
	Jan/01	250-350	1.240	2.631	1.459	23.30	34.10
	Jan/01	250-350	3.240	2.104	1.561	23.30	34.10
	Dec/01	250-350	0.925	2.328	1.470	25.00	_
	Dec/01	250-350	1.925	2.306	1.461	25.00	_
	Dec/01	250-350	2.702	2.484	1.460	25.00	_
	Jan/02	250-350	0.925	2.628	1.517	21.90	_
	Jan/02	250-350	1.925	2.198	1.464	21.90	_
	Jan/02	250-350	1.925	2.274	1.474	21.90	_
	Jan/02	250-350	2.702	2.211	1.453	21.90	_
	Mar/02	250-350	0.925	2.944	1.461	21.78	34.69
	Mar/02	250-350	1.925	2.773	1.461	21.78	34.69
	Mar/02	250-350	2.702	2.659	1.438	21.78	34.69
	May/02	250-350	0.597	2.418	1.378	20.97	34.60
	May/02	250-350	1.126	2.284	1.402	20.97	34.60
	May/02	250-350	1.726	2.244	1.424	20.97	34.60
	May/02	250-350	2.326	2.317	1.405	20.97	34.60
	July/02	250-350	0.597	2.280	1.394	22.30	34.28
	July/02	250-350	1.126	2.199	1.441	22.30	34.28
	July/02	250-350	2.326	2.040	1.431	22.30	34.28
	Aug/02	250-350	0.597	2.340	1.406	23.20	_
	Aug/02	250-350	1.126	2.309	1.406	23.20	_
	Aug/02	250-350	2.326	2.230	1.374	23.20	_

APPENDIX-2

Curriculum Vitae

CURRICULUM VITAE

Kuo-Fang Huang (Denner)

Date of Birth: 11/10/1976

E-mail: l4890107@ccmail.ncku.edu.tw

Education

1996.9-2000.7 **B.Sc. in Earth Sciences, National Cheng Kung University, Taiwan**

Research work in Geochemistry: Geochemical Analyses of Hydrothermal Vent Fluids near Guei-Shan Island offshore Northeastern Taiwan.

Supervisor: Dr. Chen-Feng You (Department of Earth Sciences, NCKU)

2001.9-2007.7 **Ph.D. in Earth Sciences, National Cheng Kung University, Taiwan**

Dissertation title: Trace element ratios and Stable Isotopic Compositions in Planktonic Foraminifera Shell Calcite: Calibration and Paleoceanographic Implications in the South China Sea

Supervisor: Dr. Chen-Feng You (Department of Earth Sciences, NCKU)

Committee: Drs. S. Luo, T.-Y. Ho, H.-L. Lin, Y.-T. Shieh, K.-S. Ho, H.-J. Yang

2006.3-2007.2 **Visiting student. Institutes of Marine and Coastal Sciences, Rutgers University.**

Research works in [1] Developments of new proxies (B/Ca, S/Ca, Nd/Ca, Zn/Ca and Ba/Ca) for planktonic foraminifera; [2] High resolution paleo-climatic records of the South China Sea over the late Holocene; [3] Applications of laser ablation technique for foraminiferal shell chemistry.

Supervisor: Dr. Yair Rosenthal (Rutgers University)

Cooperation: Drs. Rob Sherrell and Paul Field (Rutgers University)

Research Interests

- Paleoceanography and Paleoclimatology in the Pleistocene-Holocene
- Chemical Oceanography
- New analytical technique for isotopic analyses using TIMS and ICP-MS
- Biogeochemical behaviors of trace elements and isotopes in the ocean and estuary
- Pore water and hydrothermal fluid Chemistry

Technical Skills

Trace Element and Isotopes Chemistry: Purification and Pre-concentration (Seawater)

Clean and Separation of Foraminifera

Mass Spectrometry:

Inductively Coupled Plasma: (Thermal Finnigan Element I, II, and XR)

Introduction System: Solution (Aridus and APEC desolvating, and stable inlet system)

Solid (Nd:YAG Laser LUV266X and Excimer 193 nm)

Thermal Ionization: (Thermo Finnigan Triton TI and MAT 262, Positive and Negative)

Carbon and Oxygen Isotope Ratios: (Thermo Finnigan Delta ^{plus} XP)

Other Analytical Instruments:

ICP-OES: (Perkin-Elmer Optima 2000DV)

Atomic Absorption Spectrometry: (Perkin-Elmer AAnalyst 300, Graphite and Flame)

UV-Visible Spectrophotometer (Varian Cary WinUV)

Liquid ion Chromatography: (Alltech)

Gas Chromatography

Separation Chemistry:

Amberlite IRA 743 (Boron), Sr^{SPEC} (Sr, Pb, Ba, Ca); TRU resin (U and Th); Co-precipitation (trace metals, REEs); Chelex-100 resin (transition metals); Ln and Re resin (REEs and Nd isotope); Cation and Anion ion exchange resin (Mg and Li)

Other techniques:

Digestion (notably microwave and furnace); Core sediment (including identification of foraminiferal species)

Conference Abstracts

1. **Kuo-Fang Huang**, C.-F. You, C.-T. Chen, and L.-S. Fang (2000) Geochemical Study of Seafloor Hydrothermal Vents near the Guei-Shan Island offshore northeastern Taiwan. *Geological Society Annual Meeting, 251-252*.
2. **Kuo-Fang Huang**, C.-F. You, S.-J. Kao, and C.-H. Chiu (2001) Preliminary Geochemical Study of Hydrothermal Vent Fluids offshore Guei-Shan Island Northeastern Taiwan. *Geological Society Annual Meeting, 363-364*.
3. **Kuo-Fang Huang**, C.-F. You, and M.-D. Li (2002) Precise Determination of Boron in Low Concentration Natural Samples. *Geological Society Annual Meeting, 383-385*.
4. **Kuo-Fang Huang**, C.-F. You, and H.-L. Lin (2003) The Systematics of Boron and Boron Isotopes in ODP 1146 Pore Waters: Geochemical Implications. *Geological Society Annual Meeting*.
5. **Kuo-Fang Huang**, C.-F. You, H.-L. Lin, Y.-T. Shieh, and M.-D. Li (2004) Past Sea Surface Temperature Variations in the South China Sea inferred from foraminiferal shell chemistry. *2004 Joint Geosciences Assembly Meeting*.

6. **Kuo-Fang Huang**, C.-F. You, H.-L. Lin, Y.-T. Shieh, and M.-D. Li (2005) Calibration of Mg/Ca and Sr/Ca in Planktonic Foraminiferal Shells and Seawater by Time-series Sediment Trap in the South China Sea. *Workshop for 2005 Oceanographic Research Programs, Abstract Volume, 245-246.*
7. **Kuo-Fang Huang**, C.-F. You, C.-H. Chung, and I.-T. Lin (2005) Studying the Dynamic Distribution of Fresh Water Plume at the Estuary Using Sr Isotopic Compositions. *Geological Society Annual Meeting.*
8. **Kuo-Fang Huang** and C.-F. You (2007) Non-homogeneous distributions of seawater Sr isotopic composition in the coastal waters around Taiwan: Implications for submarine groundwater discharge and oceanic water masses. *2007 Taiwan Geosciences Assembly.*

International Conference Abstracts

1. C.-F. You, M.-D. Li, C.-H. Chung, and **K.-F. Huang** (2001) Boron Isotopic Compositions of Mud Volcano Fluids in Taiwan Accretionary Prism. ***2001 AGU Fall Meeting, San Francisco.***
2. **Kuo-Fang Huang**, C.-F. You, M.-D. Li, and Y.-T. Shieh (2002) High Resolution Glacial-interglacial Climatic Variations in the South China Sea during the Last 220,000Years. ***2002 AGU Fall Meeting*. *San Francisco.* PP51A-0300**.
3. **Kuo-Fang Huang**, C.-F. You, H.-L. Lin, M.-D. Li, and Y.-T. Shieh (2003) Calibration of Mg/Ca, Sr/Ca and Ba/Ca in Sediment Trap Planktonic Foraminiferal Shells and Seawater. ***2003 AGU Fall Meeting. San Francisco.* PP11A-0210**.
4. **Kuo-Fang Huang**, C.-F. You, H.-L. Lin, Y.-T. Shieh, and M.-D. Li (2005) Calibration of Mg/Ca and Sr/Ca in Planktonic Foraminiferal Shells and Seawater by Time-series Sediment Trap in the South China Sea. ***EGU General Assembly 2005.***Vienna. **EGU05-A-01123 X103**.
5. **Kuo-Fang Huang**, C.-F. You, C.-H. Chung, and I.-T. Lin (2006) Coastal Fresh Water Plume Migration Traced by High Precision Strontium Isotopic Composition in the Kao-Ping Estuary, Southern Taiwan. ***2006 Ocean Science Meeting, Hawaii.* OS16A-11**.
6. **Kuo-Fang Huang**, Y. Rosenthal, C.-F. You, H.-L. Lin, and Y.-T. Shieh (2006) B/Ca and S/Ca in Planktonic Foraminiferal Shells: Core-top Calibrations and Paleoceanographic Implications. ***2006 AGU Fall Meeting. San Francisco.* PP21C-1701**.
7. Kuo-Fang Huang and C.-F. You (2007) Non-homogeneous Distribution of Sr Isotopic Composiiton in the Coastal Seawater around Taiwan: Implications for Groundwater Discharge and Oceanic Water Masses. 2007 Asia Oceania Geosciences Society 4th Annual Meeting, Bangkok. **OS04-D1-AM1-BR2-006**.

Thesis

Kuo-Fang Huang (2000) Geochemical Analyses of Hydrothermal Vent Fluids near Guei-Shan Island offshore Northeastern Taiwan. B.S. thesis. Department of Earth Sciences, National Cheng Kung University.

Kuo-Fang Huang (2007) Trace Element Ratios and Isotopic Compositions in Planktonic Foraminifera Shell Collected from the South China Sea: Geochemical Calibration and Paleoceanographic Implication. PhD thesis. Department of Earth Sciences, National Cheng Kung University.

Journals (Published)

Kuo-Fang Huang, C.-F. You, M.-L. Shen, and H.-L. Lin (2005) Geochemistry of Major Constituents, Boron and Boron Isotopes in Pore Waters from ODP Site 1202, Okinawa Trough. *Terrestrial, Atmospheric and Oceanic Sciences*, **16**, 1, 75-93. **(SCI)**

Kuo-Fang Huang and C.-F. You (2007) Tracing Freshwater Plume Migration in the Estuary after a Typhoon Event using Sr Isotopic Ratios. *Geophysical Research Letters, 34, L02403, doi:10.1029/2006GL028253*. **(SCI)**

Kuo-Fang Huang, C.-F. You, H.-L. Lin, and Y.-T. Shieh (2007) In situ Calibration of Mg/Ca Ratio in Planktonic Foraminiferal Shells from Time-series Sediment Trap in the South China Sea. (*Geochemistry Geophysics Geosystems*. In revision). **(SCI)**

Journals (Submitted and In preparation)

Kuo-Fang Huang, Y. Rosenthal, C.-F. You, D. Oppo, H.-L. Lin and Y.-T. Shieh (2007) Reconstructions of changes in surface water pCO_2 in tropical South China Sea using the foraminiferal multiproxy approach. (will be submitted to *Geochimica Cosmochimica Acta*)

Kuo-Fang Huang and C.-F. You (2007) Non-homogeneous distributions of seawater Sr isotopic composition in the coastal waters around Taiwan: Implications for submarine groundwater discharge and oceanic water masses. (in preparation)